Investigating Solid-State Reactions via Kinetic Control of Designed Precursors

by

Hannah R. Hazel

A dissertation accepted and approved in partial fulfillment of the

requirements for the degree of

Doctor of Philosophy

in Chemistry

Dissertation Committee:

Dr. Ramesh Jasti, Chair

Dr. David C. Johnson, Advisor

Dr. Christopher Hendon, Core Member

Dr. Marian Hettiaratchi, Institutional Representative

University of Oregon

Summer 2025

© 2025 Hannah R. Hazel

This work is openly licensed via CC BY-NC-SA 4.0.

DISSERTATION ABSTRACT

Hannah R. Hazel

Doctor of Philosophy in Chemistry

Title: Investigating Solid-State Reactions via Kinetic Control of Designed Precursors

The discovery and synthesis of novel materials with tunable properties is central to advancing modern technology. There has been a recent increase in the power of computational chemistry to predict new stable phases, but there is a large gap between the number of predicted compounds and those that have been synthesized. Bridging this gap will require affectively designed syntheses to target the growth of these predicted phases. Successful synthetic design relies on an atomic level understanding of the fundamental mechanisms of solid-state reactions – diffusion and nucleation. A complete understanding of these steps remains elusive, in part due to the inherent experimental challenges associated with investigating them. Consequently, there is a critical need to develop novel approaches for using experimentally controllable parameters to isolate and investigate these fundamental mechanisms.

This dissertation investigates the use of the modulated elemental reactant (MER) method to create designed precursors that function as a platform to isolate and probe how individually tunable experimental parameters – especially local compositions, and deposited layer thicknesses and sequences – influence fundamental reaction mechanisms. Insights gained from these studies can be leveraged to synthesize new materials with controllable structure and, consequently, tunable properties. The first section (Chapters I-III) frames this work within the larger body of solid-state research, and describes the experimental methods used to synthesize and characterize all of the samples discussed herein – including the description of the development of a novel method to measure the cross-plane electronic transport properties of thin film materials. The

second section (Chapters IV-VI) focuses on using experimentally tunable parameters to study solid state growth mechanisms and how control over these mechanisms can be achieved through manipulation of designed precursors. Particular emphasis is placed on the Mo-Se and Pb-Se systems, which, due to their relatively simple phase diagrams, provide useful model frameworks for elucidating the fine details of solid-state reaction mechanisms. Through the knowledge gained in these studies, a new general method was developed to create high-energy amorphous precursors, and a series of new non-equilibrium Mo-$MoSe_2$ superlattices were grown. The third section (Chapters VII and VIII) describe the synthesis of novel heterostructures that were enabled through the understanding of reaction mechanisms gained in the proceeding chapters. A novel $(PbSe)_1(VSe_2)_1(PbSe)_m(VSe_2)_1$ homologous series was synthesized using the precise layer-sequence control afforded by the MER method. Additionally, a previously unreported ZnSe phase was stabilized within $(MoSe_2)_1(ZnSe)_n$ heterostructures, enabled by interfacial confinement between van der Waals planes of $MoSe_2$ monolayers. This work advances the already well-established capabilities of the MER method to access novel phases by leveraging its precise experimental parameter control to probe fundamental solid-state reaction mechanisms at an unprecedented atomic level. This mechanistic insight further enhances the method's potential to rationally design and synthesize previously inaccessible materials.

This dissertation includes previously published and unpublished co-authored material.

CURRICULUM VITAE

NAME OF AUTHOR: Hannah R. Hazel

GRADUATE AND UNDERGRADUATE SCHOOLS ATTENDED:

University of Oregon, Eugene OR
Pacific Lutheran University, Tacoma WA
Pierce College, Lakewood WA

DEGREES AWARDED:

Doctor of Philosophy, Chemistry, 2025, University of Oregon
Bachelor of Science, Chemistry, 2020, Pacific Lutheran University
Associate of Science, 2018, Pierce College

AREAS OF SPECIAL INTEREST:

Materials Science
Thin Film Synthesis and Characterization
Focused-Ion Beam

PROFESSIONAL EXPERIENCE:

Research Assistant, D. C. Johnson Research Group, University of Oregon, 2020-2025

FIB-SEM Technician, Samtec, 2023-2025

FIB-SEM Engineer, Sparkle Cut Diamonds Inc., 2021-2023

Research Assistant, D. Waldow Research Group, Pacific Lutheran University, 2019-2020

PUBLICATIONS:

Blackwood, H. R.; Lu, P.; Rudin, S. P.; Johnson, D. C. Nucleation controlled synthesis of designed heterostructures. Submitted to *Angewandte Chemie International Edition*. **2025.**

Weng, S.; Wang, Y.; Price, C.; **Blackwood, H. R**.; Choffel, M.; Miller, A.; Li, R.; Chen, M.; Lu, P.; Ilkhani, S.; Majumdar, A.; Johnson, D. C.; Cronin, S. B. Simultaneous Characterization of In-

Plane and Cross-Plane Resistivities in Highly Anisotropic 2D Layered Heterostructures. *ACS Nano* **2024**, *18* (37), 25405–25413.

Blackwood, H. R.; Walker, A.; Johnson, D. C. Synthesizing Amorphous Precursors through Control of Local Composition. *Chemistry of Materials* **2024**, *36* (9), 4766–4774.

Harvel, F.[‖]; Lemon, M.[‖]; Gannon, R. N.; Rudin, S. P.; Lu, P.; **Blackwood, H. R.** Johnson, D. C. 1T-FeSe2 Layers in (PbSe)1+δ(FeSe2)n – An Interlayer-Stabilized 2D Structure. *Chem. Mater.,* **2023**. 35 (18), 7521-7528.

Gannon, R. N.; Choffel, M. A.; **Blackwood, H. R**.; Wolff, N.; Lotnyk, A.; Kienle, L.; Johnson, D. C. Growth of Crystallographically Aligned PbSe Films of Controlled Thickness on Amorphous Substrates. *Zeitschrift fur Anorganische und Allgemeine Chemie* **2022**, *648*, e202200015.

ACKNOWLEDGMENTS

I can't believe how blessed I am to have so many people to thank for supporting me during this endeavor, and through my entire life. First, thank you to my advisor Dr. David C. Johnson for providing so much patience and an always open door. If I had to pick Dave's two most exceptional qualities, I think they would be 1) providing students with an incredibly welcoming, hands-on, accessible advisor who is truly passionate and truly invested in helping us become the best scientists possible; and 2) those wild analogies. Dave, thank you for your warmth, for your support, and for sharing your incredible wealth of knowledge to help shape me into a scientist capable of critical thinking and the ability to use data to answer questions. It's been a blast. I want to thank my fellow DCJ Lab members, current and past. First, thank you to Marisa Choffel for providing such a warm and comforting environment for me upon entering grad school. Your kindness, relateableness, and humor provided an unmatchably excellent lab environment. I can't imagine a better possible mentor, and friend. To Fischer Harvel and Sarah Rich, doing this journey with the two of you by my side has been an honor. Fischer, our many philosophical office chats have been such an enjoyable and valuable part of grad school that have helped get me through many tough moments. I'll cherish the memories from our trip to Germany together for a lifetime. My Sarah, we showed up on our first day in grad school in the DCJ lab together, innocent little babies, and together we've grown into independent science queens. You have become one of my dearest friends, and I couldn't be prouder of the things we've accomplished and overcome. You inspire and motivate me every day to persist, no matter what. Thank you to Celsey Price for being such a bright light in our group, you make me smile. Thank you to the newer lab members Josh Cooper and Wycliffe Misigo for adding new life and energy (and upper body strength) to our group. I'm so excited to see what each of you accomplish. Thank you to past lab members Mellie Lemon, Aaron Miller, and Renae Gannon. Mellie, thank you for making me feel comfortable entering grad school, and for becoming such a special friend. Our friendship taught me so much. Aaron, thank you for always being willing to answer my many questions and for your ability to explain complicated topics in an incredibly accessible way. Renae, thank you for being so cool that it motivated me to try to be as cool as you (I'm still trying). Thank you to each of my undergrads and rotation students, Henry Hutley, Michael O'Rourke, Megan Rammer, Teri Knaup, Annalise Walker, and Mollie Long. Thank you for teaching me how to teach and for listening to all of my unsolicited old lady life advice.

Thank you to all of the chemistry department administrative staff, we would have no idea how to do anything without your patient assistance. Special thanks to Christi Mabinuori for making entering grad school so much less scary. Thank you to everyone at CAMCOR for providing such incredible facilities and expertise. Thank you to Steve Wiemholt for sharing your depth of knowledge about electronics and vacuum systems to constantly help us when things break and for going above and beyond when it comes to explaining the intricacies of complicated systems. Your passion is obvious and inspiring. Thank you to Jefferson Garman, you and Steve are the glue holding it all together. To Valerie Brogden, knowing you and working with you has been a privilege and and honor. Few people (or maybe none) have taught me more or had a bigger direct impact on my success than you. Thank you for everything, I quite literally could not have done it without you.

Thank you to the many collaborators I've had the pleasure of working with over the past five years. Yu Wang, Sizhe Weng, and Sina Ikhani from the Stephen Cronin group at USC, your patience and hard-work during our collaboration has been much appreciated. Thank you to the office of naval research for funding the multi-university research initiative that has funded my research, and to all the groups that have been a part of this amazing collaboration (Josh Goldberger and Joseph Heremans at Ohio State University, Li Shi and Allen Macdonald at the University of Texas-Austin, Philip Kim at Harvard, and Arun Majumdar at Stanford). Thank you to Dr. Sven P. Rudin at Los Alamos National labs for always listening to our wild ideas and helping to turn them into actual calculations, your long-term relationship with the DCJ lab has been invaluable. Thank you to Ping Lu at Sandia National Lab for sharing your incredible skill at collecting beautiful microscopy images of our samples, and for always being willing to give valuable feedback on FIB lamella prep. My extreme thanks goes to Dr. Kornelius Nielsch at the Leibniz Institute for Solid State and Materials Research (IFW) in Dresden, Germany for providing me with the incredible opportunity to spend a month at the IFW learning and collecting measurements on my samples. Special thanks to Dr. Nicolas Perez Rodriguez who was my direct mentor at the IFW. Thank you for having the patience and taking the time to explain physics concepts to us lowly chemists. I had a higher concentration of "aha" moments in the month I spent learning from you than I've had in any other situation in my life thus far. You have an incredible skill for teaching and science communication and I feel very lucky to have had the opportunity to learn from you, about science and otherwise. I hope our paths cross again. Thank you to the incredible chemistry faculty at

Pacific Lutheran University. Special thanks to Dr. Dean Waldow, for allowing me to do research in your group even though I had zero previous research experience. Thank you for believing in me and giving me confidence as a blossoming young scientist. Thank you to Dr. Brian Naasz for drilling into my brain the importance of identifying sources of error, and for making me laugh. Thank you to Ted Wood at Pierce College, if not for your passion for chemistry, I never would have realized my own.

Thank you to my family. Dad, you have always been tough, hard-working, and generous; but when you became a single parent to four teenagers, you never wavered. You gave us a steadfast example of patience and love and what it looks like to be a father, to the highest degree. I am so lucky to have you as my Dad. Anita, thank you for becoming a part of our family and being such a wonderful partner to my Dad, I can't imagine him being any luckier. Elijah, thank you for being so patient with your annoying little sister for your whole life. Thank you for being exactly who you are and for providing me with an example of living authentically and never compromising yourself to fit into any specific box. Thank you for always wanting to share your passions with me, it makes me feel so special and so lucky to be able to have my big brother be one of my best friends. Esther, I can't even begin to express how proud I am of you and how thankful I am to have you as my sister. You are such a special, bright light in the world. You have overcome so much in your life and you're one of the toughest and most persistent people I've ever known. I'm so inspired by and thankful for you and your spirit. Brennan, thank you for coming into my sister's life and being such a wonderful partner to her, I'm so happy you're a part of our family. To Josiah, my little buddy. Thank you for being my best friend, thank you for making me smile, thank you for making me want to make you proud, and thank you for existing so that I can revel every day in the feeling that there is a little fragment of my soul that I get to be on the planet with at the same time. You carry an incredibly special light in you. You were her light, and I can feel her presence in you. So thank you for being here to continue to share that with me. Thank you for your passion for nature and for always reminding me that even "with all its sham, drudgery and broken dreams it is still a beautiful world." Thank you to my sweet, precious little Alex, my other best friend. You are such a joy in my life, I just absolutely adore you. Thank you for bringing so much fun and adorableness into my life, I cherish our relationship and I feel so lucky to get to be your sister. Thank you to my chosen sister, Grace. You are my heart. You are the rock that I feel holding me steady, giving me the bravery to try scary things and make hard choices. Because I know that

no matter what mistakes I make or failures I have, my rock will be there to hold me up. My Grace will be there to give me grace, and love, and warmth. Thank you to Colby for being a steadfast partner for such a significant part of my adult life. You taught me so much, and I wouldn't have achieved the things that I have without your support. Thank you for everything. Thank you to Bones, Rudy, Ferdinand, Raven, and Mayo; I know none of you can read English, but I couldn't write my acknowledgements fully and not say thank you to each of you for sharing your precious, innocent, pure little spirits with me. You have each been a joy and a delight and have provided me with so much comfort throughout the challenges of my life. Thank you to my Dalton, my Stuff, my soup snake. You made it impossible to not fall in love with you and want to run through life hand-in-hand, squeezing out every possible drop of fun, and laughter, and appreciation of the small, beautiful moments that are breath-taking in their simplicity. You make me want to slow down and revel in how wonderful life can be. And with you by my side, it really is. Finally, thank you to my mom, Amy Bergen Hamovitz. You are one of the greatest lights to have ever blessed this earth. It's easy to want to say that you left the world too soon, because I wish you were still here with me. I wish you could be here to see everything I've accomplished. I wish I could hear you tell me that you're proud of me. And I wish I could know what it would feel like to talk to you as an adult, and to become your friend. But I know that you didn't leave too soon. You left at exactly the time that you were meant to, and I am thankful for every single moment and experience in my life that has led to the beautiful life that I now have. Thank you for giving your whole self to being our mother. Thank you for teaching me to interact with the world using the scientific method. Thank you for blessing me with a love of learning, and thank you for giving me the insatiable need to never stop asking the question, "why?"

To my mom,

for weaving a love of learning into the fibers of my spirit.

TABLE OF CONTENTS

Chapter Page

LIST OF FIGURES

LIST OF TABLES

CHAPTER I
INTRODUCTION

1.0. Authorship Statement

This chapter was written for this work alone with no intention of publishing elsewhere. I am the primary author, and I received editing assistance from my advisor, David C. Johnson.

1.1. Motivation and Background

The discovery and development of new materials is an essential driving force of technological advancement, enabling constant improvements in the efficiency, size, and cost-effectiveness of the devices on which our society has grown to depend. The Silicon Age and the advent of transistors has harbored an explosion of new technologies, with a constant march toward continued miniaturization, as predicted by Moore's Law.[1] With this rapid expansion of silicon-based technology has come an increased reliance of our society on these technologies and the materials that comprise them. Forward progress in the pursuit of new and better technologies will rely on the ability of scientists to discover and develop materials with new properties that will support new and improved technologies. In just the last twenty years, the development of numerous ground-breaking new technologies has already been made possible through the discovery of new materials. A few notable examples include quantum computing,[2–4] solid-state batteries,[5–7] solar cells,[8–10] energy storage,[11,12] thermoelectrics for waste heat recovery,[13–16] and wearable electronics.[17]

In recent years, computational chemistry has become the most significant driving force for materials discovery due to the power of density functional theory (DFT) to theoretically predict thermodynamically stable new materials.[18] Many of these predicted new materials have complex unit cells or are metastable, which has created a discrepancy between the number of predicted theoretically stable materials and those that have been successfully synthesized.[19,20] A significant barrier in the synthesis of new materials is the facile formation of undesirable reaction intermediates (especially binary compounds) that prevent the formation of more complex phases.[21–23] A vital component to narrowing the gap between the number of predicted and

synthesized new materials will be increasing our understanding of what is happening atomically during the two fundamental steps of a solid-state reaction: diffusion and nucleation.

Diffusion is one of the two fundamental mechanisms of solid-state reactions. It is well-understood that because diffusion is slow, it is the rate-limiting step in most solid state reactions.[24,25] Even when energy (heat) is added to a system, atoms do not move very far. This is because the reactants usually have high melting points, and the atoms are trapped in their original crystal lattices. As a result, diffusion rates remain low. The temperature dependance of diffusion is typically understood to have Arrhenius type behavior, with higher temperatures exponentially increasing atomic mobility. As a result, in traditional direct reaction between elements, the most common tactic to overcome rate-limiting diffusion is to employ very high temperatures that make it hard to avoid growing only thermodynamic products. Multiple heating/grinding steps are often used to reduce particle sizes and shorten diffusion distances, commonly known as the traditional "heat and beat" method.[26] Fick's laws of diffusion describe how atoms move in a homogenous environment in response to a concentration gradient and how those concentration gradients change with time as diffusion progresses.[27,28] However, the heterogeneous reaction environments more commonly found during solid-state synthesis are more complex because different crystal orientations interdiffuse at different rates. While these laws are useful to understand local components of the reaction environment, they are too simple to fully describe every piece of a solid-state reaction. In a "heat and beat" synthesis, the lowest melting point species will become mobile first and "wet" the surface of any other reactants. Concentration gradients will form between reacting species, and local compositions at interfaces will determine what phases form at the interfaces. As an intermediate phase grows at an interface, it creates a diffusion barrier that further impedes the diffusion of reacting species. This leads to a sequence of phase formation over which there is very little experimental control. As a result of these factors, the overall composition of a system does not necessarily control what intermediate phase(s) will form, and phase-pure products can be challenging to achieve under these diffusion-limited constraints. In polycrystalline materials, diffusion may preferentially occur along defects like grain boundaries and dislocations. These "short-circuit" diffusion paths enhance the diffusion rates compared to bulk diffusion but further complicate solid-state systems and our ability to study them.

Nucleation is the second fundamental mechanism of a solid-state reaction. Nucleation limitations control which phases can form and when they can appear during a reaction. Classical nucleation theory (CNT) describes the critical size of an atomic cluster within a parent phase that must be exceeded to form and grow a stable nucleus of a new phase.[29–31] These nuclei undergo dynamic fluctuations in size, dissolving back into the parent phase until a nucleus exceeds a critical radius, and it becomes thermodynamically favorable for the nucleus to grow into a stable crystallite.[32,33] CNT considers two competing contributions to the total Gibbs free energy change of forming a nucleus. The volume free energy change ($\Delta G_V < 0$) is negative and provides the thermodynamic driving force for the formation of a crystalline grain. The surface energy ($\gamma > 0$) term is positive, which accounts for the energetic "cost" of generating a new interface between the nucleus and the surrounding matrix. These terms determine the free energy barrier to nucleation and define the critical nucleus size that must be exceeded for growth to become thermodynamically favorable. The critical radius ($r^* = -\frac{2\gamma}{\Delta G}$) is defined as the size at which the change in total free energy ($\Delta G(r) = \frac{4}{3}\pi r^3 \Delta G_V + 4\pi r^2 \gamma$) is maximized, and the corresponding ΔG^* ($\Delta G^* = \frac{16\pi\gamma^3}{3(\Delta G_V)^2}$) is the activation energy barrier for nucleation to proceed. Nucleation is often initiated at defects, interfaces, or grain boundaries because these sites reduce the surface energy term, lowering the thermodynamic barrier to nucleation.[34,35] CNT works well to describe nucleation in systems with relatively simple thermodynamics where the assumptions of the model hold – like homogenous nucleation in supersaturated vapors and liquids. Some of the assumptions of CNT include but are not limited to: abrupt interfaces between the nucleus and parent phase without any interfacial width or diffuse transitions, spherical nuclei, bulk thermodynamics, constant surface tension, homogenous composition, no external fields or stresses, constant temperature and pressure, and a single-step nucleation pathway. These assumptions are often invalid in real-world chemical reaction environments.[36–38] CNT cannot capture atomic-level details which are critical to understand the heterogenous nucleation favored in solid-state reactions. Non-classical models are needed to describe nucleation in the solid state.

Both diffusion and nucleation have been studied extensively, but significant gaps still exist in our understanding of what is happening at an atomic level during both of these fundamental reaction steps, especially in the solid-state.[39–41] Researchers have developed several

theoretical and computational approaches that improve upon CNT for describing nucleation in the solid state. Modern DFT theories model nucleation as a continuous pathway through free energy space, not just via a critical radius, accounting better for inhomogeneous composition, fluctuating interfaces, and non-equilibrium clusters. These theories are able to predict preferred nucleation trajectories, even for solid-solid transitions.[42] CNT assumes nucleation proceeds via a single-step formation of a bulk-like nucleus, but recent two-step nucleation models better account for intermediates that often form and rearrange into the stable phase during solid-state reactions.[43–46] One study by Peng et al. uses single-particle-resolution video microscopy of colloidal films to show a two-step nucleation mechanism with an intermediate liquid nucleus.[47] They conclude that a liquid intermediate is favorable because the necessary symmetry relations between parent and product lattices are contained within a liquid intermediate, minimizing the energy cost of solid-liquid interfaces over solid-solid interfaces. These non-classical pathways help explain why crystals sometimes form even when classical theory does not predict it. To understand how to control solid state reactions well enough to synthesize new, complex materials, experimental chemists must establish new techniques that can be used to study the fundamental reactions of diffusion and nucleation that occur in a solid-state reaction environment. Unfortunately, there are very few established experimental probes that can be used to investigate these mechanisms in a solid-state reaction environment, and a complete atomic-scale understanding of nucleation is still elusive.[48] However, over the past several decades, a gradual expansion of knowledge has led to the development of several alternative synthetic techniques that avoid the challenges presented by bulk diffusion in solid-state reactions.

Fluid-assisted synthetic techniques are one avenue to remove the constraints of diffusion, making nucleation the rate limiting step.[49] The use of a fluid reaction medium significantly increases diffusion rates, allowing for faster mixing of reactants at lower reaction temperatures than in traditional direct reaction between elements. Because the reaction is kinetically controlled, the phase with the lowest nucleation barrier forms first, potentially avoiding the thermodynamic products.[50,51] Although there are multiple examples of metastable phases being grown from fluid-mediated systems and many empirical synthetic schemes exist for specific systems, because they have not been linked to specific thermochemical principles, it is difficult to extend them to other systems.[52] Growing evidence indicates that transient metastable

intermediates form before equilibrium products, making it extremely challenging to design synthesis to target specific phases.[53,54]

Other techniques utilize gas-phase precursors deposited onto heated substrates, enabling growth to be governed primarily by surface kinetics. These techniques include chemical vapor deposition (CVD), atomic layer deposition (ALD), and pulsed laser deposition (PLD). In all of these methods, precursors are volatilized and transported in a carrier gas toward a heated substrate where reactions occur. When an atom hits the substrate, the kinetic and chemical potential energy it carries are dissipated as vibrations into the substrate and surrounding amorphous matrix, enhancing atom mobility and increasing surface diffusion.[55,56] An atom sitting in a lattice site is in a lower energy state than when it's sitting in an amorphous matrix, so atoms can further dissipate this energy by forming bonds with other atoms as part of a growing crystallite. However, for a crystallite to nucleate and grow, the nucleation energy barrier must be overcome.[57–60] To overcome this energy barrier, these techniques utilize heated substrates to provide the necessary energy. Unfortunately, while this addition of energy facilitates nucleation, it creates a reaction environment with enough energy to explore a broader portion of the 3D energy landscape, making it more difficult for the system to become kinetically trapped in local energy minima corresponding to metastable phases.

These synthetic techniques do still provide the ability to affect the identities and structure of resultant films through control of some tunable experimental variables. The substrate temperature, partial pressures of precursors, and carrier gas type and flow rate can be adjusted to manipulate the deposition rate,[61–63] the rate of surface diffusion,[64,65] and the rate of crystal nucleation.[66–68] The adsorption/desorption rates of precursor/source atoms or molecules onto the substrate is critical for controlling film growth rate, composition, and phase formation. When an atom hits the substrate, it must adsorb either chemically or physically in order to be available for incorporation into the growing crystal. Because of the Arrhenius-type temperature dependance of desorption,[69] achieving sufficiently high incorporation rates can be challenging. For example, indium has rapid desorption at elevated temperatures that hinders the growth of technologically relevant narrow-bandgap In-rich films of InGaAs.[70–73] Adsorption/desorption rates also control the local composition at the surface which will affect the film stoichiometry and subsequently what phases can nucleate.[74,75] The rate of adsorption/desorption can be controlled by the substrate temperature, carrier gas flow rate and composition, and precursor partial pressures.[76]

Slower carrier gas flow rates allow for a longer residence time for precursors near the substrate where reactions can occur, increasing the chance for precursor atoms/molecules to adsorb.[77,78] However, slow carrier gas flow rates can lead to a thicker boundary layer of stagnant gas at the substrate surface, which can slow mass transport and decrease the efficiency with which precursors are transported to the surface.[79–81] Therefore, high enough flow rates must be used to overcome this challenge and efficiently remove desorbed byproducts and unreacted precursors, maintaining clean surface sites for new potential adsorption events.

The chosen substrate material can have a powerful effect on the nucleation energy barrier,[82] adhesion, and the growth mechanics of products. The chemical affinity, binding sites, defect density, crystallinity, and orientation of the substrate can also affect how products form. Substrates can be functionalized with chemically active regions so that a film grows in specific regions while passivated regions remain uncoated, known as selective area growth (SAG).[83] The formation energy for specific phases can be decreased by selection of a substrate with an optimal chemical environment, as in the polymorph selective growth of $MoTe_2$ using specific seed layers.[84] The use of Cu substrates to catalyze the decomposition of methane in CVD graphene growth is an example of the substrate chemically participating in the reaction.[85] These techniques have become valuable in the study of thin-films for technological applications. For example, in 2014 the Nobel prize in physics was awarded to Akasaki, Amano, and Nakamura for their development of a metal-organic CVD process to grow GaN films on (0001) sapphire using an AlN buffer that was foundational in the development of blue LEDs.[86–88] However these techniques are not easily scalable and the complex, multi-component gas-phase chemistries employed in these methods create challenges in controlling the growth of phase pure products with known stoichiometries, the defect density, surface smoothness, and the thickness uniformity of resultant thin-films.[89]

Molecular beam epitaxy (MBE) is another commonly employed synthetic method that avoids the thermodynamic constraints of bulk diffusion and is instead controlled by the surface kinetics of adsorption/desorption and surface diffusion.[90,91] Additionally, MBE utilizes epitaxial substrates to reduce or eliminate nucleation barriers. By avoiding the thermodynamic constraints inherent to high-temperature synthetic methods, MBE enables the stabilization and growth of metastable phases that are inaccessible through equilibrium-based methods. Diffusion constraints typical of solid-state growth are avoided in MBE using a ballistic growth method with line-of-

sight atomic beams.[92,93] The growth rate is slower in MBE,[94] but because it is performed under ultra-high vacuum instead of at high pressures, there is an unparalleled chemical purity that provides atomic scale surface control and much higher precision over the composition, thickness, and impurity level of products.[95] In-situ monitoring techniques like reflection high-energy electron diffraction (RHEED) provide monolayer by monolayer monitoring of growth that allows for atomic-level control over the composition and thickness of products.[96,97] However, like any technique, MBE has certain limitations. This method is limited by the differing volatilities of materials at the substrate surface, as it only works reliably when all components remain stable and do not desorb under the same reaction conditions.[98–100] Source materials cannot have any reactivity with crucibles, chamber surfaces, and other experimental components.[101] Unfavorable surface kinetics and limited atomic mobility can also lead to the undesirable growth of "islands" of material instead of smooth films of uniform thickness. This phenomenon, known as Volmer-Weber growth, is a result of high interfacial energy between the substrate and deposited material.[102,103] Deposited atoms will preferentially bond to each other to more efficiently lower their total free energy instead of "wetting" the surface of the substrate. Even if the interfacial energy between deposited material and the substrate is not too high, high Ehrlich-Schwoebel barriers at step edges can lead to 3D island formation rather than smooth 2D layers.[104,105] While epitaxy is the defining strength of MBE, enabling precise nanoarchitecture tuning, crystalline alignment, and defect minimization, true epitaxy requires the use of single-crystal substrates and introduces the significant limitation of strict lattice matching.[106–108] As such, MBE cannot be readily applied to amorphous, polycrystalline, or flexible substrates which limits its industrially relevant application.[108,109]

Understanding how designed interfaces react has significant commercial significance. In solid state battery technology, interfacial reactions can lead to resistive interphases like Li dendrites or decomposition products which can degrade battery performance.[110–113] In semiconductors, reactions between semiconductors and dielectrics or metal contacts can affect carrier mobility, leakage currents, and overall device speed and lifetime. Modern complementary metal-oxide-semiconductor (CMOS) devices have replaced SiO_2 grown on Si with HfO_2 grown on Si as a high-κ gate dielectric to enable the continued scaling of transistors in advanced integrated circuits. HfO_2 has a much higher dielectric constant (~20-25) than SiO_2 (~3.9) which enables a thinner equivalent oxide thickness (EOT) without increasing gate leakage.[114,115]

Understanding how to control the reaction environment – through approaches such as surface nitridation, low-temperature ALD, and non-oxidizing annealing – to suppress the formation of an unwanted interfacial SiO_2 layer between HfO_2 and Si has been critical to enabling it's successful adoption in commercial devices.[116,117] This is just one example among many technologically relevant materials and processes that would benefit from a more fundamental understanding of the underlying mechanisms.

A major unresolved challenge in the solid-state reaction literature is the lack of atomic-scale insight into the initial stages of nucleation. Substantial research efforts have been devoted to addressing this knowledge gap, as a deeper understanding of early-stage nucleation will be a fundamental piece to the rational design of syntheses to target computationally predicted stable phases. Unfortunately, because the solid-state reaction environment contains a myriad of dynamically evolving intermediates and interfaces, they are inherently complex and challenging to study. A synthetic approach with tunable variables that imposes a constrained, kinetically controlled reaction environment – designed to isolate and interrogate individual components of a solid-state reaction at the atomic scale – would offer a promising pathway to overcome these challenges.

The method of modulated elemental reactants (MER) is a non-epitaxial thin-film growth technique that enables atomic-level precision without requiring a lattice match between the substrate and the target phase and provides access to tunable experimental variables (layer thicknesses, ratio of layer thicknesses, deposition sequence of layers) that can be used to control both diffusion and nucleation processes.[118] In MER, atomically precise elemental layers are deposited onto unheated substrates to create non-crystalline precursors that mimic the nanoarchitecture of the targeted films. These precursors are deposited at room temperature under ultra-high vacuum from pure elemental sources, creating a reaction environment that enables the highest possible precision and experimental control. The resulting precursors can be engineered – by appropriate design of the deposited elemental layering sequence – such that the most accessible pathways for free energy minimization lead them to local energy minima that correspond to metastable phases.[119] In these precursors, diffusion limitations can be overcome by depositing atomically thin elemental layers that spatially position desired reaction partners in close proximity. The 2D layers in heterostructures made with MER possess high surface area to volume ratios and consequently behave as "all-surface" systems.[120] This geometry amplifies the

influence of surface and interfacial energies, allowing nucleation behavior to be directed through topological constraints and interfacial interactions.[121] In the past, MER synthesis has relied upon tuning the ratio of deposited elemental layer thicknesses to control the compositions of amorphous precursors that ultimately control what phase(s) can nucleate.[122] While this technique effectively eliminates long-range diffusion, making nucleation the rate-limiting step, composition has been the only monitored variable and there has not been a systematic investigation of the underlying factors governing nucleation energetics. As a result, key variables influencing nucleation remain poorly understood, limiting the ability to establish predictive design rules.

1.2. Dissertation Overview

This dissertation discusses an investigation of how experimental variables can be tuned to more precisely control nucleation energies, enabling enhanced kinetic control over the growth of 2D materials. This dissertation is divided into three sections. The first section containing Chapters I-III presents the historical research background that has motivated this work, and details the experimental techniques used to synthesize and characterize the films discussed herein. Chapter I is an overview of the motivations for using MER to expand our understanding of how experimentally controllable variables can be used to affect nucleation energies during the growth of thin-films. Chapter II outlines the various x-ray techniques used to compositionally and structurally characterize the thin-film samples presented in the subsequent chapters. Chapter III describes a new method to simultaneously measure the in-plane and cross-plane electronic transport properties in 2D materials. This chapter was published in *ACS Nano* in 2024.

The second section which includes Chapters IV-VI focuses on using designed precursors synthesized with the MER method to better understand how to use experimentally controllable variables to control nucleation and expand the solid-state synthetic toolkit. Chapter IV investigates the effects of substrate crystallinity on the nucleation and growth mechanism of PbSe films. Chapter IV was published in *Zeitschrift für anorganische und allgemeine Chemie* in 2022. Chapter V discusses the development of a new general method to synthesize amorphous precursors using MER in systems that had previously been shown to always nucleate and grow during the room temperature deposition ($MoSe_2$ and PbSe). This chapter also introduces a new graphical method for visualizing deposited layer thickness and metal:chalcogen ratio together,

providing clearer insight into the effect of precursor design on reaction pathway. Chapter V was published in Chemistry of Materials in 2024. This section concludes with Chapter VI, which discusses an in-depth study of the Mo-Se system. Chapter VI uses the tools developed in Chapter V to create amorphous precursors to study nucleation energies in the Mo-Se system and how precursor design can be used to grow non-equilibrium materials.

The third and final section contains Chapters VII and VIII that describe the synthesis of novel heterostructures using the knowledge gained about nucleation control using designed precursors in the proceeding chapters. Chapter VII describes the synthesis and characterization of a novel $(PbSe)_1(VSe_2)_1(PbSe)_n(VSe_2)_1$ heterostructure with n = 1, 2, and 3. Chapter VIII describes the synthesis and characterization of a $(MoSe_2)_1(ZnSe)_n$ heterostructure. In this heterostructure, interfacial confinement is used to affect nucleation energies by controlling the interfacial surface energies, resulting in the growth of a previously unreported polymorph of ZnSe.

1.3. Bridge

This chapter provides a broad overview of the previous research that frames and motivates this work, followed by a summary of the research contained herein. The following chapter describes the experimental methods used to synthesize and characterize all of the samples discussed in this work.

CHAPTER II
EXPERIMENTAL PROCEDURES

2.0. Authorship Statement

This chapter was written for this work alone with no intention of publishing it elsewhere. I am the primary author of this chapter. I received assistance from my advisor David C. Johnson.

2.1. Synthesizing Samples Using the Modulated Elemental Reactant Method

The samples discussed in this dissertation were all synthesized with the method of modulated elemental reactants (MER). As discussed in Chapter I, the core principle behind MER is in the design of the precursors. In MER, individual elemental layers are deposited one at a time in a layering sequence that is then identically repeated as many times as necessary to reach the desired total sample thickness (usually ~300 Å). The layering sequence is designed to mimic the nanoarchitecture of the desired material. This method decreases diffusion lengths to the order of angstroms, which is orders of magnitude less than what can be achieved with other methods. The precursor design and deposition sequence are intended to produce precursors with energies higher than those of local non-equilibrium product minima, with similar enough local compositions that long range diffusion is not required. For these precursors, heterogenous nucleation is the rate-limiting step. As long as the precursors have the correct local compositions, the desired structure should be the easiest to nucleate and form first upon low temperature annealing (typically below 600 °C). However, it is also possible in some systems that nucleation and growth of certain phases may occur during the deposition process due to high surface diffusion rates. This is discussed in detail in Chapter V.

MER precursors in this thesis were prepared via physical vapor deposition using a custom-built high-vacuum vapor deposition chamber. The deposition chamber contains electron-beam guns (to deposit metals) and a Knudsen effusion cell (to deposit chalcogens). Pure elemental sources are vaporized from each source and their deposition rates are measured by quartz crystal microbalances (QCMs) positioned above each source. Metal sources are pre-melted in an arc melter before being placed into the electron-beam hearths to ensure a smooth

deposition surface and to degas the metal. The surface topology of sources affects the shape of the depositing vapor plume. Uniform and reproducible vapor plume shapes are vitally important to achieve atomic-scale precision of repeat unit thicknesses and reproducibility between deposition cycles. Magnetic raster boxes in each electron-beam gun are used to control the positions and amplitude of the beam-sweep of each electron beam. The beam-sweep and position are optimized for each individual metal, depending on the properties and deposition behavior of that metal. Generally, for metals that remain solid throughout deposition, the beam is swept over ~70% of the sample surface during deposition. Between depositions the electron beam position is manually controlled to smooth out the surface of solid metal sources in order to maintain consistent vapor plume shapes. Sources that melt completely do not require this smoothing process, as the melted surface remains smooth. A viewport is positioned above each elemental source for visual monitoring of the sources during deposition. Computer controlled pneumatic shutters are positioned above each vapor plume. A custom LabView software is used to interface with the QCMs to control how long the shutters stay open to deposit a specific thickness of each element at a time (determination of these target thicknesses is discussed in detail in section 2.2). MER uses very low deposition rates (typically between 0.1-0.9 Å/s) to further increase precision. Precursors are deposited at room temperature onto unheated substrates (usually 6" Si wafers with a native layer of SiO_2) positioned above the elemental vapor plumes. The substrate holder is continuously rotated throughout the deposition to ensure uniform deposition of each element across the substrate.

2.2. Compositional Characterization with X-ray Fluorescence

Successful precursor design is rooted in the thickness and sequence of deposited elemental layers. The target number of atoms in each elemental layer is determined by calculating the atomic areal density for each individual constituent using the unit cell geometry, lattice parameters, and number of atoms of each element in the unit cell for each individual targeted constituent. The atomic areal density is then converted to a target XRF intensity using previously established proportionality constants and a method that has been described in detail elsewhere.[1] Finally, the target XRF intensities for each element in each individual constituent are converted into a target thickness (units of fÅ) using a proportionality constant that is continuously updated after each deposition cycle to monitor the relationship between the target

and actual amounts of deposited material. Iterative application of this method produces precursors that progressively approach the ideal targeted nanoarchitecture.

XRF technology can be used to determine the elemental composition of a sample, and in the David Johnson group a unique method is used to find the absolute number of atoms/Å^2 in each sample. The XRF measurements in this study were all performed on a Rigaku Primus-II wavelength dispersive x-ray fluorescence spectrometer with a rhodium x-ray source. In XRF, samples are bombarded with high-energy x-rays that can eject inner-shell electrons. When an electron is ejected from an atom, a higher-energy electron will decay to fill the vacancy and lower the energy of the atom, and a fluorescent x-ray emission will occur. The wavelength of the emitted x-ray is characteristic to the orbital transitions of that specific element. The total thickness of MER samples is below the critical thickness at which absorption effects can be ignored, meaning that there is a linear relationship between the integrated XRF signal intensity and the absolute number of atoms per area in the sample. Figure 2.1 shows that the raw XRF

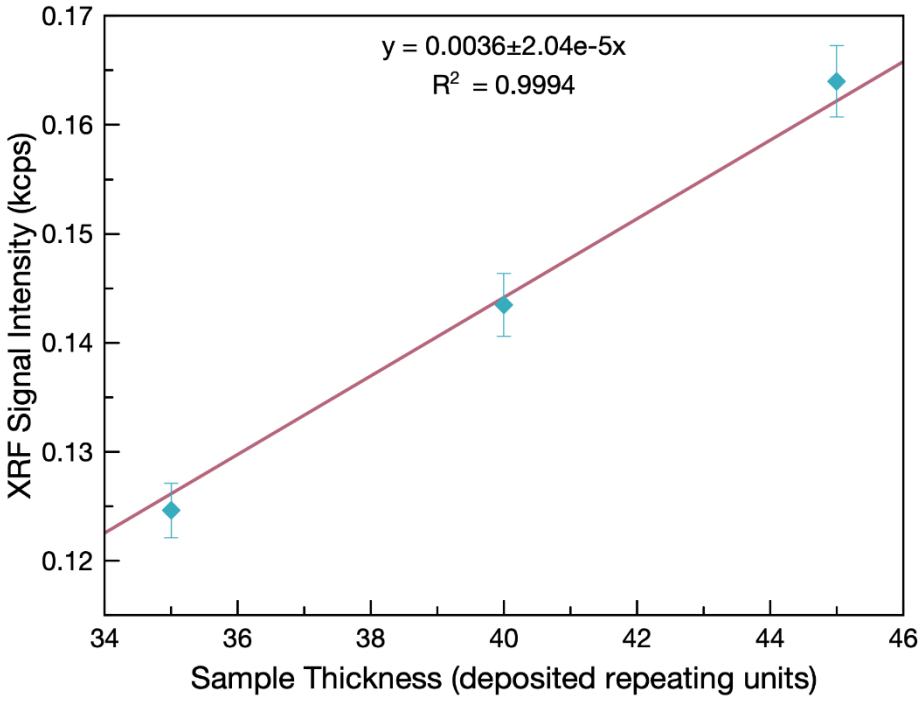

Figure 2.1. Raw XRF signal intensity data for Re in three different binary samples with either 35 (green pattern), 40 (orange pattern), or 45 (blue pattern) Re|Se repeating units, showing a linear relationship between signal intensity and the amount of deposited material. The XRF signal intensity data collected on the blank silicon substrate wafer before deposition is shown in black.

signal intensity for Re, collected on a series of binary Re|Se samples, increases systematically with sample thickness. XRF data for every element is collected on every blank silicon substrate wafer before deposition, so that the background intensity can be subtracted from the total integrated intensity. As described by Hamann et al,[1] separate characterization techniques can be used to determine the number of atoms/Å^2 in certain samples. These known amounts are used to build the XRF calibration curves that define the proportionality constant between the XRF signal intensity and the absolute number of atoms/Å^2 in any sample. These proportionality constants can then be used to find the number of atoms/Å^2 in any sample that is below the critical thickness for absorption effects.

My research has required working with several elements lacking existing XRF calibrations, prompting the development of multiple new calibration curves. New calibration curves can be built for metals (M) using the known proportionality constant for Se and the stoichiometric Se:M relationship, as long as there is a binary line phase on the equilibrium phase diagram for the appropriate M-Se system. A series of binary samples with increasing thicknesses are deposited in a repeating M|Se sequence where the Se layers are made thick enough that Se will be in excess relative to the amount of metal. After deposition the raw XRF signal intensity data for each element is collected. The sample is sequentially annealed at gradually increasing temperatures, and raw XRF signal intensity data is collected after each step. XRR and XRD techniques are used to structurally characterize the sample after each annealing step (the use of these techniques is discussed in detail in section 2.3). A decrease in the XRF signal intensity for Se as a function of annealing is monitored as excess Se sublimes from the sample. A plateau in the decreasing Se intensity signals the formation of a stable compound throughout the sample (Figure 2.2A). X-ray structural characterization is used to confirm that the sample is phase-pure. The known stoichiometric Se:M ratio for that phase can be used in conjunction with the number of Se atoms/Å^2 in that sample after annealing at that temperature calculated using the known XRF signal proportionality constant for Se to determine a new proportionality constant for the metal. For example, in a binary Zn|Se sample after the Se decrease had plateaued and structural characterization showed that the sample consisted entirely of cubic ZnSe, the sample was calculated to have 5.28(8) Se atoms/Å^2, and the following calculation shown in eq. (1) was used to calculate the Zn atoms/Å^2.

$$5.28(8)\ \frac{Se\ atoms}{Å^2} \times \frac{1\ Zn\ atom}{1\ Se\ atom} = 5.28(8)\frac{Zn\ atoms}{Å^2} \qquad (1)$$

This process is repeated for the entire series of samples of increasing thicknesses. The measured XRF signal intensity is plotted vs. the calculated atoms/Å^2 for each sample and the slope of a linear regression of these points is the new proportionality constant for the given metal. Figure 2.2B shows the new calibration curve for Zn with a proportionality constant of $0.112(3)\ \frac{kcps \times Å^2}{Zn\ atoms}$ as an example. It is important to note that the intercept for this linear regression is set to 0 because when there are zero atoms/Å^2 the XRF signal intensity must be zero.

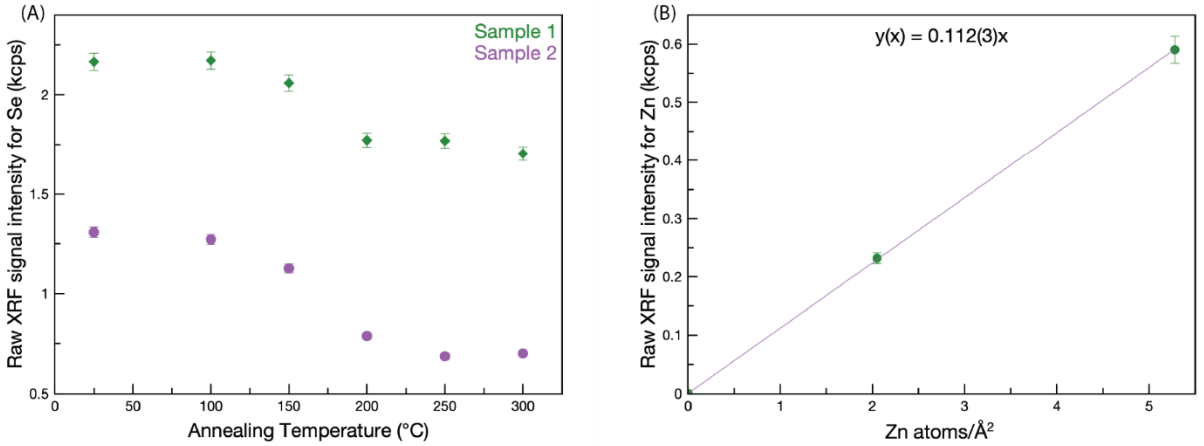

Figure 2.2. An example of the XRF data used to build an XRF calibration curve, collected on two binary Zn-Se samples. (A) The points show the raw XRF signal intensity value for Se collected on each sample after annealing at each temperature for 30 minutes. The Se loss plateau indicates the temperature at which a stable phase has grown throughout the sample. (B) The new calibration curve for Zn. The linear regression is set to go through zero, and the resulting equation for the line is shown at the top of the graph. The slope of this line is the proportionality constant for Zn.

2.3. Structural Characterization

A suite of x-ray and microscopy techniques were used to structurally characterize the samples discussed herein. All XRR and XRD data were collected on a Rigaku SmartLab diffractometer with a Cu-Kα radiation source. Cross-sectional lamellae were prepared by me on a FEI Helious 600i focused-ion beam/scanning electron microscope (FIB-SEM). A FEI Titan™ G2 80-200 scanning transmission electron microscope (STEM) with a Cs probe corrector and ChemiSTEM™ technology (X-FEG™ and SuperX™ energy-dispersive x-ray spectroscopy

(EDS) with four windowless silicon drift detectors) operated at 200 kV was used for structural and chemical analysis of the prepared cross-sectional lamellae. For STEM imaging, a high-angle annular dark-field (HAADF) detector with a collection range of 60-160 mrad was utilized.

2.3.1. X-ray Reflectivity

X-ray reflectivity (XRR) is used to determine the total sample thickness and surface roughness, and to detect changes in the electron density at the surface of the samples. XRR data is collected with a locked θ-2θ scan performed from 0-11° 2θ. In an XRR scan, incident x-rays reflect off the surface of the sample below a certain critical angle that is determined by the electron density at the surface of the sample. Above this critical angle x-rays begin to penetrate into the sample and the collected intensity is a result of incident x-rays reflecting off of the substrate/sample interface and the sample/air interface. XRR patterns contain Kiessig oscillations that arise from the constructive and destructive interference of the x-rays reflected off of these two interfaces. The periodicity of Kiessig fringes is inversely related to film thickness. Total film thickness can be calculated from the 2θ positions of Kiessig fringe maxima and a version of Braggs law modified to include refraction (eq. 2).

$$sin^2\theta_i = {\theta_c}^2 + \frac{(n_i + \Delta n)^2\lambda^2}{4t^2} \qquad (2)$$

Where θ_i is the angle of the Kiessig fringe maximum, θ_c is the position of the critical angle, n_i is the index of the Kiessig fringe, λ is the wavelength of the source radiation, and t is the total film thickness. Roughness or interdiffusion between deposited layers or on the surface of the sample reduces the amplitude of Kiessig fringes and damps the reflectivity at higher angles. The surface roughness of the sample can be estimated using the method established by Parratt.[2] Bragg reflections are also sometimes observed in low angle XRR patterns if the repeat unit thickness is large enough.

2.3.2. X-ray Diffraction

X-ray diffraction (XRD) techniques (specular, grazing incidence, and grazing incidence in-plane) are used to monitor structural changes as a function of annealing temperature and to determine the lattice parameters of resulting crystalline phases. Resulting XRD data are used to determine the optimal processing conditions for each system or specific heterostructure. XRD is

fundamentally based on the diffraction of incident x-rays from a sample, as defined by Braggs law (eq. 3).

$$2dsin\theta = n\lambda \quad (3)$$

Where d is the distance between atomic planes, θ is the angle between the incident x-ray and the atomic plane, n is the integer order of the reflection, and λ is the wavelength of the source radiation. Braggs law is satisfied and a Bragg reflection is observed only at specific angles θ, when the path-length difference between x-rays reflected off the electron density of atomic planes equals an integer multiple of the wavelength and constructive interference occurs. Specular XRD patterns are collected in a θ-2θ locked-coupled mode from 5-65° 2θ. In this scanning mode the source and detector both move in a locked-coupled manner with equal θ values. Specular XRD patterns provide information about the atomic planes growing parallel to the substrate. In a sample growing with preferential 00*l* orientation – as many MER samples do – specular XRD patterns will contain only 00*l* reflections and their 2θ positions can be used to calculate the *c*-axis lattice parameter of the crystalline structure. Grazing incidence XRD (GIXRD) scans are performed in a 2θ scanning mode, where the source x-ray incident angle is kept nearly parallel to the surface, and the detector is scanned from 5-65° 2θ. This scanning mode allows probing of a larger volume of the sample. GIXRD patterns will contain Bragg reflections from atomic planes that are aligned on angles θ with respect to the substrate. Grazing incidence in-plane XRD scans are collected in a 2θ-χ mode, with the detector scanning along the axis parallel to the sample. For samples growing with crystallographic 00*l* alignment, in-plane patterns will contain only *hk*0 reflections. Because MER samples have rotational disorder between the layers, the 2θ positions of in-plane reflections can be used to calculate the a- and b-axis lattice parameters of each individual constituent growing in the film and determine the unit cell type (cubic, hexagonal, etc.) of each individual phase that makes up the heterostructure.

2.3.3. High-Angle Annular Dark Field Scanning Transmission Electron Microscopy and Energy Dispersive X-ray Spectroscopy

HAADF-STEM and EDS data were used to further structurally and chemically characterize certain samples at the atomic scale. The standard FIB method was used to lift-out and thin electron transparent cross-sectional lamellae of select samples. In HAADF-STEM, a

focused electron beam is scanned across the electron transparent portion of the sample. An annular detector collects only electrons scattered to high angles. Because these high-angle electrons arise from Rutherford-like elastic scattering, the intensity of each atom in a HAADF image is approximately proportional to the atomic number, Z.[3] HAADF-STEM imaging offers superior atomic resolution while eliminating the phase contrast artifacts common in bright-field TEM, enabling a more straightforward and reliable interpretation of data.[4] EDS chemical maps were obtained during STEM imaging to further chemically characterize samples with atomic resolution. Elemental maps were generated from spectral images that were compiled from a series of scans over the same region to correct for spatial drift. EDS maps are used to add additional composition information – although EDS data is not quantitative – and to provide more detailed information about the specific atomic positions in the unit cell.

2.4. Electrical Characterization

Temperature- and field-dependent electronic transport and Hall measurements were carried out using a Quantum Design PPMS-16 system at the Leibniz Institute for Solid State and Materials Research (IFW Dresden). The instrument is equipped with a 16 T superconducting magnet and enables measurements over a temperature range of 1.9 to 400 K. During the deposition of samples, a 1 cm x 3 cm piece of quartz covered with a van der Pauw cross[5] shadow-mask was co-deposited alongside the silicon substrates. This parallel deposition allows the silicon sample to be annealed and used for XRF and XRD characterization, with the assumption that identical growth will occur on both substrates when subjected to the same processing conditions. After appropriate processing, samples on quartz substrates were mounted on Quantum Design transport pucks and contacted in a standard four-probe van der Pauw geometry with indium wires. Measurements were performed under high vacuum to reduce thermal exchange and protect the films from environmental effects. We collected resistivity data during both temperature and magnetic field sweeps. Temperature-dependent measurements were taken at several fixed fields, and field sweeps were carried out at constant temperatures to probe magnetoresistance. To check for hysteresis or thermal lag, data were collected during both warming and cooling cycles.

2.5. Bridge

Chapter II describes the experimental methods used to synthesize and characterize the samples discussed in all of the following chapters. The following chapter describes in detail the development and implementation of a novel method to simultaneously measure the in-plane and cross-plane electronic transport properties of thin film materials that adds another powerful tool to the characterization toolbox of solid-state chemists. This method was developed in collaboration between the David C. Johnson group and the Stephen B. Cronin group at USC.

CHAPTER III

Simultaneous Characterization of In-plane and Cross-plane Resistivities in Highly Anisotropic 2D Layered Heterostructures

3.0. Authorship Statement

This chapter was previously published in *ACS Nano* in 2024. Sizhe Weng, Yu Wang, David C. Johnson, and Stephen B. Cronin conceived and planned the experiments. Celsey Price, Marisa Choffel, Aaron Miller, and I carried out the material synthesis and characterization. Sizhe Weng carried out the experiment and analyzed the data, Yu Wang derived the models and helped carry out the COMSOL simulations. Ruoxi Li, and Mingrui Chen assisted with device characterization and electron-beam lithography. Ping Lu collected high-angle annular dark-field transmission microscopy images. Sizhe Weng, Yu Wang, David C. Johnson, and Stephen B. Cronin wrote the majority of the manuscript and all authors discussed the results and contributed to the final manuscript.

3.1. Introduction

Semiconducting heterostructures and superlattices have attracted considerable interest in the scientific and industrial communities due to their exotic properties and wide range of applications in modern electronics, thermoelectrics, and optoelectronics.[1-4] Early studies focused on III-V semiconducting heterostructures and oxide superlattices, which were mainly fabricated through epitaxial growth, such as molecular beam epitaxy (MBE)[5, 6] or metal organic chemical vapor deposition (MOCVD).[7, 8] Although many state-of-the-art electronic devices (i.e., photodetectors and light-emitting diodes) have been demonstrated, such growth methods are constrained by crystallographic symmetry similarities and lattice constant matching. More recently, van der Waals (vdW) heterostructures with vertical integration of layered materials offer an alternative approach to integrate two-dimensional materials that do not rely on strong chemical bonding between adjacent layers.[1, 9] Such hetero-integration provides a more versatile

selection of materials with disparate lattice structures, such as graphene, hexagonal boron nitride (hBN), and transition metal dichalcogenides (TMDs).[10] The optical and electrical properties of vdW heterostructures and devices have been under intensive study, and many interesting phenomena have been discovered, including ultrafast charge transfer (within 50 fs) in photoexcited MoS_2/WS_2 heterostructures, 55% external quantum efficiency of photocurrent generation in graphene/MoS_2/graphene vertical junctions,[11, 12] all-electrical single photon light emitting diodes realized in graphene/hBN/WS_2 heterostructures,[13] and graphene/hBN/graphene field effect tunneling transistors.[14] Recently, there has been a new emerging trend in vertically integrating 2D materials with traditional semiconductors and oxide superlattices, resulting in the creation of even more exotic artificial heterostructures or superlattices with atomically clean and electronically distinct interfaces.[15,16] Since the functionalities of most of the above-mentioned heterostructures and superlattices rely heavily on the carrier transport across the interfaces, studying the fundamental electrical transport properties in the cross-plane direction of vdW heterostructures is of great importance to the future development of nanoelectronics and nanophotonics.

There are few reports probing the intrinsic properties of charge carrier transport across the interfaces in vdW heterostructures due to the difficulty of separating large contact resistances from the relatively small cross-plane resistance of thin films (1-100 nm thick) in 2-probe measurements. The most common method of measuring resistivity tensors in anisotropic materials is based on the method developed by Montgomery.[17] However, their approach requires the contact width of the contacts to be less than 10% of the film thickness to measure the cross-plane resistivity accurately.[18] For 50 nm thick vdW heterostructures, it is very difficult to fabricate Ohmic metal contacts with contact widths smaller than 5 nm. Another approach used to extract the resistivity in the cross-plane direction include measuring properties in samples where regions between contact pads have been etched to varying depths to form a mesa structure, followed by applying the modified transfer line method (M-TLM).[3, 19-21] These methods require the variation of contact resistance between different devices to be much smaller than the cross-plane resistance of the material, which is challenging to achieve experimentally for a variety of reasons including surface damage from contact metal deposition, Fermi level pinning, and non-uniformity at the material/contact interface.[22, 23] Another reported approach is to sandwich the material of interest between a large bottom electrode and a small top electrode in a two-probe

measurement configuration.[24] However, the measured resistance includes the lead and contact resistance from the metal/material interface, which usually dominates in the measured total resistance in the cross-plane direction.

The approach to measure cross plane resistivity presented in this paper is based on the phenomena of current crowding, which was first extensively explored in the 1960's and 70's.[25-27] The phenomenon of current crowding has been shown to be very important in diverse areas, ranging from being an important loss mechanism in LED's[28] to increasing electromigration leading to the formation of interfacial voids.[29] Figure 3.1 illustrates the basis of current crowding using a transition line model where magenta resistors represent the interface resistance. Current flowing from the yellow to the green wires will not be the same in each of the intervening

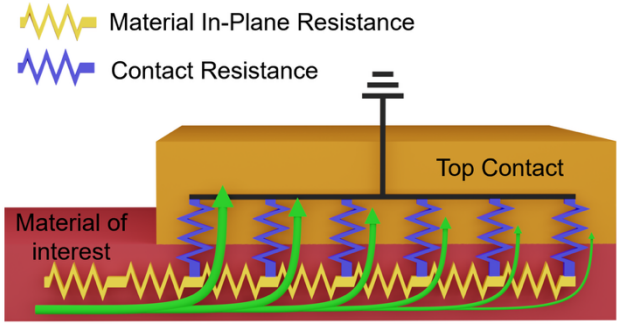

Figure 3.1. Schematic diagram of an equivalent circuit illustrating the concept of current crowding. More current flowing from the yellow to the black wires will pass through the initial intervening blue resistors than later ones, with the amount dependent on the resistivities of both the material of interest and the interface.

magenta resistors. More current will pass through the initial resistor than later ones, with the amount dependent on the resistivities of both the wires and the interface. To measure cross plane resistivity, we need to add contacts on the bottom of the sample, which adds a second interface and potential current pathway through the contact and across to the opposite contact. The transmission line model derived herein includes the bottom contact, which modifies the top current distribution if the in-plane conductivity is low.

Here, we present a new approach to characterize both the in-plane and cross-plane resistivities of ultra-thin samples. We use in-plane measurements to determine the resistances of the lithographically defined gold leads connecting the sample to the bonding pads (typically 20-100W) and the contact resistivities of the top and bottom contacts. These contributions are then subtracted from the measured two-probe total cross-plane resistance to obtain the cross-plane

resistance of the heterostructure material. The cross-plane resistivity is calculated from the cross-plane resistance using the measured sample thickness and contact areas. This approach uses a simple device geometry without needing multiple devices and/or etch steps. We demonstrate the utility of our approach by characterizing several $(PbSe)_1(VSe_2)_1$ heterostructures, all yielding 4 order of magnitude anisotropies between the in- and out-of-plane resistivities over the 6 – 300 K temperature range. This is the first time that electrical properties of nm thick van der Waals heterostructures have been characterized in both directions on the same device with contact resistances fully accounted for, and we believe this technique can be generalized and applied to characterize a wide range of thin film materials if the deposition or growth of the target material does not require epitaxial substrates.

3.2. Results and Discussion

The optical image and schematic diagram of as-fabricated device are shown in Figure 3.2a and 3.2b. In the present study, 50 unit cells of the $(PbSe)_1(VSe_2)_1$ heterostructure (~30 nm thick) are sandwiched between arrays of top and bottom electrodes with 5 contact widths ranging from 1 to 16 μm, detailed fabrication processes are demonstrated in the Method section. Figures 3.3a, 3.3b, and 3.3c show the characterization data obtained on an annealed $(PbSe)_1(VSe_2)_1$ heterostructure using the conditions described above. These data show the formation of highly crystalline materials with atomically sharp interfaces that grow with crystallographic alignment to the substrate and interlayer rotational disorder.

The completed devices are used to measure the in-plane resistivity of the material of interest using a 4-probe configuration to make sure the processing steps have not altered the properties of deposited film. We used 4 top or bottom contacts to perform a 4-probe in-plane transport measurement, in which the current is flowing between the two outer electrodes and the voltage difference between the 1 μm and 2 μm leads was measured. At each temperature, the conducting current increases from -0.2 to 0.2 mA in 50 μA incremental steps and Ohmic behavior is observed. The temperature dependent corrected in-plane resistivity, plotted in Figure A.6a. Figure A.6c shows a similar order of magnitude and temperature dependence to that previously reported by Wang et al.,[30] Hite et al.,[31] and Cordova et al.[32] The upturn in the resistivity at low temperatures results from a charge density wave transition in the monolayer

thick VSe_2 layers.[33] The in-plane resistivity data indicates that the $(PbSe)_1(VSe_2)_1$ heterostructure survived the processing steps.

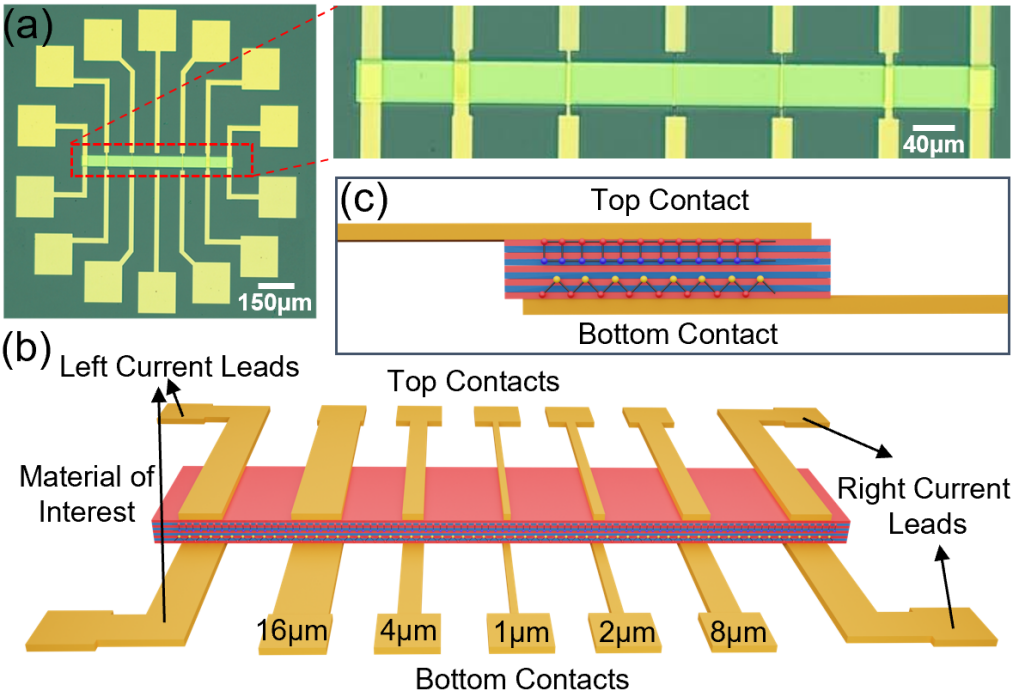

Figure 3.2. (a) Optical microscope image and (b) schematic diagram of the as-fabricated device with various contact widths from 1 to 16 μm. (c) side view of the device, shows that the top and bottom electrodes extend across the material of interest. The electrodes end at 3 μm away from the edge of the material to avoid potential short circuit between top and bottom contacts.

A sequence of 2-probe in-plane measurements using the top and bottom contacts are then conducted to determine the lead and contact resistances, as illustrated in Figure 3.4a. Current is injected through pairs of contacts, and the voltage of an adjacent contact is measured relative to ground. Typical I-V curves for the 2-probe measurements are plotted in Figure A.1 showing Ohmic behavior at the metal/heterostructure interface. The measured voltage is the sum of the potential drop due to the current flowing through the lithographically defined electrode connecting the heterostructure material to the bonding pads (i.e., leads) and the voltage drop at the end of the contact due to the fraction of the total current (1 mA) flowing through the end of the contact. This latter contribute is referred to as the contact end voltage. The amount of current flowing through the far end of the grounded contact depends on the contact width of the contact and the relative magnitude of the contact conductance with respect to the sample's in-plane

resistivity, resulting in the systematic trend in the measured voltage with contact width plotted in Figure 3.5a. The fits to these contact width-dependent curves are described below.

Figure 3.4b presents a schematic illustration of the theoretical analysis of the in-plane current flowing through a contact. Here, $V_{\mathrm{top}}(x)$ and $V_{\mathrm{bottom}}(x)$ are the electrical potential

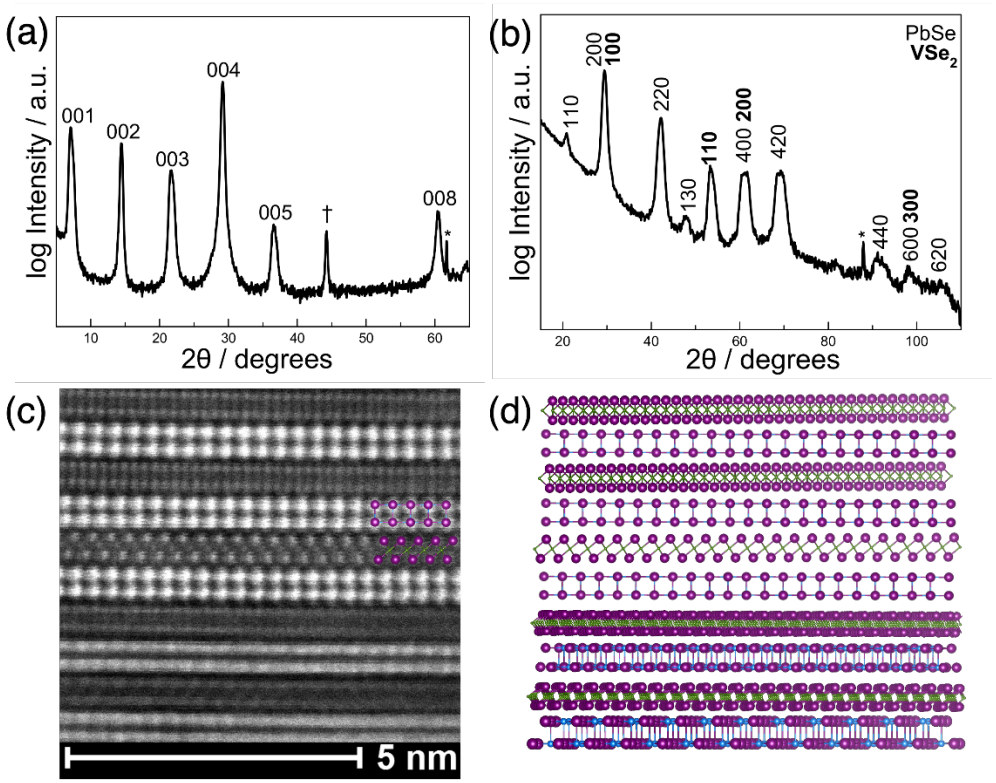

Figure 3.3. (a) The specular diffraction pattern of a $(PbSe)_1(VSe_2)_1$ heterostructure. The indices are given above each reflection. (b) Grazing incidence in plane X-ray diffraction patterns of the self-assembled $(PbSe)_1(VSe_2)_1$ heterostructure collected from a sample subjected to identical annealing conditions as the fabricated device. Indices for both the PbSe and VSe_2 sublattices are given above each reflection. (c) High-angle annular dark-field scanning transmission electron microscopy (HAADF-STEM) image of $(PbSe)_1(VSe_2)_1$ heterostructure. Colored bars show the positions of atomic planes of Pb (blue), V (green), and Se (purple). (d) A schematic of the structure of the $(PbSe)_1(VSe_2)_1$ heterostructure illustrating the off-axis rotational disorder of the constituent sublattices seen in the HAADF -STEM image.

differences between the material and the top and bottom contacts as a function of position x, measured from the inner edge of the contact. The contact resistances are modeled by adding parallel resistors on both the top and bottom of the material, and G'_{top} and G'_{bottom} represent the conductances of the interface per unit length of the top and bottom contacts, respectively.[34] We assume the contact is at an equal potential as a function of position, x, since the resistivity of the

contact material (Au) is around 10^{-8} Ω·m[36-37], which is very small comparing with the in-plane resistivity of the $(PbSe)_1(VSe_2)_1$ heterostructure. $I(x)$ represents the current flowing in the material at location x along the contact and R', the in-plane material resistance per unit length, is taken as a constant at each measurement temperature (21.8 Ω·μm^{-1} at room temperature) calculated from the in plane 4-probe resistivity measurement. The top contact is grounded while

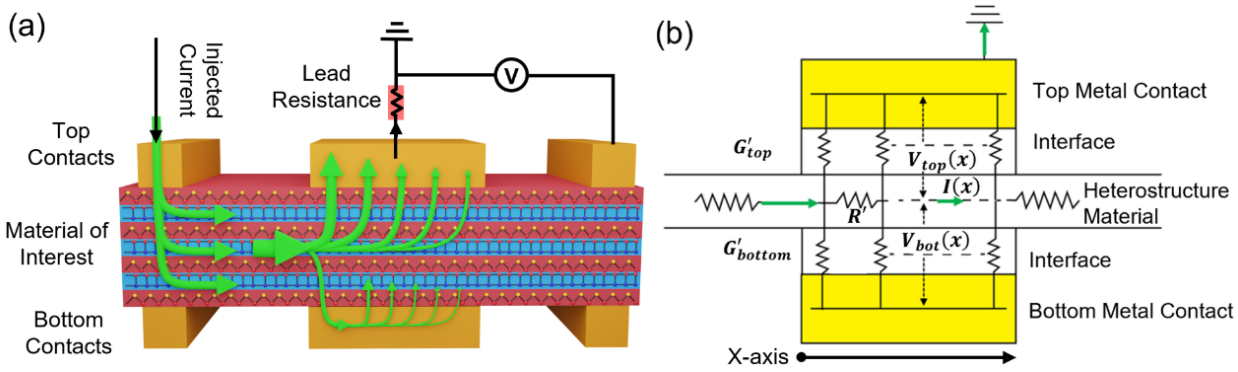

Figure 3.4. (a) Schematic diagram of the three-terminal voltage measurement showing the non-uniform current distribution in the grounded top contact and the floating bottom contact. The voltage measured is the sum of the voltage drop at the end of the top contact due to the current density there and the voltage drop across the lithographically defined gold lead connecting the material of interest to the bonding pad. The current distribution in the floating bottom contact also indicates the significance of the impact from the bottom electrode, even if only the top electrodes are being measured. (b) Equivalent circuit diagram of the in-plane and cross-plane current flow analysis. The positive x direction and the origin of the axis are indicated at the bottom.

the bottom contact is floating. Then, $V_{\text{top}}(x)$, $V_{\text{bottom}}(x)$, and $I(x)$ can be analyzed by constructing the following differential equations:

$$\frac{dV_{\text{top}}(x)}{dx} = -R'I(x) \tag{1}$$

$$\frac{dV_{\text{bottom}}(x)}{dx} = -R'I(x) \tag{2}$$

$$\frac{dI(x)}{dx} = -G'_{\text{top}}V_{\text{top}}(x) - G'_{\text{bottom}}V_{\text{bottom}}(x) \tag{3}$$

The equations are solved by applying Dirichlet and integral form boundary conditions: $I(x = 0) = I_i$, $I(x = d) = 0$, and $\int_0^d G'_{\text{top}}\text{V}_{\text{top}}(\text{x}) = I_i$, where I_i is the total current in the

material before entering the region between the contacts, and d is the contact width. Based on the above-mentioned constraints, the solutions are as follows:

$$V_{\text{top}}(x) = ZI_i \coth(\alpha d)\cosh(\alpha x) - ZI_i \sinh(\alpha x) + \frac{G'_{\text{bottom}}}{G'_{\text{top}}}\frac{I_i}{\left(G'_{\text{top}} + G'_{\text{bottom}}\right)d} \tag{4}$$

$$V_{\text{bottom}}(x) = ZI_i \coth(\alpha d)\cosh(\alpha x) - ZI_i \sinh(\alpha x) - \frac{I_i}{\left(G'_{\text{top}} + G'_{\text{bottom}}\right)d} \tag{5}$$

$$I(x) = I_i \cosh(\alpha x) - I_i \coth(\alpha d)\sinh(\alpha x) \tag{6}$$

where $Z = \sqrt{\frac{R'}{\left(G'_{\text{top}}+G'_{\text{bottom}}\right)}}$ and $\alpha = \sqrt{\left(G'_{\text{top}} + G'_{\text{bottom}}\right)R'}$. This result is similar to previous analyses for a single top contact in which the potential difference between the material and contact also follows hyperbolic decay along the contact periphery.[34, 38, 39] However, for our top and bottom contact configuration, the voltage drop across the material/contact interface contains an additional term containing the contact width d and the conductance of both top and bottom contacts. We define the contact end voltage drop as:[22]

$$V_{\text{end}} = V(x = d). \tag{6.5}$$

During the experiment, top contacts are first grounded to measure $V_{\text{end}}^{\text{top}}$ followed by bottom electrodes grounded to study $V_{\text{end}}^{\text{bot}}$ with the definitions given by:

$$V_{\text{end}}^{\text{top}} = \frac{ZI_i}{\sinh(\alpha d)} + \frac{G'_{\text{bottom}}}{G'_{\text{top}}}\frac{I_i}{\left(G'_{\text{top}} + G'_{\text{bottom}}\right)d} + R_{\text{lead}}^{\text{top}} I_i \tag{7}$$

$$V_{\text{end}}^{\text{bot}} = \frac{ZI_i}{\sinh(\alpha d)} + \frac{G'_{\text{top}}}{G'_{\text{bottom}}}\frac{I_i}{\left(G'_{\text{top}} + G'_{\text{bottom}}\right)d} + R_{\text{lead}}^{\text{bottom}} I_i \tag{8}$$

where $R_{\text{lead}}^{\text{top}}$ and $R_{\text{lead}}^{\text{bottom}}$ represent the contact lead resistances of the top and bottom electrodes, respectively. Figure 3.5a shows the contact end voltage measurements plotted with respect to contact width and the results of fitting this data to Equations 7 and 8 above. The theoretical analysis fits the data well, indicating that the floating contact on the other side must be included as it provides a parallel pathway for the current. The extracted contact lead resistivities per unit length $\rho_{\text{lead}}^{\text{top}}$ and $\rho_{\text{lead}}^{\text{bottom}}$ are 2.42 ± 0.16 and $0.85 \pm 0.16\ \Omega{\cdot}\mu m^{-1}$, respectively. The fitted values of G'_{top} and G'_{bottom} are $(7.91 \pm 0.72) \times 10^{-3}$ and $(11.7 \pm 1.6) \times 10^{-3}\ \Omega^{-1}{\cdot}\mu m^{-1}$, resulting in contact resistivities of $(5.1 \pm 0.6) \times 103$ and $(3.4 \pm 0.6) \times 103\ \Omega{\cdot}\mu m^2$ for the top and bottom

contacts, respectively. These values are on the same order of magnitude as that of Au/WSe_2 interface reported previously.[40]

The cross-plane resistances were measured between top and bottom contact pairs with different contact widths. The measured resistance is the sum of the two contact resistances (determined from G'_{top} and G'_{bottom}), the two contact leads resistances ($R_{\mathrm{lead}}^{\mathrm{top}}$ and $R_{\mathrm{lead}}^{\mathrm{bottom}}$), and the cross-plane resistance of the material itself. Figure 3.5b presents the extracted cross-plane resistances plotted with respect to the contact width. Since the width of the contacts in the other dimension (perpendicular to the current flow) is kept constant (i.e., 40 μm), one would expect the extracted material cross-plane resistance to vary as 1/d if the current is confined to the area of the contact as it crosses the sample, which is shown as the fitted line in Figure 3.5b. While there is considerable error, mainly due to taking the difference of two large numbers, the systematic 1/d trend in resistance with contact width indicates the uniformity of both the top and bottom contacts across the sample. The fitted average cross-plane resistivity from this simple model is 160,000 $\pm$ 50,000 Ω·μm, which is 4 orders of magnitude larger than the measured in-plane resistivity.

A potential source of systematic error in converting the cross-plane resistance into a resistivity lies in assuming that the cross-sectional area is equal to the contact dimensions. Depending on the sample resistivity and thickness, there will be broadening of the flowing pathway of the injected current in the sample after passing through the contacts. This effect becomes especially important as the contact widths become smaller and/or the sample becomes thicker. There is an inherent tradeoff in choosing the contact widths. The impact of lateral current spreading is smaller as contact widths are increased. However, larger contact widths result in smaller cross-plane resistances, which results in larger uncertainties after the large contact and lead resistances are subtracted from the measured total cross-plane resistance. Smaller contact widths give larger cross-plane resistances after the contact and lead resistances are subtracted from the measured cross-plane resistance. However, current spreading needs to be considered when converting the resistances to cross-plane resistivities. In the sample studied, the impact of lateral current spreading is small as evidenced by the observed 1/d dependence of contact resistance versus contact width in Figure 3.5b. The Figure A.2 contains simulations of current spreading as functions of sample thicknesses and contact widths, which also shows small current broadening effect when sample thickness is in tens of nanometers.

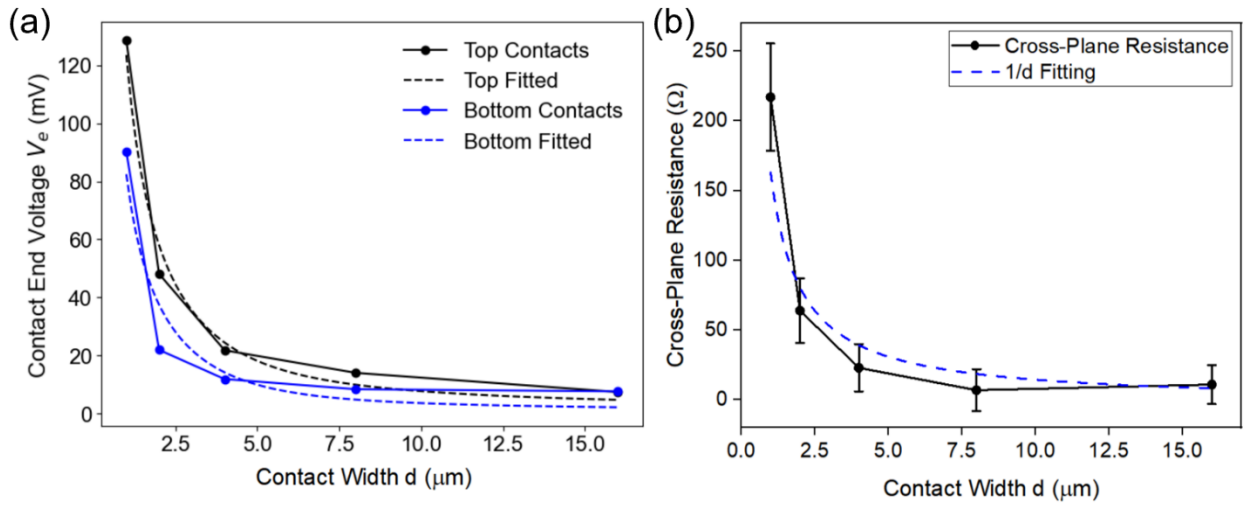

Figure 3.5. (a) The measured voltage drop plotted as a function of the contact width. As the contact width becomes larger, the current density at the end of the contact approaches zero, and the measured voltage approaches the voltage drop due to the gold lead connecting the material of interest to the bonding pad. (b) The contact-subtracted cross-plane resistance plotted as a function of contact width. Since the contact lengths (perpendicular to the direction of current flow) are all equal, the resistance should vary as 1/d. The blue curve is the best fit through the data points.

We measured the temperature dependent of the cross-plane resistivity through the 1 μm and 2 μm leads to probe possible mechanisms for the very large difference between the in plane and cross plane resistivities. Considering the experimental trade-offs discussed above, the relatively small contact areas of the 1 μm and 2 μm widths maximize the sample cross-plane resistance, which is advantageous when subtracting the interface and lead resistances from the total measured cross plane resistance. We measured the systematic change in the contact end voltage with contact width at six different temperatures, which were used to determine the contact conductances and lead resistances at each temperature (See Figure A.3 for the fits of the contact end voltages). The change in the lead resistances with temperature (Figure 3.6b) are consistent with the expected temperature dependence of the metallic gold leads.[41, 42] Within the experimental error, the measured contact conductances are temperature independent (Figure 3.6a).

Despite their importance in electromechanical devices, there are surprisingly few reports of large area contact conductances because of the strong dependence of interface conductance on surface roughness, contamination, and other non-uniformities. The difficulties in reproducibly preparing interfaces make measurement of intrinsic interface resistances challenging. A recently reported

island size dependent electrical contact resistance of nanoscale gold islands on graphite with atomically flat interfaces using conductive atomic force microscopy showed that the total measured resistance is the sum of the resistances between the tip and the gold and the gold and the graphite, which were challenging to separate.[43] The temperature independent conductance values we observed are reasonable, given the metallic nature of the gold contacts and VSe_2 surface layers of our heterostructure. The temperature dependent measurement of both cross-plane and in-plane material resistivities is plotted in Figure 3.6c. The resistivity in the cross-plane direction with 2 μm width shows a value of around 160,000 Ω·μm throughout the entire temperature range, decreasing smoothly by about 5% to a minimum value at ~ 100 K before increasing by the same amount as the temperature is decreased to 6 K (Figure A.6b). The Temperature dependence is very similar to the measured in plane resistivity, which has a minimum resistivity at a similar temperature that is 2% smaller than the room temperature value. This indicates that the charge density wave transition is also observed in the cross-plane transport of $(PbSe)_1(VSe_2)_1$ heterostructure, which has not been reported before. The net result is that ratio of the cross-plane resistivity divided by the in-plane resistivity is relatively constant as a function of temperature, varying between 7400-7600.

Previous studies have shown similar high anisotropy between the resistivity along the c-axis and a-axis in bulk highly oriented pyrolytic graphite (HOPG), and they attributed the conducting mechanism in the cross-plane direction to thermal excitation of charge carriers across stacking fault potential barriers as well as impurity-assisted interlayer hopping.[44] This leads to non-linear I-V curves, which are also reported in cross-plane studies of $NbSe_2$ and HfS_2 multilayer flakes.[24] High resistivity anisotropy has also been observed in In_2Se_3 nanowires, in which semiconducting and metallic behaviors are observed along different crystal directions.[45] However, all the findings mentioned above only involve single component materials. For vdW heterostructures, the anisotropy is mostly attributed to the weekly interacting van der Waals gap between two adjacent layers,[21, 46, 47] Heungdong et al. has reported an anisotropy of 2000 from Sb_2Te_3/GeTe superlattice films.[21] These values are similar to our measured anisotropy.

The four-order-of-magnitude ratio of cross-plane to in-plane resistivity found for $(PbSe)_1(VSe_2)_1$ heterostructure in our study is of similar magnitude to previous reports for misfit layer compounds. Misfit layer compounds are a family of materials containing transition metal dichalcogenide layers interleaved with rock salt structured layers $(MX)_{1+d}TX_2$ where M is Sn,

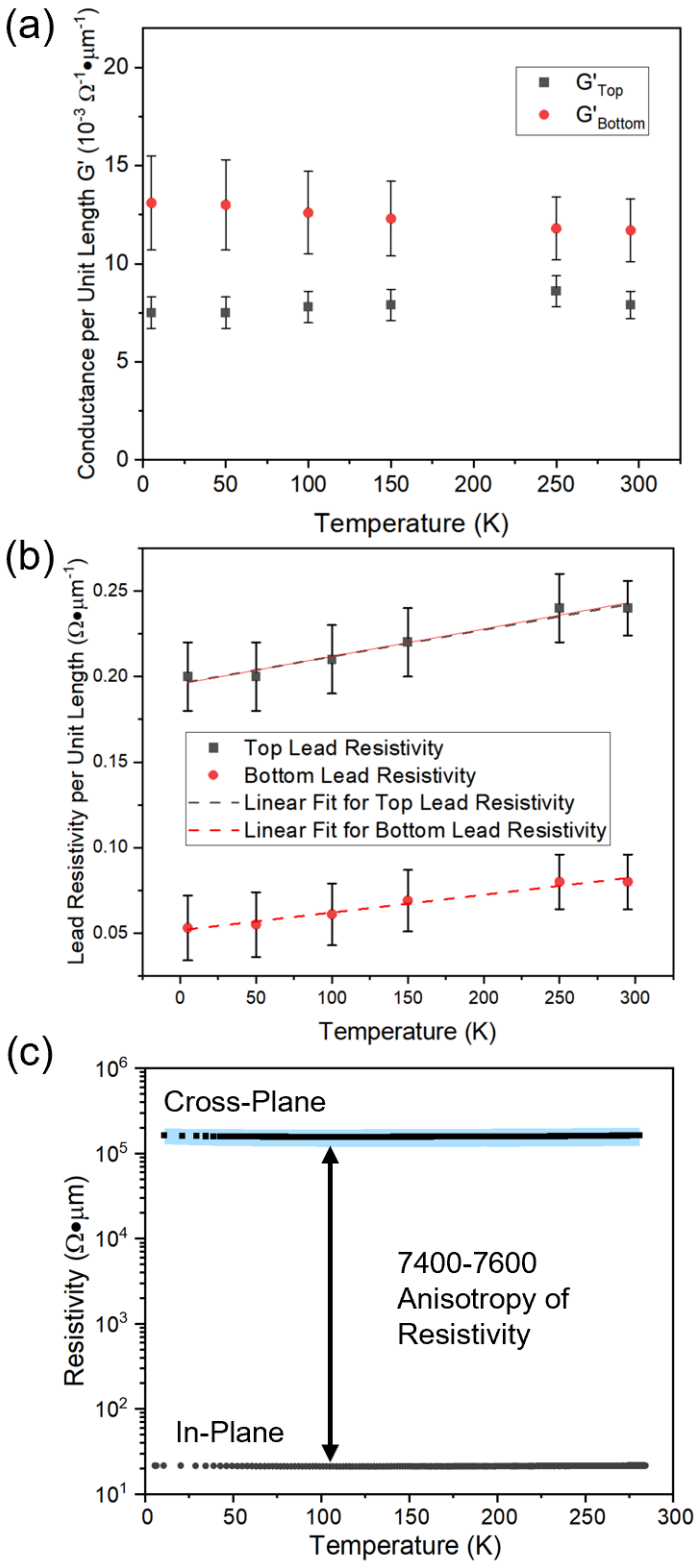

Figure 3.6. Temperature dependence of (a) interface contact conductance per unit length, and (b) subtracted lead resistivity per unit length of top and bottom electrodes. (c) Extracted cross-plane and in-plane resistivities of (PbSe)1(VSe2)1 heterostructure plotted with respect to temperature.

Pb, Bi or a rare earth metal, X is S or Se, d is the misfit parameter determined for the ratio of unit cell areas of the two constituents and T is Ti, V, Nb or Ta. The $(PbSe)_1(VSe_2)_1$ investigated in this work differs from a misfit layer compound by having turbostratic disorder between the PbSe and VSe_2 planes. Prior reports of anisotropy of electrical resistivity of misfit layer compounds ranged from factors of 50 to 10,000 depending on the compound investigated.[48] Our measured anisotropy falls within the range previously reported. The only report of the temperature dependence of the anisotropy of a misfit layer compound, $(SnS)_{1.17}NbS_2$, was also temperature independent.[43] Both $(SnS)_{1.17}NbS_2$ and $(PbSe)_1(VSe_2)_1$ consists of a structural layer that is a small bandgap semiconductor as a bulk phase (SnSe or PbSe) and alternating with a transition metal dichalcogenide which is metallic as a bulk phase (NbS_2 or VSe_2). One would expect the cross-plane transport to be dominated by the small band gap semiconductor while the in-plane transport to be dominated by the metallic layer. For alternating thick layers of these materials, one would expect a temperature dependent anisotropy due to the temperature dependent carrier concentration of the semiconducting layer. The similar temperature dependences of the in-plane and cross-plane resistivities of our data suggest both conductivities are related to the density of states of the VSe_2 monolayers. Naively, one would expect the conduction band wave function to exponentially decay outside of the metallic layer. The spatial extent of the wavefunction is measured by scanning tunneling spectroscopy and is on the order of a nanometer. Since the PbSe layer is only 0.6 nm thick, the conduction bands of adjacent VSe_2 layers overlap within the PbSe. In this simple picture, the density of states of this overlapped region is 7500 times lower than the density of states within a VSe_2 layer. While this hypothesis needs to be tested by synthesizing heterostructures with thicker PbSe layers between VSe_2 layers, the ability to measure and subtract the lead and contact resistances from the total measured resistivity overcomes the inherent limitations of two lead resistance measurements in the cross-plane direction.

There are several experimental limitations to the approach presented herein to measure cross-plane resistivity, which depends on being able to extract top and bottom lead and contact resistances from contact end voltage measurements. This requires observing the contact end voltage increase as contacts are reduced in contact width, which depends on the ratio of the conductance of the contact to that of the sample. As the ratio increases, current crowding increases and lead contact width needs to be decreased to observe a voltage increase. Conversely, a reduced ratio requires thicker lead widths to obtain a contact end voltage dominated by the lead

resistance. Since the conductance of the sample increases with sample thickness and different materials can be chosen to vary the contact conductance, there are some experimental parameters that can be tuned to optimize the experiment. However, samples with high in-plane resistances relative to the contact will be challenging to measure.

The second experimental factor to consider is sample thicknesses, which can often be adjusted to optimize the experiment. Thicker samples will increase the cross-plane sample resistance, increasing the percentage of the total cross-plane resistance caused by the sample. Increasing sample thickness will also, however, increase the broadening of the current path through the sample in the cross-plane measurement. To probe this factor, we simulated various conditions using the COMSOL Multiphysics software package as shown in Figure A.2 (See Appendix A). Current broadening increases dramatically as sample thickness increases, but as sample thickness decreases, the electrical potential gradient change becomes limited to the near contact region. The lateral current profiles near the edges of contacts are similar to each other, which indicates that the current broadening effect is about the same across all the contacts with different contact widths. In this thickness regime, the graph of the material's cross-plane resistance versus contact width will approach zero much quicker than a 1/d dependence as a result of the current broadening. One can compensate for this factor by fitting the data to 1/(d+b), where b is the extent of the current broadening.

Based on the discussion in the previous two paragraphs, the approach presented herein to measure cross-plane resistivity is best suited to anisotropic samples aligned such that the high resistivity direction is perpendicular to the sample substrate. High cross-plane resistivity for the material being examined allows film thickness to be kept small enough that current broadening is minimized and also results in a smaller percentage of the total measured cross-plane resistance due to the lead and contact resistances. Low in-plane resistivity enables current crowding to be measured with contact widths that can be prepared with optical lithography. Isotropic materials will be challenging to measure, as low resistivity materials will result in most of the total measured cross-plane resistance due to the lead and contact resistances. Subtracting two large numbers to obtain a small remainder leads to a large error in the remainder. High resistivity isotropic materials will require ultrathin contact widths to measure a change in the contact end voltage, as the current will concentrate at the beginning of the contact. Fortunately, there are many heterostructures where anisotropic behavior is expected. Another concern that arises is the

possibility that the conduction behavior might be dominated by other mechanisms, such as tunneling and conductive filament (CF) formation through defects. In the future, we will verify the cross-plane conduction behavior by varying the film thicknesses and layer composition, as well as performing hysteresis measurements. Additionally, vdW monolayers and heterostructures have shown promising results in photochemical and photoelectrochemical reactions due to their high surface-to-volume ratio, strong photoabsorption, and intrinsically hosted catalytic sites.[49-51] While the catalytic performances in various reactions have been intensively studied, their conversion efficiencies also rely on charge carrier transport along both in-plane and cross-plane directions.[52, 53] We believe our developed measurement technique will provide additional insights into future photocatalyst design.

3.3. Conclusions

In conclusion, we have fabricated and tested a facile method to measure the intrinsic cross-plane and in-plane resistivities of van der Waals heterostructures. By flowing current along the in-plane direction, the gold lead resistances and interface conductances of the top and bottom electrodes are first quantified by measuring the variation in current crowding as a function of contact width. The interface and lead resistances can then be subtracted from the total measured cross-plane resistance to obtain the cross-plane resistivity of the sample. We find that the in-plane and cross-plane contact resistances of the measured $(PbSe)_1(VSe_2)_1$ heterostructure differ by a factor of 7500. Within the temperature range from 6 to 300 K, the difference in the electric resistivity between the cross-plane and in-plane directions is temperature independent, suggesting that the cross-plane resistivity is due to overlap of the wavefunction of adjacent VSe_2 layers in the $(PbSe)_1(VSe_2)_1$ heterostructure. We also reported the first observation of charge density wave transition in the cross-plane transport of $(PbSe)_1(VSe_2)_1$ heterostructure. We believe the developed framework of accurate characterization of in-plane and cross-plane resistivity, measured on the same sample, will be highly beneficial to the whole thin film research community.

3.4. Materials and Method

3.4.1. Device Fabrication

The device is fabricated by first patterning an array of five contact widths from 1 to 16 μm using electron beam lithography (Raith EBPG 5200) on oxidized Si substrates. 30 nm thick

Ti/Au is deposited on the pattern yielding a pattern of different width bottom contacts after lift-off. A second lithography step is used to define a rectangular window (600 μm × 40 μm) on the bottom electrodes. The material of interest is then deposited onto the patterned substrate. A second array of electrodes is then patterned to serve as top contacts aligned directly above the bottom contacts. To minimize sample heating during deposition of the top contacts, the substrates are approximately 1 m from the metal sources and the deposition rate is round 1 Å/s.

3.4.2. Heterostructure Synthesis and Characterization

Precursors were deposited on <100> Si wafers with native oxide using a custom-built physical deposition chamber. Elemental V (99.995%, Alfa Aesar) and Pb (99.8%, Alfa Aesar) were deposited using 6 keV electron beam guns while elemental Se (99.99%, Alfa Aesar) was deposited using a Knudsen effusion cell. Elemental layers were deposited by exposing the substrate to a plume of atoms from the heated sources. The time the substrate was exposed was controlled by pneumatic shutters that close after the desired thickness has been deposited. The desired thickness was measured using a quartz crystal microbalance and the sequence and thickness of elemental layers can be controlled using custom LabView software. The number of atoms of each element deposited was measured using X-ray fluorescence (XRF) using a Rigaku Primus II ZSX spectrometer. The measured XRF intensities were converted into the number of atoms per unit area for each constituent as described by Hamann and coworkers.[35] The period of the deposited sequence of layers was measured using X-ray reflectivity (XRR).

The precursors were converted to the targeted heterostructure by ex situ annealing at 300°C for 30 minutes on a hot plate in an inert N_2 atmosphere (O_2 < 0.8 ppm). Specular X-ray diffraction (XRD), X-ray reflectivity (XRR) and grazing incidence in-plane X-ray diffraction (GIPXRD) patterns were collected using a Rigaku Smartlab diffractometer, also with Cu-Kα radiation (λ = 0.15418 nm). LeBail fitting of the GIPXRD data was performed on FullProf Suite to obtain lattice parameters. An FEI Titan G2 80−200 STEM with a Cs probe corrector and ChemiSTEM technology (X-FEG and Super-X EDS with four windowless silicon drift detectors) operated at 200 kV were used to obtain high-angle annular dark-field (HAADF) images and EDS scans over selected regions.

3.5. Bridge

Chapter III concludes the detailed description of experimental methods with the description of a novel method we developed to measure in-plane and cross-plane electronic transport properties of thin film materials. The next chapter begins the second section of this dissertation that focuses on using the manipulation of controllable experimental variables to investigate nucleation and growth mechanisms. Chapter IV specifically describes an investigation of how substrate crystallinity affects the nucleation and growth mechanism of PbSe.

CHAPTER IV

Growth of Crystallographically Aligned PbSe of Controlled Thickness on Mostly Amorphous Substrates

4.0. Authorship Statement

This chapter was previously published in *Zeitschrift für anorganische und allgemeine Chemie* (ZAAC) in 2022. Renae N. Gannon is the primary author. Marisa M. Choffel and I assisted with sample preparation and data collection and analysis. Niklas Wolff, Andriy Lotnyk, and Lorenz Kienle helped collect and analyze high-angle annular dark-field scanning transmission electron microscopy images and energy-dispersive x-ray spectroscopy data. David C. Johnson acted as the advisor for this project. All authors helped to write and edit the manuscript.

4.1. Introduction

Lead selenide (PbSe), a direct-bandgap semiconducting material with a cubic rock salt structure, is of interest to many due to its thermoelectric and photoconductive properties.[1–8] The high thermoelectric performance of doped PbSe films has led to exploring its potential use in efficient conversion of industrial waste heat into storable electrical energy.[9–11] PbSe has been investigated for photodetection applications because it absorbs a broad and uniform section of the electromagnetic spectrum.[6,12,13] Researchers have explored the changes in these properties as a function of changes in impurities, alloying extent, strain, and surface treatments to optimize performance.[9,14–22] Several investigations have reported that these properties depend on the thickness of PbSe.[8,20,23,24] Theoretical investigations have predicted that a monolayer of PbSe would be a two-dimensional topological insulator.[25]

Researchers have attempted to prepare monolayers of PbSe and smooth films of PbSe of controlled thickness using a variety of different synthetic approaches. Molecular beam epitaxy (MBE) on a variety of different substrates has resulted in island growth of PbSe, leading to rough films.[26–28] A variety of single crystal substrates that are close to having a lattice match with PbSe were tried, but island formation rather than smooth films were obtained. The substrates were heated to different temperatures to vary the mobility of the deposited atoms, but growth

preferentially occurs on the first PbSe that forms rather than the substrate at all of the temperatures investigated. Another challenge that has impacted growth using MBE or atomic layer deposition (ALD) is the large difference in the thermal expansion coefficients of PbSe and most substrates that have been used, which results in the generation of dislocations upon cooling due to large mechanical strains.[18,29–31] The density of dislocations can be reduced by annealing after deposition or by using a patterned (111)-oriented silicon substrate, but the density remains too high for most applications.[28] Chemical bath deposition and solution based epitaxial methods, which also enable the mobile Pb and Se ions to explore multiple growth sites, experience similar problems despite reduced temperatures.[8,23,24,32] This has led researchers to explore the use of buffer layers between substrate and PbSe.[18,33–35] For example, BaF_2/CaF_2 was used as a buffer layer to grow epitaxial PbSe layers with MBE on Si, but the resulting films cracked, making them unsuitable for device applications.[27] To obtain high quality crack-free PbSe on BaF_2/CaF_2, the buffer layers had to be grown with MBE and the PbSe with liquid phase epitaxy in order to overcome mismatch of thermal expansion coefficients.[27] The growth of single crystals of PbSe was accomplished using chemical solution deposition onto a buffer layer of PbS atop a GaAs substrate. However, the quality of the films produced by this method varied with thickness.[32] An interesting recent reference reported the growth of nanoplatelets of PbSe on MoSe2 monolayers, a non-lattice matched substrate.[36] Single bilayer thick layers of PbSe were also reported in a number of different misfit layer compounds, $(PbSe)_1(TSe_2)_n$, where T = Ti, V, Nb, Mo and W.[37–42] These compounds are called misfit layer compounds as there is not an epitaxial relationship between the two constituents.

The growth of PbSe via a Volmer-Weber mode[43] where islands rather than smooth films form, indicates that the interaction between the deposited Pb and Se atoms and the PbSe islands is stronger than the interaction between them and the substrate. The ability to synthesize misfit layer compounds with PbSe that are thermodynamically stable suggests that the interaction between the PbSe layer and the dichalcogenide is stronger than the interaction of PbSe with itself. This led us to explore the growth of PbSe on amorphous V-Se and mostly amorphous Mo-Se coated silicon (with native oxide) substrates. We deposited these layers on substrates that were nominally at room temperature. We found that PbSe formed during the deposition regardless of substrate or the amount of Pb and Se deposited. Samples deposited on Si with native SiO_2 formed rough films with no crystallographic alignment to the substrate. Samples

deposited on the amorphous V-Se and mostly amorphous Mo-Se coated substrates formed crystallographically aligned and atomically smooth PbSe. If the amount of PbSe deposited was close to an integral number of PbSe bilayers, Laue oscillations were clearly visible on the 002 reflection of PbSe indicating the quality of the deposited films. These results suggest that a precise number of smooth and crystallographically aligned PbSe layers can be grown without epitaxy on amorphous substrates if the interaction between the depositing Pb and Se atoms with the substrate is stronger than with PbSe.

4.2. Experimental

Precursors were deposited on unheated, rotating (111) Si substrates with native SiO_2 layers in a custom high vacuum ($<10^{-6}$ torr) physical vapor deposition chamber from elemental sources (Pb, Mo, V, Se). Electron beam guns were used to deposit Pb, Mo, and V. A Knudson effusion cell was used to deposit Se. Shutters programmed to open and close based on the desired input thickness were used to control the amount of each element deposited. Quartz crystal microbalances were used to monitor the deposition rate and determine the amount of time shutters remained open. Samples were transferred to a nitrogen glovebox (less than 0.2 ppm oxygen) to be stored. They were also annealed on a hot plate in the glovebox. Samples were exposed to air during the transfer from the deposition system and while being characterized.

Specular X-ray diffraction and X-ray reflectivity (XRR) patterns were collected on a Bruker D8 diffractometer with Cu-Kα radiation in θ-2θ locked-coupled scan mode. In-plane and Grazing incidence XRD (GXRD) patterns were collected on a Rigaku Smartlab diffractometer with Cu-Kα radiation and parallel beam (PB) and parallel-beam/parallel slit analyzer (PB/PSA) optics, respectively. The total number of atoms/$Å^2$ for each element was determined using X-ray fluorescence (XRF).[22]

Cross sections of Pb|Se|Pb on SiO_2/Si and as-deposited 16 bilayers of Pb|Se on Mo|Se were prepared using the focused-ion-beam method (FIB). Scanning transmission electron microscopy (STEM) images were acquired in high-angle annular dark field (HAADF) mode on a probe CS-corrected Titan3 G2 60–300 microscope operating at an accelerating voltage of 300 kV using a probe-forming aperture of 25 mrad and annular ranges of 80-200 mrad on the detector. Nanoscale chemical analysis via energy dispersive X-ray spectroscopy (EDS) was

performed in STEM mode using a Super-X detector setup with 4 symmetrically aligned in-column detectors.

4.3. Results and Discussion

Precursors were prepared where the thickness of deposited Pb and Se layers were varied to explore the growth of PbSe at low temperatures on a variety of substrates with a goal of preparing smooth ultrathin films a precise number of unit cells thick. Samples with thick (10-20 nm) elemental layers were deposited at nominally room temperature onto Si with native SiO_2. Pb was deposited first followed by Se and the other sample was capped with a second Pb layer (Pb|Se and Pb|Se|Pb). Elementally modulated precursors with 8 and 16 repeating Pb|Se layers were deposited on Si with native SiO_2 where the amount of each element deposited in each Pb|Se layer sequence targeted a single bilayer of crystalline PbSe. To probe the impact of surface structure, elementally modulated precursors of Pb|Se were also prepared on top of Mo|Se or V|Se layers, which were deposited on Si substrates with native SiO_2 immediately before the Pb|Se bilayers. The targeted amount of Mo or V and Se deposited per M|Se layer equaled that required for single $MoSe_2$ or VSe_2 trilayers, respectively. The number of Pb|Se layers in the precursor structure was varied to determine the effect of total thickness on the roughness of the PbSe that formed. The X-ray reflectivity patterns of all samples did not contain Bragg maxima, indicating that the Pb|Se layers intermixed completely during the deposition. The total experimental atoms/Å^2 of Pb and Se are reported in Table 4.1 for each precursor. The Pb|Se precursor was found to have excess Se (50%) and the Pb|Se|Pb precursor was found to have excess of Pb (12%) relative to stoichiometric PbSe. We calculated the number of possible PbSe bilayers based on the amount of Pb in the precursors assuming that 0.1065 atoms/Å^2 of Pb and Se are needed to form one bilayer of 100 oriented PbSe.

Table 4.1. Total experimental atoms/Å^2 were determined via X-ray fluorescence, where Se also includes the amount used in M(Mo,V)|Se layers. The number of PbSe layers was calculated using the total Pb atoms/Å^2, where 0.1065 atoms/Å^2 are needed to form one bilayer of PbSe.

Substrate	Precursor structure	Total Atoms/Å^2			# possible PbSe
		Pb	Se	M	
Native SiO_2	Pb|Se	1.57(2)	4.7(3)	-	15

	Pb|Se|Pb	3.58(2)	2.2(3)	-	20
Native SiO_2	8 Pb|Se	0.88(2)	1.1(3)	-	8
4 V|Se	16 Pb|Se	1.68(2)	2.8(3)	0.4(3)	15
8 Mo|Se	128 Pb|Se	12.5(2)	14.6(3)	0.82(1)	117
	64 Pb|Se	6.41(3)	9.0(5)	0.83(1)	60
	32 Pb|Se	3.17(7)	5.7(8)	0.83(1)	29
	16 Pb|Se	1.9(1)	3(1)	0.83(1)	17
	8 Pb|Se	0.9(3)	2(1)	0.82(1)	7

The Pb|Se and Pb|Se|Pb precursors were prepared on native SiO_2 coated Si substrates to provide a baseline to understand the reaction of Pb and Se. X-ray reflectivity patterns of both samples (Figure 4.1a) contained only the first few Kiessig fringes, indicating that the samples are rough. Roughness was quantified from the XRR patterns using the formula derived by Parratt.[44] The Pb|Se|Pb sample has a higher root mean square roughness (Rq ≈ 30 Å) than that calculated for the Pb|Se sample (Rq ≈ 20 Å). Specular XRD of the as-deposited samples indicated that PbSe formed during deposition with no preferred alignment to the Si substrate (S1). All reflections in the grazing incidence X-ray diffraction (GXRD) patterns are consistent with the known rock-salt PbSe structure (Figure 4.1b). The resulting a-axis lattice parameter of 6.11(1) Å for the Pb|Se and Pb|Se|Pb samples agrees with that reported previously for PbSe (a = 6.117 Å).[45]

A cross section of the sample with the Pb|Se|Pb layering sequence was prepared and HAADF-STEM was used to investigate the sample's morphology. The HAADF-STEM/EDS revealed the formation of PbSe islands coated with Pb(Se) oxides, presumably due to the exposure of the sample to air both before and after preparing the cross sections when transporting it to the instruments (Figure 4.2a). The images of the EDS maps (Figure 4.2b) of the entire film revealed the presence of a thick surface oxide layer that contains mostly Pb and O, which is consistent with the difference in STEM intensities. The size of the PbSe islands and the resulting surface topology is consistent with the surface roughness calculated from the XRR data. A higher magnification HAADF-STEM image contains crystalline regions with lattice fringes (Figure 4.2c) that are consistent with PbSe. On occasion, the presence of lattice fringes which are not consistent with the cubic PbSe phase have been observed, presumably a Pb-Se-O phase, but identification was inconclusive.

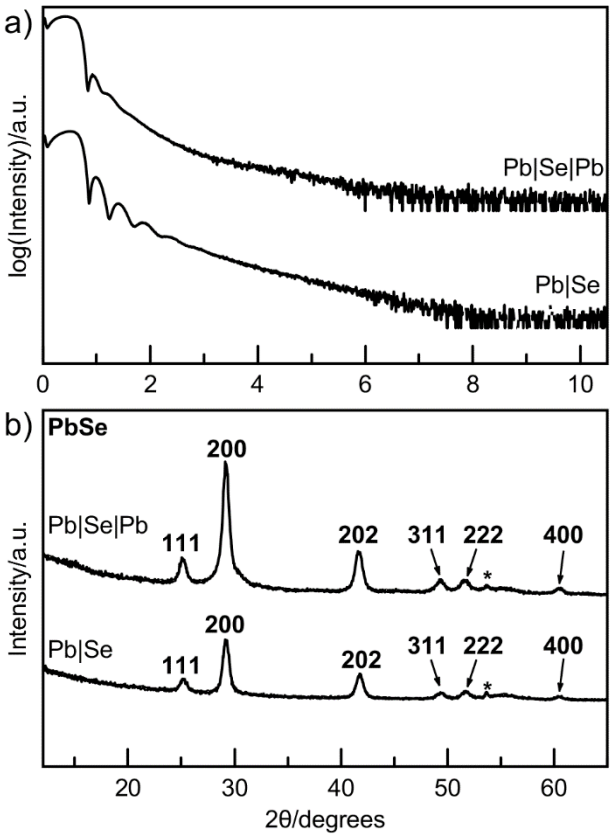

Figure 4.1. a) X-ray reflectivity patterns of as-deposited Pb|Se and Pb|Se|Pb precursors. b) Grazing incidence X-ray diffraction where labeled indices apply to as-deposited Pb|Se and Pb|Se|Pb precursors and are consistent with PbSe ($Fm\bar{3}m$). Asterisks indicate substrate reflections or are an artifact of the diffractometer.

The XRD and STEM data both show that PbSe forms before annealing the sample, presumably during the deposition. After the first Pb layer is deposited, Se reacts during deposition with the Pb layer and significant interdiffusion of Pb and Se occurs to form islands of PbSe, even though the substrate is not heated. Island growth suggests that the interaction of the reacting Pb and Se atoms with the formed PbSe must be stronger than with the native SiO_2 coated Si substrate. When all of the first deposited Pb layer has reacted to form PbSe, the rest of the Se deposited forms an elemental layer. This then reacts with the 2nd layer of Pb deposited. The excess Pb in the sample forms oxides from exposure to atmosphere as the sample is transferred to a dry box for storage, as the sample is characterized using XRR and XRD or during the STEM sample preparation and transport to the instrument. This presumed sequence of reactions is consistent with prior reports of island growth of PbSe during MBE or during ALD growth on a variety of substrates, including SiO_2.[2,46]

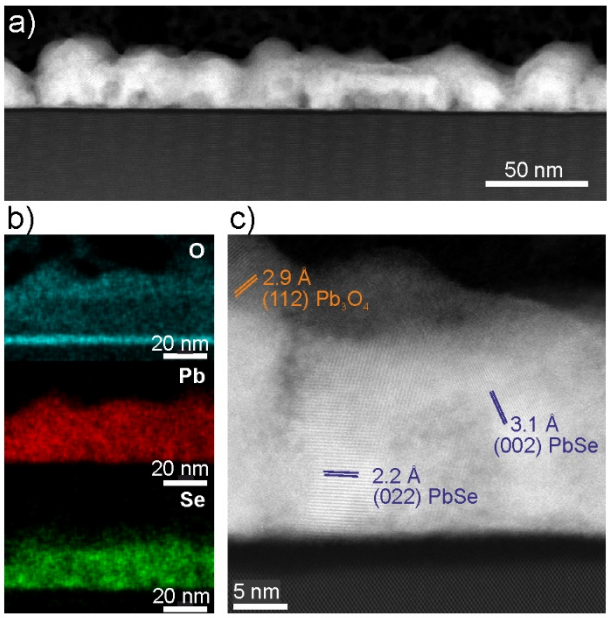

Figure 4.2. a) HAADF-STEM image of a cross section of the as-deposited Pb|Se|Pb (62% Pb) sample which shows PbSe islands. b) EDS elemental maps indicating an Pb-rich oxide layer and c) higher magnification HAADF-STEM image with crystalline regions that have lattice fringes consistent with Pb oxides or rock-salt PbSe.

The elemental modulated precursors with thinner Pb|Se layers have much smaller diffusion lengths (< 1 nm). A sample with 8 bilayers of PbSe deposited on Si with native SiO_2 was prepared as a baseline for PbSe growth. Composition and diffraction data was collected before and after the precursor was annealed to 300 °C for 30 minutes, which were the annealing conditions used in a previous study of thicker PbSe layers.[41] After annealing, the sample contained 0.875 Pb atoms/Å^2 and 0.839 Se atoms/Å^2, which suggests that 8 bilayers of 100 orientated PbSe could form. Similar to the bulk PbSe samples, the XRR pattern of this sample (Figure 4.3a) before and after annealing indicates that the PbSe layer is rough (Rq ≈ 13 Å), which suggests that Island growth occurs during the deposition of the film. Specular XRD patterns of the as-deposited sample and after annealing to 300 °C both contain reflections that can all be indexed as hkl reflections of PbSe, indicating that randomly oriented PbSe grains form during deposition (Figure B.2). The reflections in the in-plane XRD pattern can also be indexed as hkl reflections of PbSe (Figure 4.3b). The systematic absences are consistent with the PbSe $Fm\bar{3}m$ space group, and the calculated a axis lattice parameter of 6.11(1) Å agrees with that reported previously for PbSe (6.117 Å).[45] These results agree with prior work where 16, 32, and

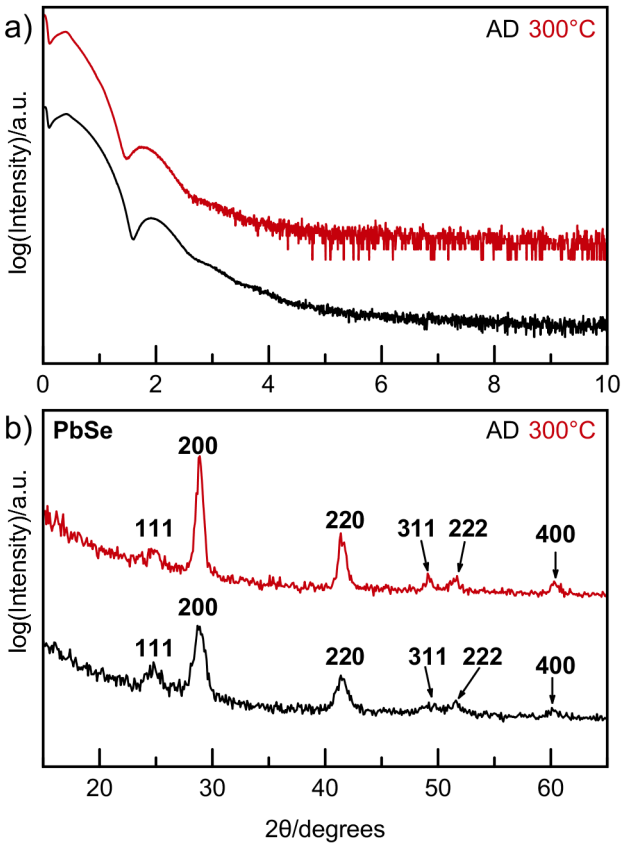

Figure 4.3. a) X-ray reflectivity pattern of the 8 Pb|Se precursor on Si with native SiO_2 as-deposited (AD) and annealed to 300 °C. b) In-plane diffraction where labeled indices correspond to PbSe ($Fm\bar{3}m$).

82 repeating layers of PbSe were deposited on Si with native SiO_2 yielding rough PbSe films where the grains are randomly oriented.[41]

To form atomically smooth layers, we speculated that we needed to switch the substrate to one with a stronger interaction with PbSe. $(PbSe)_1(VSe_2)_1$ is a known, thermodynamically stable compound and a recent investigation showed that Pb|Se layers deposited on VSe_2 form atomically smooth layers of PbSe. To expand this previous study, we prepared a modulated precursor containing 16 repeating layers of Pb|Se deposited on 4 RU of V|Se, which were deposited onto Si with native SiO_2. This precursor was annealed under the same conditions as the 8 Pb|Se precursor (300 °C, 30 minutes). After annealing, the sample contained 1.65(1) Pb atoms/Å^2, 0.42(1) V atoms/Å^2, and 2.56(1) Se atoms/Å^2 measured by XRF. This is enough material to form 15 bilayers of PbSe and 4 trilayers of VSe_2, assuming 0.1026 V atoms/Å^2 and 0.2051 Se atoms/Å^2 are needed to make one trilayer of VSe_2. X-ray reflectivity patterns (Figure 4.4a) contain Kiessig fringes out to 5° 2θ, indicating that the as-deposited sample is significantly

smoother than those deposited onto native SiO_2 on Si. The XRR pattern after annealing is more complex as the VSe_2 crystallizes, leading to an interference pattern from the VSe_2 and PbSe layers. The as-deposited specular XRD (Figure 4.4b) pattern contains only 00*l* reflections from PbSe, indicating that the PbSe is crystallographically aligned and that the V|Se layers are amorphous. Laue oscillations are present on the 002 PbSe reflection of the as-deposited sample, which indicates that the majority of the film is an integral number of unit cells thick. The number of unit cells determines the spacing of the Laue oscillations, enabling us to calculate that 15 unit cells are present in both the as-deposited and annealed sample. This agrees with the number of PbSe layers possible calculated from the XRF data in Table 4.1. In-plane XRD (Figure B.3) contains only *hk*0 reflections from PbSe in the as-deposited sample, which confirms that PbSe formed crystallographically aligned on amorphous V|Se upon deposition. After annealing the sample at 300 °C, the specular and in-plane diffraction patterns indicate that VSe_2 crystallized. The VSe_2 is crystallographically aligned to the Si/SiO_2, as only 00*l* reflections are observed in the specular diffraction pattern and only *hk*0 reflections are present in the in-plane diffraction pattern. The PbSe remains crystallographically aligned, but the line widths decrease indicating that Ostwald ripening occurs during the anneal. The spacing of the Laue oscillations remains the same as in the as-deposited sample, indicating that 15 PbSe bilayers are still present after annealing.

The formation of crystallographically aligned films of constant thickness on an amorphous substrate during deposition surprised us. To confirm this result, we decided to investigate the formation of PbSe from Pb|Se layers deposited on Mo|Se layers. $(PbSe)_m(MoSe_2)_n$ heterostuctures are metastable, but form from precursors containing repeating sequences of m Pb|Se and n Mo|Se layers containing the number of atoms of Pb and Se in each Pb|Se layer required to form a bilayer of PbSe and the number of atoms of Mo and Se in each Mo|Se layer required to form a trilayer of $MoSe_2$. Binary $MoSe_2$ from modulated precursors does not begin to crystallize until temperatures are above 300 °C, and annealing above 500 °C in a Se atmosphere is required to form completely crystalized $MoSe_2$ layers.[47] The samples we prepared contain the same number of Mo|Se layers and between 8 and 128 Pb|Se bilayers.

The specular XRD patterns for all of the as-deposited $(Pb|Se)_n$ samples deposited on 8 Mo|Se layers are shown in Figure 4.5. The broad reflection at $2\theta \approx 13°$ a result of the repeating Mo|Se layers in the precursors and contains intensity both from the repeating sequence of Mo

rich and poor regions due to the deposition sequence and from any small crystalline $MoSe_2$ domains. The linewidth of this reflection is consistent in each of the samples due to the identical number of Mo|Se bilayers deposited. The intensity decreases as the number of Pb|Se bilayers deposited increases because of the reduced X-ray intensity that transmits through the Pb-Se layer. Precursors with 8, 16, and 32 Pb|Se layers also contain only 00*l* reflections from PbSe, which indicates that crystallographically aligned PbSe forms during deposition on the eight

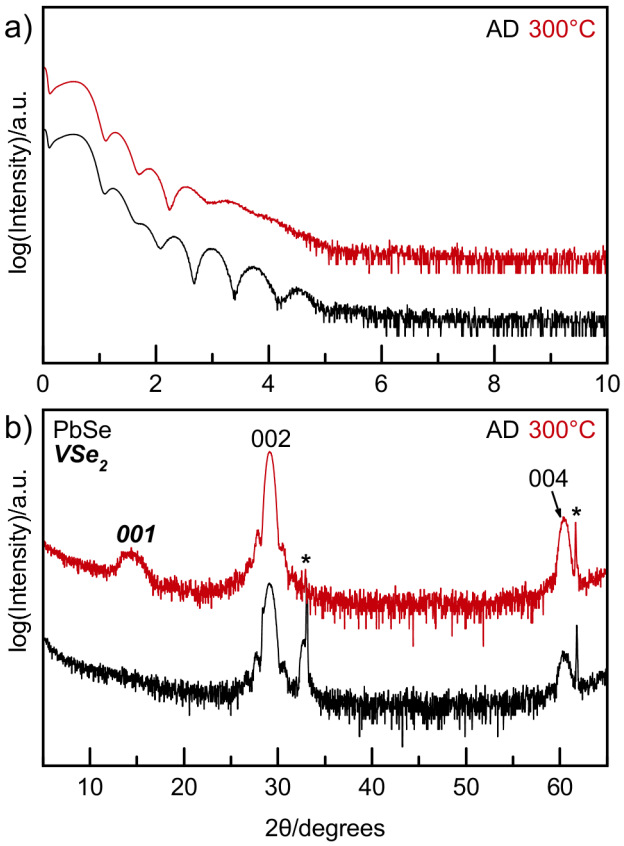

Figure 4.4. a) X-ray reflectivity pattern of the 16 RU Pb|Se precursor as-deposited (AD) and annealed on 4 RU V|Se. b) Specular X-ray diffraction pattern where labeled indices are consistent with only 00*l* reflections from a PbSe ($Fm\bar{3}m$) unit cell or a hexagonal VSe_2 ($P\bar{3}m1$). Asterisks belong to substrate peaks or are an artifact of the diffractometer.

Mo|Se layers initially deposited. Laue oscillations are present in the samples with 8 and 16 Pb|Se layers, indicating that the PbSe layers are smooth and have a consistent, finite number of unit cells present across most of the film. Based on the positions of the Laue oscillations, 7 and 15 PbSe unit cells (c = 6.13(5) Å) are present in the 8 Pb|Se and 16 Pb|Se precursors, respectively, which agrees with the amount of Pb deposited determined via XRF. Precursors with 64 and 128

Pb|Se layers contain non-00*l* reflections, indicating that randomly oriented PbSe crystallites form during the deposition, similar to what was seen in bulk samples deposited on the native SiO_2 layer on Si wafers. This suggests that the interaction with the substrate is important to prevent nucleation of grains that are not crystallographically aligned.

A cross section of the as-deposited 16 Pb|Se on Mo|Se was prepared and investigated with HAADF-STEM (Figure 4.6). Figure 4.6a contains a HAADF-STEM image of the entire film, which revealed partially crystalline regions of $MoSe_2$ on the Si/SiO_2 substrate, followed by a maximum of 7 unit cells of PbSe, and a thick amorphous layer on the surface. EDS maps

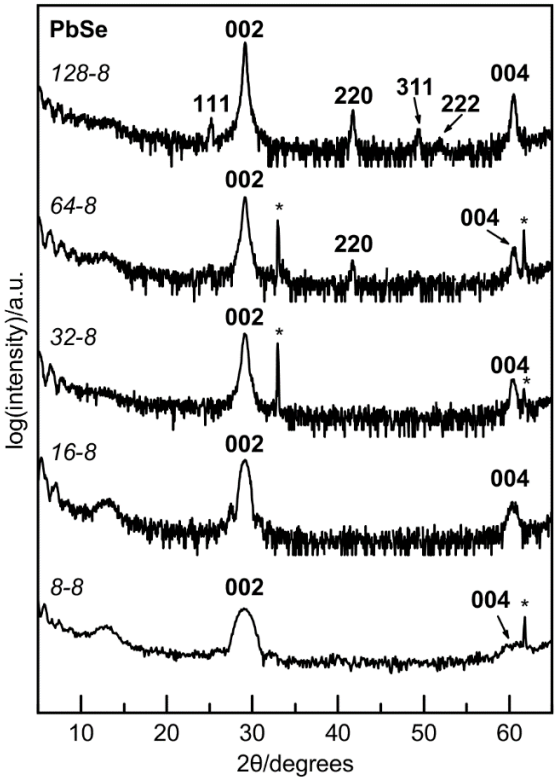

Figure 4.5. Specular X-ray diffraction patterns for Pb|Se on Mo|Se precursors after deposition. Numbers in italics indicate the number of Pb|Se – Mo|Se layers deposited. All indexed reflections are consistent with a rocksalt-type PbSe unit cell. The reflection at $2\theta \approx 13°$ is from the artificial layering of Mo|Se layers and any crystalline $MoSe_2$ domains. The asterisks indicate substrate reflections.

(Figure 4.6b) show that the thick amorphous layer on the surface contains primarily Pb and O. The discrepancy with the diffraction data suggests that the sample surface oxidized before or after the preparation of the cross section. The FIB might also have altered the sample, increasing the amount of crystallized $MoSe_2$ and the amount of Pb oxidized. In this sample, the Pb-oxide is amorphous rather than crystalline like that seen in the bulk Pb|Se sample (Figure 4.2) where

oxidation of excess Pb likely occurred prior to preparation of the cross section, creating a protective cap over PbSe domains. Despite potential changes to the sample, Figure 4.6c and 4.6d show that the crystalized PbSe layers are aligned with the partially crystallized $MoSe_2$ base layer.

The 32 Pb|Se precursor is the thickest precursor that remained crystallographically aligned to the substrate and we followed the evolving structure as a function of annealing temperature with specular XRR and XRD (Figure 4.7). The as-deposited XRR pattern is complex for this sample, containing information on both the thickness of the Mo-Se layer and the Pb-Se layer. The broader Kiessig fringes at higher angle yield a thickness of ~55 Å, which is consistent with the expected thickness of the 8 Mo|Se bilayers deposited. The smaller period Kiessig fringes at lower angles yield a thickness of ~192 Å, which is consistent with the 32 Pb|Se bilayers deposited. The pattern evolves considerably as the sample is annealed at higher temperatures. The regularity and intensity of the smaller period Kiessig fringes increases as

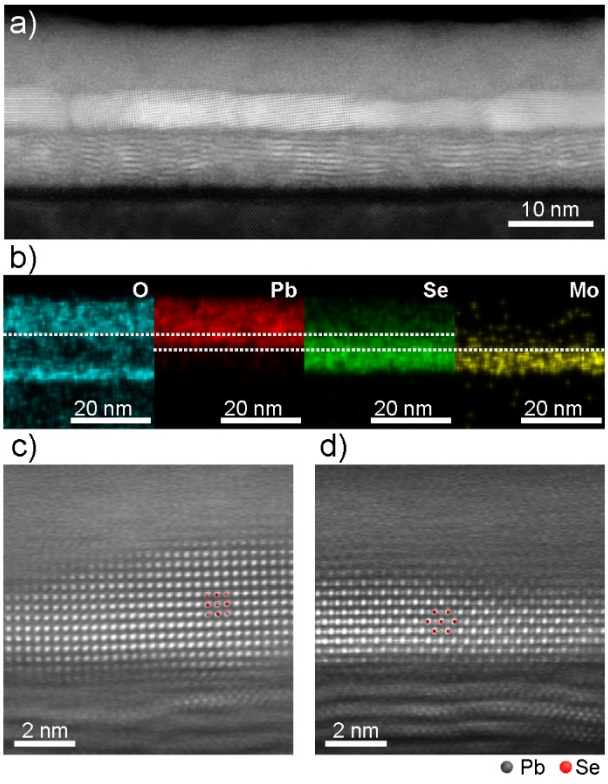

Figure 4.6. STEM data obtained on a cross section of an as-deposited sample containing 16 deposited Pb|Se bilayers on 8 Mo|Se bilayers. a) HAADF-STEM image showing relatively smooth crystalline grains of PbSe on top of irregular small crystalline domains of $MoSe_2$. b) EDS elemental maps demonstrate oxidation of the Pb|Se precursor. c and d) Noise-filtered HRSTEM (HAADF) images depicting crystalline regions of cubic PbSe in [100] and [110] orientations (see superimposed models).

annealing temperature increases, which is concurrent with a growth in the intensity of the 002 reflection of PbSe in the specular scans. This suggests that the PbSe remains smooth as it crystalizes. Conversely, the intensity of the broader Kiessig fringes from the initially deposited Mo|Se bilayers decrease while the $MoSe_2$ reflection at $2\theta \approx 13°$ increases as annealing temperature increases. This suggests that domains of $MoSe_2$ are not as smooth as the initially deposited layers, consistent with the STEM images shown in Figure 4.6. The as-deposited specular XRD contains only the 002 and 004 reflections from PbSe, which indicates that the PbSe crystallized during the deposition, indicating that the PbSe is aligned to the Mo-Se layer before $MoSe_2$ has crystallized. Laue oscillations appear on the 002 reflection after annealing at 300 °C and remain until annealing above 500 °C. Analysis of Laue oscillations indicate that 29 PbSe unit cells formed after annealing, which agrees with the number of PbSe layers expected to form based on measurements of the amount of Pb present in the film from XRF data (Table B.1). At 300 °C, the 001 reflection consistent with $MoSe_2$ has higher intensity, sharpens and shifts from that seen in the lower temperature scans, coinciding with the loss of the Mo-Se Kiessig fringes in the XRR. The 003 reflection is also present after annealing at 300 °C. The 004 reflection grows in, and intensities of all $MoSe_2$ reflections increase in intensity with further annealing. The c-axis lattice parameter decreases slightly with annealing temperature to c = 6.52(4) Å, which is slightly larger than that reported for bulk $MoSe_2$ (6.46 Å).[48]

All of the remaining samples were annealed at 400 °C to explore the impact of annealing on the morphology of the films and the PbSe that formed on annealing. The number of layers expected to form after annealing were determined from measurements of the amount of Mo, Pb and Se present in the film from XRF for all samples, which can be found in the table in the supporting information (Table B.1). The number of $MoSe_2$ layers was determined by assuming Se was used to form the number of PbSe layers possible, and that 0.2135 Se atoms/$Å^2$ are needed to form one trilayer of $MoSe_2$. With Se loss after annealing, some excess elemental Mo may be present in precursors. Figure 4.8 contains XRR and XRD data from the 64 and 128 Pb|Se bilayer samples. The as-deposited scans contain broad Kiessig fringes from the Mo|Se layers and smaller Kiessig fringes from PbSe in the precursor, which are also present in the samples with thinner PbSe layers. After annealing, both samples become smoother and the non-00*l* reflections are no longer present in the specular XRD pattern. This indicates that the PbSe layer are mostly crystallographically aligned to the partially crystalline $MoSe_2$ layers. Laue oscillations are not

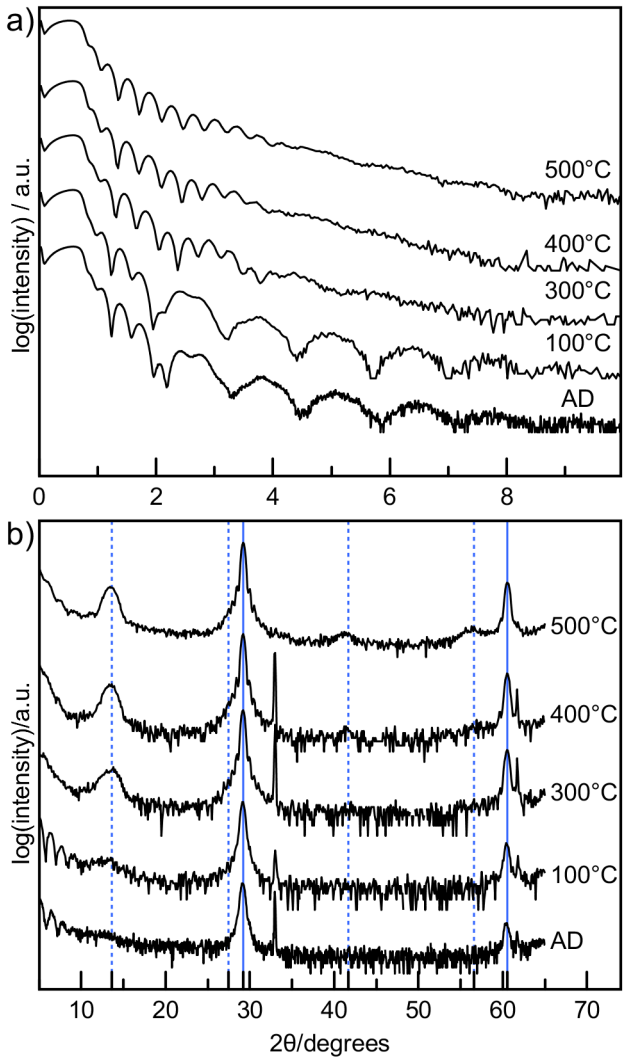

Figure 4.7. a) X-ray reflectivity patterns and b) specular X-ray diffraction as a function of annealing for the 32 Pb|Se – 8 Mo|Se precursor. Solid vertical blue lines represent the expected 00*l* reflection positions for a PbSe unit cell, and dashed vertical blue lines represent expected 00*l* reflection positions for $MoSe_2$.

observed, indicating that the crystalline domains are not consistently the same thickness across the area probed by the X-ray beam. The diffraction scans collected on the samples with 8 and 16 Pb|Se layers after annealing at 400 °C are shown in Figure 4.9. The XRR patterns remain complex after annealing, containing interference from both the PbSe and Mo|Se layers. The Kiessig fringes from the interference with the layers persists to higher angles after annealing, indicating that the samples become smoother. The high angle specular diffraction scans indicate that the PbSe layers remain crystallographically aligned after annealing. Laue oscillations are present in both samples after annealing. The number of unit cells calculated from the Laue oscillations was determined to be 7 and 15 unit cells in both the as-deposited and annealed

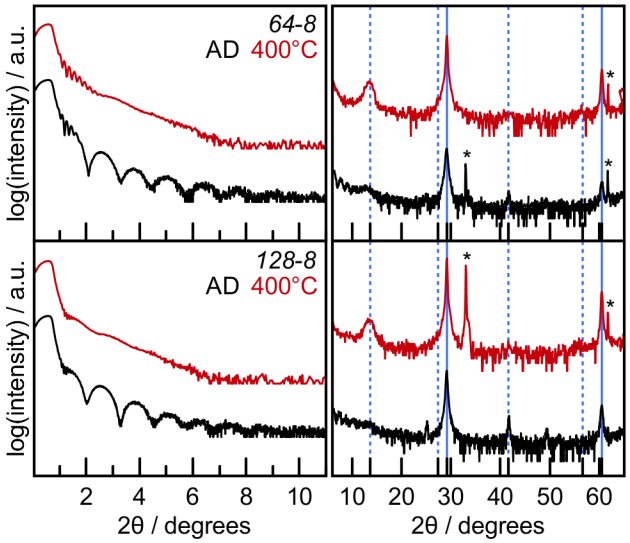

Figure 4.8. X-ray reflectivity patterns (left) and specular X-ray diffraction patterns (right) as a function of annealing for the 64 Pb|Se – 8 Mo|Se precursor (top) and 128 Pb|Se – 8 Mo|Se precursor (bottom). Solid vertical blue lines represent the expected 00*l* reflection positions for a PbSe unit cell, and dashed vertical blue lines represent expected 00*l* reflection positions for $MoSe_2$. The asterisks indicate substrate reflections.

samples corresponding to the 8 and 16 Pb|Se repeating bilayer thick precursors that were deposited, respectively. The difference between the number of unit cells formed and the number of Pb|Se layers deposited results from a deficiency of Pb in the deposited bilayers. The broad reflection from the Mo-Se layers at $2\theta \approx 13°$ shifts to higher angle, sharpens, and increases in intensity after the precursor is annealed at 400 °C. Weak higher angle 00*l* reflections from crystalline $MoSe_2$ also are present in the scans of the annealed precursors. This data suggests that the morphology and structure of the PbSe layer does not change as the underlying $MoSe_2$ layer crystallizes.

4.4. Conclusions

These results suggest that strong interactions between substrate and growing film are necessary to form smooth, crystallographically aligned layers. The substrate does not need to be crystalline, as crystallographically aligned PbSe forms on mostly amorphous Mo|Se and V|Se coated Si substrates during nominally room temperature deposition. The thicker PbSe bilayers can be annealed at low temperatures to increase the amount of crystallographic alignment. The number of PbSe bilayers formed depends on the amount of Pb (or Se) deposited. If the amount of Pb deposited is close to that required for an integral number of unit cells and there is sufficient

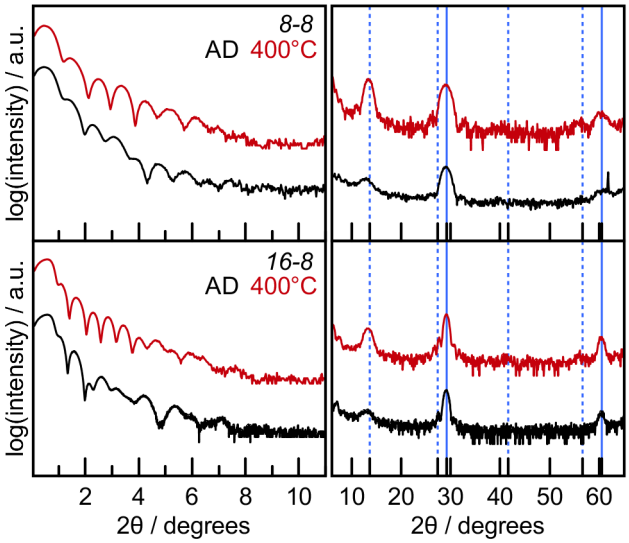

Figure 4.9. X-ray reflectivity patterns (left) and specular X-ray diffraction patterns (right) as a function of annealing for the 8 Pb|Se – 8 Mo|Se precursor (top) and 16 Pb|Se – 8 Mo|Se precursor (bottom). Solid vertical blue lines represent the expected 00*l* reflection positions for a PbSe unit cell, and dashed vertical blue lines represent expected 00*l* reflection positions for $MoSe_2$.

Se, Laue oscillations are present in the as-deposited samples, and they remain present after annealing. The Laue oscillations reflect the quality and uniformity of the crystalline PbSe domains. While prior studies typically explored epitaxial growth, this study demonstrates that the substrate does not need to be crystalline to form smooth PbSe with crystallographic alignment. While a drawback of using an amorphous substrate is that the orientation of different regions of the film can't be controlled, the crystallographic alignment and atomically smooth thicknesses of the PbSe formed in this study contrasts with prior reports, where island growth occurred on substrates with near epitaxial relationships with PbSe.

4.5. Bridge

Chapter IV describes how substrate crystallinity affects the growth of PbSe thin films. Chapter V continues the discussion of how experimentally controllable variables can be used to isolate and investigate solid state growth mechanisms by investigating how deposited layer thicknesses and local composition can be used to manipulate the growth of Mo-Se films. A new, generally applicable method to suppress nucleation and achieve amorphous precursors is presented.

CHAPTER V

Synthesizing Amorphous Precursors Through Control of Local Composition

5.0. Authorship Statement

Chapter V was published in *Chemistry of Materials* in 2024. I am the primary author of the manuscript. Annalise Walker aided in data collection and interpretation. David C. Johnson acted as my advisor and contributed to writing and editing the manuscript.

5.1. Introduction

Understanding how to control reactions between elements is critical to advance technology and to synthesize predicted new compounds. For example, the development of metal silicides as contacts in silicon integrated circuits[1] was accelerated by the development of empirical rules to predict what compound forms first at the reacting interface between metal and silicon. Walser and Bene's first phase rule provided insight to the species formed at reacting interfaces.[2] It suggested that the deepest eutectic was the most stable amorphous composition which likely formed at the reacting interface from the initial interdiffusion of the elements.[2] The congruently melting compound with the highest melting point adjacent to the eutectic was suggested to be the compound that formed first, as it was the compound closest in composition to the amorphous phase with the largest driving force to nucleate. In the synthesis of predicted new compounds, a key challenge is avoiding the formation of thermodynamically stable compounds at the interface between reacting elements. For example, the compound $FeSb_3$ was predicted to have interesting thermoelectric properties but could not be made by direct reaction of the elements as it is thermodynamically unstable relative to a mixture of $FeSb_2$ and Sb. The synthesis of $FeSb_3$ was only possible through using an Sb rich amorphous precursor as a reaction intermediate to favor nucleation and growth of $FeSb_3$.[3] More recently, Persson theoretically showed that the amorphous phase sets an energetic upper bound for synthesizability of metastable crystalline polymorphs,[4] highlighting how an amorphous phase of controlled

composition is a very general and useful reaction intermediate in the synthesis of predicted compounds.[5]

It can be very challenging, however, to experimentally prepare amorphous intermediates with controlled composition, resulting in several experimental approaches being developed, each with associated benefits and disadvantages. The "splat quenching" process allows amorphous solid and metastable crystalline phases to be trapped through extremely rapid cooling of a melt.[6] The goal is to cool fast enough through the glass transition temperature that the atomic rearrangements necessary for nucleation cannot occur. It has been successful in the synthesis of even some fairly complex metastable structures[6] and in improving the microstructure of resultant films.[7] The lack of control over phase purity,[8,9] variation of thicknesses of resultant films,[7] and the rate and uniformity of cooling across the cooling surface, however, has limited widespread use of this method to synthesize predicted metastable phases.[10,11] Another synthetic route to amorphous phases is the destruction of crystallinity by bombardment with high-energy ionizing particles.[12–15] The ability of this method to precisely control composition and location of implanted ions makes it of widespread technologic relevance in semiconductor manufacturing.[12,15–18] However, since ion beams are typically focused to a small area and the deposited amount of ions is proportional to time, this approach is more suited for doping applications than for synthesis. A variety of vacuum deposition techniques have also been used to synthesize amorphous intermediates, based on the condensation of vapor phase species onto a substrate.[12,19] Amorphous solids with higher densities, lower enthalpies, and greater kinetic stability[20–23] than those synthesized with other techniques have been prepared, with the required substrate temperature being directly linked to the stability of the resultant glasses.[22,24] Designed amorphous composition modulations can be prepared by sequentially depositing different elements. In the modulated elemental reactants (MER) approach, for example, atomically thin layers are sequentially deposited onto an ambient temperature substrate to create precursors of designed composition and layering sequence that mimics the nanoarchitecture of targeted crystalline products.[3, 25–30] Low temperature annealing of the modulated precursors can result in a homogeneous amorphous phase if mixing of the layers occurs before nucleation can occur.[31–34] None of these vacuum deposition approaches yield amorphous products, however, if nucleation occurs during deposition. For example, Pb-Se[35] and Mo-Se[36] precursors form PbSe and $MoSe_2$

respectively over a large composition range when these elements are sequentially deposited in the MER approach.

Herein, we show that amorphous intermediates can be made in the Pb-Se and Mo-Se systems by depositing precursors on a nominally room temperature substrate with ultrathin sub-monolayer elemental layers and non-stoichiometric compositions. We hypothesize that the local coordination sphere of the atoms is completed, and the resulting heat dissipated before additional atoms arrive in the next layer deposited. The unheated substrate limits the extent of diffusion and local rearrangements that can occur during deposition. We believe this approach is general because longer range diffusion and local coordination changes are necessary for nucleation embryos to form if local compositions are different from the stoichiometry of the compound being nucleated. This approach to avoiding the nucleation of binary compounds should be even more effective in ternary and quaternary systems, as the additional elements should suppress nucleation of binary compounds.

5.2. Methods and Materials

Samples were deposited on unheated 7.5 by 2.5 cm <100> Si wafer rectangle substrates with a native oxide layer in a custom vapor deposition chamber described in detail previously.[26,37] Elemental Se (99.99%, Alfa Aesar) was deposited with a Knudsen effusion cell, while elemental Mo (99.995%, Alfa Aesar) and Pb (99.8%, Alfa Aesar) were deposited using 6 keV electron beam guns. A custom LabView software program was used in conjunction with quartz crystal microbalances to measure deposition rates and control the position of pneumatic shutters above the vapor plume of each source. By closing each shutter based on the integrated amount of material deposited after opening, the thickness of each element deposited in each repeating unit of the layered samples was controlled. Elemental bilayers of Mo|Se or Pb|Se were sequentially deposited with varying elemental layer thicknesses to probe the reactions occurring during the deposition as a function of layer thicknesses and composition. The evolution of the samples as a function of temperature and time was also investigated to determine if homogeneous amorphous intermediates formed from elementally layered precursors. Samples were stored and annealed in a drybox with a N_2 atmosphere with less than 2 ppm of O_2.

A variety of x-ray scans (reflectivity, specular, in-plane and grazing incidence) were collected using a Rigaku SmartLab diffractometer with a copper Kα radiation source to

structurally characterize the samples after deposition and each annealing step. Composition was measured via x-ray fluorescence (XRF) on a Rigaku ZSX Primus II wavelength-dispersive X-ray fluorescence spectrometer with a rhodium source using a previously published proportionality constant relating background-corrected XRF signal intensity to the absolute number of atoms/Å^2 for each element.[38]

5.3. Results

20 $MoSe_2$ precursors with varying repeat unit thicknesses and Se/Mo ratios were prepared by depositing alternating Mo and Se layers onto a near room temperature substrate to probe the impact of diffusion lengths and composition on reaction intermediates, reaction rates, and the resultant microstructure of films. The data obtained on the as-deposited samples using XRF, XRR and XRD are summarized in Figure 5.1 (numerical data is contained in Table C.1), where the axes are the total number of $MoSe_2$ structured monolayers that could crystallize given the number of Mo or Se atoms per area present in each deposited repeating Mo|Se sequence. The as-deposited samples shown in blue have Bragg reflections consistent with $MoSe_2$ in their

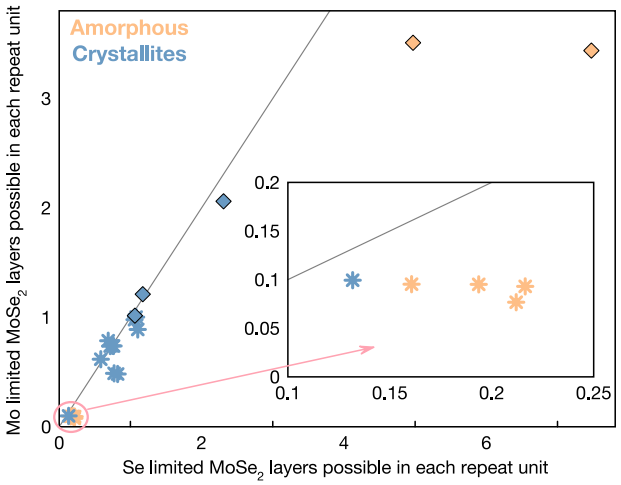

Figure 5.1. The composition of the 20 samples prepared in this study are presented in terms of how many single $MoSe_2$ layers can be formed based on the amount of Mo and Se deposited in each repeat unit. The grey line is the composition of stoichiometric $MoSe_2$. Precursors that remain x-ray amorphous are represented in orange and precursors that have crystallized during deposition are represented in blue. Precursors represented by stars do not have discernible Bragg reflections resulting from the sequential deposition of Mo and Se elemental layers in their XRR or XRD scans. Precursors represented by diamonds have Bragg reflections from the sequential layering of Mo and Se.

Specular and in-plane diffraction patterns. The orange symbols represent as-deposited samples that are x-ray amorphous. Both composition and layer thicknesses influence whether $MoSe_2$ nucleates and grows during the deposition, how the samples evolve with annealing, and the final microstructure of the $MoSe_2$ formed. The samples can be divided into three groups based on their structural differences. In the following paragraphs we describe their as-deposited structures and how the structure of samples in each group evolves as a function of annealing temperature.

Group 1 contains the samples with the thickest elemental layers, the orange diamonds in Figure 5.1, which were x-ray amorphous after deposition and have Bragg reflections at small 2θ values from the deposited composition modulation. Figure 5.2 contains XRR scans for sample 20, which is representative of this group, as-deposited and after annealing at different temperatures. The as-deposited XRR scan contains Kiessig oscillations from the interference of the x-rays between the front and back of the film and 1st and 2nd order Bragg reflections from the repeating composition gradients from the sequential deposition of the elements. The intensity of the 1st order reflection and the presence of a 2nd order reflection indicate alternating regions that are Mo and Se rich, with a composition gradient region between them. Annealing the sample results in interdiffusion of the elements, resulting in the intensity of the 1st and 2nd order reflections decreasing during each annealing step as the composition difference between the Mo

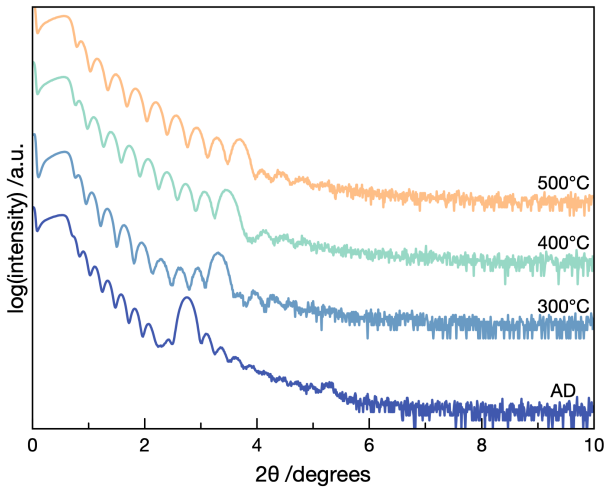

Figure 5.2. X-ray reflectivity scans of a representative Group 1 sample, containing repeating elemental layers that are thicker than required to form a monolayer of $MoSe_2$. Patterns collected after each subsequent annealing temperature are stacked vertically by artificially offsetting the intensity values, starting with the as-deposited (AD) pattern in dark blue on the bottom. This stacking sequence and labeling is used for all subsequent diffraction patterns.

and Se rich layers is reduced. The 1st order Bragg reflection in the XRR also shifts to higher angle as annealing temperature is increased, consistent with the loss of Se during each annealing step measured with XRF.

Representative Group 1 specular diffraction scans are shown in Figure 5.3. The specular pattern of the precursor only contains a very broad maxima near 12° 2θ from diffuse scattering of the still elementally modulated amorphous precursor. After annealing at 300°C, only 00*l* reflections in the specular diffraction are observed that are consistent with the nucleation and growth of $MoSe_2$ crystallites that are crystallographically aligned with the substrate. After annealing at 500°C the reflections present in the diffraction data are consistent with the sample containing more and larger grains of crystallographically aligned $MoSe_2$, but the sample has a Se/Mo ratio of 1.6 due to a competition between formation of $MoSe_2$ and loss of Se when annealed in an open system. Some remnants of initial layering remain as evidenced by the continued presence of a weak first order Bragg reflection in the XRR pattern. This indicates that Se is lost faster than $MoSe_2$ can be formed, presumably due to the strength of Mo-Mo bonds in the Mo rich region of the sample.

The in-plane XRD patterns, shown in Figure 5.4, are consistent with the specular diffraction data. The as-deposited scan contains a very broad maxima centered at ~35° 2θ resulting from diffuse scattering, which is consistent with an amorphous as-deposited sample.

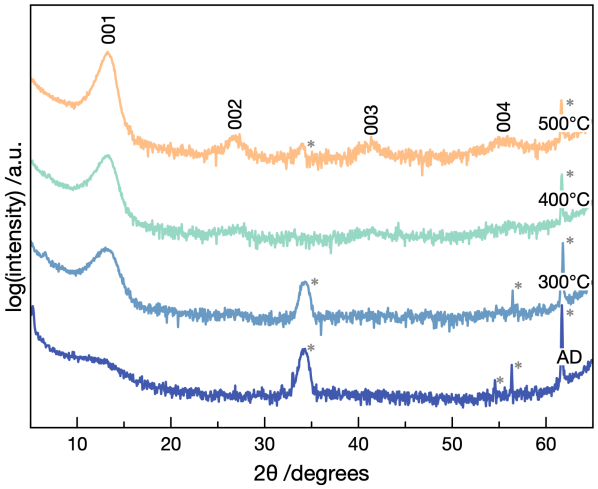

Figure 5.3. Specular diffraction data showing the evolution of a representative Group 1 sample. Labeled indices are consistent with $MoSe_2$. Asterisks mark substrate and stage reflections.

After annealing at 300°C, *hk*0 reflections are observed, consistent with the nucleation and growth of $MoSe_2$ crystallites that are crystallographically aligned with the substrate. The in-plane diffraction scan still contains a broad, low intensity maximum from the remaining amorphous matrix, consistent with the continued presence of the Bragg reflection from layering in the XRR scan. After annealing at 500°C, only *hk*0 reflections from $MoSe_2$ are present.

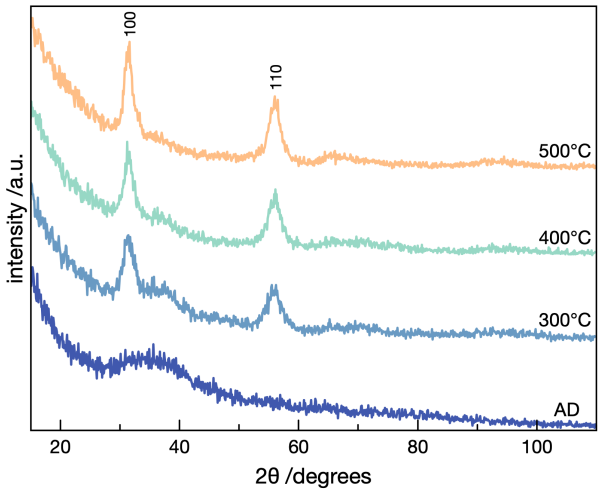

Figure 5.4. In-plane diffraction data showing the structural evolution of a representative Group 1 sample. Labeled indices are consistent with $MoSe_2$.

Figure 5.5 depicts a schematic representation of the evolution of the precursor structure based on the diffraction data. A color gradient is used to represent the composition of the sample, where orange is pure Se and blue is pure Mo. Alternating Mo and Se-rich layers are shown to have an interdiffused region between them, consistent with the presence of Bragg reflections from the elemental layering. Figure 5.5b presents a schematic representation of the sample after annealing at 300°C, containing $MoSe_2$ crystallites surrounded by Se-rich regions embedded in the still layered matrix. The in- plane and out-of-plane grain sizes in Figure 5.5b are consistent with those calculated using the Scherrer equation, which indicates that growth parallel occurs faster than growth perpendicular to the substrate. Figure 5.5c presents a schematic representation of the sample after annealing at 500°C. These results are consistent with those reported by Fister et. al.,[32] showing that $MoSe_2$ nucleates and grows at the interface before the composition gradient can be eliminated by diffusion.

Group 2 contains the samples that crystallize during deposition (the blue symbols in Figure 5.1). As-deposited and after annealing XRR scans from sample 13 in this group are shown in Figure 5.6. The as-deposited sample has Kiessig oscillations that die out around 4° 2θ. The Kiessig fringes extend to higher angles as the samples are annealed at higher temperatures, indicating the roughness in the film decreases with annealing. The total sample thickness calculated from the positions of Kiessig fringes decreases after annealing at higher temperatures,

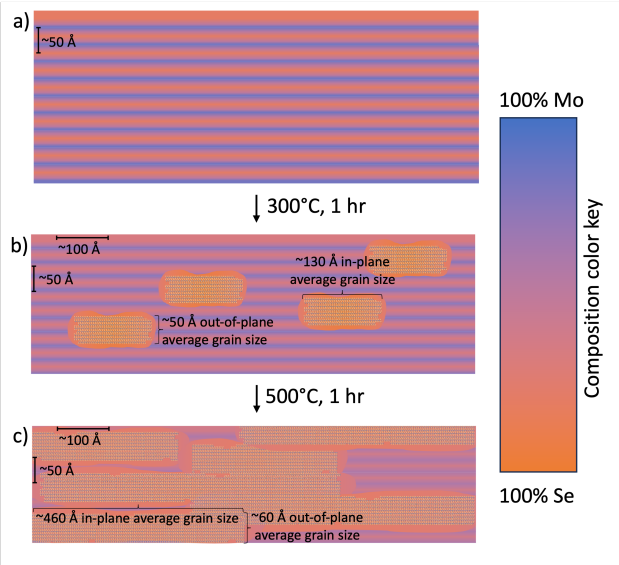

Figure 5.5. Schematic of the initial structure and subsequent evolution with annealing of Group 1 samples with alternating thick Mo and Se layers, deduced by analysis of the XRR and XRD data. a. The as-deposited sample containing alternating Mo and Se rich regions indicated by the color modulation that reflects the local compositions. b. The sample after annealing at 300°C for 1 hour, showing crystallographically aligned $MoSe_2$ grains scaled to sizes obtained from Scherrer analysis of the diffraction data. Growth of the $MoSe_2$ grains has decreased the concentration of Mo in the surrounding matrix. Interdiffusion has reduced the composition The difference between Mo-rich and Se-rich regions. c. After annealing at 500°C for 1 hour, the $MoSe_2$ grains are larger, with most growth occurring in the in-plane direction. Interdiffusion has further reduced the composition difference between Mo and Se-rich regions.

consistent with the loss of Se during annealing as measured by XRF. The XRF data shows that the Se/Mo ratio is 2 after annealing at 500°C, consistent with the formation of $MoSe_2$.

The as-deposited specular diffraction data (Figure 5.7) contains 00*l* reflections from crystalline $MoSe_2$ and weak intensity from the initial layering of the elements between 12 and 12.5° 2θ. The position of the weak intensity from the initial layering is consistent with the Mo|Se

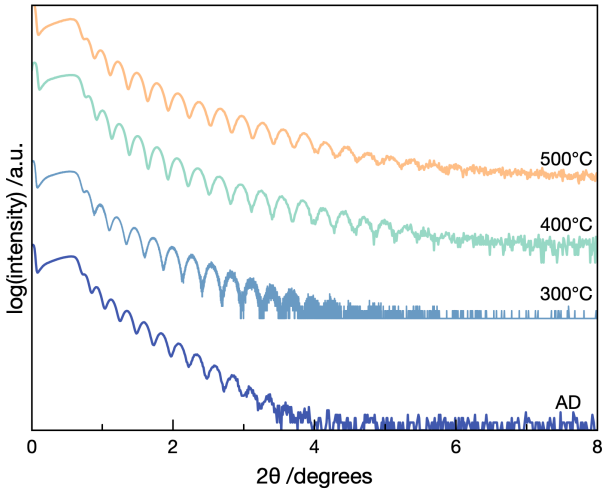

Figure 5.6. X-ray reflectivity scans of a representative Group 2 sample, containing repeating elemental layers that are slightly thicker than a monolayer.

repeat layer thickness calculated by dividing the total thickness obtained from the Kiessig oscillations by the number of Mo|Se layers deposited. The intensity of the layering reflection is much lower than in the samples in Group 1, indicating a smaller electron density difference between the Mo-rich and Se-rich regions in these samples than in Group 1 samples.

The c-axis lattice parameter calculated from the 00*l* reflections in the specular diffraction scans is consistent with the formation of $MoSe_2$. The intensity of the 00*l* reflections increases and linewidth decreases much faster with annealing than observed in the Group 1 sample, reflecting a much faster growth rate perpendicular to the substrate. Laue oscillations, resulting from the film consisting of crystallographically aligned domains of nearly equal thickness, are observed around the 001 reflection after annealing at 400 and 500°C, as shown in Figure 5.7b. The average size of the coherently diffracting domains calculated from the spacing of the Laue oscillations after annealing at 500°C is 43 $MoSe_2$ monolayers. The total thickness from the crystallographic domains causing Laue oscillations can be calculated by multiplying the number of monolayers in the domains (43) by the d-spacing calculated from the positions of 00*l* reflections (6.522(5) Å), yielding a total thickness of 280.4(2) Å. This is only slightly thinner than the total calculated thickness from Kiessig oscillations, 289.4(2) Å, indicating that almost the entire film thickness has crystalized. The number of Laue oscillations observed on either side of the Bragg reflection is related to the width of the distribution of domain sizes about the average. For this sample, the width indicates that the domains range from approximately 40 to 44 monolayers thick.

The in-plane diffraction pattern, Figure 5.8, contains reflections that can all be indexed as *hk*0 reflections from a hexagonal unit cell yielding an a-axis lattice parameter, 3.31(1) Å, that is slightly larger than previously reported values for bulk $MoSe_2$ (3.288(1) Å[39]) but consistent with previously reported values for $MoSe_2$ thin films made with the MER method, which have turbostratic disorder.[36] The intensity of these reflections increases, and the line width decreases as annealing temperature is increased, indicating that more of the sample is $MoSe_2$ with larger average in-plane domain size.

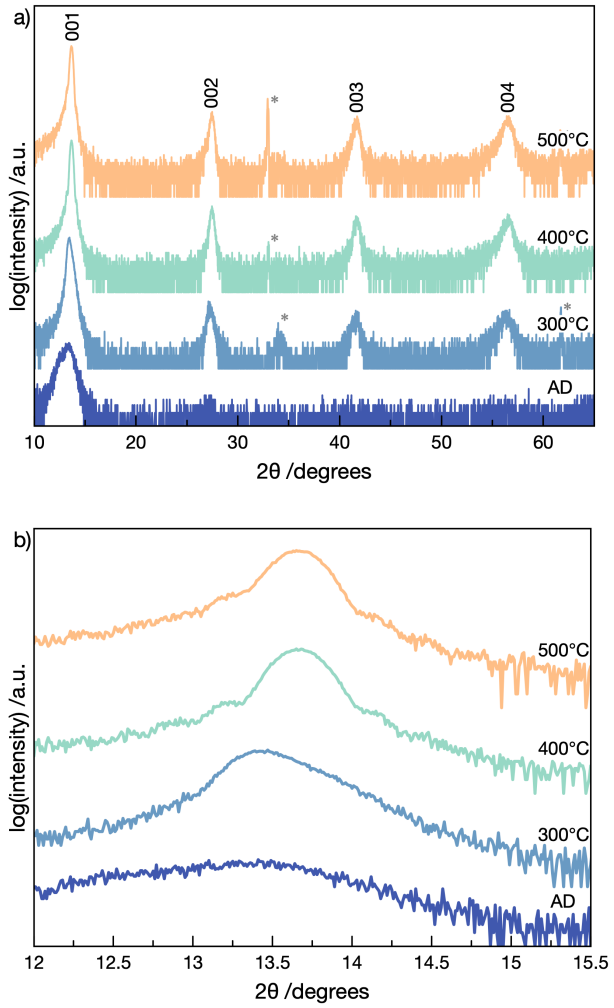

Figure 5.7. a. Specular diffraction data showing the evolution of a representative Group 2 sample. The Group 2 sample chosen had layer thicknesses greater than a monolayer, resulting in the broad maximum on the low angle side of the 001 reflection in the as-deposited sample. b. An expansion of the 001 reflection to see the Laue oscillations more easily at the higher annealing temperatures. Labeled indices are consistent with $MoSe_2$. Asterisks mark substrate and stage reflections.

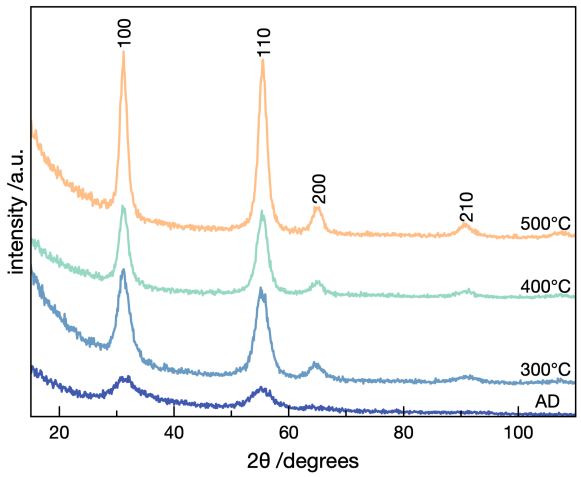

Figure 5.8. In-plane diffraction data showing the structural evolution of a representative Group 2 sample. Labeled indices are consistent with $MoSe_2$.

Figure 5.9 schematically summarizes the analysis of the diffraction data collected from Group 2 samples. $MoSe_2$ forms crystallographically aligned during the deposition surrounded by a Mo depleted shell within an elementally modulated matrix (Figure 5.9a). The amount of $MoSe_2$ increases with annealing and the $MoSe_2$ grains become larger both perpendicular and parallel to the substrate as illustrated schematically in Figure 5.9b. Almost the entire film is crystallographically aligned $MoSe_2$ after annealing at 500°C (Figure 5.9c). These results are consistent with those discussed by Miller, et al.,[40] confirming that if compositions close to a 2:1 ratio of Se:Mo are present as the film is deposited, $MoSe_2$ will nucleate and grow during deposition.

Figure 5.10 contains as-deposited diffraction data for a representative sample of Group 3 as well as data collected after each annealing step. Group 3 contains samples from the previously unexplored regime with ultrathin repeating Mo|Se layers containing significantly less than a monolayer worth of Mo and Se in each repeat unit. The as-deposited XRR data is like that obtained for Group 1 and 2 samples, containing Kiessig oscillations that terminate at nearly the same angle. The change in the spacing of the oscillations after annealing indicates that total sample thickness decreases with annealing. After annealing at 300°C, an 001 Bragg reflection grows in the specular diffraction pattern near 13° 2θ and *hk*0 reflections appear in the in-plane pattern, consistent with the presence of small grains of $MoSe_2$. This is a lower nucleation and

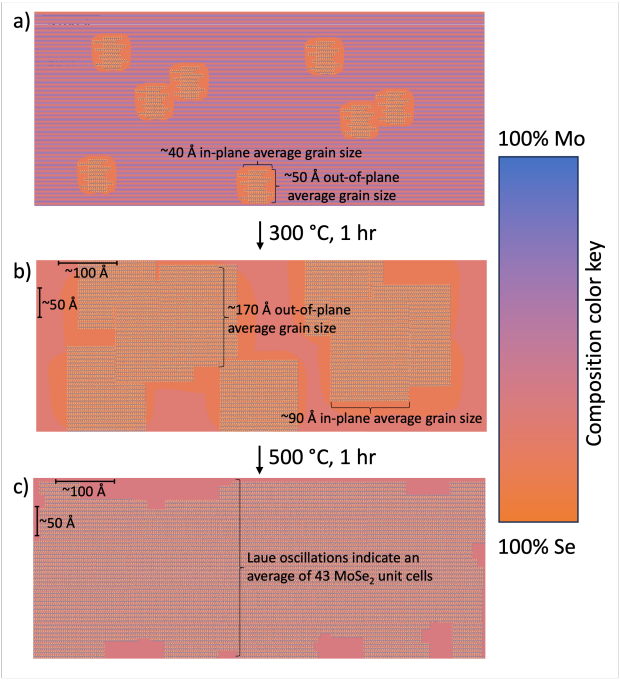

Figure 5.9. Schematic of the evolution of structure with annealing for Group 2 samples, which have alternating layers of Mo and Se with the total bilayer thickness close to the c-axis lattice parameter of $MoSe_2$. a. The as-deposited sample contains $MoSe_2$ grains that nucleated and grew during deposition. The average size of the domains, shown in the schematic, was obtained from Scherrer analysis of specular and in-plane reflections as discussed in the text. Since the total composition is Se rich relative to $MoSe_2$, growth of the $MoSe_2$ grains results in Se rich regions surrounding them. b. The crystallites grow significantly during annealing at 300°C for 1 hour, depleting the concentration of Mo for larger distances around them. The rapid growth at this temperature relative to samples in Group 1 and 3 is a consequence of the layer thicknesses of the artificial modulation resulting in shorter diffusion lengths. c. After annealing at 500°C for 1 hour, the crystalline domains span almost the entire film thickness. The roughness is estimated from the decay of the Laue oscillations around the 00*l* reflections in the specular diffraction pattern.

growth temperature than seen in Group 1 samples, due to the higher diffusion rate in the Se rich amorphous phase compared with the more Mo rich gradient of composition at the interface present in Group 1 samples. These reflections grow continuously as a function of annealing at higher temperature, but even after annealing at 500°C, the intensities remain much lower than for the samples in either Group 1 or 2. The lower intensities result from decreased crystallographic alignment of the $MoSe_2$ grains as reflected in significantly broader rocking curve scans. The Se/Mo ratio decreases from ~3 in the as-deposited sample to ~1.8 after annealing at 500°C,

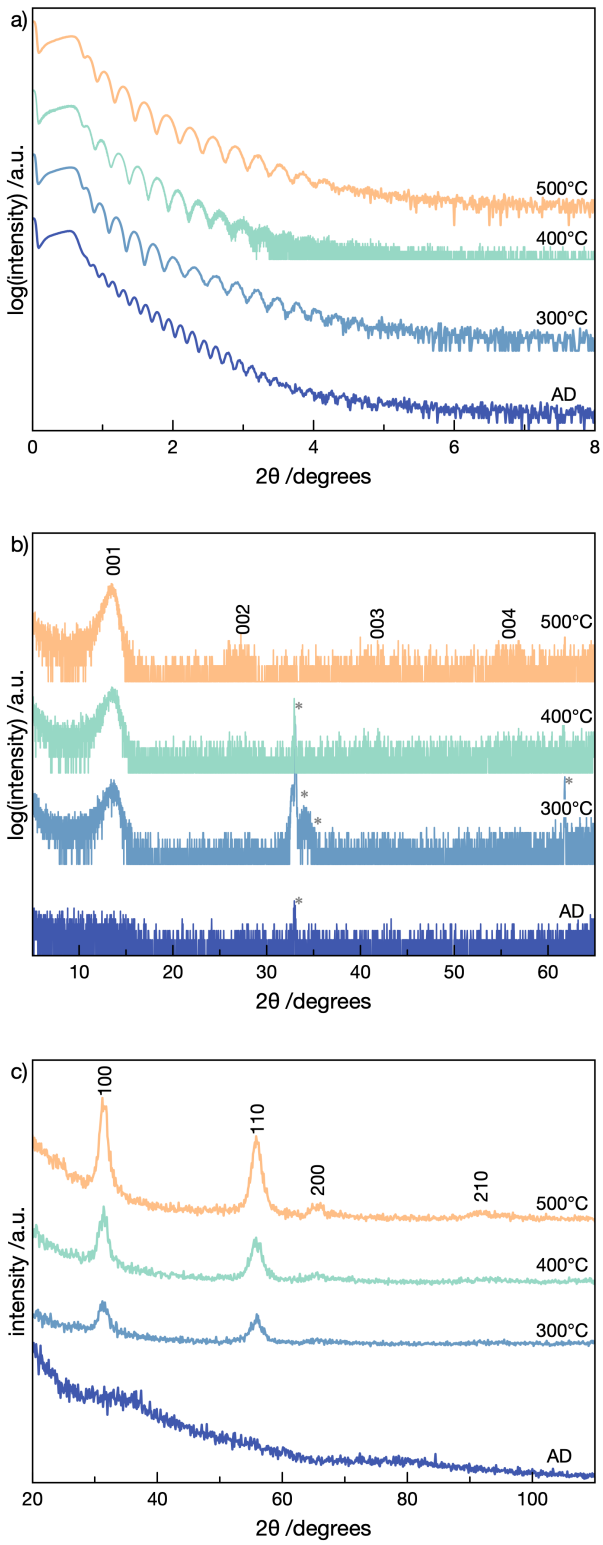

Figure 5.10. Diffraction data showing the evolution of a representative sample from Group 3. a. X-ray reflectivity b. Specular x-ray diffraction c. Grazing incidence in-plane x-ray diffraction. Labeled indices are consistent with $MoSe_2$. Asterisks mark substrate reflections and diffractometer artifacts.

indicating that Se evaporates faster in an open system than $MoSe_2$ forms. The diffraction data shows that a homogenous x-ray amorphous phase can be prepared by depositing ultrathin layers at non-stoichiometric compositions.

To probe if depositing non-stoichiometric ultra-thin layers results in amorphous as-deposited films in other systems reported to nucleate and grow binary compounds during deposition, we prepared several binary Pb|Se films as shown in Figure 5.11. The as-deposited samples were characterized using XRF, XRR and XRD (data is in SI). To obtain higher intensities of reflections from the randomly orientated PbSe grains, grazing incidence scans were collected. The grazing incidence diffraction patterns for the thinnest repeat layer thicknesses (Figure 5.12) clearly show that three samples with composition closest to the stoichiometry of PbSe crystallize with random orientation during the deposition (blue patterns), which is consistent with prior reports,41 and three samples that are more Se rich remain x-ray amorphous (orange patterns). Above the pink arc (Figure 5.11), large enough areas of local compositions the

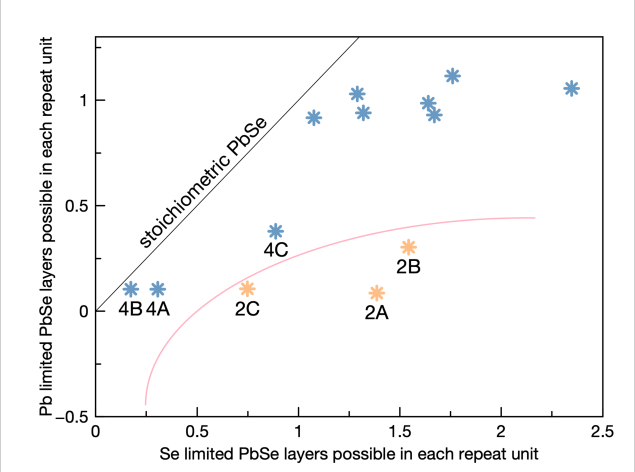

Figure 5.11. A summary of Pb-Se samples graphed as the number of PbSe monolayers that could crystallize with the amount of Pb versus the amount of Se deposited in each repeat Pb|Se sequence. Samples that are x-ray amorphous after deposition are represented in orange and precursors that crystallized during deposition are represented in blue. None of these samples have discernible Bragg reflections resulting from the sequential deposition of elements.

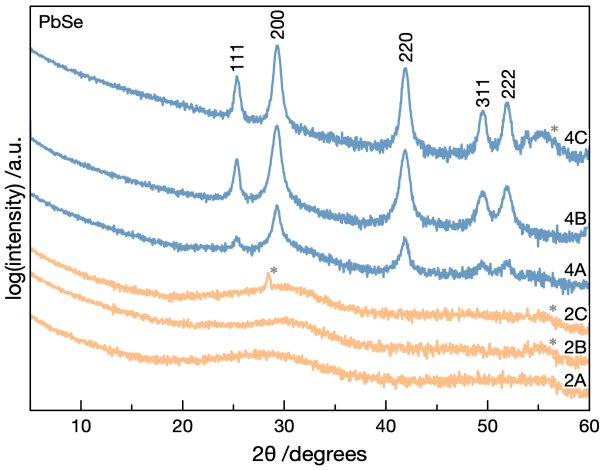

Figure 5.12. As-deposited grazing incidence x-ray diffraction patterns of the six thinnest Pb|Se samples in Figure 5.11. Samples 2A, 2B, and 2C remain x-ray amorphous during the deposition (orange patterns). Samples 4A, 4B, and 4C all crystallize PbSe with random orientation with respect to the substrate (blue patterns). Labeled indices are consistent with PbSe. Asterisks mark substrate reflections and diffractometer artifacts.

close to a 1:1 ratio of Pb:Se are present at the interface between the Pb and Se deposited layers to permit the nucleation of PbSe during deposition (the blue points in Figure 5.11). Once nucleated, surface diffusion rates are high enough for growth during the deposition and larger Pb layer thicknesses result in larger grains due to the increased local supply of Pb. Excess Se reduces grain sizes because Se accumulates at the crystal growth front, increasing the diffusion lengths of Pb atoms moving to the growth front. Pb deposited on the Se rich regions can also result in additional nucleation of PbSe grains. Below the pink arc, there are no regions with composition close enough to the stoichiometry of PbSe that are large enough to permit PbSe to nucleate (the orange points in Figure 5.11). The local concentration of Pb on the surface of the Se rich film is too low for Pb to agglomerate to form regions close enough to the stoichiometry of PbSe for it to nucleate. To our knowledge, this is the first report of successfully preparing amorphous Pb-Se films by vacuum deposition.

5.4. Discussion

Prior literature on vapor phase deposition suggests that the as-deposited structure of samples depends on the temperature of the surface, the relative diffusion rates of the atoms on the surface and in the bulk, and the relative nucleation energy to potential crystalline compounds.

The data presented herein indicates that the as-deposited structure of the samples also depends on the evolving surface composition as the deposition is toggled between elements and the thickness of the deposited layers is varied. During deposition, as M or X atoms hit the surface of the growing film, the atoms lower their free energy by completing their coordination shells, forming M-M, M-X, and/or X-X bonds. The energy released from these reactions creates local, short term "hot spots" which enables the atoms to further optimize their local coordination. If the local temperature is high enough and the local composition is close enough to the stoichiometry of a compound in a large enough area, sufficient rearrangement can occur to result in nucleation. This is the case for PbSe and $MoSe_2$ samples shown in blue in Figures 5.1 and 5.11. If local movement of atoms is limited by bonds formed during the deposition and/or low substrate temperatures, the sequential deposition of M and X can result in alternating amorphous $M_{rich}|X$ and $M|X_{rich}$ layers with or without crystalline M_xX_y at the interfaces depending on the size and energetics required to nucleate various compounds. This compositional modulation results in Bragg reflections in the XRR patterns of these samples. If the repeat layer thicknesses are thin enough or diffusion rates are high enough, the M and X atoms will completely interdiffuse during deposition and no Bragg reflections from the layering will be observed in the XRR patterns. Since nucleation requires the formation of a finite volume with composition close enough to the stoichiometry of the forming compound to create an embryo, the key to obtaining an amorphous film is to design precursors without these regions. If ultra-thin sub-monolayer M and X layers are deposited on substrates at a low enough temperature with compositions far enough from the stoichiometries of crystalline compounds, a homogenous amorphous phase is formed as atoms optimize their local coordination with available adjacent atoms. This is the case for the $MoSe_2$ and PbSe samples represented by orange stars in Figures 5.1 and 5.11.

Figure 5.13 presents a graphic representation of the evolution of Group 3 $MoSe_2$ samples which have this precursor design. A homogenous x-ray amorphous film (Figure 5.13a) is formed because limited surface mobility of deposited Mo atoms prevents the formation of regions with compositions close enough to the stoichiometry of $MoSe_2$ for nucleation to occur. To nucleate $MoSe_2$ from the amorphous as-deposited sample, M atoms need to diffuse, aggregating to form regions with local compositions close enough to $MoSe_2$ for nucleation embryos to form within an X rich matrix. This requires sufficient energy for diffusion, large enough composition

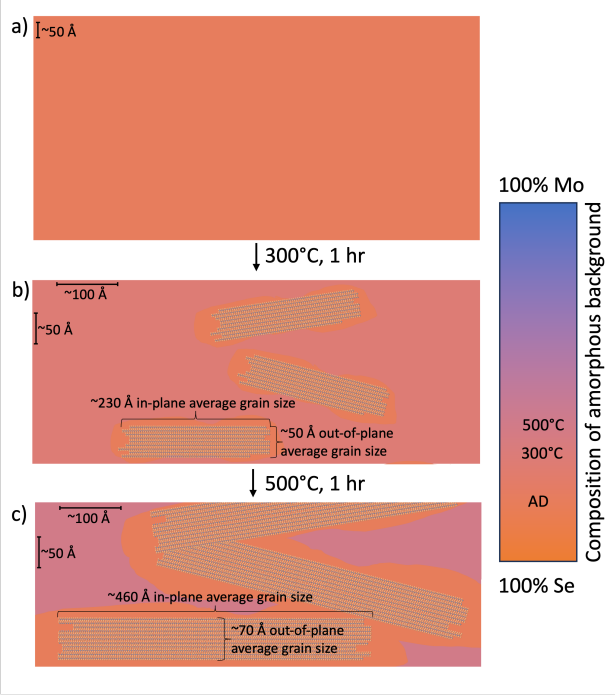

Figure 5.13. Graphic representation of the evolution of Group 3 samples. a. XRR data from the as-deposited sample indicates that the sequentially deposited layers of Mo and Se completely mix during the deposition forming a homogenous precursor. The color is representative of a Se:Mo ratio of ~4:1 (scale on right). Specular and in-plane diffraction data do not contain any reflections, suggesting that $MoSe_2$ does not nucleate during the deposition. b. The diffraction data indicates that $MoSe_2$ nucleates and grows during annealing at 300°C for 1 hour. The grains in the schematic are scaled to sizes obtained from Scherrer analysis, showing that growth occurs faster within individual $MoSe_2$ layers, presumably due to challenges in nucleating adjacent layers of $MoSe_2$. c. The sample after annealing at 500°C for 1 hour, which results in significant grain growth and probably additional nucleation of $MoSe_2$ grains. The grains are not crystallographically aligned to the substrate due to the smaller amounts of Mo deposited in each Mo|Se bilayer. More grains (and less amorphous matrix) are present in the actual sample than shown, as the overlapping of grains with different orientation through the cross section of the film is challenging to illustrate.

fluctuations to occur, and for breaking the bonds required for the local coordination to evolve. Enough energy is provided by annealing the sample at 300°C (Figure 5.13b) for this to occur. Since diffusion of M atoms occurs from multiple directions, nucleation occurs with random orientation and subsequent growth results in a random crystallographic orientation. As the nucleated grains grow, excess X is pushed in front of the crystal growth front creating a composition gradient and continued growth requires that M atoms diffuse through this increasingly thick X-rich region. Crystal growth competes with Se being lost due to evaporation

when annealing is done in an open system. This results in a final Se:Mo ratio less than 2:1 due to amorphous metal rich regions between $MoSe_2$ grains (Figure 5.13c).

5.5. Conclusions

Amorphous precursors are recognized as the highest possible energy reaction intermediates, which makes them ideal reaction intermediates for the synthesis of predicted compounds, especially those that are metastable relative to mixtures of thermodynamically stable compounds. The results presented herein suggest that homogenous amorphous precursors can be prepared by sequentially depositing sub-monolayer thick elemental layers on a cold enough substrate with an average composition that differs from the stoichiometry of known compounds. We hypothesize that this works because of the chemistry that occurs as atoms impinge the sample surface. Atoms optimize their local coordination spheres within the limits imposed by the local temperature and preexisting coordination environments of surface and near-surface atoms. By controlling the absolute thicknesses and ratio of elements in each repeating Mo|Se sequence, the local compositions and resulting coordination environments can be tuned. Sub-monolayer thicknesses and compositions away from known compounds prevent the formation of large enough regions with local compositions and bonding similar enough to a compound. This inhibits nucleation of the compound. Consequently, these samples remain x-ray amorphous during the deposition if surface diffusion rates are sufficiently small, which requires low substrate temperatures. For nucleation to occur, a sufficient volume with local composition close to the stoichiometry of a compound needs to self-assemble. Therefore, an as-deposited amorphous film must be annealed at a high enough temperature for atoms to diffuse to create a local fluctuation close to the composition of the nucleating compound with a large enough volume and rearrange preexisting bonds for nucleation to occur. Depositing sub-monolayer thick layers with compositions that differ from the stoichiometry of known compounds avoids the nucleation of thermodynamic phases during deposition, providing a general route to homogeneous amorphous solids with controlled local compositions to probe the nucleation and growth of predicted compounds.

5.6. Bridge

Chapter V presents an in-depth study of how layer thickness and local composition can be tuned to manipulate the way that Mo and Se react during the deposition process, and how these variables can be used to affect the final structure of the resulting film after annealing. During this study a new method was developed to deposit amorphous precursors in systems that were previously observed to always nucleate and grow thermodynamically stable binary compounds during the deposition process. Chapter VI builds on the insights gained from this study of the Mo-Se system to further investigate how high nucleation barriers suppress phase formation and to deepen our understanding of how these elevated nucleation energies and the deposition of designed layer thicknesses can be leveraged to stabilize non-equilibrium structures, resulting in the synthesis of a series of non-equilibrium Mo-$MoSe_2$ superlattices.

CHAPTER VI

Nucleation Controlled Synthesis of Designed Heterostructures

6.0. Authorship Statement

This chapter has been submitted for publication in *Angewandte Chemie International Edition*. I am the primary author. Ping Lu collected high-angle annular dark-field transmission electron microscopy images and energy dispersive x-ray spectroscopy data at Sandia National Laboratories. Sven P. Rudin performed density functional theory calculations at Los Alamos National Laboratory. David C. Johnson acted as my advisor and assisted in writing the manuscript. All authors assisted in editing the manuscript.

6.1. Introduction

The synthesis of computationally predicted crystalline phases with exceptional properties is an attractive challenge for solid-state chemists. However, only a small percentage of predicted compounds have been experimentally prepared, even though many were calculated to be thermodynamically stable, or nearly so, relative to known compounds. Our limited understanding of how synthetic variables impact the energy barriers for both diffusion and nucleation in the energy landscape results in the lack of control of reaction pathways, intermediates and resulting products.[1] Traditional solid-state growth occurs in a diffusion-limited, heterogeneous environment where a sequence of phase formation occurs at the interfaces between reacting species.[2–7] Concentration gradients at interfaces, which depend on diffusion rates at specific interfaces, and the relative magnitude of nucleation barriers within these concentration gradients determine which compound forms.[8,9] The easiest compound to nucleate forms first, which is not necessarily the most thermodynamically stable compound, and growth of this compound creates new concentration gradients,[10] leading to a sequence of intermediate compounds before the system attains equilibrium. Since interdiffusion of solids is slow and often the rate limiting step in the synthesis of solids, fluid phases (fluxes, eutectics, melts, …) are often used to increase diffusion rates, especially at low temperatures. In the resulting solutions nucleation is typically the rate limiting step, but there is little knowledge of the species in the fluid phase, how the species and their concentrations change as the composition and/or temperature is varied, and the

solubility constants of various potential compounds in the solution.[11,12] Our limited understanding of how experimental variables impact both the topology of the free energy landscape and the reaction path is a consequence of the lack of experimental probes for the complex, potentially heterogenous solid state and solution based systems.[10,11,13]

Nucleation, rather than diffusion, can be the rate-limiting step in the formation of a compound as a system evolves through the complex energy landscape when diffusion rates are high or diffusion distances are small. The classic picture of nucleation involves atom-by-atom addition to an embryo whose volume energy must overcome the surface energy to form a crystalline grain that can proceed to grow.[9,14,15] More recently, non-classical pathways have been proposed that involve the collision and fusing of two embryos.[12,16,17] Unlike in solution-phase nucleation, solid-state nucleation of inorganic materials is complicated by stresses caused by density differences between reactants and products, by slow diffusion rates that result in concentration gradients at interfaces, and also and by the need to nucleate voids to account for volume changes. Heterogeneous nucleation at interfaces dominates solid state reaction pathways.[7,9,16,17] Recent studies have provided a variety of new insights and new solid-state nucleation models,[9,16–18] including the suggestion that liquid intermediates reduce nucleation energies because liquid-solid interfaces are lower energy than solid-solid interfaces. However, investigating local early-stage solid-state reaction environments and the distribution of embryos before nucleation occurs is experimentally very difficult to study.[19] New methods to probe the impact of experimental parameters on the rate limiting steps in potential synthetic pathways are needed to successfully design the synthesis of predicted novel materials.

One approach to experimentally simplifying the solid-state reaction pathway is to prepare homogenous amorphous solid-state reaction precursors. This eliminates the constraints imposed by long range diffusion driven by concentration gradients. The barrier for nucleation involves growing a large enough embryo with a local composition close to the stoichiometry of the compound for nucleation to occur. Amorphous phases can be prepared using ultra-fast cooling rates (~106 K/sec),[20] complex mixtures of elements that prefer different coordination environments[21] to kinetically inhibit nucleation or depositing ultra-thin elemental layers. Several studies show that composition can control what nucleates from an amorphous intermediate, even enabling the formation of metastable binary compounds.[22,23] Two questions that have not been addressed, however, are 1); the relationship between the complexity of the structure of a

compound its ability to nucleate from a homogenous amorphous alloy that matches its stoichiometry and 2); the influence of adjacent regions with different compositions on nucleation.

To explore these questions, we examined the Mo-Se system because it only contains two thermodynamically stable compounds, $MoSe_2$ and Mo_6Se_8 with very different unit cell complexities (Figure 6.1). Precursors were prepared by sequentially depositing sub-monolayer amounts of each element in both simple (Mo|Se) and complex (|a x Mo| + b x |Se|Mo) sequences (see Figure 6.2) to control local composition. $MoSe_2$ nucleates and grows during the deposition of samples deposited in a Mo|Se sequence of ultrathin layers with Mo:Se ratios close to 1:2. Films prepared with Mo:Se ratio close to 3:4 form amorphous films. The critical size of an embryo required for growth to lower the total free energy depends on the difference between the decrease in free energy due to the formation of the crystalline domain and the increase in free

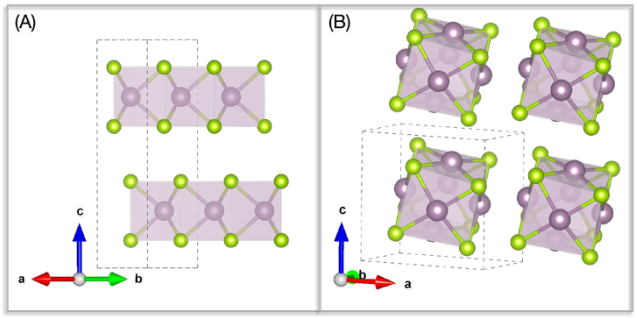

Figure 6.1. The crystal structure of $MoSe_2$ and Mo_6Se_8. Dotted lines outline the unit cell for each phase. A) $MoSe_2$ is a layered compound with Mo in the center of trigonal prisms of Se atoms that share edges to form a Se-Mo-Se trilayer. There is a van der Waals gap separating the trilayers of edge-sharing trigonal prisms. B) The Mo_6Se_8 structure is built up of octahedra of Mo atoms with each of the 8 triangular faces capped by a Se atom. The resulting "cubes" have a rhombohedral distortion.[24]

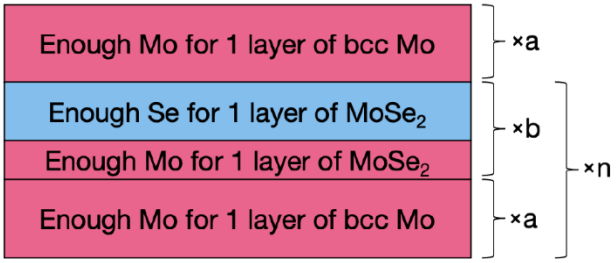

Figure 6.2. An idealized schematic of the |a x Mo| + b x |Mo|Se| layering sequence for group C precursors.

energy due to the creation of the interface and strain induced due to volume changes during the formation of the domain. We were surprised that $MoSe_2$ nucleated and grew from amorphous Mo rich samples. In the more complex layer sequences designed to form $[Mo_a|(Mo|Se)_b]_n$ heterostructures, Mo metal nucleated and grew during the deposition process and small grains of $MoSe_2$ nucleated and grew when more than two Mo|Se bilayers ($b > 2$) were deposited. If $b < 2$, Mo metal and an amorphous Mo-Se region formed rather than the thermodynamically more stable Mo_6Se_8 compound. We estimated the minimum size required for an $MoSe_2$ embryo to be kinetically stable using an 'island' approach described in detail elsewhere.[25] We discovered that $MoSe_2$ embryos between Mo layers needed to be more than two $MoSe_2$ trilayers thick to maintain their structure when relaxed in a DFT calculation. The $[Mo_a|(Mo|Se)_b]_n$ heterostructures are kinetically stable to at least 550 °C. These findings suggest that heterostructures containing designed intergrowths of simple crystal structures are synthetically accessible using designed sequences of layers to control local compositions and are kinetically stable once formed.

6.2. Results and Discussion

In this investigation, 12 precursors were deposited with layers of Mo and Se with either Mo|Se or Moa|(Mo|Se)b structured repeating sequences. Precursors in group A contained Mo|Se bilayers where the amount of Mo and Se per bilayer contained a slight excess of Se relative to a 1:2 ratio of Mo:Se. The six group B precursors had ultrathin repeating Mo|Se bilayers designed to form amorphous intermediates with homogeneous compositions close to a 3 to 4 ratio of Mo to Se. Three of the group B samples contained a slight excess of Se and the other three had a slight excess of Mo. The repeating layer sequences in group C were more complicated, consisting of a several unit cell thick layer of Mo followed by Mo|Se bilayer(s) designed to form a single $MoSe_2$ layer per bilayer (Figure 2). These samples were all capped with a layer of Mo with the same number of unit cells as the Mo layers within the repeating sequence. The 4 group C samples all had Mo:Se ratios larger than 3:4. The deposited layer sequences, the number of repeating layers deposited, the compositions determined via X-ray fluorescence (XRF), the total sample thicknesses, and the repeat layer thicknesses for all 12 samples are summarized in Table 6.1.

Diffraction data were collected on the group A precursors both before and after annealing and data from a representative sample are shown in Figure 3. The diffraction data of the as-

deposited precursors in group A contains a broad reflection near 13.5° 2θ from small $MoSe_2$ crystallites. After annealing using previously reported conditions that optimized the formation of $MoSe_2$ films,[26,27] XRF data indicates that the slight excess of Se contained in the as-deposited

Table 6.1. A summary of the deposition information and measured compositions and thicknesses of the as-deposited samples. The number of Mo atoms and Se atoms were determined from x-ray fluorescence data. The total sample thickness was determined using the 2θ position of Kiessig fringe maxima in the x-ray reflectivity pattern and Braggs law modified to account for refraction. The average thickness of the deposited repeating sequence was calculated by dividing the total sample thickness by the number of repeating sequences deposited. The error in each reported value is given in parentheses after the last significant digit.

Sample Name	Repeating Sequence	Number of Repeating Sequences Deposited (n)	Mo per Repeating Sequence (atoms/Å^2)	Se per Repeating Sequence (atoms/Å^2)	Mo/Se ratio	Sample Thickness (Å)	Average Thickness of Deposited Repeating Sequence (Å)
A1	$(Mo\|Se)_n$	46	0.107(1)	0.224(3)	0.478(8)	329.2(3)	7.157(7)
A2	$(Mo\|Se)_n$	54	0.103(1)	0.223(3)	0.462(7)	385.0(4)	7.130(7)
B1	$(Mo\|Se)_n$	268	0.0243(2)	0.0337(5)	0.72(1)	355.4(6)	1.326(2)
B2	$(Mo\|Se)_n$	268	0.0246(2)	0.0339(5)	0.73(1)	353(2)	1.317(7)
B3	$(Mo\|Se)_n$	268	0.0249(2)	0.0331(5)	0.75(1)	358.8(6)	1.339(2)
B4	$(Mo\|Se)_n$	500	0.0122(1)	0.0151(2)	0.81(1)	307.3(7)	0.615(1)
B5	$(Mo\|Se)_n$	500	0.0124(1)	0.0150(2)	0.82(1)	310(1)	0.620(2)
B6	$(Mo\|Se)_n$	500	0.0126(1)	0.0148(2)	0.85(1)	311.9(7)	0.624(1)
C1	$[Mo_5\|(Mo\|Se)_1]_n$	13 + Mo_5[a]	14.3(1)[c]	0.238(4)	4.64(7)	347.1(9)	25(2)[d]
C2	$[Mo_5\|(Mo\|Se)_2]_n$	5 + Mo_5[a]	8.57(9)[c]	0.443(7)	3.87(6)	202.1(4)	33.7(6)[d]
C3	$[Mo_{10}\|(Mo\|Se)_5]_n$	4 + Mo_{10}[b]	12.3(1)[c]	1.06(2)	2.88(5)	376.4(7)	74.9(6)[d]
C4	$[Mo_5\|(Mo\|Se)_{10}]_n$	3 + Mo_5[a]	6.47(6)[c]	2.39(4)	0.90(1)	355(1)	88.5(1)[d]

[a] Samples C1, C2, and C4 were capped with 5 unit cells worth of Mo after deposition of the repeating sequences; [b] Sample C3 was capped with 10 unit cells worth of Mo after deposition of the repeating sequences; [c] For samples C1, C2, C3, and C4 the number in the "Mo per Repeating Sequence" column is the total number of Mo atoms/Å2 in the sample; [d] For samples C1, C2, C3, and C4 the average thickness of deposited repeating sequence values are calculated using Braggs law modified for refraction and the 2θ position of the first order Bragg reflection in each samples x-ray reflectivity pattern.

samples sublimated, resulting in a final Se/Mo ratio of 2.0(1). Figure 6.3 contains a region of the specular XRD for both samples after annealing, showing the well resolved Laue oscillations that result from the integer number of $MoSe_2$ layers in the crystalline domains. Laue oscillations that extend this far from the Bragg reflections will only be observed if there is a consistent number of

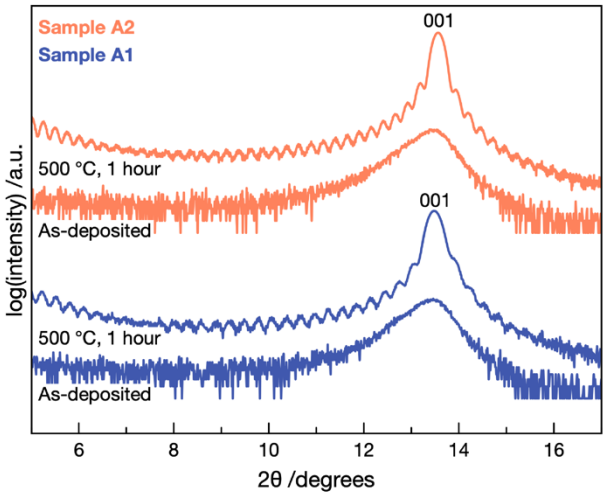

Figure 6.3. Specular x-ray diffraction patterns of both samples from group A before and after annealing at 500 °C for 1 hour. The bottom two, blue patterns are for sample A1. The top two, orange patterns are for sample A2. The pattern is cropped to 5-17° 2θ to highlight the Laue oscillations extending from the 001 reflection of the crystallographically aligned planes of $MoSe_2$ trilayer growing in both samples.

unit cells in most of the diffracting domains. Using the analysis suggested by Miller,[28] sample A1 contained 46(1) $MoSe_2$ trilayers per diffracting domain and sample A2 has 54(1) $MoSe_2$ trilayers per diffracting domain. These domain thicknesses are consistent with the amount of Mo in the films within the experimental error of the XRF measurement. The as-deposited and after annealing data from group A samples demonstrate that nucleation and growth of the simple unit cell of $MoSe_2$ occurs during deposition from samples near the stoichiometry of $MoSe_2$, and that crystallographically aligned $MoSe_2$ domains of uniform size perpendicular to the substrate result from annealing.

X-ray reflectivity (XRR) and specular, grazing incidence, and in-plane x-ray diffraction (XRD) data were collected directly after deposition for group B samples. The precursors contained only Kiessig fringes in their XRR patterns, which were used to extract the total sample thickness using Braggs law modified to include refraction (Table 1). The as-deposited XRR scan for sample B5 is shown in Figure 6.4A and the XRR scans of all the samples are in Figure S6.1. Roughness was calculated using the formula derived by Parratt.[29] All samples have a roughness in the range of 10 Å. Dividing the total thickness by the number of repeating layers deposited yields the average thickness of the Mo-Se units in each sample, which are summarized in Table 6.1. Bragg reflections from modulation of the elements are not observed since the average

thicknesses of each elemental layer in the Mo|Se bilayers are much less than a monolayer and the roughness of the samples are larger than the thicknesses of the bilayers. The as-deposited specular XRD pattern for sample B5 is shown in Figure 6.4B and the remaining as deposited specular patterns for all the samples are shown in Figure S6.2. The specular and grazing incidence patterns contain a broad low-intensity reflection around 12° 2θ, corresponding to a d-spacing of approximately 7.5 Å. To our knowledge, no known molybdenum selenide has reflections at this angle. $MoSe_2$ has a *c*-axis lattice parameter of 12.927(4) Å[30] for the 2H polymorph unit cell (~6.5 Å per $MoSe_2$ trilayer), and 6.85 Å for the trilayer of the metastable 1T polymorph.[31] There is an additional broad maximum at around 40° 2θ in the grazing diffraction pattern which is also observed in the in-plane pattern (Figure 6.4D) which we attribute to diffuse scattering. This data indicates that neither $MoSe_2$ nor Mo_6Se_8 domains are present in group B as-deposited samples.

Composition and diffraction data were collected after annealing group B samples at increasing temperatures to induce nucleation, and a representative set of data are shown in Figure 6.4. The amounts of each element (calculated from XRF data) remain constant within error throughout the annealing study (Figure S3). The Kiessig fringes in the XRR patterns decrease in intensity at higher angles as annealing temperature increases, indicating that the surface roughness increases (Figure 4A). The specular and grazing incidence patterns shown in Figure 4B and 4C change only slightly as the annealing temperature is increased. The reflection near 11° 2θ initially decreases in intensity before increasing in intensity and shifting to higher angles after annealing at 400 °C. The in-plane diffraction data (Figure 4D) has several very weak reflections appearing as the annealing temperature increases above 450 °C. After annealing at 500 °C, these reflections can be indexed as *hk*0 reflections from a hexagonal unit cell, yielding an *a*-axis lattice parameter of 3.298(3) Å. This is within the range of *a*-axis lattice parameters reported for $MoSe_2$.[32–34] The diffraction data is consistent with the formation of small $MoSe_2$ grains in an amorphous Mo-Se matrix. We see no evidence for the crystallization of Mo or the formation of Mo_6Se_8.

The formation of $MoSe_2$ rather than Mo_6Se_8 as this sample is annealed was surprising given the homogenous composition of the sample with a Mo to Se ratio of approximately 3:4. Nucleation of $MoSe_2$ requires diffusion of either Se or Mo to create a fluctuation in local composition to form a region with a 1:2 ratio of Mo:Se in an amorphous matrix with an average

composition of 43% Mo and 57% Se. The reorganized volume includes the critical nucleus of $MoSe_2$ and a region that is Mo rich around it. Nucleation of Mo_6Se_8 would require only local rearrangements of coordination to create the Mo_6 octahedra capped by Se that are the basis of the Mo_6Se_8 structure. $MoSe_2$ and Mo_6Se_8 have different dependences of the surface energy on the size of the critical nuclei. The low surface energy of the van der Waals plane between $MoSe_2$ layers results in the surface energy being dominated by the edges, so the surface energy approximately scales with the radius of hexagonal $MoSe_2$ platelets. The three-dimensional structure of Mo_6Se_8 results in the surface energy scaling as a function of the radius squared of the

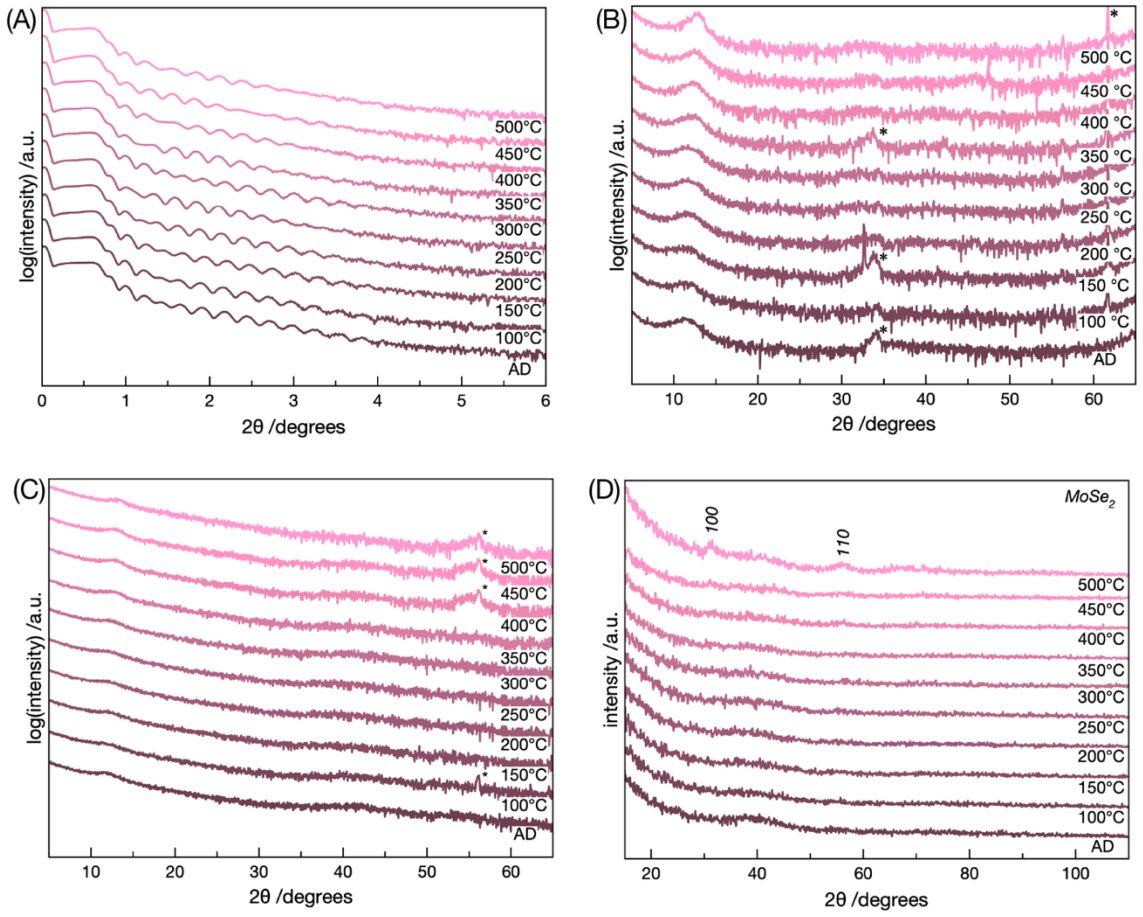

Figure 6.4. X-ray reflectivity and x-ray diffraction data collected after each annealing step of an annealing study performed on a representative group B sample, sample B5. (a) XRR data show that the surface roughness and total sample thickness do not change significantly throughout the annealing study. (b, c) Specular and grazing-incidence XRD patterns all contain one broad, low-intensity reflection that grows slightly with annealing. (d) In-plane XRD patterns contain no reflections until after annealing at 500 °C, when low intensity reflections consistent with $MoSe_2$ appear. Asterisks indicate substrate and stage reflections.

critical nucleus. The observed nucleation of $MoSe_2$ suggests its lower surface energy compensates for the larger volume rearrangement required to form a stoichiometric nucleus of $MoSe_2$ in a matrix that is Mo-rich.

DFT calculations were performed to estimate the size dependence of the stability of $MoSe_2$ nuclei in a Mo-rich environment. As shown in Figure 6.5, $MoSe_2$ structured islands with varying thicknesses of $MoSe_2$ were constructed between Mo layers, and the complete systems were allowed to relax in DFT calculations. The empty space around the islands enables the atoms to rearrange to lower the total energy. Our calculations show that a single Se-Mo-Se trilayer (far left column of Figure 6.5) reacts with the adjacent Mo layer and the layers fully diffuse together when relaxed. Two Se-Mo-Se trilayers also react with the adjacent Mo layers and sufficient interdiffusion occurs to disrupt the initially well-ordered Se-Mo-Se structure. Increasing the

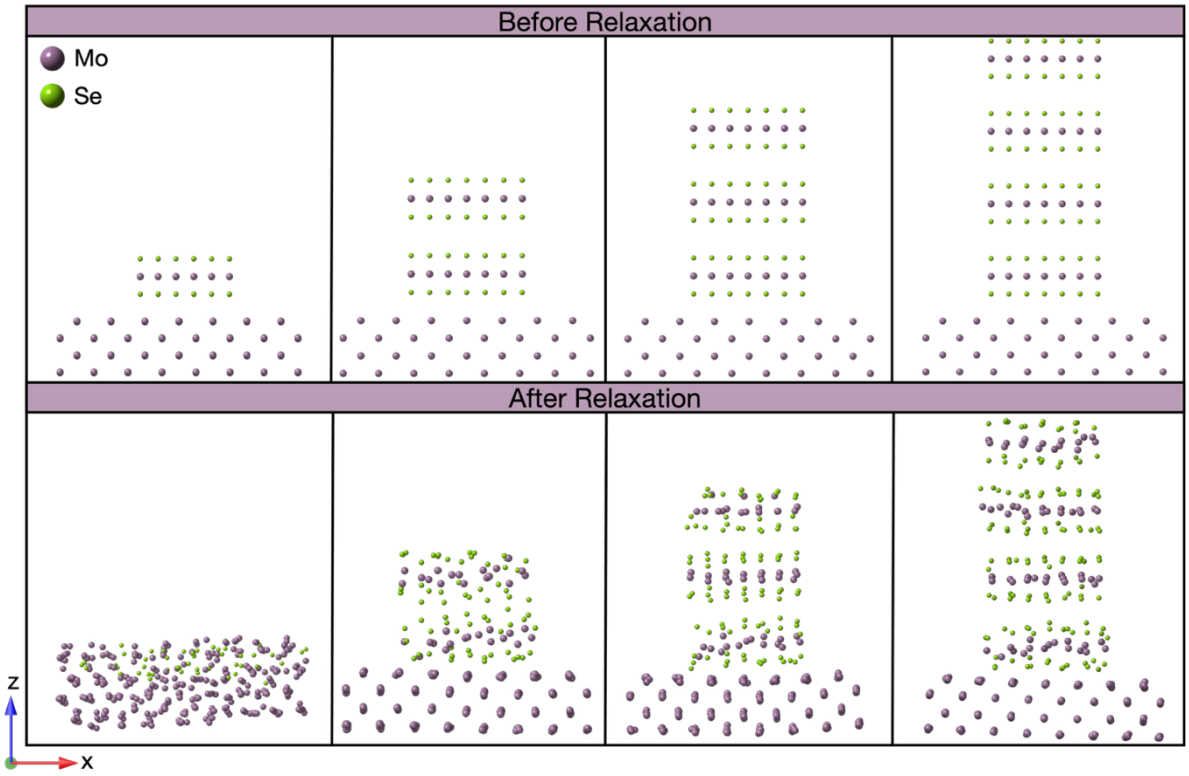

Figure 6.5. The top set of figures contains the initial atomic structure of crystalline islands of Se-Mo-Se trilayers placed next to thick layers of Mo. The bottom set of figures contains the structures after being relaxed during DFT structural optimization. Mo atoms are shown in purple and Se atoms are shown in green.

thickness by including >2 trilayers resulted in the islands maintaining the $MoSe_2$ crystal structure, which indicates that crystallites of $MoSe_2$ will nucleate in these films.

The inability to nucleate Mo_6Se_8 in Mo rich films led us to design the group C samples, which were prepared to probe the ability to kinetically trap $Mo_a(MoSe_2)_b$ heterostructures from precursors with designed nanoarchitectures. XRF data show that all four samples are Mo-rich and should form mixtures of Mo and Mo_6Se_8 at equilibrium (Table 1). Figure 6.6 contains the as-deposited XRR, specular, and in-plane diffraction scans of the four samples deposited following the layer sequence shown in Figure 6.2. The XRR patterns all contain intensity from Kiessig fringes, Bragg reflections from the elemental layers that result from the sequential deposition, and intensity from domains of any heterostructure that has nucleated and grown during the deposition. The black tick-marks in Figure 6.6A show the expected 2θ positions of reflections from the elementally modulated repeating layer sequence calculated from the position of the first order reflection using Braggs law corrected for refraction. The positions of observed Bragg reflections match these predicted positions at lower angles, with deviations at higher diffraction angles in samples C3 and C4 resulting from intensity from both Bragg reflections from the elementally modulated layers and Bragg reflections from heterostructure domains that formed during the deposition. The specular diffraction patterns (Figure 6.6B) of samples C3 and C4, which have b = 5 and 10 respectively, have broad, low intensity reflections at angles consistent with the expected 2θ positions for the 00*l* reflections of small, crystallographically aligned grains of $MoSe_2$.[26,27] Sharp reflections from the modulation of the elements during the deposition and crystalline domains forming in the Mo-Se or Mo region of the deposited sequence are apparent to approximately 15° 2θ. The specular diffraction patterns of samples C1 and C2, with b = 1 and 2 respectively, differ from those of C3 and C4 as they do not have any intensity at angles where 00*l* reflections for $MoSe_2$ are expected. These samples have a higher angle low-intensity broad Mo 110 reflection near 2θ = 40° from small grains of Mo. In-plane XRD data collected on the as-deposited group C samples is shown in Figure 6.6C. All the samples contain a reflection ~ 40° 2θ from bcc Mo. Samples C3 and C4 also contain *hk*0 reflections that can be indexed to a hexagonal unit cell, consistent with the growth of small grains of $MoSe_2$ during the deposition. Samples C1, C2 and C3 have a weak and very broad reflection near 70° 2θ from the 112 Mo reflection.

Sample C3 was annealed at increasing temperatures to follow the evolution of its structure and probe the kinetic stability of Mo-$MoSe_2$ interfaces. XRF data collected after the final annealing step show that the amount of Mo and Se in the sample did not change during the annealing steps. XRR, specular XRD, and in-plane XRD data collected after each annealing step are shown in Figure 6.7. The experimental position of Kiessig/Laue oscillations and Bragg reflections in the XRR patterns (Figure 6.7A) shift to slightly higher angles as the annealing temperature increases, indicating that the total sample thickness and the thickness of the repeating sequences decreased during annealing. The intensity of the Bragg reflections from the modulation in the electron density resulting from the deposited layer sequence do not change significantly, indicating that the Mo and Mo-Se regions do not appreciably interdiffuse during the annealing steps. The diffraction data, Figures 6.7B and 6.7C, indicate that the layering reflections in the as-deposited sample remain after annealing, while the intensity of reflections from crystallographically aligned $MoSe_2$ and randomly oriented Mo crystals increases after each annealing step. After annealing at 550 °C, broad diffraction maxima in the specular diffraction pattern consistent with small grains of $MoSe_2$ coexist with sharper maxima consistent with the initial layered nanoarchitecture from the deposition of 4 repeating units containing 5 Mo|Se layers + a thicker Mo layer.

A high-angle annular dark-field scanning transmission electron microscopy (HAADF-STEM) image of a cross-sectional lamella of sample C3 prepared after annealing at 550 °C (Figure 6.8) was collected to provide additional structural information. The HAADF-STEM image shows that the sample consists of alternating layers of randomly oriented grains of Mo and 3-5 layers of $MoSe_2$, with local variations in the thickness of each constituent in the repeating sequences. An energy-dispersive x-ray spectroscopy (EDS) map (Figure S6.4) also indicates that the sample consists of a heterostructure with discrete alternating Mo and Se-rich layers. The STEM images in Figure 8 are consistent with the diffraction patterns in Figures 6.7B and 6.7C. The narrow Bragg reflections from the heterostructure end at ~12° 2θ in the specular diffraction pattern (Figure 6.7B) due to the varying local thicknesses of the Mo and Mo-Se regions, instead of extending to higher angles as expected for a perfect heterostructure (see the blue pattern in Figure 6.7B). The broad intensity maxima at ~12° 2θ is the 001 reflection from $MoSe_2$ domains that are ~4 trilayers thick. Weak broad 00*l* reflections where l = 2-4 from these $MoSe_2$ domains

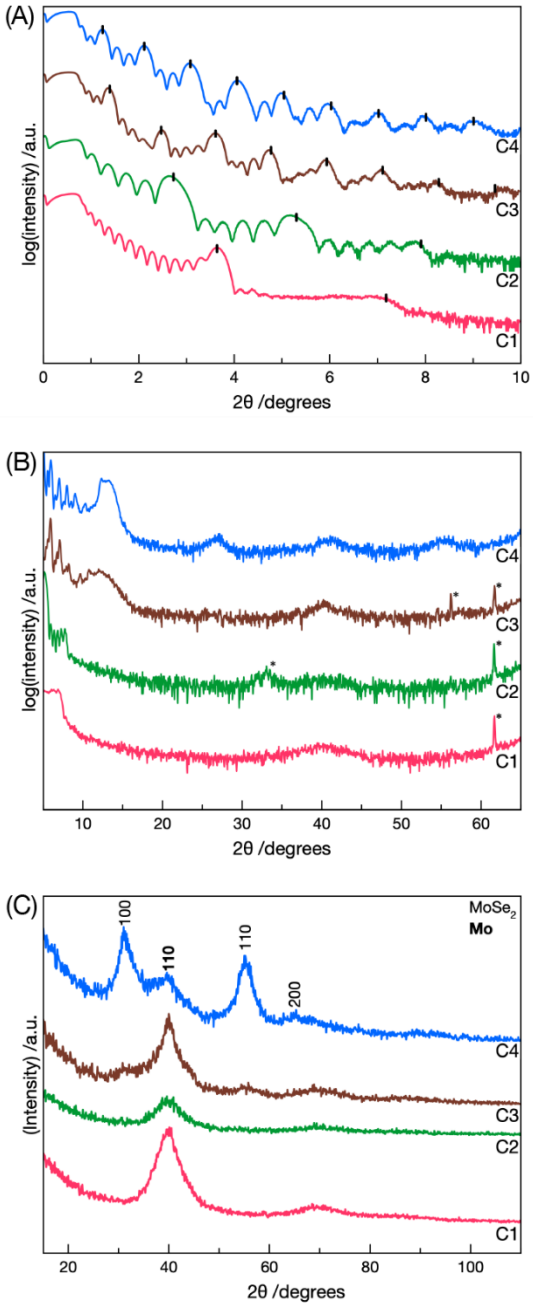

Figure 6.6. As-deposited x-ray reflectivity and x-ray diffraction data for the group C samples. (A) XRR patterns for each group C sample collected after deposition. Black tick-marks show the expected positions of Bragg reflections calculated using Braggs law modified to include refraction and the 2θ positions of the first Bragg reflection present in each pattern. (B) Specular XRD patterns contain a mix of Bragg reflections from the elementally modulated repeating layer sequence, any crystalline heterostructure that is present, diffuse scattering (C1, C2, and C3), and small grains of $MoSe_2$ (C3 and C4). (C) In-plane XRD patterns contain a reflection near 40° 2θ and reflections that can be indexed to a hexagonal unit cell in sample C4. Reflection indices are shown in bold text for Mo and regular text for $MoSe_2$. Asterisks indicate substrate and stage reflections.

are also present in the experimental specular pattern. Broad intensity from these domains is observed because of the local deviations in layer to layer spacing. The increase in the intensity of these broad maxima reflects an increase in the total volume of $MoSe_2$ domains as annealing temperature increases. The sharp Bragg reflections in the XRR and specular XRD patterns from the heterostructure yield an average lattice parameter of 72.2(6) Å after annealing at 550 °C, slightly thinner than the as deposited elemental modulation due to the denser crystalline layers. The experimental positions of some of the 00*l* reflections deviate from the expected positions (the red tick-marks in Figure 6.7A) for the average unit cell size due to the high density of defects. The disappearance of the broad intensity around 40 °C in the as-deposited specular (Figure 6.7B) and in-plane (Figure 6.7C) XRD patterns, caused by diffuse scattering from amorphous regions in the as-deposited sample, is consistent with the predominance of crystalline domains in the STEM images. The in-plane reflections after annealing at 550 °C can be indexed to two different unit cells. A set of *hk*0 reflections can be indexed to a hexagonal unit cell with an *a*-axis lattice parameter of 3.28(1) Å, consistent with previously reported values for $MoSe_2$.[32–34] A second set of *hkl* reflections can be indexed to a cubic unit cell with an *a*-axis lattice parameter of 3.16(1) Å, which is slightly larger than previously reported values for bcc Mo metal.[35,36] The diffraction and HAADF-STEM data are self-consistent and indicate that the deposited precursor forms a $[Mo_a|(Mo|Se)_b]_n$ heterostructure where a = ~10, b = 3-5, and n = 4, capped with an extra ~10 layers of Mo.

Figure 6.9 contains XRR and XRD data collected after annealing all four group C samples at 550 °C for 30 minutes. The XRR patterns (Figure 6.9A) contain Kiessig fringes, Laue oscillations, and Bragg reflections. The black tick-marks label the expected 2θ positions for Bragg reflections calculated using Braggs law modified to include refraction and the average d-spacing of all present Bragg reflections in each respective pattern. The specular XRD patterns (Figure 6.9B) contain sharp reflections from the crystalline heterostructure and broader 00*l* reflections from finite thickness $MoSe_2$ domains in samples C3 and C4 with a d-spacing of 6.7(1) Å and 6.58(3) Å respectively. The in-plane XRD patterns (Figure 6.9C) for samples C3 and C4 contain two sets of reflections that can be indexed to a cubic and a hexagonal unit cell consistent with the presence of Mo and $MoSe_2$. The in-plane XRD patterns for samples C1 and C2 only contain reflections that can be indexed to a cubic unit cell consistent with the presence of small

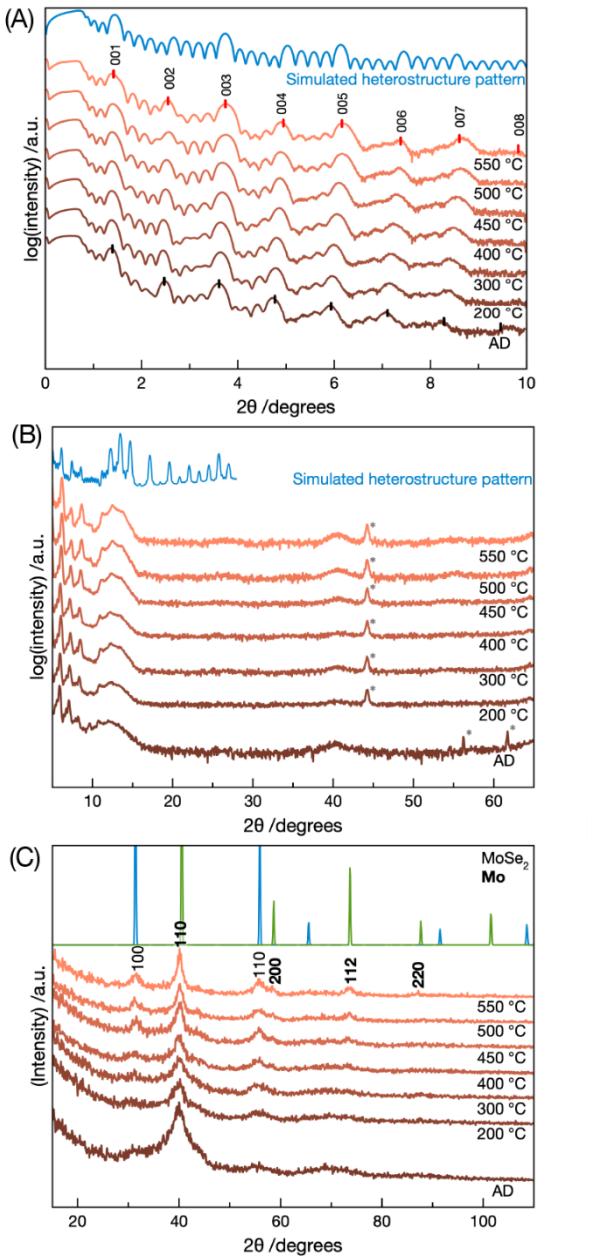

Figure 6.7. X-ray data collected after annealing sample C3 at the temperatures shown under the related pattern. (A) XRR patterns, where black tick-marks indicate the expected angles of 00*l* Bragg reflections from the elementally modulated layers calculated from the 2θ position of the first Bragg reflection in the as-deposited (AD) pattern. Red tick-marks label the expected positions of Bragg reflections from the average repeating layer thickness calculated from the 2θ positions of the indexed reflections. The blue pattern shows a calculated XRR pattern from a perfect model of the targeted heterostructure. (B) Specular XRD patterns and a calculated XRD pattern from an ideal model of the targeted heterostructure. (C) In-plane XRD patterns with indices shown above reflections used to calculate the lattice parameters of the unit cells. Indices are shown in bold text for Mo and regular text for $MoSe_2$. The blue pattern is a simulated *hk*0 pattern for $MoSe_2$ and the green pattern is a literature powder pattern for bcc Mo. Asterisks indicate substrate and stage reflections.

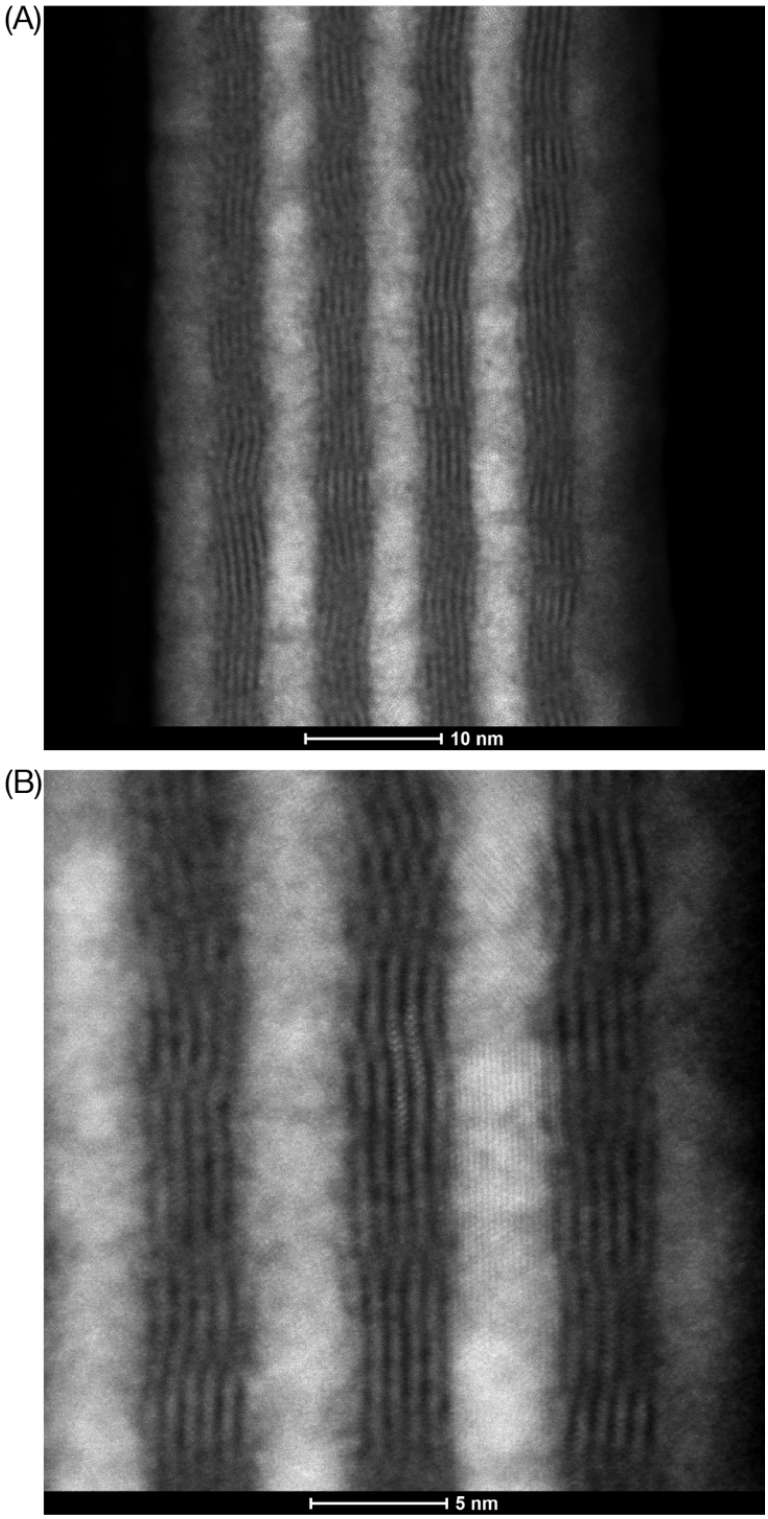

Figure 6.8. (a) HAADF-STEM image of the same representative Mo-$MoSe_2$ sample that was characterized with XRD techniques after annealing at 550 °C for 30 minutes. (b) Higher magnification image of the same sample shows alternating layers of $MoSe_2$ and randomly oriented Mo.

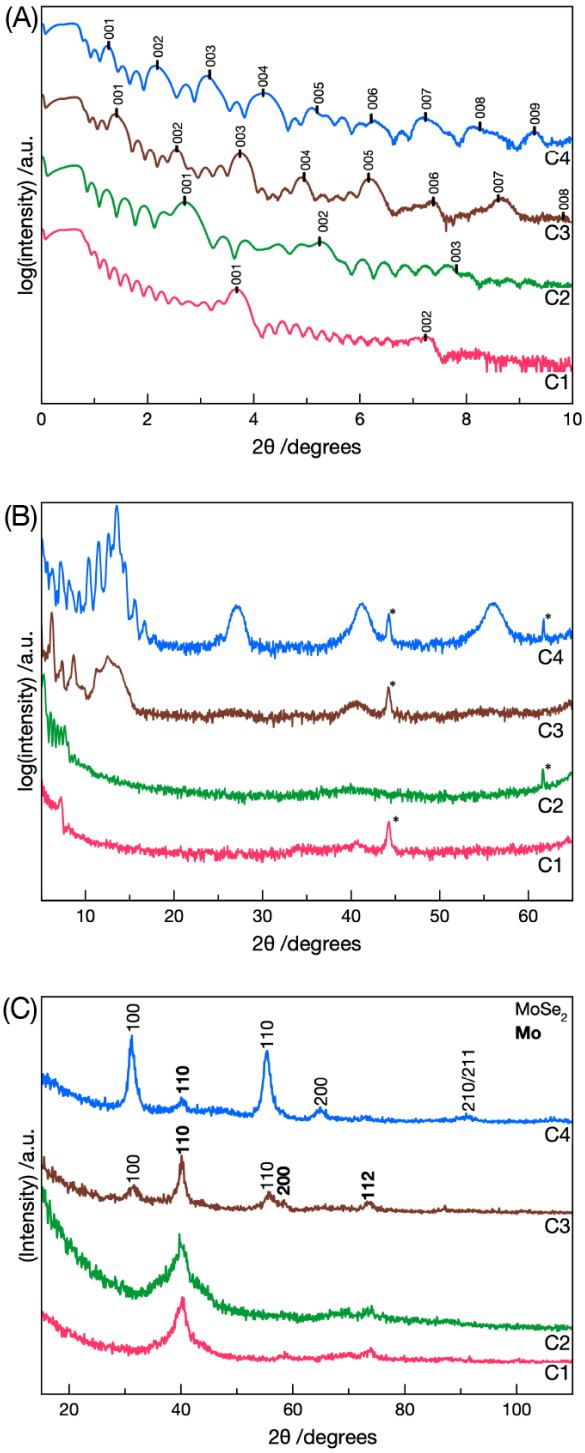

Figure 6.9. X-ray data collected after annealing the four C sample at 550 °C for 30 minutes. (A) XRR patterns where black tick-marks indicate the expected angles of 00*l* Bragg reflections from the average d-spacing calculated from the 2θ positions of the indexed reflections. (B) Specular XRD patterns. (C) In-plane XRD patterns with indices shown in bold text for Mo and regular text for $MoSe_2$ above reflections used to calculate lattice parameters. Asterisks indicate substrate and stage reflections.

Table 6.2. A summary of the lattice parameters calculated from the data presented in Figure 6.9. The average d-spacing of the repeating sequence was calculated using Braggs law modified to include refraction and the 2θ position of each sharp Bragg reflection present in the XRR and XRD patterns for each respective sample. The error in each reported value is given in parentheses after the last significant digit.

Sample Name	Average d-spacing of repeating sequence (Å)	D-spacing of any present $MoSe_2$ crystallites (Å)	*a*-axis lattice parameter for cubic unit cell (Å)	*a*-axis lattice parameter for hexagonal unit cell (Å)
C1	24.6(1)	-	3.16(2)	-
C2	34.2(6)	-	3.17(1)	-
C3	72.2(6)	6.7(1)	3.16(1)	3.28(1)
C4	86(1)	6.58(3)	3.21(5)	3.31(1)

domains of Mo. The modulation in electron density that remains after annealing is from alternating layers of crystalline Mo and an amorphous Mo-Se alloy. The lattice parameters calculated from the diffraction data presented in Figure 6.9 are summarized in Table 6.2.

The diffraction data from the annealed group C samples indicate that samples with more than two Mo|Se deposited bilayers in the repeating sequence of elemental layers form $[Mo_a|(Mo|Se)_b]_n$ heterostructures with a and b determined by the amount of Mo and Se in the repeating sequence. In samples with two or fewer Mo|Se bilayers in the repeating sequence, $MoSe_2$ does not form during deposition and does not nucleate even when the films are annealed at 550 °C. The modulation from crystalline Mo and amorphous Mo-Se alloy is kinetically stable with respect to forming a layer of $MoSe_2$ because the Mo-Se alloy is either too Mo rich or too thin to nucleate $MoSe_2$ or the diffusion rates are too small at the temperatures explored to permit a large enough fluctuation for nucleation to occur.[26] The diffraction data agrees with the DFT calculations, lending some confidence that the "Island" approach contains the essence of the nucleation process.

6.3. Conclusions

The data presented herein shows that nucleation limits what compounds can form during deposition and when annealing homogenous amorphous intermediates or precursors with designed composition gradients. This study shows that compounds with simple crystal structures can crystalize from homogeneous intermediates rather than the thermodynamic products

expected at their compositions from phase diagrams as a consequence of compounds with complex unit cells having higher nucleation barriers. We suggest that an inherent difference in nucleation energies for structures with different complexities enables the preparation of kinetically stable ordered intergrowths of constituents with simple crystal structures from designed precursors. Many new materials consisting of intergrowths of known phases potentially can be prepared on the length scale of several unit cell dimensions. Developing successful synthesis pathways for new predicted materials will depend on increasing our fundamental understanding of how experimental parameters influence the two generally recognized barriers to the synthesis of compounds – nucleation and diffusion. While elementally modulated precursors can eliminate long range diffusion barriers, high nucleation barriers can prevent the successful synthesis of both thermodynamically stable compounds and those theoretically predicted to be stable.

6.4. Materials and Methods

Precursors were prepared on unheated <100> Si wafers (3″ × 1″ rectangles) with native oxide layers using a custom-built physical vapor deposition chamber, as described previously.[40,41] Elemental Se (99.99%, Alfa Aesar) was deposited using a Knudsen effusion cell, while Mo (99.995%, Alfa Aesar) was deposited using a 6 keV electron beam gun. The deposition process was controlled using a custom LabView interface in conjunction with quartz crystal microbalances to measure deposition rates and regulate the operation of pneumatic shutters above each vapor plume. By adjusting the duration each shutter remained open, the desired number of atoms per unit area for each element was deposited to form repeating sequences of elemental layers that mimic the nanoarchitecture of the desired crystalline product. These sequences were designed to grow $[Mo_a|(Mo|Se)_b]_n$ architectures, with the $(Mo|Se)_b$ units designed to form an Se-Mo-Se trilayer and the Moa layers designed to form Mo metal with the bulk bcc structure. The amounts of each element deposited were quantified via ex situ x-ray fluorescence (XRF) on a Rigaku ZSX Primus II wavelength-dispersive spectrometer with a Rh x-ray source. XRF intensities were converted to atoms/Å^2 using known proportionality constants derived from thermodynamically stable films, as described previously.[42] Structural characterization was performed on the as-deposited precursors using a range of x-ray techniques, including X-ray reflectivity (XRR), specular X-ray diffraction (XRD), and grazing incidence in-

plane XRD (GIPXRD), using Cu Kα radiation (λ = 0.15418 nm) on a Rigaku SmartLab diffractometer. XRR provided total film thickness and roughness from Kiessig fringes, while XRD and GIPXRD were used to determine crystallinity, repeating unit thicknesses, and lattice parameters. Post-deposition annealing was performed in a nitrogen drybox with O_2 levels below 2 ppm, using a stepwise temperature increase (starting at 200 °C and increasing in 50 °C or 100 °C increments, depending on the sample). Structural evolution was monitored after each annealing step using the aforementioned x-ray techniques.

The transmission electron microscopy (TEM) specimen was prepared in a cross-section by focused ion beam (FIB), using e-beam carbon as a protective layer. A FEI TitanTM G2 80-200 scanning TEM (STEM) with a Cs probe corrector and ChemiSTEMTM technology (X-FEGTM and SuperXTM EDS with four windowless silicon drift detectors) operated at 200 kV was used in structural and chemical analysis of the TEM samples. For STEM imaging, a high-angle annular dark-field (HAADF) detector with a collection range of 60-160 mrad was utilized. Chemical mapping was performed through the acquisition of STEM EDS spectral images, which were obtained as a series of frames. The same region was scanned multiple times, and spatial drift corrections were applied to compile the spectral image data. Elemental maps were subsequently generated from the spectral images by selecting appropriate EDS energy windows for each element.

The density functional theory (DFT) calculations were performed with the VASP package.[43,44] The electronic states were treated with the projector augmented wave method,[45] in the generalized gradient approximation of Perdew, Burke, and Ernzerhof,46 with first-order Methfessel-Paxton smearing (width 27 meV),[47] and a cutoff energy for the plane wave basis set of 280.7 eV. The k-point meshes were chosen for each simulation cell such that their density is at least 40 per $Å^{-1}$. The convergence criteria were 10^{-5} eV for the electronic self-consistency loop and 10^{-4} eV for the ionic relaxation. Van der Waals interactions were accounted for with the Tkatchenko-Scheffler method.[48]

6.5. Bridge

This chapter demonstrates how high nucleation barriers can be strategically exploited to stabilize non-equilibrium phases and highlights how precise control over the nanoarchitecture of precursors enables the synthesis of materials inaccessible by conventional methods. The

following chapter continues this theme by presenting the synthesis and electronic characterization of a novel homologous series of $(PbSe)_1(VSe_2)_1(PbSe)_m(VSe_2)_1$ heterostructures, which is achievable through the tunable layer-by-layer design enabled by the MER approach.

CHAPTER VII

Electronic Behavior of an Asymmetrical $(PbSe)_1(VSe_2)_1(PbSe)_m(VSe_2)_1$ Heterostructure with a Charge Density Wave Transition

7.0. Authorship Statement

This chapter will be submitted for publication in *Chemistry of Materials*. I am the primary author, and Shannon S. Fender and Dimitri L. M. Cordova also contributed significantly to writing the manuscript. Ping Lu collected high-angle annular dark-field transmission electron microscopy and energy dispersive x-ray spectroscopy data. Kornelius Nielsch and Nicolas Perez Rodriquez helped with collecting and interpreting electrical transport data. David C. Johnson acted as my advisor and contributed to editing the manuscript.

7.1. Introduction

2D monolayers and heterostructures containing them have gained significant interest since the isolation of graphene in 2004 and the discovery that properties vary based on thickness and substrate.[1] New emergent properties result from a reduction in dimensionality as thickness approaches a monolayer, and the potential applicability of these phenomena has resulted in significant growth of this research area. Due to a broad range of properties and the ability to cleave bulk crystals to monolayer thicknesses via the "scotch tape" method, transition metal dichalcogenides (TMDs) have become popular materials in this research community and many interesting phenomena have been explored.[2] For example, Mo and W dichalcogenides change from indirect semiconductors as bulk compounds to direct bandgap semiconductors as monolayers.[3–6] Proximity induced superconductivity has been investigated in dichalcogenide monolayers.[7,8] Topological surface conductivity has been discovered in bismuth chalcogenides and $MoTe_2$.[9–11] Ultralow thermal conductivity was discovered in turbostratically disordered structures.[12] Both charge density wave phenomena and magnetic ground states have been found to differ in monolayers versus thicker layers.[13–16] These and other emergent properties of monolayer materials often vary depending on the substrate, an effect that itself is a newly studied phenomenon. There have been many excellent reviews of this research area.[17–20]

The sensitivity of monolayer properties with respect to substrates prompted researchers to investigate the correlation between nanoarchitecture and properties of designed stacks of different 2D layers.[21–23] Geim initially proposed an analogy between monolayers and Legos, where the properties of the monolayers were conserved in heterostructures. The interactions between neighboring layers have been found, however, to be powerful tools to induce new properties and to engineer 2D materials for specific applications by tuning existing properties.[24,25] This is a rapidly growing research area, and there are many papers predicting emergent properties and quantum states and how properties vary with the nanoarchitecture of the heterostructure. New experimental tools to either synthesize or cleave and stack layers of different materials in designed specific sequences has resulted in experimentally testing many of these predictions.[26,27] Modifying the nanoarchitecture of 2D heterostructures via the number and/or sequence of layers provides additional experimental parameters that can be used to induce specific properties.[23,28,29]

As an example of the rapid pace of this field and the impact of layers adjacent to monolayers, VSe_2 has been the focus of numerous theoretical calculations and experimental investigations since it was predicted that monolayers of VSe_2 would be ferromagnetic.[30–36] Bulk VSe_2 is metallic, and shows a charge density wave (CDW) transition as temperature is decreased.[37–39] The literature contains papers providing evidence that VSe_2 monolayers are ferromagnetic,[40] but also a number of papers that disagree with this prediction.[41,42] One consensus is that the sensitivity of VSe_2 monolayers to oxidation makes sample preparation and measurement more challenging. One approach to prevent oxidation of VSe_2 monolayers is to encapsulate the monolayer with inert layers and or to prepare heterostructures containing monolayers of VSe_2 with non-magnetic and insulating constituents. The CDW transition changes as VSe_2 is paired with different constituent layers in heterostructures and as the constituent layer thicknesses are varied. The variation of the properties of VSe_2 monolayers as the identity of the adjacent layers is varied from SnSe, to PbSe, to BiSe clearly demonstrates the impact of the interaction between 2D layers in heterostructures on properties.[41,43,44]

This paper probes the complex interlayer interaction between VSe_2 and PbSe in $(PbSe)_1(VSe_2)_1(PbSe)_m(VSe_2)_1$ heterostructures, measuring the change in transport properties as interlayer distance and nanoarchitecture is varied. This system was chosen because the misfit compound $(PbSe)_1(VSe_2)_1$ is thermodynamically stable relative to a bulk mixture of PbSe and

VSe_2. This implies that the interaction between PbSe and VSe_2 constituents is stronger than a typical van der Waals interaction. $(PbSe)_1(VSe_2)_1(PbSe)_m(VSe_2)_1$ heterostructures have either symmetric (m = 1) or asymmetric ($m \geq 2$) environments relative to the VSe_2 monolayers. The asymmetric environments remove the mirror plane at the vanadium plane in the crystal structures. The $(PbSe)_1(VSe_2)_1(PbSe)_m(VSe_2)_1$ heterostructures where m = 1, 2, and 3 were synthesized from designed precursors using the modulated elemental reactant approach, structurally characterized using XRD and cross section STEM, and electrical transport properties (resistivity and Hall) were measured. Systematic changes in the CDW transition as a function of m illustrate the ability of adjacent layers to tune properties.

7.2. Experimental Methods

Precursors containing a sequence of elemental layers were designed to form $(PbSe)_1(VSe_2)_1(PbSe)_m(VSe_2)_1$, where $1 \leq m \leq 3$. The precursors were prepared in a custom-built vacuum deposition chamber[45] and pressures were kept below 5 x 10^{-7} torr during deposition. Samples were prepared by sequentially evaporating Pb (99.8% Alfa Aesar), V (99.995% Alfa Aesar), and Se (99.99% Alfa Aesar) in the sequence V|Se|$(Pb|Se)_m$|V|Se|Pb|Se (m = 1-3). Pb and V were deposited using 6 keV electron beam guns while Se was deposited using a Knudsen effusion cell. The deposition rates were controlled by quartz crystal monitors that monitor the mass of each element deposited. Target rates were 0.6 Å/s for V, 0.4 Å/s for Pb and 0.9 Å/s for Se. The amount of each element, the order of the deposited layers in each sequence, and the total number of times the layer sequence is repeated were controlled by a custom LabView program. The program controls pneumatic shutters that open and close based on the amount of material deposited on the quartz crystal monitor, using either integrated thickness or the product of the deposition rate and time. This procedure is described elsewhere.[46] The samples were deposited on (100) silicon wafers for structural characterization and on masked, polished quartz substrates for electrical measurements. The sequence of elemental layers was deposited until a total thickness of approximately 30 nm was reached. The precursors were annealed for 45-60 minutes at temperatures between 100°C – 400°C in an inert atmosphere, with oxygen concentration < 1 ppm. The precursors were examined using a variety of techniques, both as-deposited and after annealing at different temperatures, to determine their compositions and structures. The amount of each element deposited was determined by X-ray fluorescence (XRF) using a Rigaku Primus

II ZSX spectrometer. The XRF data analysis method of Hamann et. al, was used to convert intensity to the amount of each element per unit area.[47] The background intensities from the substrates were subtracted from the total intensity. Out-of-plane specular x-ray diffraction (XRD) and x-ray reflectivity (XRR) were collected on a Bruker D8 Discover diffractometer with Cu Kα radiation (λ = 0.15418 nm) and Bragg-Brentano θ-2θ optics geometry. Specular diffraction shows the evolution of the superlattice and was used to determine the c-axis parameter and d-spacing of $(PbSe)_1(VSe_2)_1(PbSe)_m(VSe_2)_1$. XRR data was used to determine film uniformity and thickness. Bragg's law corrected for refraction was used to calculate thickness and the Parratt equation was used to determine thickness uniformity. In-plane XRD was taken on a Rigaku SmartLab Diffractometer, also equipped with Cu Kα radiation, to determine the basal plane structure and follow the evolution of the substituents. Le Bail fitting of the diffraction scans was used to determine lattice parameters using GSAS II software. High-angle annular dark-field scanning transmission electron microscopy (HAADF-STEM) images were collected by a FEI Titan™ G2 80-200 STEM with a Cs probe corrector, operated at 200 kV, using an annular detector with a collection range of 60-160 mrad. STEM samples were prepared by focused ion beam technique. Temperature dependent electrical resistivity and Hall measurements were determined using the Van der Pauw technique[48] in a temperature range of 1.8 – 300 K.

7.3. Results and Discussion

Precursors for each of the compounds $(PbSe)_1(VSe_2)_1(PbSe)_m(VSe_2)_1$ with m =1−3 were prepared by depositing specific sequences of elemental layers, using the method of modulated elemental reactants. The number of atoms of each element in the Pb|Se and V|Se layers was controlled to match the number required to form single unit cells of PbSe and VSe_2, respectively. As described previously,[49] the target number of atoms deposited for each layer in each precursor was calculated from the crystal structure of the respective constituents. Based on Cordova's previous results, we assumed each V|Se bilayer would form a single plane of VSe_2 where the (001) planes were crystallographically aligned to the substrate and that each Pb|Se bilayer will form a bilayer of PbSe with the square basal plane (002) aligned with the substrate.[44] The elemental layers were deposited in the order of $V|Se|[Pb|Se]_m|V|Se|Pb|Se$ to increase the crystallographic alignment of the PbSe layers.[44] The prepared precursors were characterized using XRF, XRR, and XRD. The information obtained is summarized in Table 7.1. The amount

of each element deposited in the repeating layer of each precursor was measured using XRF. A previously published calibration method was used to convert the XRF counts for each element into the number of atoms per unit area.[47]

Table 7.1. As-deposited structural and compositional data for the precursors.

m	Deposited atoms/Å^2*repeat unit			Total Precursor Thickness (Å)	Number of Deposited Repeat Units	Modulation Length (Å)
$(PbSe)_1(VSe_2)_1(PbSe)_m(VSe_2)_1$	Pb	V	Se			
1	0.226(2)	0.201(4)	0.59(2)	310.6(4)	25	12.4(4)
2	0.314(3)	0.216(4)	0.74(2)	481.5(8)	16	31.6(4)
3	0.427(4)	0.201(4)	0.83(3)	382.1(4)	10	38.4(4)

XRR patterns were collected on each precursors before annealing (Figure 7.1). The XRR patterns of the precursors all contain Kiessig fringes from the incomplete destructive interference of the finite number of layer sequences in each precursor and Bragg reflections from the constructive interference between the layer sequences. The number of minima between the Bragg reflections is equal to the number of repeat units deposited minus one. The Bragg maxima can be indexed by a single integer, yielding the thicknesses of the repeating precursor sequence (modulation length) using Braggs law corrected for refraction. The inset figure shows the precursor modulation lengths determined from these scans plotted versus *m*. The thickness of the deposited Pb|Se|V|Se|(Pb|Se)$_m$|V|Se sequence increases linearly as *m* is increased. The angle where the Kiessig fringes can no longer be observed was related to the roughness of the layers in the film using Parratt's relationship,[50] which indicated that the roughness in the films was 0.2-0.3 Å. The XRR patterns are consistent with the nanoarchitectures of the targeted precursors, chosen to mimic the structure of the desired products.

We investigated the changes in structure of a $(PbSe)_1(VSe_2)_1(PbSe)_2(VSe_2)_1$ (m=2) precursor as a function of annealing temperatures using XRD (see Figure 7.2) in order to optimize the conditions required to self-assemble the targeted heterostructures from the precursors. The as-deposited diffraction pattern contains contributions from two different sources as indicated by different reflection linewidths. Sharper low angle reflections arise from the

artificial modulation of the layered precursor, yielding a value of 30.6(4) Å for the modulation length in the as-deposited precursor. Broad high order reflections (13-40° 2θ) indicate long range order in the film, presumably due to the crystalline formation of the targeted heterostructure during the deposition. These higher angle reflections yield a value of 30.83(3) Å for the *c*-axis lattice parameter in the as-deposited precursor. As annealing temperature is increased to 300°C,

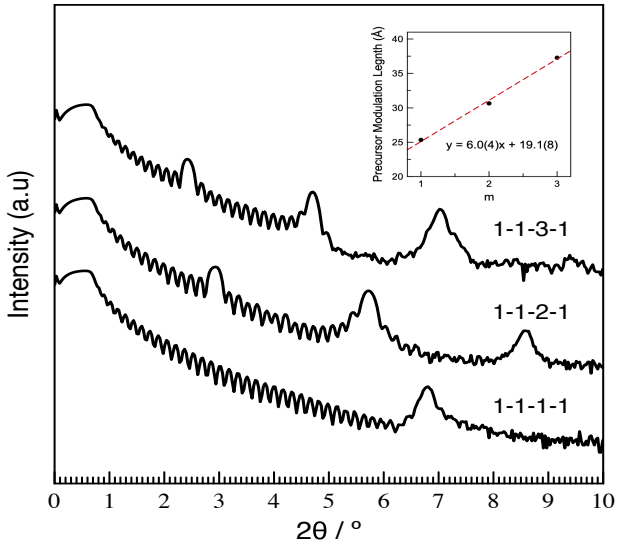

Figure 7.1. XRR patterns of the precursors and the relationship between modulation length and *m* (inset), where values are plotted along with its regression. Slope corresponds to the thickness of the Pb|Se precursor, and the y intercept is the thickness of two V|Se layers and one Pb|Se layer.

the higher order peaks sharpen and increase in intensity and the low angle reflections shift to align with higher order reflections as the crystalline heterostructure forms. The in plane (*hk*0) diffraction (Figure 7.2B) also show increases in peak intensity and sharpness as annealing temperature increases. The reflections in the in-plane pattern can be indexed to either a square or hexagonal unit cell, and the resulting lattice parameters are consistent with the structures of PbSe and VSe_2, respectively.[44] Optimal annealing time and temperature was chosen to obtain the highest intensity and lowest FWHM of reflections in the specular and in plane diffraction patterns.

The XRR and specular XRD patterns obtained on all samples after annealing with the optimized annealing conditions are shown in Figure 7.3. The XRR patterns contain Bragg reflections from the heterostructures formed and Kiessig/Laue fringes due to the finite number of unit cells (Figure 7.3A). The reflections in the specular diffraction patterns (Figure 7.3B) can all

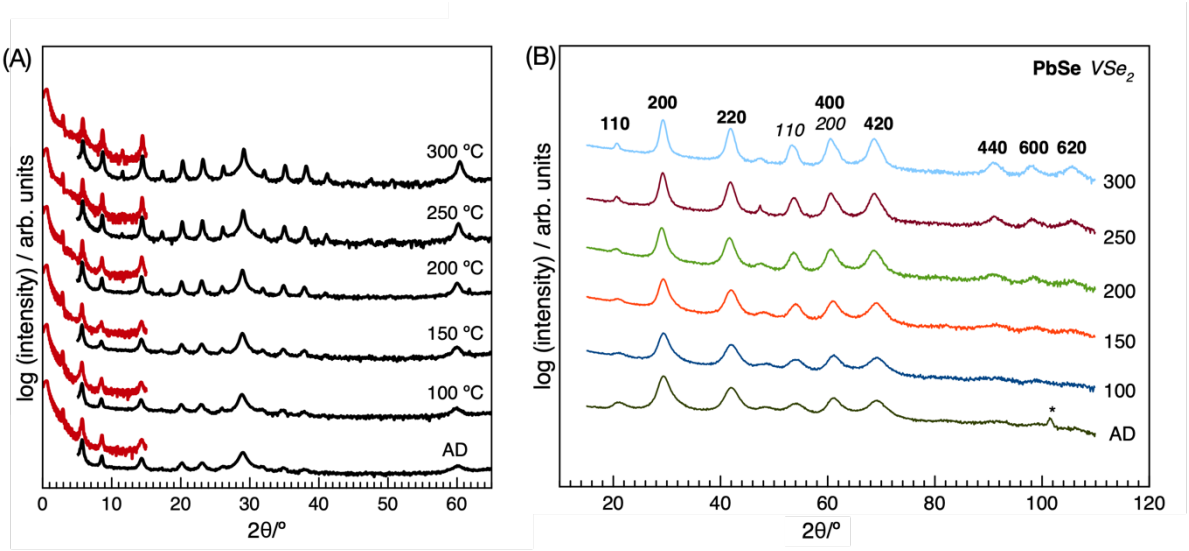

Figure 7.2. (A) XRR (red) and specular XRD patterns (black) collected as a function of annealing temperature for $(PbSe)_1(VSe_2)_1(PbSe)_2(VSe_2)_1$, where samples were annealed for 1 hour and reflections can be indexed as (00*l*) reflections. (B) In-plane XRD patterns collected on the same sample after each annealing temperature show only *hk*0 reflections that can be indexed to square and hexagonal unit cells, that are consistent with reflections that would be expected from PbSe and VSe_2.[44] Indices for reflections consistent with PbSe are shown in bold text, and indices for reflections consistent with VSe_2 are shown in regular text. Diffraction artifacts from the Si substrate are marked with * symbols.

be indexed as 00*l* reflections yielding *c*-axis lattice parameters of 12.243(7) Å, 30.673(5) Å, and 36.76(1) Å for m = 1, 2, and 3, respectively, using Braggs Law. The *c*-axis lattice parameter of each compound is smaller than the modulation length of the as-deposited precursor due to the higher density of the compound relative to the precursor and the loss of excess selenium during annealing.

Atomic imaging was obtained through HAADF-STEM, providing crystal structure information that could be used to calculate atomic positions within the unit cell. The zone axis images (Figure 7.4A) show a rock salt structure for the PbSe layer, and octahedral VSe_2 layers. The varied crystallographic orientations of the PbSe and VSe_2 layers are the result of turbostratic disorder found in ferecrystalline compounds.[51] A line imaging software was used to measure the intensity of light in HAADF-STEM imaging, taken across vertical planes in the subset image of Figure 7.4B. The aggregate values were scaled to match the dimensions of the image and then fit to gaussian peaks, where the maxima indicate the position of the atom. The energy-dispersive x-

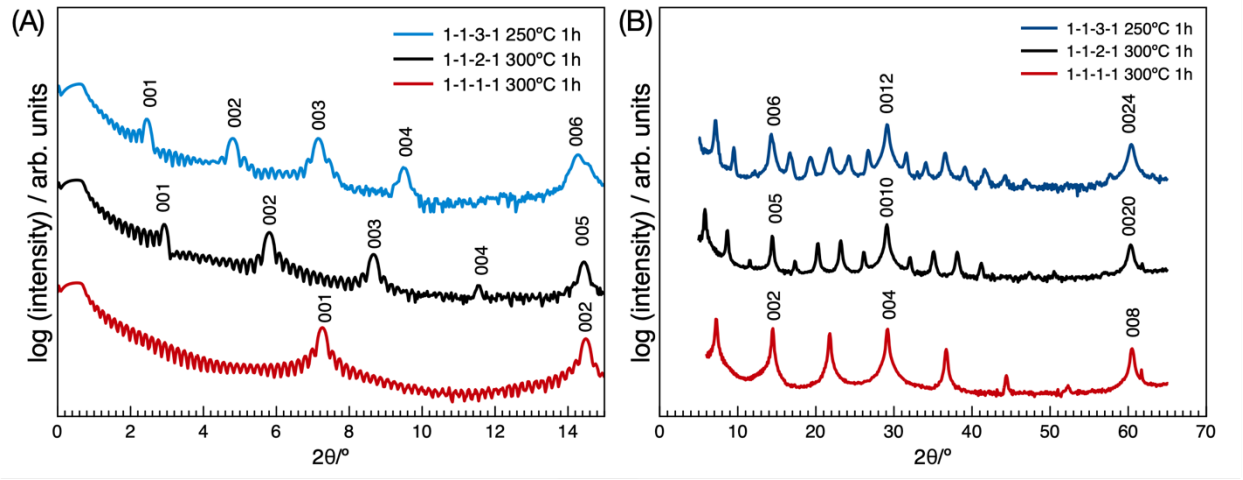

Figure 7.3. (A) XRR shows film uniformity of m= 1-3 samples annealed at their respective optimal annealing conditions. (B) Specular x-ray diffraction shows Bragg reflections from an ordered superlattice of m= 1-3 samples annealed to their optimal annealing conditions.

ray spectroscopy map shown in Figure 7.5 is consistent with the targeted structure containing PbSe and VSe_2 layers. Two selenium peaks flank each vanadium atom, consistent with the formation of a Se-V-Se trilayer found in VSe_2. Lead peaks are paired with selenium peaks in the isolated bilayer, and are located at the same distance, which is consistent with the formation of a PbSe bilayer with a rock salt structure. The selenium peaks are more obscured in the double layer of PbSe in the $(PbSe)_1(VSe_2)_1(PbSe)_2(VSe_2)_1$ heterostructure. Puckering for PbSe cannot be confirmed due to sample size and noise in the EDS map.

Temperature dependent resistivity data was collected for each sample after annealing at its optimal conditions (Figure 7.6). The magnitude of the resistivities, ~ 10^{-5} ohm cm, is in the lower range observed for transition metals, but is consistent with previous reports of $[(PbSe)_{1+\delta}](VSe_2)_n$ and $[(PbSe)_{1+\delta}]_m(VSe_2)$ samples.[52,53] The magnitude of the room temperature resistivity increases systematically as *m* is increased. This increase is expected as the percentage of the film that is semiconducting PbSe is increased.[16,44,54] However, the magnitude difference between the $m = 1$ and $m = 2$ sample is much smaller than between the $m = 2$ and $m = 3$ sample. In all three samples the resistivity gradually decreases with temperature, until a charge density transition occurs, which sharply increases the resistivity. The CDW transition temperature is determined using a cubic spline interpolation of the data to find the exact temperature at which the slope changes from negative to positive. In the $m = 1$ sample the transition occurs around 138 K, with a steep increase in resistivity until it begins to plateau at ~10 K. The resistivity remains

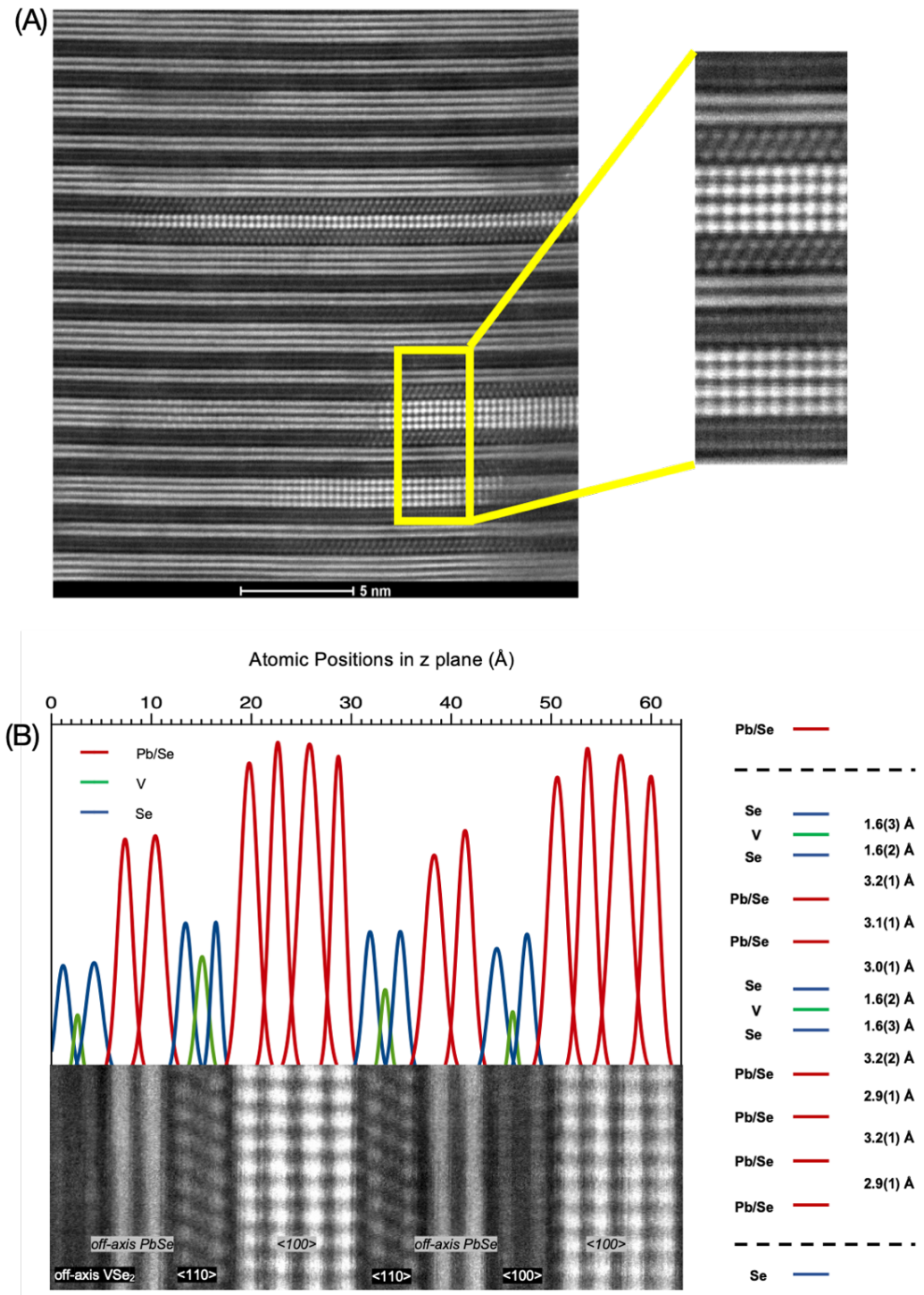

Figure 7.4. (A) HAADF-STEM image of the $(PbSe)_1(VSe_2)_1(PbSe)_2(VSe_2)_1$ heterostructure after annealing at its optimal conditions shows that the film consists of alternating layers of PbSe and VSe_2 with the targeted nanoarchitecture. (B) Linear profile from a rectangular section of the STEM image shows approximate z atomic plane positions in a repeat unit.

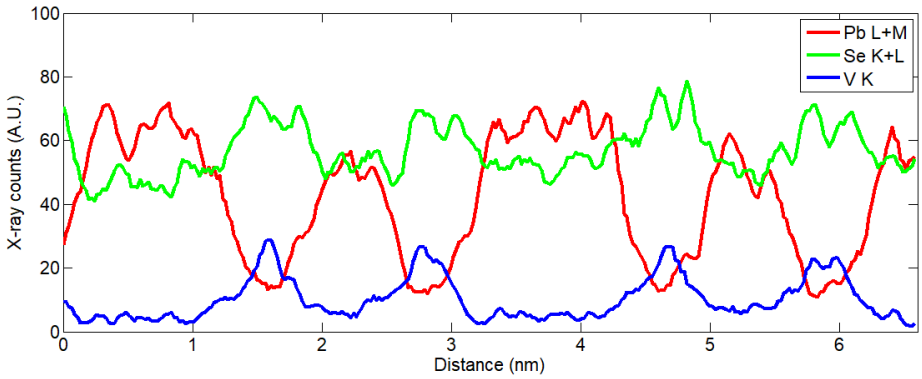

Figure 7.5. EDS map shows elemental compositions as a function of distance perpendicular to the substrate, providing an approximation of atomic plane positions.

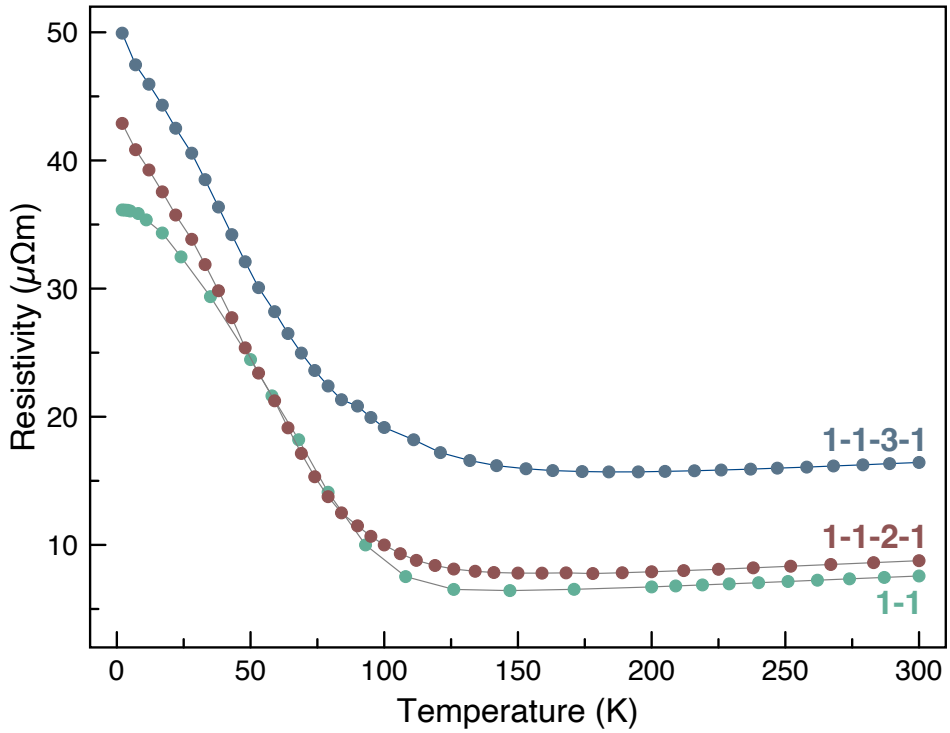

Figure 7.6. Temperature dependent resistivity data collected on samples $m = 1$ (green pattern, labeled 1-1), $m = 2$ (pink pattern, labeled 1-1-2-1), and $m = 3$ (blue pattern, labeled 1-1-3-1).

constant within error below 4 K. In the $m = 2$ and $m = 3$ samples the transition occurs near 156 K and 189 K, respectively. For both samples, the resistivity then increases continuously until the lowest measured temperature is reached. The linear decrease in resistivity as temperature is decreased above the CDW transition is consistent with the metallic behavior expected for the VSe_2 monolayers, which are expected to dominate the in-plane transport behavior if the PbSe

layers are semiconducting, as previously reported in $[(SnSe)_{1+\delta}]_m(NbSe_2)$, $[(PbSe)_{1+\delta}](VSe_2)_n$, and $[(PbSe)_{+\delta}]_m(VSe_2)$ systems.[52,55] According to the model presented by Geim of 2D van der Waals heterostructures that are assembled like stacks of LEGOs,[21] the simplest picture would envision that in-plane transport properties are a composite of the properties of each individual constituent. In this case, in-plane transport would be a combination of the behavior in a small bandgap semiconductor with low carrier concentration (PbSe) and a metallic layer (VSe_2). If this simple picture fits, the room temperature in-plane resistance for all three samples should scale systematically with the number of PbSe layers in each repeat unit. As shown in Figure 7.7, however, there is some deviation from this simple non-interaction picture in the samples studied here as well as in previously published $(PbSe)_m(VSe_2)_n$ compounds.[16,44] Although most of the samples appear to follow a linear trend, the $m = 3$ sample from this study is a significant outlier. Some or all of this deviation could result from non-stoichiometries, as shown by Flambigl and co-authors.[56] Additionally, this study is the first investigation of samples designed to place the VSe_2 monolayer in an asymmetric environment, breaking the mirror plane symmetry across the V atomic plane found in the previously reported homologous series. The increased deviation from the expected trend as a function of asymmetry indicates that the interfacial interactions and

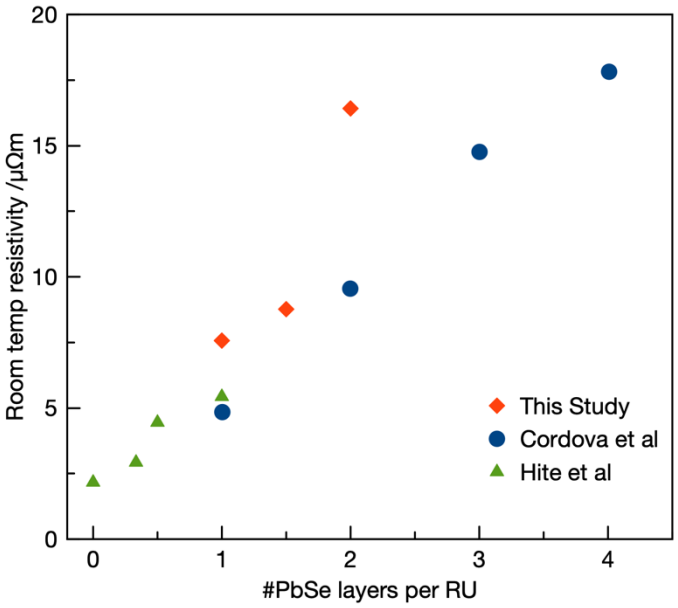

Figure 7.7. Room temperature resistivity values plotted versus the number of PbSe layer per repeat unit (RU) in the samples studied here (orange diamonds), a series of $(VSe_2)_1[(PbSe)_{1+\delta}]_m$ samples studied previously (blue circles),[44] and a series of $(VSe_2)_n(PbSe)_{1+\delta}$ samples studied previously (green triangles).[16]

distances between VSe_2 layers play an important role in the electronic transport mechanism of these samples. This conclusion is supported by previous reports that demonstrate how changing interfacial interactions can affect charge transfer between layers and impact mobility.[16]

Hall data was collected on the samples to gain further information about their transport properties, and the temperature dependent carrier concentrations for the three samples studied here are shown in Figure 7.8A. The Hall coefficient was found to be negative for all samples, indicating electrons as the majority carrier, consistent with the sign of the Hall coefficient reported for bulk VSe_2. In a previous study of a series of $[(PbSe)_{1+\delta}]_m(VSe_2)_1$ samples with (m = 1, 2, 3, 4), the Hall coefficient was reported to be positive for all samples, indicating holes as the majority carrier.[44] We confirmed that we have a negative Hall coefficient in the samples measured, leading us to suspect a sign mistake in the previously published paper. Carrier concentrations were calculated from the Hall measurements using a single-band model approximation. It has been shown previously that this approximation is an over-simplification of the transport in even binary VSe_2,[57] and we expect the transport in these heterostructures to be even more complicated. However, approximations of carrier concentration using the single band model can still be a useful tool to analyze trends in the changes of electronic transport in this series of samples. The $m = 1$ sample (50% VSe_2) has the highest carrier concentration, followed by the $m = 2$ sample (40% VSe_2), followed by the $m = 3$ sample (~33% VSe_2). The trend of decreasing carrier concentration with decreasing VSe_2 percentage fits the simple non-interaction model discussed above. However, previous reports agree that PbSe at least somewhat contributes to the conduction, which complicates things.[16,58]

There are distinct differences in the temperature dependance of the Hall data for the three samples studied here, illustrating the complexity of the transport properties in this system. The temperature dependance of the carrier concentration for the $m = 1$ sample is similar to what has been reported previously for $(PbSe)_1(VSe_2)_1$ in a study of $(PbSe)_m(VSe_2)_1$ samples with increasing m,[44] where the carrier concentration gradually increases as temperature is decreased until the transition temperature is reached, at which point there is a sharp drop in carriers that plateaus at the lowest measured temperatures. Interestingly, in an older study of $(PbSe)_1(VSe_2)_n$ samples with increasing n,[16] the $n = 1$ sample exhibited different behavior. Hite and coauthors report that the carrier concentration in the $n = 1$ sample remains nearly constant until the transition temperature is reached, at which point the Hall coefficient increases by a factor of

about 8.[16] Interestingly, the temperature dependance of the $m = 3$ sample studied here – which has the highest level of asymmetry – mimics this symmetric $n = 1$ sample previously reported by Hite and coauthors. This difference in behavior between previous studies and the samples studied here further highlights the sensitivity of the complex electronic transport in this system to non-stoichiometries and structural defects.

Deviations from the expected temperature dependance can be used to hypothesize the physical origin of the observed behavior. In normal metal and semiconductor behavior, a small decrease in carrier concentration and small increase in mobility is expected with decreasing temperature. However, this behavior relies on the assumption that the lattice and band structure remain constant. When this "normal" behavior is not obeyed, these assumptions cannot be true. In the $m = 1$ and $m = 2$ samples studied here, the increase in carrier concentration as a function of decreasing temperature is most likely due to a structural change that causes the conduction band to bend, decreasing the bandgap. The corresponding decrease in mobility (Figure 7.8B) implies that this structural change increases the interaction between electrons and their cores. At the

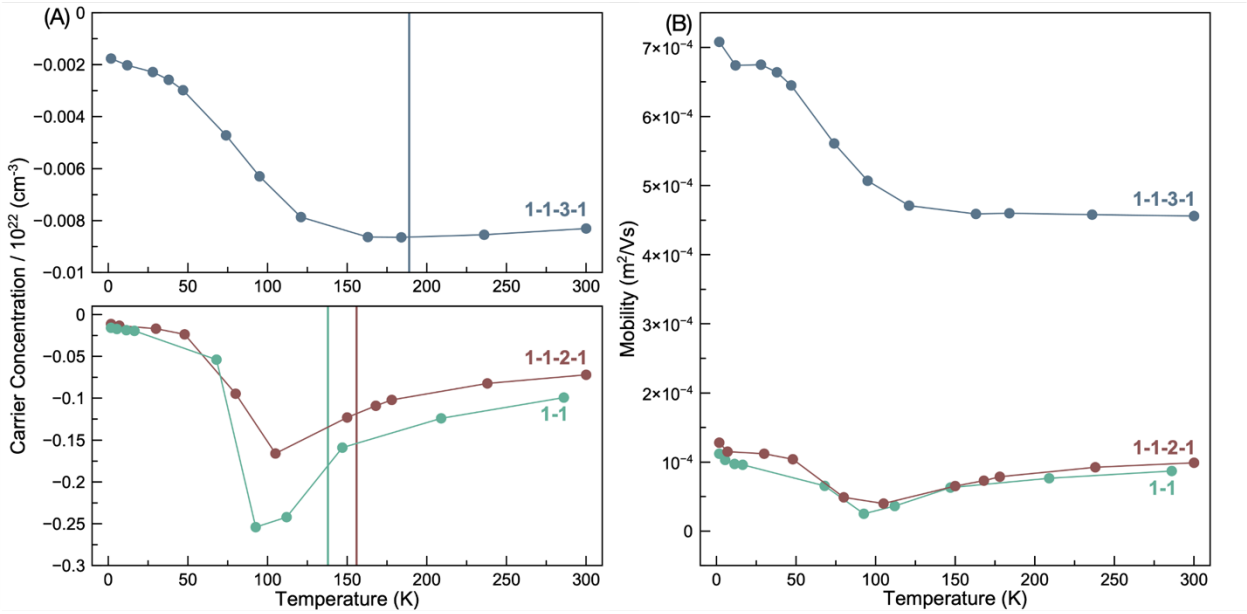

Figure 7.8. (A) Temperature dependent carrier concentrations for the three samples studied here. The CDW transition temperature for each sample determined from the resistivity data is shown as a vertical line with colors corresponding to the color of the data points for each sample. (B) Temperature dependent single conducting band mobilities calculated from $\mu = R_H/\rho$, where μ is the mobility, R_H is the Hall coefficient, and ρ is the resistivity. Data for the $m = 1$ sample is shown in green and labeled 1-1. Data for the $m = 2$ sample is shown in pink and labeled 1-1-2-1. Data for the $m = 3$ sample is shown in blue and labeled 1-1-3-1.

CDW onset temperatures the carrier concentrations then decrease significantly. If this temperature marks the end of the structural changes that are occurring, the normal "freezing out" process of carriers would continue on as expected, as the carrier concentration then decreases with temperature.

7.4. Conclusions

In this study, we synthesized and characterized a series of novel $(PbSe)_1(VSe_2)_1(PbSe)_m(VSe_2)_1$ compounds with m = 1–3 to investigate how properties are affected by interfacial interactions and asymmetry. Structural characterization (XRR, XRD, HAADF-STEM, EDS) confirmed the formation of layered heterostructures with the intended nanoarchitectures. Electronic transport measurements show that the transition temperature of a CDW in these heterostructures increases with increasing *m*. This suggests that interlayer interactions and stacking asymmetry play a role in determining the transition temperature, which agrees with previous studies. Some unique deviation from expected transport trends indicates that electronic behavior is highly sensitive to local structure and composition. The resistivity and Hall data deviate from simple models that suggest the properties of a material should be a composite of the properties of the individual constituents. These deviations underscore the significant role of interlayer electronic coupling in determining the overall transport behavior. Notably, asymmetry introduced by increasing *m* disrupts mirror-plane symmetry across the V atomic plane and enhances deviation from expected trends, highlighting the sensitivity of transport behavior to subtle structural modifications. Carrier concentration and mobility data further support this picture. Low-*m* samples show an increase in carrier concentration with decreasing temperature, which is consistent with a structural change that modifies the band structure. The mobility decreases at the same temperatures, suggesting increased electron–lattice interactions. At the CDW onset, carrier concentration begins to decrease, consistent with the "freezing out" of carriers at lower temperatures. In contrast, the m = 3 sample demonstrates a different temperature dependance, potentially due to increased asymmetry and isolation of VSe_2 layers, which changes the interfacial interactions and charge transfer. These results show that tuning the layering sequence and symmetry in heterostructures can be used to manipulate collective electronic behavior. This work highlights the utility of synthetic design in engineering

interlayer interactions and provides a path forward for tailoring electronic transport properties in layered heterostructures.

7.5. Bridge

Chapter VII details the synthesis of a series of novel heterostructures made possible by precise control of precursor design, enabling access to a structure unattainable by conventional techniques. Chapter VIII builds on this by presenting the synthesis of a second novel heterostructure, $(MoSe_2)_1(ZnSe)_n$, which stabilizes a previously unreported phase of ZnSe. This achievement is made possible by fine-tuned control over experimental parameters and by the mechanistic insights into solid-state reactions developed throughout the preceding chapters.

Chapter VIII

Interfacial Stabilization of a New ZnSe Phase in $(MoSe_2)_1(ZnSe)_n$ Heterostructures

8.0. Authorship Statement

This chapter will be submitted for publication in *Nature Materials*. I am the primary author. Henry Hutley helped with data collection and analysis. Sven P. Rudin performed DFT calculations. Ping Lu collected HAADF-STEM and EDS data. David C. Johnson acted as my supervisor and assisted with interpreting data and writing and editing the manuscript.

8.1. Introduction

Following the discovery of graphene,[1] two-dimensional (2D) materials have been the subject of extensive investigation. It is now a well-known phenomenon that reducing a materials dimensionality from its bulk form to a monolayer can result in pronounced changes to its physical properties. Some properties that emerge at the monolayer limit have significant technological significance, particularly in the context of ongoing efforts to miniaturize electronic and optoelectronic devices.[2–5] Transition metal dichalcogenides (TMDs) are one particularly notable class of materials that have significant potential applications in next-generation technology, especially when decreased to the monolayer limit. TMDs have promising potential in logic applications,[6] photodetectors and photovoltaics,[7] memory devices,[8] and spintronics,[9] to name a few. TMDs have a MX_2 formula and an X-M-X sandwich structure where M is a transition metal and X is a chalcogen (S, Se, or Te). TMDs are layered compounds, with all bonds terminating within each layer and only van der Waals interactions between the layers.[10] The 2D layered structure of TMDs makes them ideal candidates for studying emergent properties at the monolayer limit. A classic example is the indirect to direct bandgap transition when MoS_2 is decreased from the bulk to a monolayer. The direct-gap behavior of monolayer MoS_2 makes it very promising for applications in transistors, LEDs, and photoresistors.[11,12] Understanding how the structure and properties of a wider range of materials evolve with decreasing thickness is essential, as these changes directly impact the performance and design of next-generation devices.

One powerful avenue for harnessing the unique properties of monolayers is through the growth of designed heterostructures. In heterostructures, individual constituents with specific properties can be layered in specific ways – even down to a monolayer – to tune the overall properties of the resultant material. By modulating the nanoarchitecture (layer thickness, sequence, and constituents) of a material, the physical properties (electronic, optical, and mechanical) can be tuned.[13–16] Misfit layer compounds (MLCs) are a distinct class of heterostructures that offer significant potential for tailoring physical properties through structural and compositional modulation.[17,18] MLCs have a $[(MX)_{1+\delta}]_m[TX_2]_n$ structure where M = a metal (often Sn, Pb, Bi, or a rare earth), T = a transition metal (, and X = a chalcogen (S, Se, Te); *m* and *n* are integers representing the number of MX or TX_2 layers; and δ is the "misfit parameter" (usually ranging from 0.07 to 0.28[19]), which describes the lattice mismatch between the two incommensurate MX and TX_2 systems. MLCs have been used to isolate structures that are unstable in the bulk and to study the "substituent effects" of adjacent layers that can be used to target the growth of otherwise unstable phases with unique properties.[20–22] The Bi-Se system serves as a compelling example of how adjacent layers within a heterostructure can influence and direct the nucleation and growth of target phases. Although BiSe is unstable as a bulk phase, it's growth has been stabilized in MLCs via charge donation to an adjacent electron accepting layer.[23,24] In an example reported by Choffel et al, the charge donation from BiSe to an adjacent $MoSe_2$ stabilized the formation of a high percentage of metallic 1T-$MoSe_2$ over the thermodynamically stable semiconducting 2H-$MoSe_2$.[25] These results indicate that for some materials that can't be reduced to a monolayer using other methods, growth inside a heterostructure may be a potential avenue to study some materials at the monolayer limit.

In this study we report the synthesis and structural characterization of a unique $(MoSe_2)_1[(ZnSe)_{1+\delta}]_n$ heterostructure using the method of modulated elemental reactants (MER). $MoSe_2$ is a widely studied group VI TMD semiconductor, with extensive characterization of its structural, electronic, and optical properties across bulk, monolayer, and heterostructured forms.[26–29] However, monolayer ZnSe has not been reported, as part of a heterostructure or otherwise. We show that the growth of a heterostructure in this system is very sensitive to the composition of the deposited precursors. The n = 1 heterostructure forms well from specific precursor compositions; however, slight variations in local stoichiometry lead to phase segregation upon annealing, resulting in the formation of the binary compounds $MoSe_2$ and

ZnSe. In precursors designed to grow n = 2 and n = 4 heterostructures, the samples remain elementally layered without growing a well-ordered heterostructure at the annealing temperatures investigated. Using diffraction, scanning transmission electron microscopy, energy dispersive x-ray spectroscopy, and Rietveld refinement data, we show that monolayers of ZnSe can be stabilized in a heterostructure; and that when confined between the van der Waals planes of adjacent $MoSe_2$ layers, a monolayer of ZnSe adopts a previously unreported structure. These results suggest that confined volumes within heterostructures can be harnessed to study the unique structure and properties of a wide range of materials at the monolayer limit.

8.2. Results and Discussion

A series of six samples was deposited to determine how elemental layer thickness can be used to kinetically control the reactions between Mo and Zn with Se in layered ternary thin-films. The samples were deposited with a repeating $Mo|Se|(Zn|Se)_n$ sequence designed to grow $(MoSe_2)_1(ZnSe)_n$ heterostructure with n = 1, 2, and 4. X-ray fluorescence (XRF), x-ray reflectivity (XRR), and x-ray diffraction (XRD) data were collected on each precursor directly after deposition. The sample IDs, deposited layering sequences, number of deposited repeating units (RUs), number of atoms/Å^2 in each RU, total sample thicknesses, RU thicknesses, and surface roughness for each sample are summarized in Table 8.1.

Table 8.1. A summary of the deposition information and measured compositions and thicknesses of the as-deposited samples. The number of Mo, Zn, and Se atoms were determined from x-ray fluorescence data. The total sample thickness was determined using the 2θ position of Kiessig fringe maxima in the x-ray reflectivity pattern and Braggs law modified to account for refraction. The average thickness of the deposited repeating unit (RU) was calculated by dividing the total sample thickness by the number of repeating units deposited. The error in each reported value is given in parentheses after the last significant digit.

Sample Name	Repeating Sequence	Number of Deposited RU (n)	Mo per RU (atoms/Å^2)	Zn per RU (atoms/Å^2)	Se per RU (atoms/Å^2)	Average Total Thickness (Å)	Average Thickness of Deposited RU (Å)	RU Thickness from Position of First Order Bragg Reflection (Å)
2A	$(Mo\|Se)_1(Zn\|Se)_1$	24	0.0928(9)	0.162(3)	0.517(8)	370.7(5)	15.45(2)	14.9(6)
2B	$(Mo\|Se)_1(Zn\|Se)_2$	16	0.0929(9)	0.312(6)	0.71(1)	349.2(2)	21.83(1)	21(1)

2C	$(Mo\|Se)_1(Zn\|Se)_4$	10	0.100(1)	0.57(1)	1.10(2)	346.9(4)	34.69(4)	34(2)
3A	$(Mo\|Se)_1(Zn\|Se)_1$	24	0.108(1)	0.229(5)	0.366(5)	337.7(3)	14.07(1)	13.5(6)
3B	$(Mo\|Se)_1(Zn\|Se)_2$	16	0.109(1)	0.440(9)	0.518(8)	328.0(6)	20.50(4)	20(1)
3C	$(Mo\|Se)_1(Zn\|Se)_4$	10	0.104(1)	0.83(2)	0.79(1)	314.6(7)	31.46(7)	31(2)

X-ray fluorescence (XRF) data collected after deposition were used to determine the absolute number of Mo, Zn, and Se atoms/Å^2 in each precursor. The data is shown graphically in Figure 8.1. The x- and y-axes of Figure 8.1 show the number of atoms/Å^2 of Zn and Mo, respectively, as measured via XRF. The red horizontal line shows the target number of Mo atoms/Å^2 required to grow a monolayer of $MoSe_2$ per RU. Because only a monolayer of $MoSe_2$ is targeted in each sample, the target number of Mo atoms remains constant. The vertical lines show the target numbers of Zn atoms/Å^2 required in each RU to grow each of three different unit cell types for ZnSe – yellow for bulk-type cubic ZnSe, indigo for bulk-type hexagonal ZnSe, and turquoise for ZnSe with the experimentally determined unit cell type and lattice parameters discussed in detail below. The target amounts of Zn atoms/Å^2 required in each RU increase with increasing *n*. Each set of vertical lines for each associated *n* value (shown above the graph) are shaded in grey. The circular data points in Figure 8.1 show the number of atoms/Å^2 in each deposited precursor, as determined from XRF data collected on each sample directly after deposition. The data show that samples 3A and 3B have more Mo than necessary in each RU to grow a monolayer of $MoSe_2$ and the amount of Zn in each RU is slightly more than that needed to grow cubic ZnSe and slightly less than that needed to grow either type of hexagonal ZnSe. Sample 3C has enough Mo in each RU to grow a monolayer of $MoSe_2$ but it is deficient in Zn with respect to all three ZnSe unit cell types. Samples 2A, 2B, and 2C are significantly deficient in Mo, but 2A and 2B have more Zn than necessary to grow any ZnSe unit cell type. Sample 2C has enough Zn to grow any ZnSe unit cell type.

XRR, specular XRD, and grazing incidence in-plane XRD scans collected for each of the six precursors directly after deposition are shown in Figure 8.2. The XRR patterns (Figure 8.2A) contain Kiessig/Laue oscillations and Bragg reflections from the repeating electron density gradient of the deposited elemental layers (hereafter referred to as “layering reflections”). The Keissig oscillations are well resolved above 8° 2θ for all six samples, indicating that they have

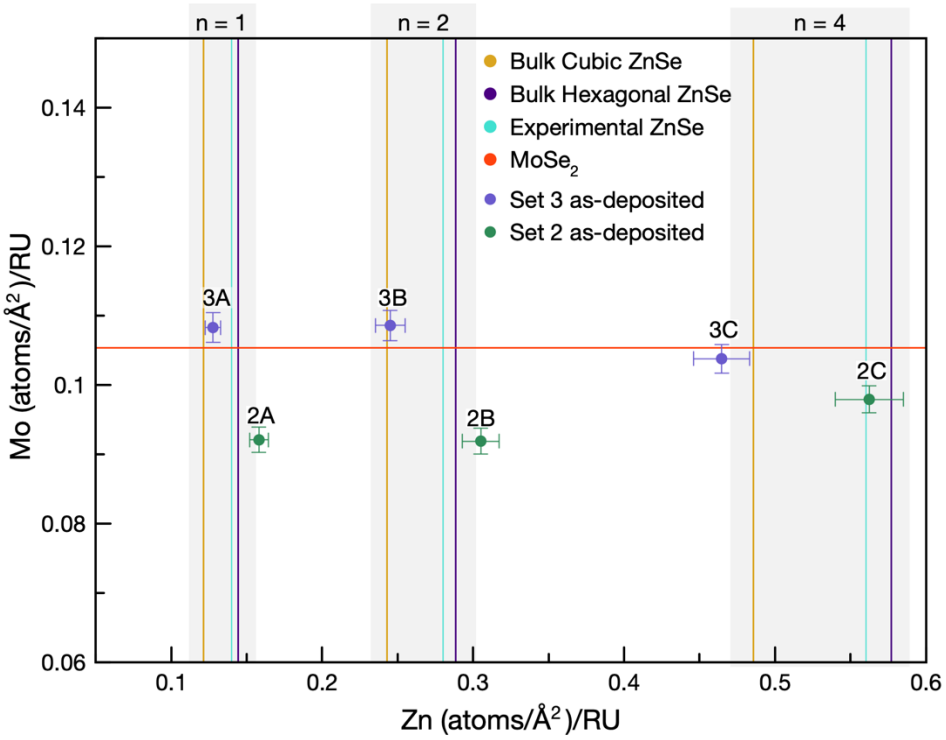

Figure 8.1. X-ray fluorescence data collected directly after deposition for both metals (Mo and Zn) in the 6 precursors. The red horizontal line shows the number of Mo [atoms/Å^2]/repeating unit (RU) necessary to grow a monolayer of $MoSe_2$. The vertical lines shows the number of Zn [atoms/Å^2]/RU necessary to grow a monolayer of cubic ZnSe (yellow), wurtzite ZnSe (indigo), and the experimentally determined P-3m1 type ZnSe (turquoise). The green circles show the amounts of each metal in each RU in the set 2 samples. The purple circles show the amounts of each metal in each RU in the set 3 samples.

very smooth surfaces. The total sample thicknesses calculated from the positions of the Kiessig oscillations and Braggs law modified to include refraction are shown in Table 8.1. The average repeating unit thicknesses shown in Table 8.1 calculated by dividing the total sample thickness by the number of deposited repeating units and by using the 2θ position of the first order Bragg reflections agree with each other within error. The repeating unit thickness values of the as-deposited samples are consistent with the expected thickness of Mo-Se and Zn-Se layers containing enough atoms to grow $MoSe_2$ and ZnSe, respectively, with ~10% excess Se. The presence of low-angle Bragg reflections indicates that the elemental layers do not mix during the deposition and the resulting samples are heterogenous and layered. The specular XRD patterns (Figure 8.2B) contain layering reflections below 20° 2θ and broad, low-intensity reflections above 20° 2θ from small grains of either the heterostructure or the individual constituents ($MoSe_2$ or ZnSe) that nucleated and grew during the deposition (depending on the sample). All

six precursor samples contain some intensity near 27° 2θ, in the expected position for the (111) reflection of bulk ZnSe.[1–7] Sample 3A contains an additional broad, low-intensity reflection near 20° 2θ. The two low-intensity reflections in sample 3A can be indexed to a unit cell with a *c*-axis lattice parameter of 13.5(1) Å. The expected 2θ positions of all 00*l* Bragg reflections for a unit cell with this d-spacing are shown (including error) as orange bars in Figure 8.2B above the pattern for sample 3A. The two layering reflections align with these expected Bragg reflection positions because the precursors are designed to mimic the nanoarchitecture of the desired crystalline heterostructure, so the deposited repeating elemental layers are the same thickness as one unit cell of the desired crystalline heterostructure. The grazing incidence in-plane XRD patterns (Figure 8.2C) contain reflections from the d-spacing of atomic planes perpendicular to the substrate. Samples 2A, 2B, and 3B contain only broad, low-intensity reflections from diffuse scattering or very small crystallites. Sample 3A contains one set of low intensity reflections near the expected positions for a hexagonal unit cell with a d-spacing of ~3.3 Å, as expected for $MoSe_2$ (the reflections near 30° and 55° 2θ). The other two low-intensity reflections (near 25° and 45° 2θ) can be indexed to a hexagonal unit cell with a d-spacing of ~4 Å, which is near the expected a-axis lattice parameter for the wurtzite form of bulk ZnSe. Samples 2C and 3C both have a set of more intense reflections in the expected positions for 111 and 220 reflections for the cubic form of bulk ZnSe (~27° and 45° 2θ, respectively), as well as a low-intensity reflection near the expected position for the 113 reflection (~53° 2θ).[30–36] As- deposited data suggest that sample 3A has the highest probability of heterostructure formation; therefore, it was selected for a stepwise annealing study to monitor structural evolution as a function of temperature.
XRF, XRR, and XRD data were collected after each annealing step. The XRF data show that the number of Zn and Mo atoms/$Å^2$ remain constant within error throughout the study and the number of Se atoms/$Å^2$ decreases with annealing. A graph of the change in the total Se/metal ratio as a function of annealing is shown in Figure 8.3. The total Se/metal ratio starts to decrease after annealing at 250 °C and reaches a ratio of 1.5 after annealing at 300 °C, which is the expected ratio for a heterostructure consisting of $MoSe_2$ and ZnSe. After annealing at 400 °C the ratio drops below 1.5.

XRR and XRD data collected on sample 3A after each of a series of annealing steps are shown in Figure 8.4. The XRR patterns contain a mixture of Kiessig and Laue oscillations. There is no discernible phase shift between Kiessig and Laue oscillations, making them

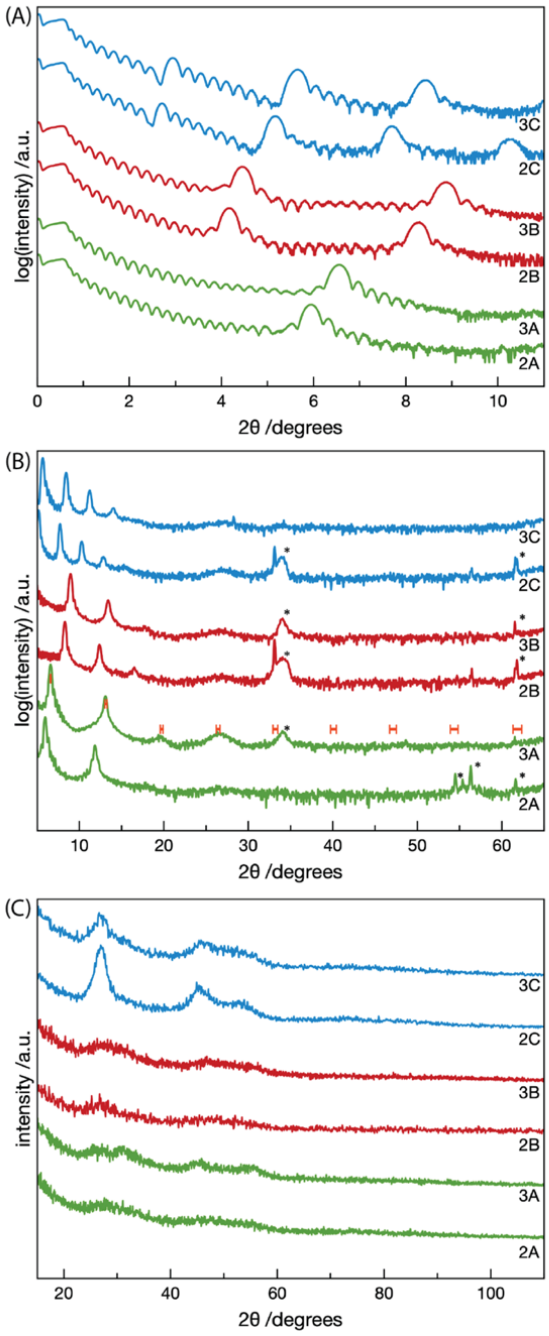

Figure 8.2. XRR and XRD patterns collected on all six precursors directly after deposition. Green patterns are for samples designed to grow an n=1 structure. Red patterns are for samples designed to grow an n=2 structure. Blue patterns are for samples designed to grow an n=4 structure. (A) X-ray reflectivity patterns contain Kiessig oscillations and Bragg reflections from the average d-spacing of the deposited elemental layering sequence. (B) Specular XRD patterns contain sharp Bragg reflections from elemental layering and broad, low-intensity reflections from small crystallites and/or diffuse scattering. (C) In-plane XRD patterns contain broad, low-intensity reflections from small grains of each individual constituent.

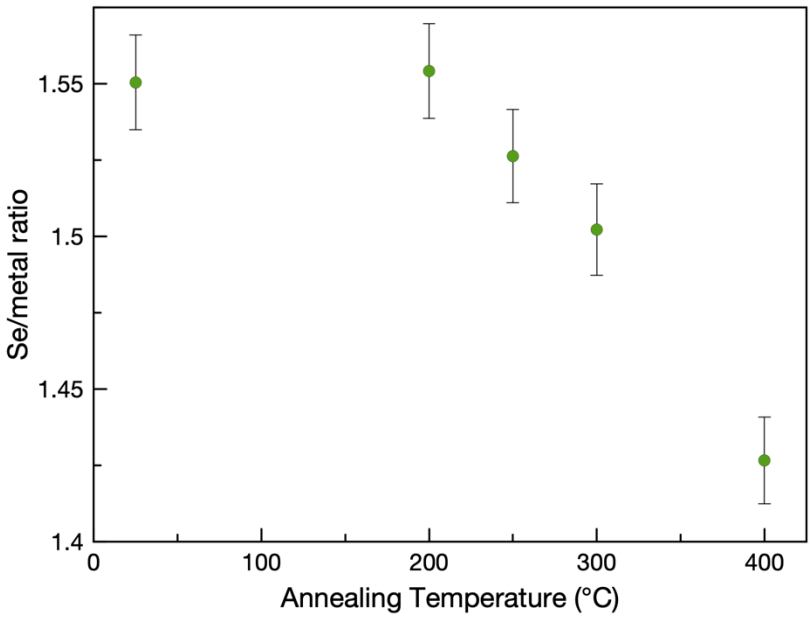

Figure 8.3. A graph showing the change in total Se/metal atoms ratio as a function of annealing temperature, using the numbers of atoms/Å^2 of each element calculated from XRF data collected after each annealing step.

indistinguishable. The oscillation periodicity can be used to calculate the total sample thickness using a version of Braggs law modified to include refraction. The calculated total sample thickness changes by < 2% until annealing at 400 °C when the total sample thickness decreases by ~20Å, coinciding with a sharp loss of Se from the sample as measured via XRF. The Bragg reflection shifts to higher angles after annealing at 200 °C, indicating crystallization of the heterostructure and a reduction in d-spacing from the initially mostly amorphous, elementally modulated structure. The Bragg reflection does not shift further at higher annealing temperatures. A set of 00l Bragg reflections in the specular XRD patterns increase in intensity until annealing at 400 °C when the intensities decrease slightly (Figure 8.4B). After annealing at 300 °C the reflections can be indexed to a unit cell with a c-axis lattice parameter of 13.29(2) Å. Using the method reported by Miller et al,[37] the periodicity of Laue oscillations extending from the 001 reflection after annealing at 300 °C can be modeled to determine the average number of coherently diffracting unit cells. As shown in Figure S8.1, the Laue oscillations indicate that there is an average of 22 unit cells in the coherently diffracting domain. The large 2θ range of Laue oscillations extending from the Bragg reflection indicate a very low deviation in this average number of coherently diffracting unit cells. The total thickness of the diffracting domain

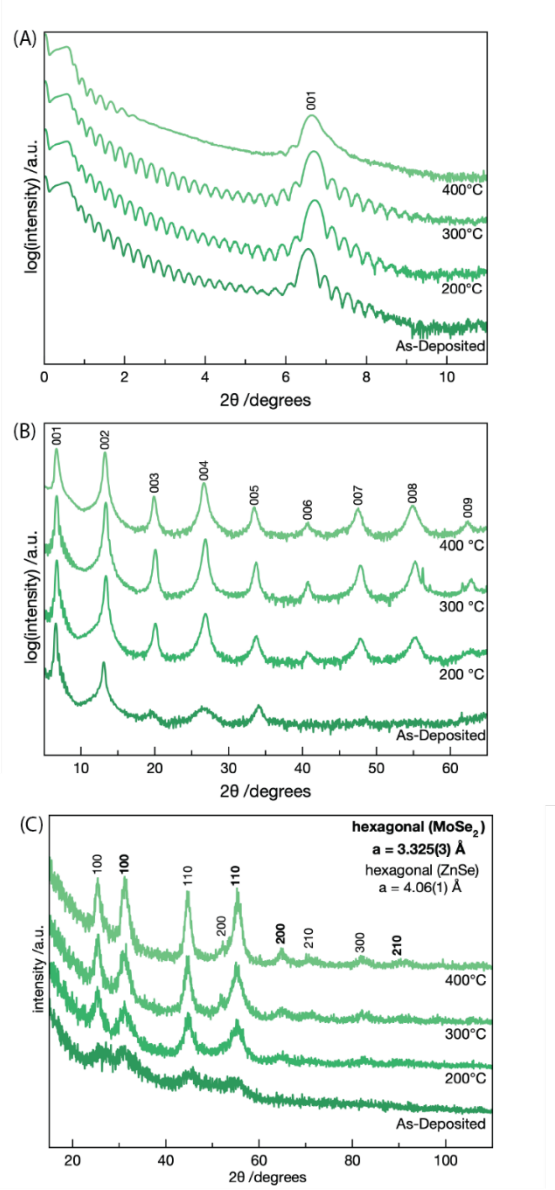

Figure 8.4. XRR and XRD data collected on sample 3A after each of a series of annealing steps. The annealing temperature is listed underneath the associated pattern. (A) XRR patterns contain Kiessig and Laue oscillations and the first order Bragg reflection from the d-spacing of the elemental layering (in the as-deposited pattern) that turns into the 001 Bragg reflection for the $(MoSe_2)_1(ZnSe)_1$ heterostructure that crystallizes after annealing. (B) The as-deposited specular XRD pattern contains Bragg reflections from both elemental layering (sharper reflections) and the crystalline heterostructure (broader reflections). The annealed specular XRD patterns contain 00*l* Bragg reflections from crystallographically aligned layers of the crystalline heterostructure. The indices for each reflection are listed above the associated reflection. (C) The grazing incidence in-plane XRD patterns contain two sets of reflections that can be indexed to hexagonal unit cells for the two individual constituents of the heterostructure ($MoSe_2$ and ZnSe). The indices used to calculate the *a*-axis lattice parameters for each constituent are shown above each associated reflection. The indices in bold text label the reflections from $MoSe_2$ and the indices in regular text label the reflections from ZnSe.

(calculated by multiplying the calculated unit cell c-axis lattice parameter by the number of unit cells) is 292.4(4) Å, which is ~40 Å less than the total sample thickness calculated from Laue oscillations. This thickness discrepancy indicates the presence of a secondary phase either above or below the crystalline heterostructure domains. The Laue oscillations present between the Bragg reflections become less well-resolved after annealing at 400 °C. The grazing incidence in-plane XRD patterns contain reflections that continuously increase in intensity as a function of annealing. Due to the rotational disorder between layers that is characteristic to MER samples, the reflections present in in-plane diffraction patterns can be used to calculate the lattice parameters in the a-b plane for each individual constituent in the heterostructure. The reflections present after annealing can be indexed to two hexagonal unit cells with different a-axis lattice parameters. The higher angle set of reflections can be indexed to a hexagonal unit cell with an a-axis lattice parameter of 3.325(3) Å, consistent with $MoSe_2$.[38] The indices for this set of reflections are shown in bold text above the associated reflections in Figure 8.4C. The lower angle set of reflections can be indexed to a hexagonal unit cell with an a-axis lattice parameter of 4.06(1) Å, which is slightly larger than the expected a-axis lattice parameter for the bulk-type hexagonal phase of ZnSe.[39,40] The indices for this set of reflections are shown in regular text above the associated reflections in Figure 8.4C. Both sets of reflections contain only hk0 reflections, indicating that both constituents grow with crystallographic alignment parallel to the substrate. The continuous increase in intensity for all present reflections as annealing temperature is increased indicates that crystalline grains continue to grow laterally even after growth perpendicular to the substrate has stopped.

Figure 8.5 contains high-angle annular dark-field scanning transmission electron microscopy (HAADF-STEM) images that were collected on a cross-sectional lamella of sample 3A after annealing at 300 °C for 30 minutes to further structurally characterize the heterostructure. Figure 8.5A shows the entire film thickness. $MoSe_2$ and ZnSe layers are readily distinguishable in HAADF-STEM images due to the Z-contrast, where the higher atomic number of Mo results in higher intensity, rendering $MoSe_2$ layers brighter than ZnSe layers. Additionally, the Se atoms in the $MoSe_2$ layer appear brighter than those in the ZnSe layer because they have twice the atomic density down the zone axis in $MoSe_2$ than in ZnSe. The silicon substrate is coated with a thin layer of amorphous native SiO_2, leading to structural disorder in the initial layers of the heterostructure before local interfacial interactions and topological constraints

promote the development of more ordered stacking further from the substrate. A secondary phase approximately 40 Å thick is evident at the surface of the film. The presence of this secondary phase is supported by the discrepancy between the thickness derived from the coherently diffracting domains that contribute to Laue oscillations, and the total film thickness determined from the periodicity of Kiessig fringes in the XRR pattern. Figure 8.5A shows ~22 unit cells of the $(MoSe_2)_1(ZnSe)_1$ heterostructure, also in agreement with the derived size of the coherently diffracting domain determined via Laue oscillation modeling mentioned in the previous paragraph. Figure 8.5C shows an elemental line profile of a portion of the sample. The elemental intensities graphed in Figure 8.5C are plotted as a function of distance perpendicular to the substrate. The elemental line profile shows Se-Mo-Se layers alternating with what appears to be a Se-Zn-Zn-Se layer. Only some Zn peaks have a high enough resolution to show a distinct split peak that corresponds to a Zn double layer, so further investigation was required for accurate structural characterization of the ZnSe layer.

To determine if the HAADF-STEM and STEM-EDS data is representative of the entire sample and to confirm atomic positions, a one-dimensional Rietveld refinement was performed using a model created from the approximate atomic plane positions determined from the HAADF-STEM and STEM-EDS data. As shown in Figure 8.5D, the refinement provides a reasonable fit to the experimental specular XRD pattern, even when plotted on a logarithmic scale. The atomic spacings gleaned from the Rietveld refinement are shown in Figure 8.5D. The refinement confirmed that there is a Zn double layer and that the Zn and Se atoms are in nearly the same plane.

Figure 8.5B shows a higher magnification HAADF-STEM image with atomic resolution. This image better shows the bonding arrangement of atoms and provides information about each unit cell that is not present in the diffraction data. The rotational disorder between layers gives rise to the presence of multiple zone axes from each individual constituent. The classic 110 zone axis for hexagonal $MoSe_2$ is readily apparent, with the Se atoms on a diagonal across a single plane of Mo atoms. The XRF data showing a 1:1 Zn:Se ratio, the a-axis lattice parameter calculated from in-plane diffraction data, the atomic positions obtained through Rietveld refinement, and the HAADF-STEM image are collectively used to determine the ZnSe unit cell type and identify the corresponding zone axes. All of this data together indicates that the ZnSe monolayer adopts a P-3m1 space group when confined between the van der Waals surfaces of

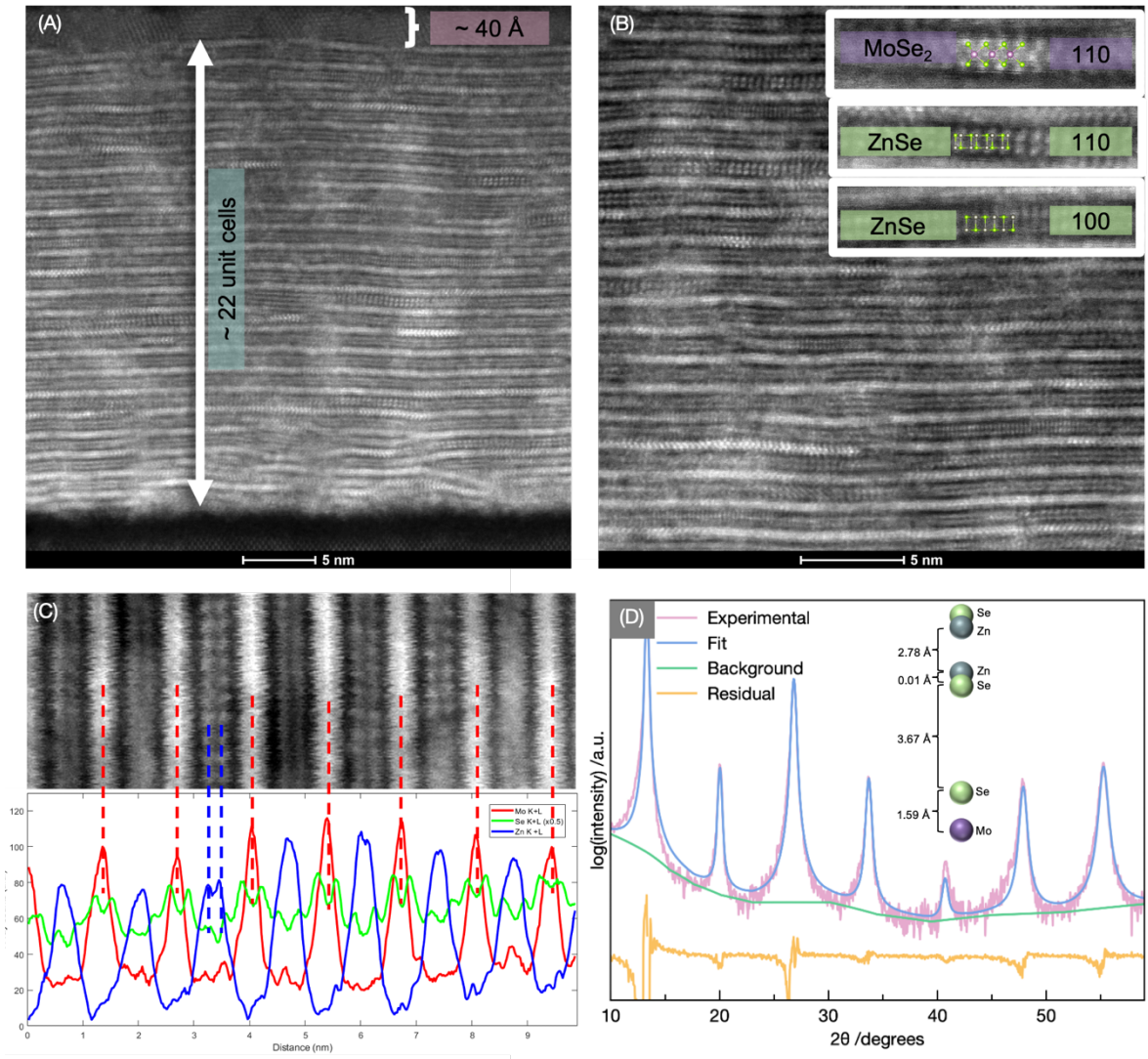

Figure 8.5. HAADF-STEM images and STEM-EDS data collected on sample 3A after annealing at 300 °C for 30 minutes. (A) The entire film thickness, showing approximately 22 unit cells of $(MoSe_2)_1(ZnSe)_1$ and approximately 30 Å of a secondary phase on the top of the film. (B) A slightly higher magnification image contains zone axis from layers of $MoSe_2$ and ZnSe with interlayer rotational disorder.

adjacent $MoSe_2$ layers. The 100 and 110 zone axes for this unit cell type are seen throughout the HAADF-STEM image, shown in Figure 8.5B. In this unique ZnSe phase all atoms are tetrahedrally coordinated and there is hexagonal coordination in the a-b plane and rectangular coordination in the c-axis direction, perpendicular to the substrate.

After determining the ideal annealing conditions from the annealing study of sample 3A, the remaining precursors were annealed under the same conditions to investigate how precursor nanoarchitecture and composition affects heterostructure formation and the final structure of each constituent. Figure 8.6 shows XRR and XRD data collected after annealing all samples at

300 °C for 30 minutes. Figures 8.6A and 8.6B show the data for both samples targeted to grow the n = 1 heterostructure. XRR data (Figure 8.6A) indicate a slight reduction in surface roughness of sample 3A after annealing (green patterns), evidenced by the extension of Kiessig fringes to higher 2θ; and that the d-spacing from the low angle Bragg reflections decreases slightly, as shown by a slightly shift to higher angle of the Bragg reflection. In contrast, the XRR data for sample 2A (purple patterns) indicate a significant increase in surface roughness, evidenced by the disappearance of Kiessig fringes down to ~2° 2θ; and that the elemental layers completely mix after annealing, indicated by the disappearance of the Bragg reflection. The specular XRD data (Figure 8.6B) show that the n = 1 heterostructure forms in sample 3A, but sample 2A decomposes into the two binary compounds, ZnSe and $MoSe_2$. Figures 8.6C and 8.6D show the data for both samples targeted to grow the n = 2 heterostructure. XRR data (Figure 8.6C) show that in both samples, the d-spacing of the elemental layering increases after annealing, with all Bragg reflections shifting to slightly lower angles. Both samples maintain their surface smoothness after annealing, although sample 3B (orange patterns) gets slightly smoother. Specular XRD data indicate that the n = 2 heterostructure does not form throughout the sample, although regions of the sample may contain the crystalline heterostructure. The increased intensity of the 111 reflection for cubic ZnSe apparent near 27° 2θ indicates a slight increase in the size and number of ZnSe grains growing outside of any heterostructures regions that may be present. Figures 8.6E and 8.6F show the data for both samples targeted to grow the n = 4 heterostructure. The XRR and specular XRD data closely resemble those from the n = 2 samples, indicating an increase in elemental layering d-spacing, minimal (or no) heterostructure growth, and an increase in the size and number of cubic ZnSe grains.

Grazing incidence in-plane XRD data provide deeper insight into the lateral structural evolution with annealing of the samples (Figure 8.7). In all samples, the formation of hexagonal $MoSe_2$ is evident, with the strongest reflections corresponding to the 100 and 110 planes. For samples 2B, 2C, and 3C only $MoSe_2$ reflections can be indexed. The additional reflections in these three samples cannot be consistently indexed to either cubic or hexagonal unit cells, suggesting the presence of a disordered or mixed-phase ZnSe structure. This is consistent with previously reported polytypism of ZnSe.[41,42] The remaining reflections progressively approach the positions expected for a cubic unit cell with an *a*-axis lattice parameter of 5.67 Å – as expected for bulk cubic ZnSe[33,34] – with increasing *n*, indicating that mixed phase regions

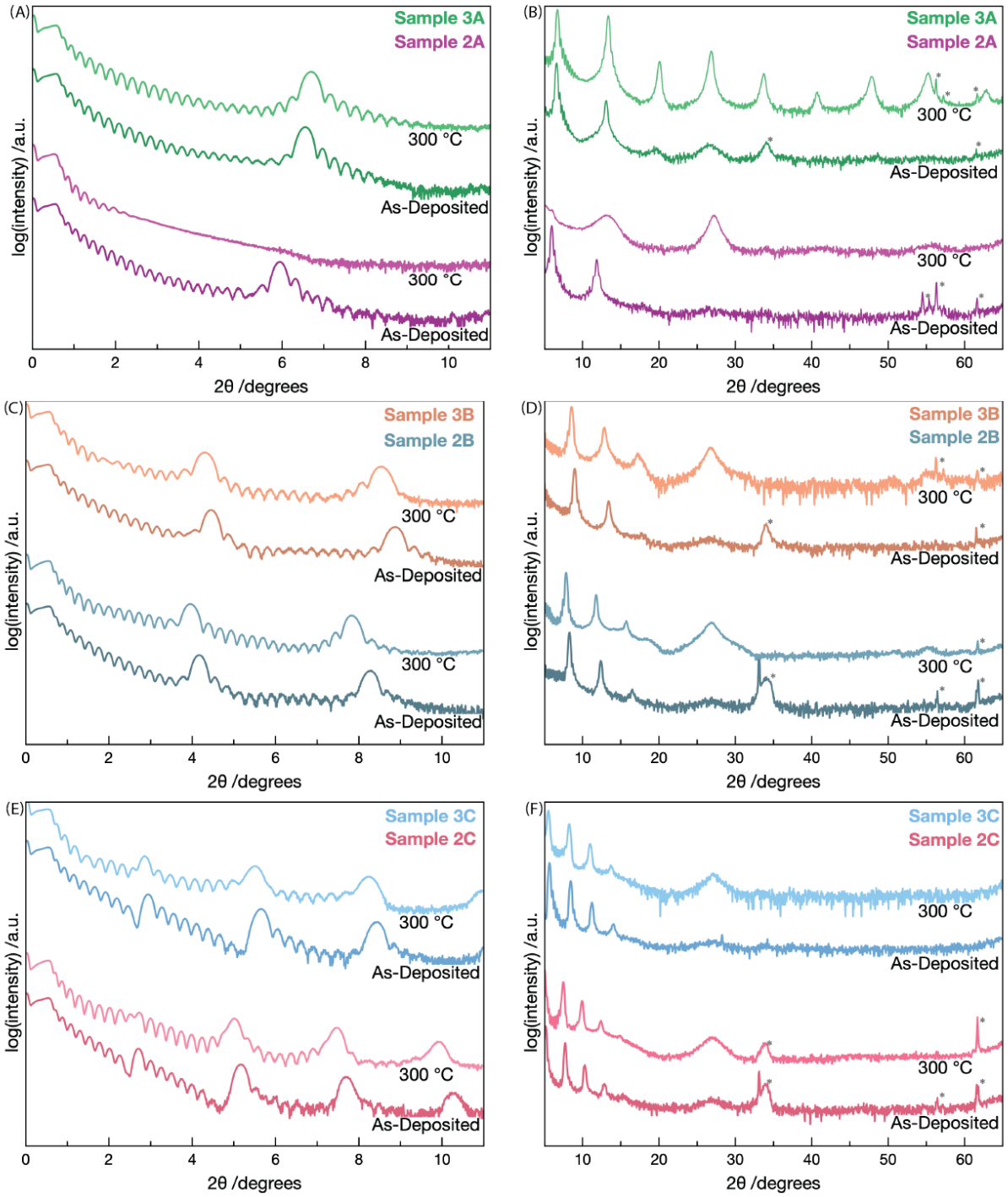

Figure 8.6. X-ray reflectivity (XRR) and specular x-ray diffraction (XRD) data collected directly after deposition (patterns labeled "As-deposited") and after annealing at 300 °C for 30 minutes (patterns labeled "300 °C") for all six samples studied herein. (A, B) XRR and specular XRD patterns for samples targeted to grow n = 1 heterostructures (2A, 3A). (C, D) XRR and specular XRD patterns for samples targeted to grow n = 2 heterostructures (2B, 3B). (E, F) XRR and specular XRD patterns for samples targeted to grow n = 4 heterostructures (2C, 3C). Asterisks mark substrate and stage reflections.

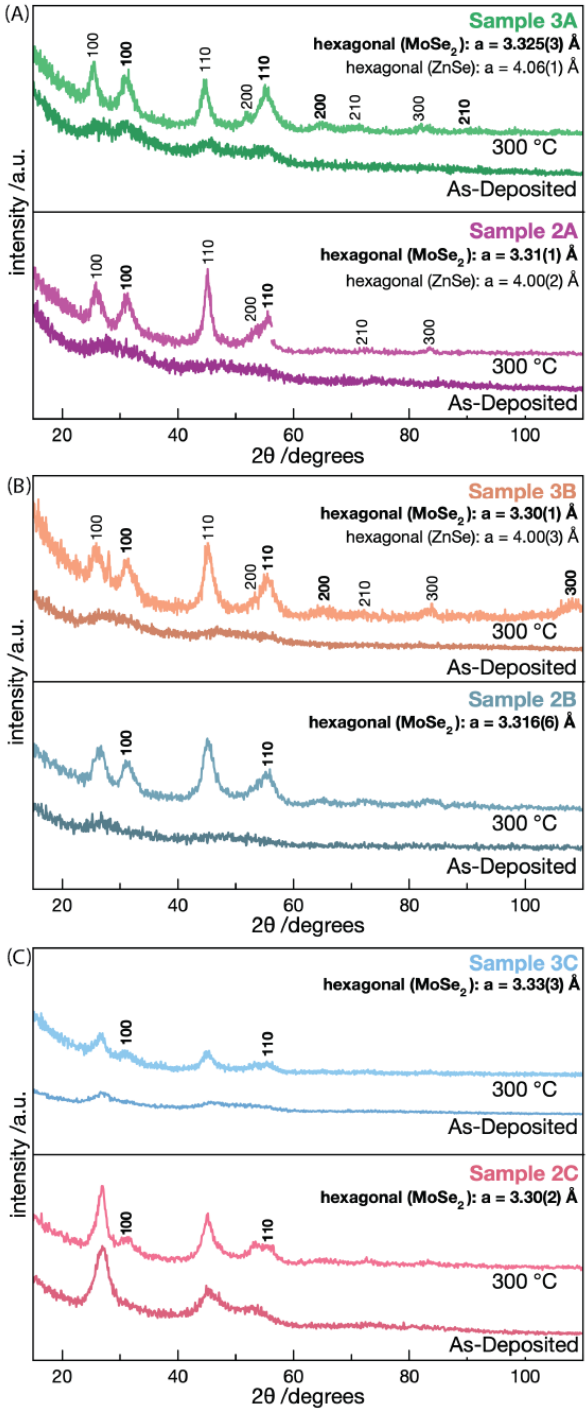

Figure 8.7. Grazing incidence in-plane x-ray diffraction patterns collected on all six samples directly after deposition (patterns labeled "As-deposited") and after annealing at 300 °C for 30 minutes (patterns labeled "300 °C"). The indices used to calculate *a*-axis lattice parameters are shown above each associated reflection. Indices for reflections associated with $MoSe_2$ are shown in bold text. Indices for reflections associated with ZnSe are shown in regular text. (A) Patterns for samples targeted to grow the n = 1 heterostructure (2A, 3A). (B) Patterns for samples targeted to grow the n = 2 heterostructure (2B, 3B). (C) Patterns for samples targeted to grow the n = 4 heterostructure (2C, 3C).

decrease and bulk growth behavior is approached as the ZnSe layer gets thicker. In contrast, the non-$MoSe_2$ reflections observed in samples 2A, 3A, and 3B can be indexed to a hexagonal lattice with an *a*-axis lattice parameter of ~4Å, as expected for the wurtzite form of bulk ZnSe.[40] Interestingly, this hexagonal character persists in 3B but is not evident in 2B, suggesting that the phase that nucleates is highly sensitive to a combination of local composition, local strain, and interface-induced distortion. Notably, the reflections indexed to $MoSe_2$ in the n = 4 samples are significantly lower in intensity, indicating that the lateral domain size of $MoSe_2$ grains in these samples are significantly reduced; potentially due to interference from larger ZnSe grains that disrupt coherent in-plane growth of $MoSe_2$ grains.

8.3. Conclusions

These results reveal that heterostructure formation in the MoZnSe system is governed by a delicate interplay between local composition, elemental layer thickness, and phase stability; and that when confined to a monolayer between van der Waals planes, ZnSe adopts a previously unreported phase. In the set 2 samples (2A, 2B, and 2C), the absence of sufficient Mo to form layers of $MoSe_2$ allows binary ZnSe to nucleate and grow uncontrollably through the elemental layering, disrupting heterostructure formation. As ZnSe layers grow thicker in these samples (increasing *n*), the reflections in the XRD patterns progressively evolve toward those of a bulk-like cubic phase, indicating reduced structural distortion. In contrast, the set 3 samples (3A, 3B, and 3C) contain adequate Mo to support $MoSe_2$ formation, yet heterostructure growth still fails in samples 3B and 3C. Notably, only sample 3A – despite being slightly Zn-deficient – successfully yields the heterostructure. This suggests that precursors must fall within a narrow compositional and structural window to allow ZnSe to adopt the necessary phase to be stable at or near the monolayer limit, facilitating heterostructure formation. We propose that when the ZnSe layer is limited to a monolayer in thickness, it can adopt a distorted structure stabilized by confinement between the van der Waals planes of $MoSe_2$ layers. This confinement permits all Zn and Se atoms to achieve tetrahedral coordination while minimizing unfavorable interactions and completing coordination spheres. Once the ZnSe layer exceeds this monolayer thickness, as in samples 3B and 3C, the confinement effect is lost, leading to the formation of a disordered or mixed-phase ZnSe. This behavior aligns with ZnSe's well-known polytypism, which is highly sensitive to composition, local strain, and dimensionality.[41,42] These results suggest that even

materials that are typically unstable as monolayers can be stabilized at the monolayer limit through stabilizing confinement between van der Waals planes, potentially enabling the emergence of novel phases.

8.4. Bridge

This chapter describes how a novel phase of ZnSe can be stabilized via interfacial confinement in $(MoSe_2)_1(ZnSe)_n$ heterostructures. The following chapter summarizes the overall conclusions made from the work presented in this dissertation.

CHAPTER IX
Conclusions and Summary

9.0. Authorship Statement

This chapter was written for this work only with no intention of publishing elsewhere. I am the primary author of this chapter. David C. Johnson acted as my supervisor and assisted with editing.

9.1. Conclusions and Summary

The design and synthesis of new materials capable of supporting continued device miniaturization remain key challenges limiting technological advancement. This has led to a rapid expansion of 2D materials research, driven by the intrinsic low dimensionality of 2D materials which makes them ideal candidates for addressing the challenges of device miniaturization. New emergent properties are frequently observed when materials are reduced to the monolayer limit. One strategy to harness the emergent properties of 2D materials is to integrate them into heterostructures composed of constituents with desirable properties, enabling further control over the overall material properties. Additionally, interfacial interactions between stacked 2D layers may further modify the physical properties, making layer sequence design a powerful experimental parameter for tuning heterostructure behavior. However, controlling which phases nucleate and grow in these complex systems requires a detailed understanding of the early-stage mechanisms of solid-sate reactions – namely, diffusion and nucleation. Continued development of experimental probes to investigate these fundamental solid-state reaction mechanisms is essential for advancing our understanding of solid-state materials growth. These insights are essential for leveraging heterostructure design and experimentally tunable variables to enable the predictive synthesis of new materials with properties tailored for emerging technologies.

This dissertation highlights the power of the modulated elemental reactant (MER) method to grow novel heterostructures and utilize controllable experimental variables – especially local compositions and deposited layer sequence and thickness – to investigate solid state growth mechanisms. MER uses atomically thin elemental layers to minimize the typically

rate-limiting influence of diffusion in solid state reactions. The deposited layer sequences and thicknesses can be tuned to design precursors that mimic the nanoarchitecture of the desired crystalline product, allowing low-temperature annealing to promote the growth of the targeted phase(s). Because this method emphasizes kinetic control over thermodynamic equilibrium, it can favor the formation of novel, often metastable phases that sit in local energy minima in the 3D free energy landscape that are inaccessible to synthetic techniques lacking such precise control over precursor nanoarchitecture. In addition to deposited layer sequence, local composition is another experimental variable that is tunable in MER. Our implementation of x-ray fluorescence (XRF) technology enables precise quantification of the absolute number of atoms per unit area in each deposited sample. This facilitates the application of statistical process control methods to iteratively refine deposition parameters, ensuring that each repeating sequence contains the exact atomic areal density required to synthesize the targeted structure. Because of these experimentally tunable parameters, MER provides a platform to investigate solid-state reaction mechanisms with atomic-scale precision. It enables systematic probing of the early stages of nucleation and growth under kinetically constrained conditions, offering insights into how controllable variables can be used to influence phase selection and growth pathways.

This dissertation begins with an overview of the previous work that has been done to elucidate the fundamental mechanisms of diffusion and nucleation during solid-state growth, followed by an examination of how various synthetic techniques have been used to address these challenges. After introducing how to make samples using the MER method, I describe the characterization techniques – XRF, x-ray reflectivity, x-ray diffraction, high-angle annular dark-filed transmission electron microscopy, energy dispersive x-ray spectroscopy, and physical property measurements – that are used in conjunction with MER to characterize the resulting samples. These methods enable precise tracking of structural evolution as a function of annealing and were foundational to the conclusions drawn in later chapters. A novel general method for simultaneously measuring in-plane and cross-plane electronic transport properties is presented in Chapter 3, further demonstrating the versatility of MER by proving its lithographic compatibility. This compatibility is essential for enabling these challenging measurements, which will be critical for evaluating the potential technological applicability of new materials.

Chapters 4-6 detail the use of experimentally tunable parameters in the MER method as probes to isolate and investigate distinct aspects of solid-state growth, thereby advancing our

mechanistic understanding of these processes. The simple Pb-Se and Mo-Se systems serve as frameworks for these studies, with a particular emphasis on the Mo-Se system. This system was used to investigate the reaction pathways occurring during the MER deposition process, and how variations in deposited layer thickness and local compositions can be used to influence these reaction pathways and the resulting thin-film structures. These insights enabled the development of a novel generalizable method for synthesizing high-energy amorphous precursors, even in systems that typically nucleate and grow the thermodynamically stable binary phases during deposition. Additionally, I used the Mo-Se system to better understand nucleation barriers and how high nucleation barriers can be leveraged to access non-equilibrium structures. These experiments emphasize that the reaction pathway can, in some cases, influence or even determine the final product obtained in solid-state synthesis.

Chapters 7 and 8 describe the synthesis and characterization of novel heterostructures, made possible by applying the knowledge gained from the studies detailed in the preceding chapters. The $(PbSe)_1(VSe_2)_1(PbSe)_m(VSe_2)_1$ heterostructure exemplifies a novel material whose synthesis is made possible by the layer sequence control unique to MER. This structure highlights the importance of sequence tailoring, as it enables precise tuning of material properties. In Chapter 8, I show that a novel phase of ZnSe can be grow by interfacial stabilization in a $(MoSe_1)(ZnSe)_1$ heterostructure. This study demonstrates that the formation of certain new materials can be highly sensitive to local composition, underscoring the value of the MER method for its precise control over compositional tuning. The novel structures presented here demonstrate the value of MER's experimentally tunable parameters – layer sequence and local composition – in stabilizing new phases and enabling synthesis at the monolayer limit, an essential step toward uncovering emergent properties with potential technological relevance.

Collectively, these studies provide a coherent picture of how kinetic control through rational precursor design enables the discovery and stabilization of novel phases and offers an experimental route to studying the mechanisms of solid-state nucleation. While no unified atomic-level model yet exists for early-stage solid-state reactions, this work shows that carefully designed experiments using MER can provide critical insights that bring us closer to that goal. Ultimately, this dissertation advances the vision of predictive synthesis by demonstrating how heterostructure design and experimentally tunable parameters can be harnessed to realize computationally predicted materials and to access new regions of phase space. The findings

presented here not only deepen our understanding of solid-state reactions, but also offer broadly applicable strategies for designing and synthesizing the next generation of functional materials.

APPENDIX A

Supporting Information for

Chapter III

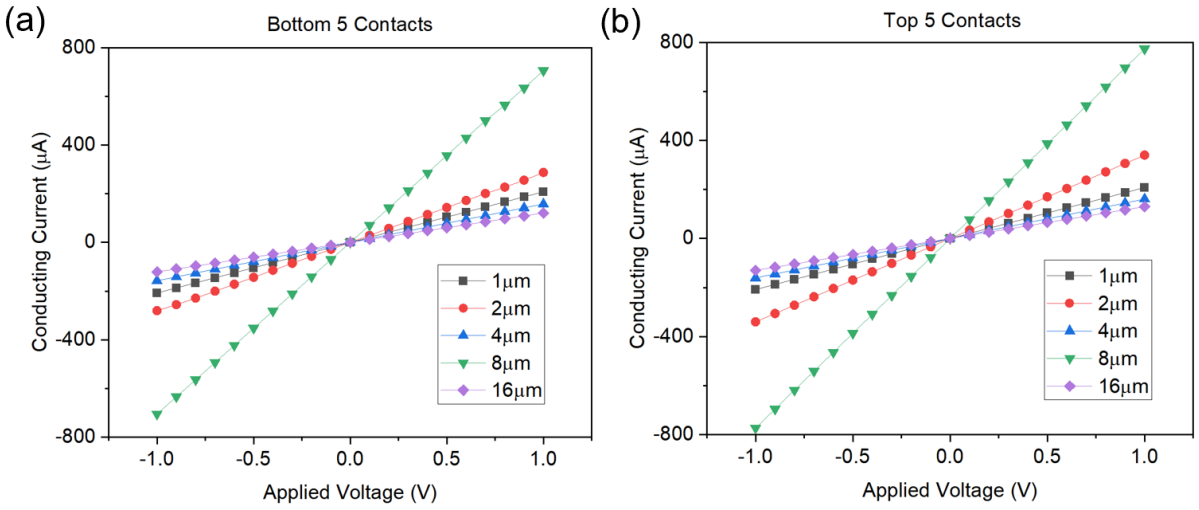

Figure A.1. 2-probe measurements from current injection leads to all the ten contacts are plotted, suggesting high quality Ohmic contacts are formed at the interfaces.

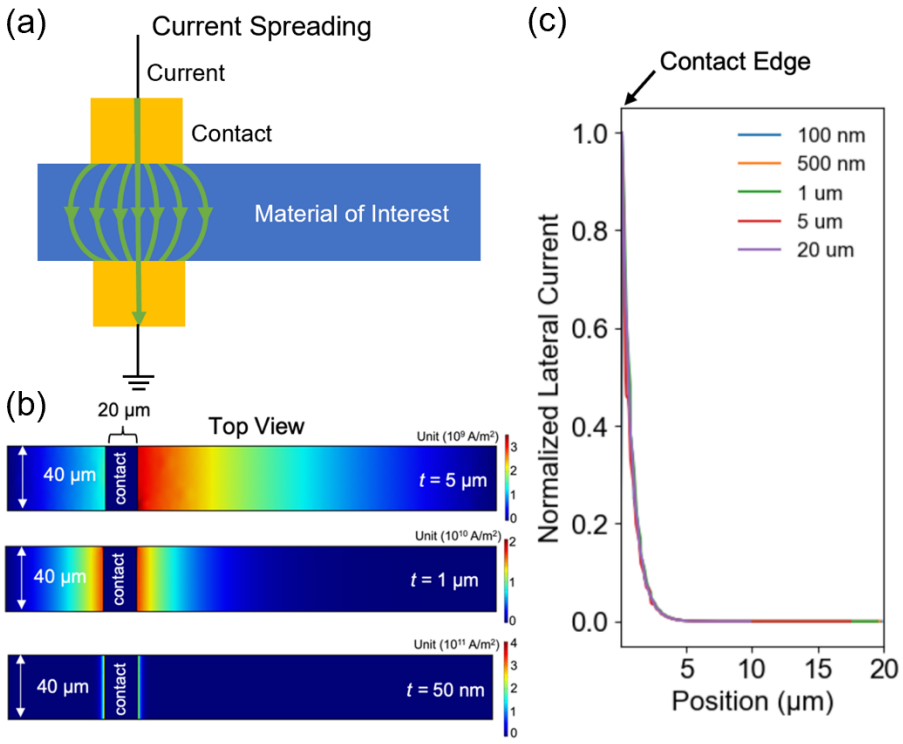

Figure A.2. (a) Schematic diagram illustrating the phenomenon of current spreading (i.e., current flowing in the out-of-plane direction during the cross-plane resistance measurement). (b) Simulated lateral current mapping for different sample thicknesses from 5 μm to 50 nm. (c) Simulated normalized lateral current plotted as a function of distance from the edge of the contact with sample thickness of 30 nm, plotted here for of contacts with various linewidths from 20 μm to 100 nm.

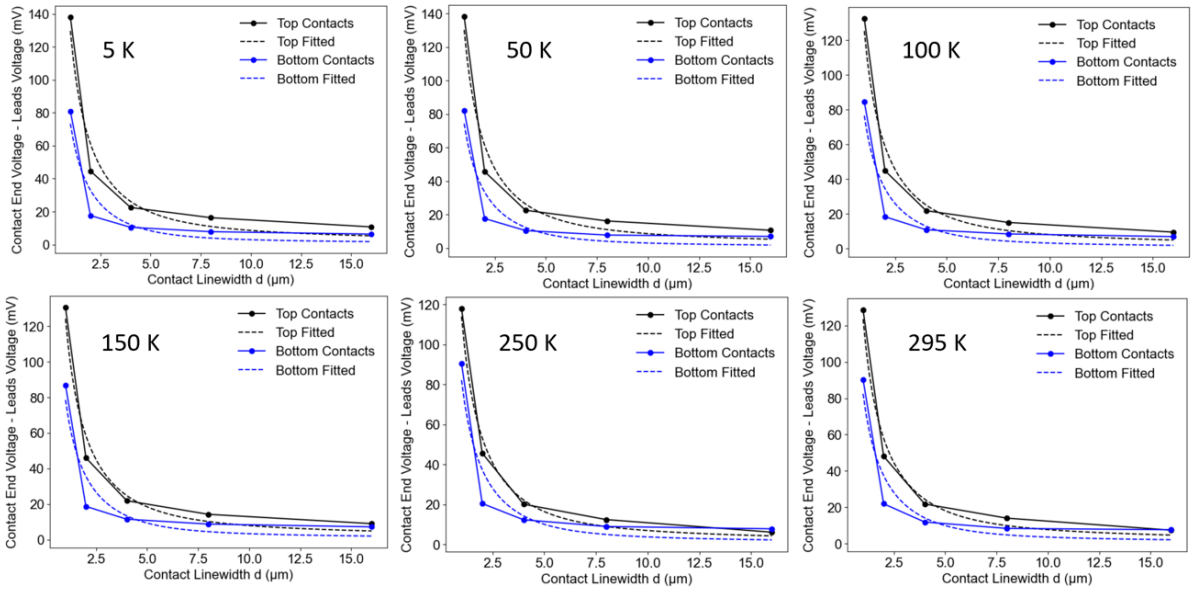

Figure A.3. The contact end voltages of top and bottom electrodes measured at different temperatures.

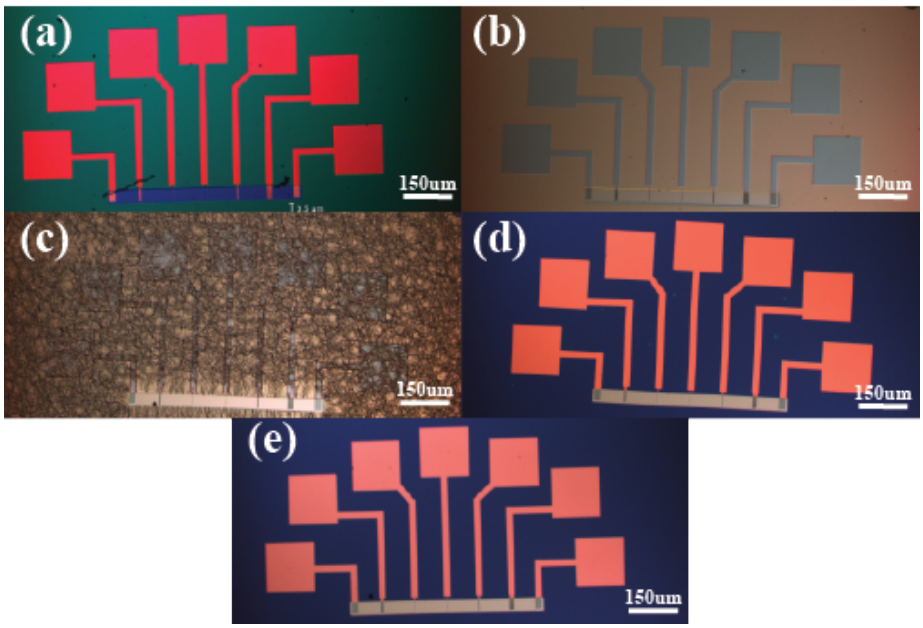

Figure A.4. Optical imaging of the device preparation steps (a) bottom contacts before depositing the film, (b) after deposition, (c) after the first annealing step, (d) after lift-off, and (e) after the final annealing step.

The David C. Johnson lab has studied a variety of VSe_2-containing heterostructures due to the presence of charge density wave (CDW) behavior. When decreased to a monolayer, this CDW behavior is increased substantially.[1] The group has also observed that the onset temperature of the CDW can be systematically shifted to higher temperatures by increasing *m* in a $(SnSe)_m(VSe_2)_1$ heterostructure.[2] Interestingly, when this same experiment was repeated with a $(PbSe)_m(VSe_2)_1$ heterostructure, there didn't appear to be a relationship between *m* and the CDW onset temperature, indicating that the identity of the spacer layer has a more significant effect on the CDW than the thickness of this layer.[3]

The process for fabrication of the bottom contacts and top contacts is described in the methods section. $(PbSe)_1(VSe_2)_1$ was synthesized using the modulated elemental reactants (MER) technique in a custom-built ultrahigh vacuum chamber. The precursor was prepared by evaporating elemental sources onto the prepared device using an electron beam gun in the sequence V|Se|Pb|Se for a total of 22 layers, ending with an additional V|Se sequence, as shown in Figure A.4(b). A precursor film was also simultaneously deposited on a Si wafer for film characterization. The film was then pre-annealed at 110ºC for 5 minutes in a nitrogen atmosphere to begin crystallization, Figure A.4(c). The photoresist was then lifted off using an acetone bath,

leaving the film on the desired electrical contact areas, Figure A.4(d). The final annealing step was done in a nitrogen atmosphere at 300ºC for 1 hour, Figure A.4(e).

Table A.1. Thickness and lattice parameter values for sample in Figure 3.1 c, d.

Thickness (Å)	*c*-lattice (Å) (superlattice)	PbSe *a*-lattice (Å)	VSe_2 *a*-lattice (Å)
270.5(9)	12.26(1)	6.14(1)	3.38(2)

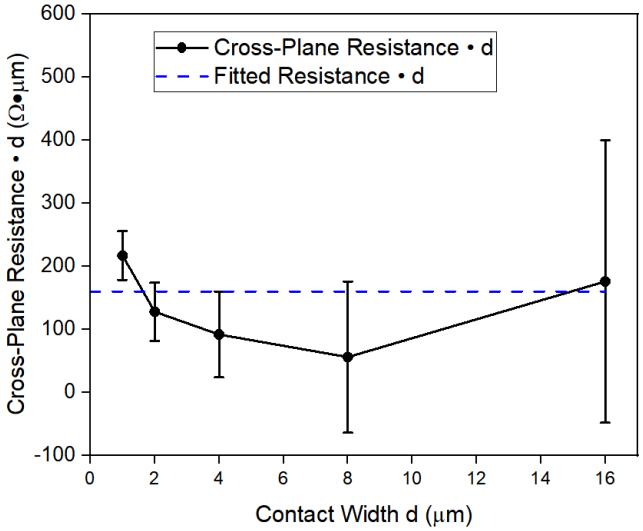

Figure A.5. Plot of cross-plane resistance times contact width d versus d, blue dash line shows the fitted value. The large error bar for the 16 μm reflects the small difference between the total cross plane resistance and the sum of the contact and interface resistances. The error bar for the widths results from potential residual sidewall photoresist and potential misalignments between the top and bottom contacts. This width error has the largest impact on the thinnest contact width.

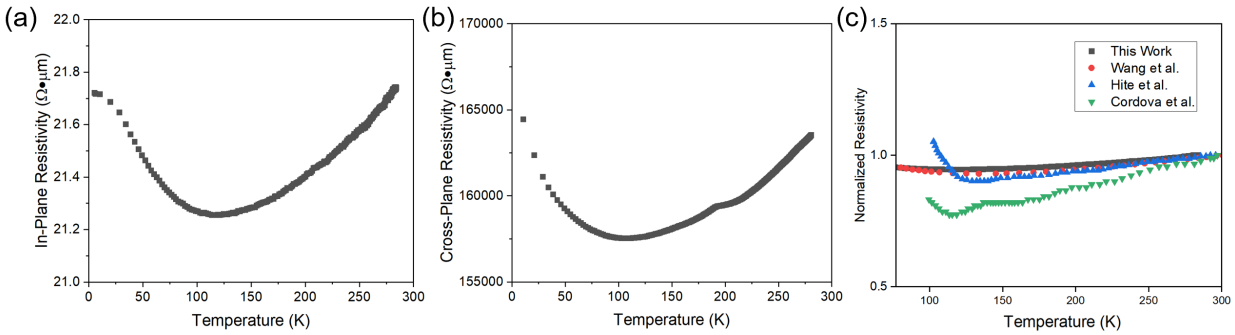

Figure A.6. (a) In-plane and (b) cross-plane resistivity of the $(PbSe)_1(VSe_2)_1$ material, which show minimum resistivities at around 100 K. This indicates that the charge density wave transition is also observed in the cross-plane transport of $(PbSe)_1(VSe_2)_1$ heterostructure. (c) Temperature-dependent room temperature normalized resistivity of (PbSe)1(VSe2)1 from this investigation compared with prior published results. The magnitude of the resistivity and the depth of the resistivity minimum sensitively depends on the carrier concentration which varies with the stoichiometry of the sample.

APPENDIX B

Supporting Information for Chapter IV

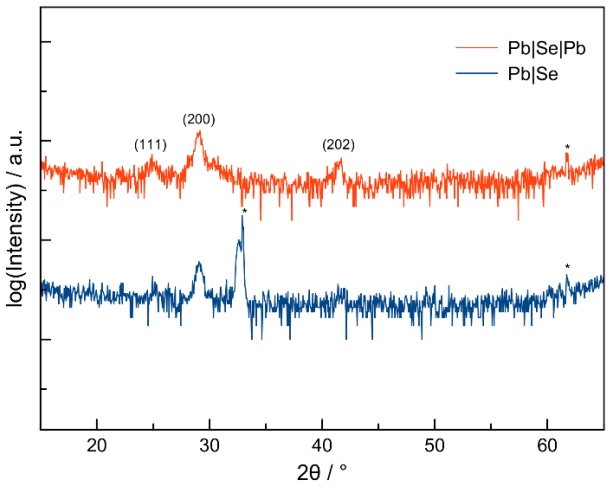

Figure B.1. Specular XRD of as-deposited Pb|Se|Pb and Pb|Se precursors, where labeled indices are applicable to both patterns and correspond to PbSe (Fm3m).

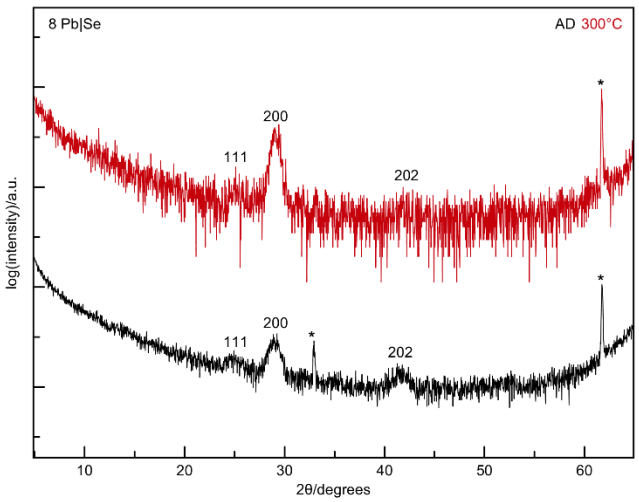

Figure B.2. Specular XRD pattern of the 8 Pb|Se sample as-deposited (black) and annealed to 300°C. Labeled indices are consistent with a PbSe (Fm3m). Reflections marked with an asterisk are from the substrate.

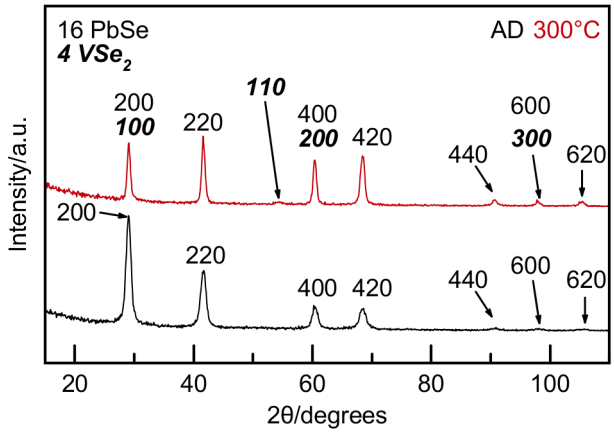

Figure B.3. In-plane XRD pattern of the 16 Pb|Se on 4 V|Se sample as-deposited (black) and annealed to 300°C. Labeled indices are consistent with a PbSe (Fm3m) or hexagonal VSe_2 unit cell. Only PbSe reflections are present in the as-deposited sample, which is consistent with specular XRD.

Table B.1. Total experimental atoms/Å^2 after annealing to 400°C were determined via X-ray fluorescence, where Se also includes the amount used in Mo|Se layers. The number of PbSe layers was calculated using the total Pb atoms/Å^2, where 0.1065 atoms/Å^2 are needed to form one bilayer of PbSe. The number of $MoSe_2$ layers possible was calculated using the remaining Se available after 0.1065 atoms/Å^2 of Se per PbSe is used, and assuming 0.2135 atoms/Å^2 is needed to form a trilayer of $MoSe_2$.

Substrate	Precursor structure	Total Experimental Atoms/Å^2 after annealing			# PbSe layers possible	# $MoSe_2$ layers possible
		Pb	Se	Mo		
8 repeating units Mo|Se	128 Pb|Se	12.38(2)	13.0(3)	0.82(1)	116	3
	64 Pb|Se	6.16(3)	7.6(5)	0.83(1)	58	6
	32 Pb|Se	3.12(7)	4.8(8)	0.83(1)	29	7
	16 Pb|Se	1.6(1)	3.3(1)	0.83(1)	15	7
	8 Pb|Se	0.8(3)	2.4(1)	0.82(1)	7	7

APPENDIX C

Supporting Information for Chapter V

Table C.1. Deposition parameters and resulting composition and structural information for each of the 20 as-deposited Mo-Se samples used to create Figure 5.1 in the text.

Sample #	# of as-deposited (AD) repeat units (RU)	Atoms/Å^2*RU		Atoms/Å^2		Total AD Thickness (Å)	Thickness of deposited Mo|Se repeating bilayer (Å)	% of $MoSe_2$ monolayer in each RU			Presence of Bragg reflections in AD specular and in-plane XRD
		Mo	Se	Mo	Se			Mo	Se	Se/Mo ratio	
1	400	0.0081(6)	0.045(1)	3.2(2)	17.9(4)	538.0(3)	-	7.7(5)%	21.2(6)%	5.5(4)	No
2	400	0.0098(7)	0.046(1)	3.9(3)	18.2(4)	558.7(2)	-	9.3(7)%	21.6(6)%	4.7(4)	No
3	400	0.0100(7)	0.034(1)	4.0(3)	13.5(4)	418.8(6)	-	9.5(7)%	16.1(5)%	3.4(3)	No
4	400	0.0100(7)	0.041(1)	4.0(3)	16.3(4)	503.6(2)	-	9.5(7)%	19.4(6)%	4.1(3)	No
5	400	0.0105(7)	0.0278(8)	4.2(3)	11.1(3)	343.4(3)	-	9.9(7)%	13.2(4)%	2.7(2)	Yes
6	90	0.051(4)	0.173(5)	4.6(4)	15.6(5)	490.6(6)	-	48(3)%	82(2)%	3.4(3)	Yes
7	90	0.051(4)	0.163(5)	4.6(4)	14.6(4)	473.4(3)	-	49(3)%	77(2)%	3.2(3)	Yes
8	92	0.065(5)	0.123(4)	6.0(5)	11.3(4)	361.3(6)	-	62(4)%	58(2)%	1.9(2)	Yes
9	90	0.078(5)	0.151(5)	7.0(4)	13.6(4)	438.1(1)	-	74(5)%	72(2)%	1.9(2)	Yes
10	80	0.078(5)	0.161(5)	6.2(4)	12.9(4)	410.0(2)	-	74(5)%	76(2)%	2.1(2)	Yes
11	90	0.078(5)	0.158(5)	7.0(4)	14.2(4)	465.2(3)	-	74(5)%	75(2)%	2.0(2)	Yes
12	90	0.083(6)	0.145(4)	7.5(5)	13.1(4)	428(1)	-	79(6)%	69(2)%	1.8(1)	Yes
13	46	0.094(7)	0.233(7)	4.3(3)	10.7(3)	335.3(3)	7.0(5)	89(6)%	110(3)%	2.5(2)	Yes
14	54	0.103(7)	0.223(7)	5.6(4)	12.0(4)	384.3(3)	-	98(7)%	106(3)%	2.2(2)	Yes
15	38	0.106(7)	0.228(7)	4.0(3)	8.7(3)	272.8(5)	-	100(7)%	108(3)%	2.2(2)	Yes
16	46	0.107(7)	0.224(7)	4.9(3)	10.3(3)	330.0(6)	6.7(5)	102(7)%	106(3)%	2.1(2)	Yes
17	46	0.128(9)	0.247(7)	5.9(4)	11.4(3)	371.1(6)	8.1(4)	121(8)%	117(4)%	1.9(2)	Yes
18	16	0.22(2)	0.49(1)	3.5(3)	7.8(2)	270.0(5)	16(1)	206(14)%	231(7)%	2.2(2)	Yes
19	10	0.36(3)	1.58(5)	3.6(3)	15.8(5)	488.7(7)	45(4)	344(24)%	748(22)%	4.3(3)	No
20	10	0.37(3)	1.05(3)	3.7(3)	10.5(3)	340.0(8)	32(2)	351(25)%	497(15)%	2.8(2)	No

Table C.2. Deposition parameters and resulting composition and structural information for each of the 6 as-deposited Pb-Se samples used to create Figure 5.11 in the text.

Sample #	# of as-deposited (AD) repeat units (RU)	Atoms/Å^2*RU		Atoms/Å^2		Total AD Thickness (Å)	% of PbSe monolayer in each RU			Presence of Bragg reflections in AD grazing incidence scan
		Pb	Se	Pb	Se		Pb	Se	Se/Pb ratio	
2A	450	0.0091(3)	0.148(4)	4.1(1)	66(2)	-	8.6%	138.6%	16.2	No
2B	160	0.032(1)	0.164(5)	5.2(2)	26.3(8)	-	30.3%	154.3%	5.1	No
2C	450	0.0113(3)	0.080(2)	5.1(2)	36(1)	-	10.6%	74.8%	7.1	No
4A	400	0.0111(3)	0.033(1)	4.4(1)	13.0(4)	506.2(4)	10.4%	30.6%	2.9	Yes
4B	300	0.0111(3)	0.0185(6)	3.3(1)	5.5(2)	259.4(6)	10.4%	17.3%	1.7	Yes
4C	150	0.040(1)	0.095(3)	6.1(2)	14.2(4)	642.3(9)	37.9%	89%	2.3	Yes

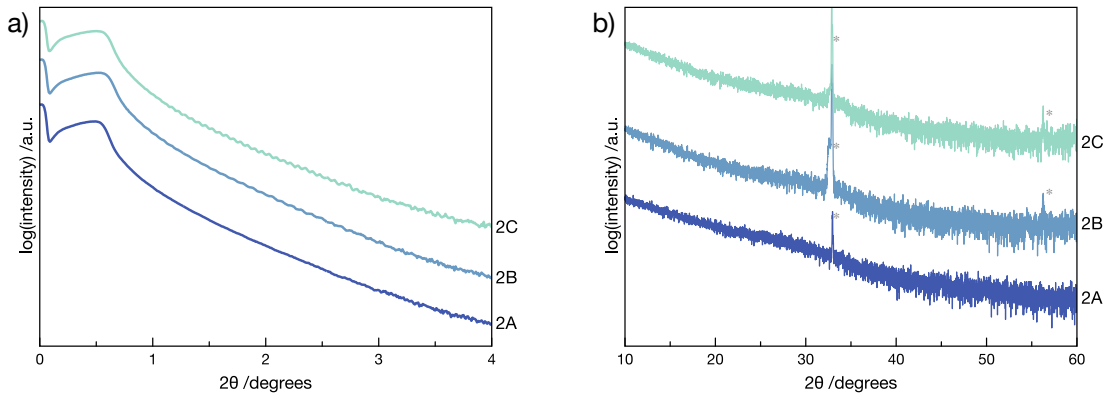

Figure C.1. XRR and specular XRD of Pb-Se samples that remain x-ray amorphous during the deposition process. a. XRR. b. specular XRD. Asterisks mark substrate and stage reflections.

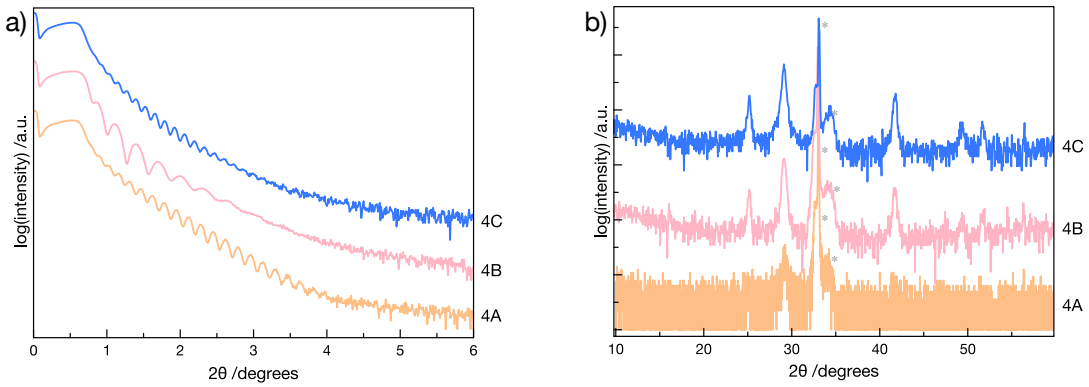

Figure C.2. XRR and specular XRD of Pb-Se samples that nucleate PbSe during the deposition process. a. XRR b. specular XRD. Asterisks mark substrate and stage reflections.

APPENDIX D

Supporting Information for Chapter VI

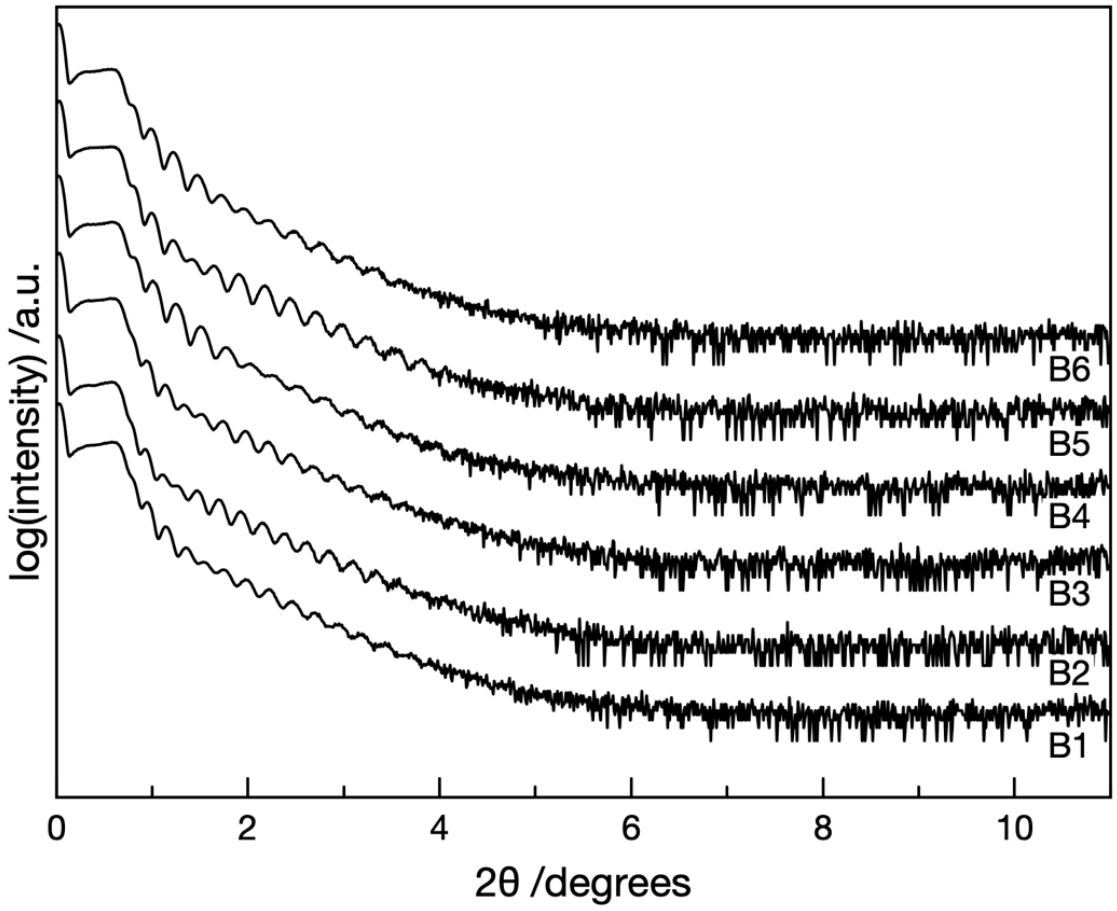

Figure D.1. X-ray reflectivity patterns for all 6 group B samples collected directly after deposition, before the samples were annealed. The sample ids are shown underneath each associated pattern.

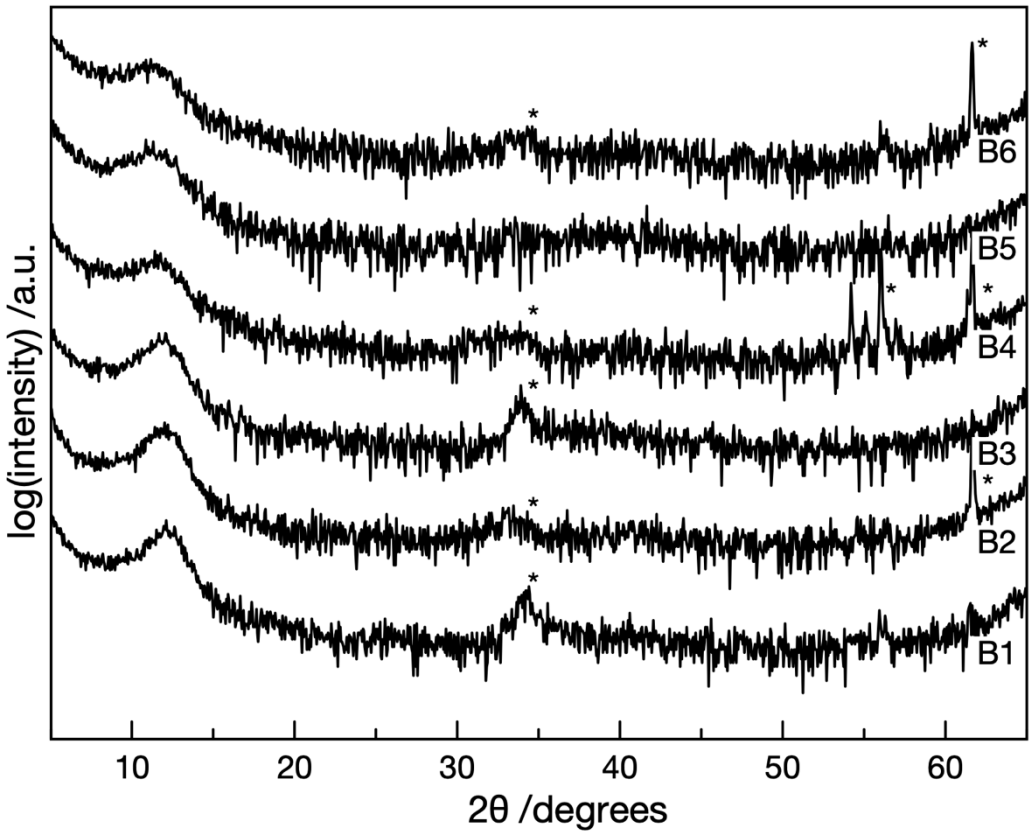

Figure D.2. Specular x-ray diffraction patterns collected directly after deposition, before the samples were annealed. The sample ids are shown underneath each associated pattern. Asterisks mark substrate and stage reflections.

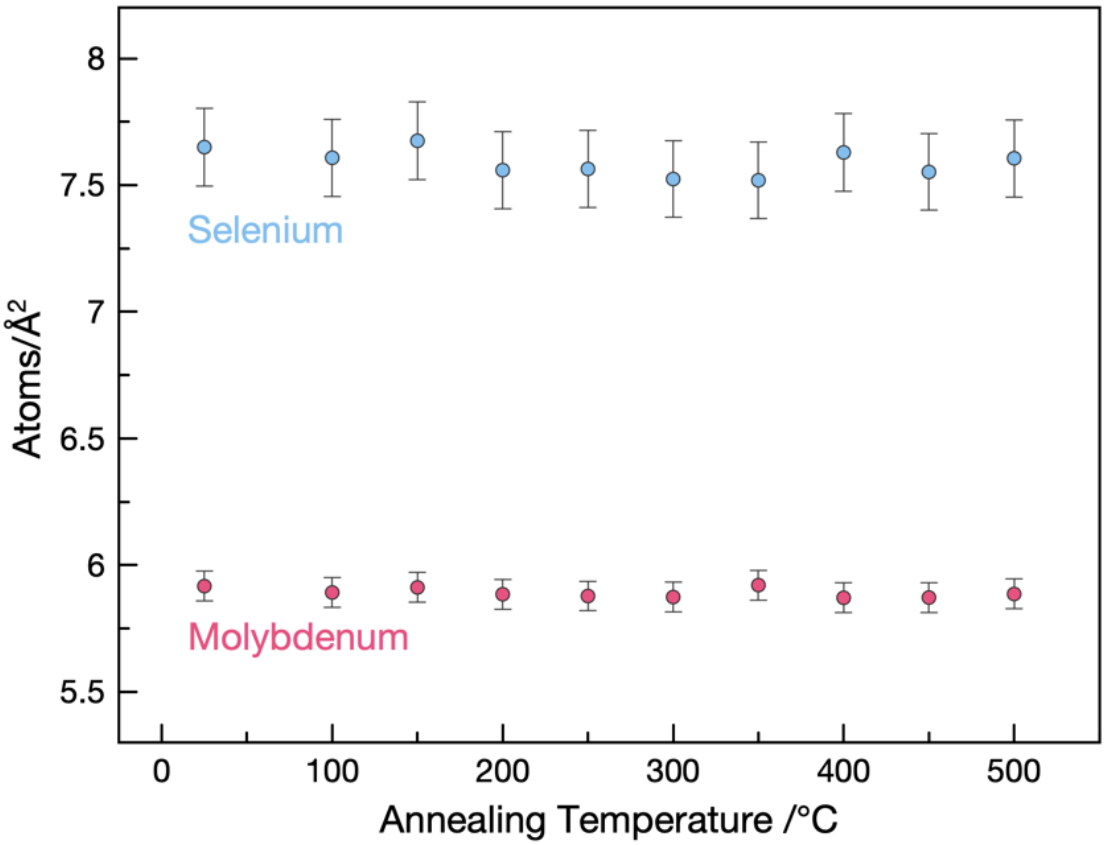

Figure D.3. Change in the number of atoms/Å^2 of Se (blue dots) and Mo (pink dots) in sample B5, as measured with x-ray fluorescence after annealing for 30 minutes at each temperature. The first point at 25 °C was collected immediately after deposition at room temperature.

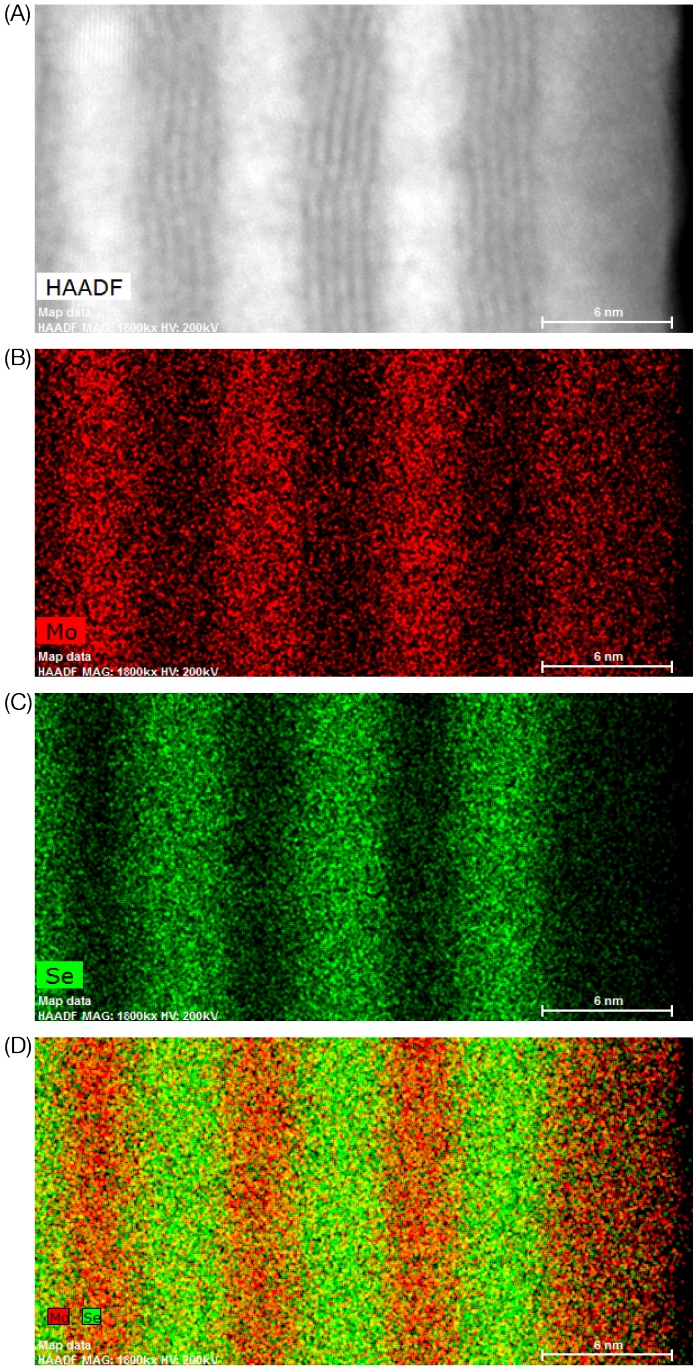

Figure D.4. Elemental maps generated from STEM-EDS spectral images of sample C3 after annealing at 550 °C for 30 minutes. (A) High-angle annular dark-field scanning transmission electron microscopy image of the sample region from which the elemental maps were generated. (B) Elemental map with signal from Mo shown in red. (C) Elemental map with signal from Se shown in green. (D) Elemental map with signals from both Mo (red) and Se (green) overlaid, showing alternating regions of higher density in either Mo or Se.

REFERENCES CITED

CHAPTER I

(1) Moore, G. E. Cramming More Components into Integrated Circuits. *Electronics* **1965**, *38* (8), 114–117. https://doi.org/10.1111/j.1467-9469.2011.00765.x.

(2) Zhang, G.; Cheng, Y.; Chou, J.-P.; Gali, A. Material Platforms for Defect Qubits and Single-Photon Emitters. *Appl. Phys. Rev.* **2020**, *7* (3), 031308. https://doi.org/10.1063/5.0006075.

(3) Kjaergaard, M.; Schwartz, M. E.; Braumüller, J.; Krantz, P.; Wang, J. I.-J.; Gustavsson, S.; Oliver, W. D. Superconducting Qubits: Current State of Play. *Annu. Rev. Condens. Matter Phys.* **2020**, *11* (1), 369–395. https://doi.org/10.1146/annurev-conmatphys-031119-050605.

(4) Goyal, R. K.; Maharaj, S.; Kumar, P.; Chandrasekhar, M. Exploring Quantum Materials and Applications: A Review. *J. Mater. Sci. Mater. Eng.* **2025**, *20* (1), 4. https://doi.org/10.1186/s40712-024-00202-7.

(5) Machín, A.; Morant, C.; Márquez, F. Advancements and Challenges in Solid-State Battery Technology: An In-Depth Review of Solid Electrolytes and Anode Innovations. *Batteries* **2024**, *10* (1), 29. https://doi.org/10.3390/batteries10010029.

(6) Janek, J.; Zeier, W. G. A Solid Future for Battery Development. *Nat. Energy* **2016**, *1* (9), 1–4. https://doi.org/10.1038/nenergy.2016.141.

(7) Lu, P.; Xia, Y.; Huang, Y.; Li, Z.; Wu, Y.; Wang, X.; Sun, G.; Shi, S.; Sha, Z.; Chen, L.; Li, H.; Wu, F. Wide-Temperature, Long-Cycling, and High-Loading Pyrite All-Solid-State Batteries Enabled by Argyrodite Thioarsenate Superionic Conductor. *Adv. Funct. Mater.* **2023**, *33* (8), 2211211. https://doi.org/10.1002/adfm.202211211.

(8) Niu, G.; Guo, X.; Wang, L. Review of Recent Progress in Chemical Stability of Perovskite Solar Cells. *J. Mater. Chem. A* **2015**, *3* (17), 8970–8980. https://doi.org/10.1039/C4TA04994B.

(9) Suresh Kumar, N.; Chandra Babu Naidu, K. A Review on Perovskite Solar Cells (PSCs), Materials and Applications. *J. Materiomics* **2021**, *7* (5), 940–956. https://doi.org/10.1016/j.jmat.2021.04.002.

(10) Pastuszak, J.; Węgierek, P. Photovoltaic Cell Generations and Current Research Directions for Their Development. *Materials* **2022**, *15* (16), 5542. https://doi.org/10.3390/ma15165542.

(11) Ozodakhon, A.; Joshi, A.; Saritha, G.; Alzubaidi, L. H.; Selvan, K. S.; Chaudhary, A. Novel Materials for High-Performance Energy Storage Devices. *E3S Web Conf.* **2024**, *540*, 11008. https://doi.org/10.1051/e3sconf/202454011008.

(12) Eswaramoorthy, N.; Nallusamy, S.; Selvaraj, Y.; Shyma, A. P.; Mandal, M.; Elangovan, V. MXenes and Their Composites for Energy Storage: Current Status and Future Perspectives. In *Materials for Boosting Energy Storage. Volume 1: Advances in Sustainable Energy Technologies*; ACS Symposium Series; American Chemical Society, 2024; Vol. 1477, pp 75–96. https://doi.org/10.1021/bk-2024-1477.ch004.

(13) Tien, T. N.; Vu, Q. K.; Duy, V. N.; Tien, T. N.; Vu, Q. K.; Duy, V. N. Novel Designs of Thermoelectric Generator for Automotive Waste Heat Recovery: A Review. *AIMS Energy* **2022**, *10* (4), 922–942. https://doi.org/10.3934/energy.2022042.

(14) Bu, Z.; Zhang, X.; Hu, Y.; Chen, Z.; Lin, S.; Li, W.; Xiao, C.; Pei, Y. A Record Thermoelectric Efficiency in Tellurium-Free Modules for Low-Grade Waste Heat Recovery. *Nat. Commun.* **2022**, *13* (1), 237. https://doi.org/10.1038/s41467-021-27916-y.

(15) Fitriani; Ovik, R.; Long, B. D.; Barma, M. C.; Riaz, M.; Sabri, M. F. M.; Said, S. M.; Saidur, R. A Review on Nanostructures of High-Temperature Thermoelectric Materials for Waste Heat Recovery. *Renew. Sustain. Energy Rev.* **2016**, *64*, 635–659. https://doi.org/10.1016/j.rser.2016.06.035.

(16) Saha, M.; Tregenza, O.; Twelftree, J.; Hulston, C. A Review of Thermoelectric Generators for Waste Heat Recovery in Marine Applications. *Sustain. Energy Technol. Assess.* **2023**, *59*, 103394. https://doi.org/10.1016/j.seta.2023.103394.

(17) Park, S.; Heo, S. W.; Lee, W.; Inoue, D.; Jiang, Z.; Yu, K.; Jinno, H.; Hashizume, D.; Sekino, M.; Yokota, T.; Fukuda, K.; Tajima, K.; Someya, T. Self-Powered Ultra-Flexible

Electronics via Nano-Grating-Patterned Organic Photovoltaics. *Nature* **2018**, *561* (7724), 516–521. https://doi.org/10.1038/s41586-018-0536-x.

(18) Zou, H.; Zhao, H.; Lu, M.; Wang, J.; Deng, Z.; Wang, J. Predicting Thermodynamic Stability of Inorganic Compounds Using Ensemble Machine Learning Based on Electron Configuration. *Nat. Commun.* **2025**, *16* (1), 203. https://doi.org/10.1038/s41467-024-55525-y.

(19) Therrien, F.; Jones, E. B.; Stevanović, V. Metastable Materials Discovery in the Age of Large-Scale Computation. *Appl. Phys. Rev.* **2021**, *8* (3), 031310. https://doi.org/10.1063/5.0049453.

(20) Antoniuk, E. R.; Cheon, G.; Wang, G.; Bernstein, D.; Cai, W.; Reed, E. J. Predicting the Synthesizability of Crystalline Inorganic Materials from the Data of Known Material Compositions. *Npj Comput. Mater.* **2023**, *9* (1), 1–11. https://doi.org/10.1038/s41524-023-01114-4.

(21) Chen, J.; Cross, S. R.; Miara, L. J.; Cho, J.-J.; Wang, Y.; Sun, W. Navigating Phase Diagram Complexity to Guide Robotic Inorganic Materials Synthesis. *Nat. Synth.* **2024**, *3* (5), 606–614. https://doi.org/10.1038/s44160-024-00502-y.

(22) McDermott, M. J.; McBride, B. C.; Regier, C. E.; Tran, G. T.; Chen, Y.; Corrao, A. A.; Gallant, M. C.; Kamm, G. E.; Bartel, C. J.; Chapman, K. W.; Khalifah, P. G.; Ceder, G.; Neilson, J. R.; Persson, K. A. Assessing Thermodynamic Selectivity of Solid-State Reactions for the Predictive Synthesis of Inorganic Materials. *ACS Cent. Sci.* **2023**, *9* (10), 1957–1975. https://doi.org/10.1021/acscentsci.3c01051.

(23) Szymanski, N. J.; Nevatia, P.; Bartel, C. J.; Zeng, Y.; Ceder, G. Autonomous and Dynamic Precursor Selection for Solid-State Materials Synthesis. *Nat. Commun.* **2023**, *14* (1), 6956. https://doi.org/10.1038/s41467-023-42329-9.

(24) Pijolat, M.; Soustelle, M. Experimental Tests to Validate the Rate-Limiting Step Assumption Used in the Kinetic Analysis of Solid-State Reactions. *Thermochim. Acta* **2008**, *478* (1–2), 34–40. https://doi.org/10.1016/j.tca.2008.08.013.

(25) Martinolich, A. J.; Kurzman, J. A.; Neilson, J. R. Circumventing Diffusion in Kinetically Controlled Solid-State Metathesis Reactions. *J. Am. Chem. Soc.* **2016**, *138* (34), 11031–11037. https://doi.org/10.1021/jacs.6b06367.

(26) Gleiter, H. NANOCRYSTALLINE MATERIALS. *Prog. Mater. Sci.* **1989**, *33* (4), 223–315.

(27) Fick, A. Ueber Diffusion. *Ann. Phys.* **1855**, *170* (1), 59–86. https://doi.org/10.1002/andp.18551700105.

(28) Tyrrell, H. J. V. The Origin and Present Status of Fick's Diffusion Law. *J. Chem. Educ.* **1964**, *41* (7), 397. https://doi.org/10.1021/ed041p397.

(29) Sa, B. Comparison of Classical Nucleation Theory and Modern Theory of Phase Transition. *J. Adv. Chem. Eng.* **2017**, *07* (01). https://doi.org/10.4172/2090-4568.1000177.

(30) Gebauer, D.; Cölfen, H. Prenucleation Clusters and Non-Classical Nucleation. *Nano Today* **2011**, *6* (6), 564–584. https://doi.org/10.1016/j.nantod.2011.10.005.

(31) Ruckenstein, E.; Djikaev, Y. S. Recent Developments in the Kinetic Theory of Nucleation. *Adv. Colloid Interface Sci.* **2005**, *118* (1–3), 51–72. https://doi.org/10.1016/j.cis.2005.06.001.

(32) Oxtoby, D. W. Nucleation of First-Order Phase Transitions. *Acc. Chem. Res.* **1998**, *31* (2), 91–97. https://doi.org/10.1021/ar9702278.

(33) Iwamatsu, M. Nucleation and Growth by Diffusion under Ostwald-Freundlich Boundary Condition. *J. Chem. Phys.* **2014**, *140* (6), 064702. https://doi.org/10.1063/1.4865108.

(34) Bi, Y.; Cao, B.; Li, T. Enhanced Heterogeneous Ice Nucleation by Special Surface Geometry. *Nat. Commun.* **2017**, *8* (1), 15372. https://doi.org/10.1038/ncomms15372.

(35) Peng, Y.; Li, W.; Still, T.; Yodh, A. G.; Han, Y. In Situ Observation of Coalescence of Nuclei in Colloidal Crystal-Crystal Transitions. *Nat. Commun.* **2023**, *14* (1), 4905. https://doi.org/10.1038/s41467-023-40627-w.

(36) Merikanto, J.; Zapadinsky, E.; Lauri, A.; Vehkamäki, H. Origin of the Failure of Classical Nucleation Theory: Incorrect Description of the Smallest Clusters. *Phys. Rev. Lett.* **2007**, *98* (14), 145702. https://doi.org/10.1103/PhysRevLett.98.145702.

(37) Cheng, B.; Ceriotti, M. Bridging the Gap between Atomistic and Macroscopic Models of Homogeneous Nucleation. *J. Chem. Phys.* **2017**, *146* (3), 034106. https://doi.org/10.1063/1.4973883.

(38) Gebauer, D.; Raiteri, P.; Gale, J. D.; Cölfen, H. On Classical and Non-Classical Views on Nucleation. *Am. J. Sci.* **2018**, *318* (9), 969–988. https://doi.org/10.2475/09.2018.05.

(39) Khawam, A.; Flanagan, D. R. Solid-State Kinetic Models: Basics and Mathematical Fundamentals. *J. Phys. Chem. B* **2006**, *110* (35), 17315–17328. https://doi.org/10.1021/jp062746a.

(40) Fan, Z.; Men, H. An Overview on Atomistic Mechanisms of Heterogeneous Nucleation. *Metals* **2022**, *12* (9), 1547. https://doi.org/10.3390/met12091547.

(41) Chesser, I.; Koju, R. K.; Mishin, Y. Atomic-Level Mechanisms of Short-Circuit Diffusion in Materials. *Int. J. Mater. Res.* **2024**, *115* (2), 85–105. https://doi.org/10.1515/ijmr-2023-0202.

(42) Lutsko, J. F. How Crystals Form: A Theory of Nucleation Pathways. *Sci. Adv.* **2019**, *5* (4), eaav7399. https://doi.org/10.1126/sciadv.aav7399.

(43) Erdemir, D.; Lee, A. Y.; Myerson, A. S. Nucleation of Crystals from Solution: Classical and Two-Step Models. *Acc. Chem. Res.* **2009**, *42* (5), 621–629. https://doi.org/10.1021/ar800217x.

(44) Sun, Y.; Zhang, F.; Mendelev, M. I.; Wentzcovitch, R. M.; Ho, K.-M. Two-Step Nucleation of the Earth's Inner Core. *Proc. Natl. Acad. Sci.* **2022**, *119* (2), e2113059119. https://doi.org/10.1073/pnas.2113059119.

(45) Li, M.; Yue, Z.; Chen, Y.; Tong, H.; Tanaka, H.; Tan, P. Revealing Thermally-Activated Nucleation Pathways of Diffusionless Solid-to-Solid Transition. *Nat. Commun.* **2021**, *12* (1), 4042. https://doi.org/10.1038/s41467-021-24256-9.

(46) Fei, L.; Gan, X.; Ng, S. M.; Wang, H.; Xu, M.; Lu, W.; Zhou, Y.; Leung, C. W.; Mak, C.-L.; Wang, Y. Observable Two-Step Nucleation Mechanism in Solid-State Formation

of Tungsten Carbide. *ACS Nano* **2019**, *13* (1), 681–688. https://doi.org/10.1021/acsnano.8b07864.

(47) Peng, Y.; Wang, F.; Wang, Z.; Alsayed, A. M.; Zhang, Z.; Yodh, A. G.; Han, Y. Two-Step Nucleation Mechanism in Solid–Solid Phase Transitions. *Nat. Mater.* **2015**, *14* (1), 101–108. https://doi.org/10.1038/nmat4083.

(48) Schüth, F.; Bussian, P.; Ågren, P.; Schunk, S.; Lindén, M. Techniques for Analyzing the Early Stages of Crystallization Reactions. *Solid State Sci.* **2001**, *3* (7), 801–808. https://doi.org/10.1016/S1293-2558(01)01199-2.

(49) Vekilov, P. G. Nucleation. *Cryst. Growth Des.* **2010**, *10* (12), 5007–5019. https://doi.org/10.1021/cg1011633.

(50) Huertas, F. J.; Fiore, S.; Huertas, F.; Linares, J. Experimental Study of the Hydrothermal Formation of Kaolinite. *Chem. Geol.* **1999**, *156* (1–4), 171–190. https://doi.org/10.1016/S0009-2541(98)00180-6.

(51) Kojima, S.; Nagase, T. Precipitation of Metastable Phases and Kinetics of Solution-Mediated Phase Transformation. *J. Mineral. Petrol. Econ. Geol.* **1999**, *94* (10), 377–388. https://doi.org/10.2465/ganko.94.377.

(52) Chen, B.-R.; Sun, W.; Kitchaev, D. A.; Mangum, J. S.; Thampy, V.; Garten, L. M.; Ginley, D. S.; Gorman, B. P.; Stone, K. H.; Ceder, G.; Toney, M. F.; Schelhas, L. T. Understanding Crystallization Pathways Leading to Manganese Oxide Polymorph Formation. *Nat. Commun.* **2018**, *9* (1), 2553. https://doi.org/10.1038/s41467-018-04917-y.

(53) Gopalakrishnan, J. Chimie Douce Approaches to the Synthesis of Metastable Oxide Materials. *Chem. Mater.* **1995**, *7* (7), 1265–1275. https://doi.org/10.1021/cm00055a001.

(54) Lee, S.; Wi, H. S.; Jo, W.; Cho, Y. C.; Lee, H. H.; Jeong, S.-Y.; Kim, Y.-I.; Lee, G. W. Multiple Pathways of Crystal Nucleation in an Extremely Supersaturated Aqueous Potassium Dihydrogen Phosphate (KDP) Solution Droplet. *Proc. Natl. Acad. Sci. U. S. A.* **2016**, *113* (48), 13618–13623. https://doi.org/10.1073/pnas.1604938113.

(55) Rittmeyer, S. P.; Bukas, V. J.; Reuter, K. Energy Dissipation at Metal Surfaces. *Adv. Phys. X* **2018**, *3* (1), 1381574. https://doi.org/10.1080/23746149.2017.1381574.

(56) Farahvash, A.; Willard, A. P. A Theory of Phonon-Induced Friction on Molecular Adsorbates. *Proc. Natl. Acad. Sci.* **2024**, *121* (31), e2400589121. https://doi.org/10.1073/pnas.2400589121.

(57) Zhou, J.; Zhou, Y.; Tang, W. Molecular Mechanism of Organic Crystal Nucleation: A Perspective of Solution Chemistry and Polymorphism. *Crystals* **2022**, *12* (7), 980. https://doi.org/10.3390/cryst12070980.

(58) Oxtoby, D. W. Homogeneous Nucleation: Theory and Experiment. *J. Phys. Condens. Matter* **1992**, *4*, 7627–7650.

(59) Ford, I. J. Statistical Mechanics of Nucleation: A Review. *Proc. Inst. Mech. Eng. Part C J. Mech. Eng. Sci.* **2004**, *218* (8), 883–899. https://doi.org/10.1243/0954406041474183.

(60) Sleutel, M.; Lutsko, J.; Van Driessche, A. E. S.; Durán-Olivencia, M. A.; Maes, D. Observing Classical Nucleation Theory at Work by Monitoring Phase Transitions with Molecular Precision. *Nat. Commun.* **2014**, *5* (1), 5598. https://doi.org/10.1038/ncomms6598.

(61) Rashad, A.; Sali, J. V.; Marathe, B. R.; Takwale, M. G.; Shaligram, A. D. The Effect of Substrate Temperature on P-CVD Deposited a-SiGe : H FIlms.

(62) Wang, Y.; Peng, L.; Zhao, Y.; Wu, J.; Fang, H.; Chen, H.; Wang, T. Numerical Study of Tungsten Growth in a Chemical Vapor Deposition Reactor. *ACS Omega* **2025**, *10* (18), 18571–18582. https://doi.org/10.1021/acsomega.4c11244.

(63) Douglas, E. A.; Mahony, P.; Starbuck, A.; Pomerene, A.; Trotter, D. C.; DeRose, C. T. Effect of Precursors on Propagation Loss for Plasma-Enhanced Chemical Vapor Deposition of SiN_x:H Waveguides. *Opt. Mater. Express* **2016**, *6* (9), 2892–2903. https://doi.org/10.1364/OME.6.002892.

(64) Corat, E. J.; Goodwin, D. G. Temperature Dependence of Species Concentrations near the Substrate during Diamond Chemical Vapor Deposition. *J. Appl. Phys.* **1993**, *74* (3), 2021–2029. https://doi.org/10.1063/1.354765.

(65) Sun, L.; Yuan, G.; Gao, L.; Yang, J.; Chhowalla, M.; Gharahcheshmeh, M. H.; Gleason, K. K.; Choi, Y. S.; Hong, B. H.; Liu, Z. Chemical Vapour Deposition. *Nat. Rev. Methods Primer* **2021**, *1* (1), 5. https://doi.org/10.1038/s43586-020-00005-y.

(66) Zhang, W.; Xia, Y.; Shi, W.; Wang, L.; Fang, Z. Effect of Substrate Temperature on the Selective Deposition of Diamond FIlms.

(67) Ali, M.; Qazi, I. A. Effect of Substrate Temperature on Hot-Filament CVD Grown Diamond Films at Constant Filament Current. *Int. J. Surf. Sci. Eng.* **2012**, *6* (3), 214. https://doi.org/10.1504/IJSURFSE.2012.049054.

(68) Li, N.; Zhen, Z.; Zhang, R.; Xu, Z.; Zheng, Z.; He, L. Nucleation and Growth Dynamics of Graphene Grown by Radio Frequency Plasma-Enhanced Chemical Vapor Deposition. *Sci. Rep.* **2021**, *11* (1), 6007. https://doi.org/10.1038/s41598-021-85537-3.

(69) Bruno, G.; Losurdo, M.; Kim, T.-H.; Brown, A. Adsorption and Desorption Kinetics of Ga on GaN(0001): Application of Wolkenstein Theory. *Phys. Rev. B* **2010**, *82* (7), 075326. https://doi.org/10.1103/PhysRevB.82.075326.

(70) Coleiny, G.; Venkat, R. Theoretical Study of in Desorption during MBE Growth of InGaAs/GaAs. *J. Cryst. Growth* **2003**, *250* (1–2), 22–28. https://doi.org/10.1016/S0022-0248(02)02209-1.

(71) Zhang, Z.; Miao, G.; Song, H.; Jiang, H.; Li, Z.; Li, D.; Sun, X.; Chen, Y. Performance of High Indium Content InGaAs P-i-n Detector: A Simulation Study. *World J. Eng. Technol.* **2015**, *3* (4), 6–10. https://doi.org/10.4236/wjet.2015.34B002.

(72) Takamoto, T.; Kaneiwa, M.; Imaizumi, M.; Yamaguchi, M. InGaP/GaAs-Based Multijunction Solar Cells. *Prog. Photovolt. Res. Appl.* **2005**, *13* (6), 495–511. https://doi.org/10.1002/pip.642.

(73) Sidhu, R.; Ning Duan; Campbell, J. C.; Holmes, A. L. A Long-Wavelength Photodiode on InP Using Lattice-Matched GaInAs-GaAsSb Type-II Quantum Wells. *IEEE Photonics Technol. Lett.* **2005**, *17* (12), 2715–2717. https://doi.org/10.1109/LPT.2005.859163.

(74) Prakash, A.; Xu, P.; Wu, X.; Haugstad, G.; Wang, X.; Jalan, B. Adsorption-Controlled Growth and the Influence of Stoichiometry on Electronic Transport in Hybrid Molecular Beam Epitaxy-Grown $BaSnO_3$ Films. *J. Mater. Chem. C* **2017**, *5* (23), 5730–5736. https://doi.org/10.1039/C7TC00190H.

(75) Havelia, S.; Wang, S.; Skowronski, M.; Salvador, P. A. Controlling the Bi Content, Phase Formation, and Epitaxial Nature of $BiMnO_3$ Thin Films Fabricated Using Conventional

Pulsed Laser Deposition, Hybrid Pulsed Laser Deposition, and Solid State Epitaxy. *J. Appl. Phys.* **2009**, *106* (12), 123509. https://doi.org/10.1063/1.3266142.

(76) Toe, M. Z.; Tan, W. K.; Muto, H.; Kawamura, G.; Matsuda, A.; Yaacob, K. A. B.; Pung, S.-Y. Effect of Carrier Gas Flow Rates on the Structural and Optical Properties of ZnO Films Deposited Using an Aerosol Deposition Technique. *Electron. Mater.* **2022**, *3* (4), 332–343. https://doi.org/10.3390/electronicmat3040027.

(77) Aarik, J.; Aidla, A.; Kasikov, A.; Mändar, H.; Rammula, R.; Sammelselg, V. Influence of Carrier Gas Pressure and Flow Rate on Atomic Layer Deposition of HfO_2 and ZrO_2 Thin Films. *Appl. Surf. Sci.* **2006**, *252* (16), 5723–5734. https://doi.org/10.1016/j.apsusc.2005.07.067.

(78) Bai, M.; Wen, S.; Zhao, J.; Du, Y.; Xie, F.; Liu, H. Effect of Carrier Gas Flow Field on Chemical Vapor Deposition of 2D MoS_2 Crystal. *Coatings* **2021**, *11* (5), 547. https://doi.org/10.3390/coatings11050547.

(79) Esposito, F.; Bosi, M.; Attolini, G.; Rossi, F.; Fornari, R.; Fabbri, F.; Seravalli, L. Influence of the Carrier Gas Flow in the CVD Synthesis of 2-Dimensional MoS_2 Based on the Spin-Coating of Liquid Molybdenum Precursors. *Nanomaterials* **2024**, *14* (21), 1749. https://doi.org/10.3390/nano14211749.

(80) Aghajani, H.; Hosseini, N.; Mirzakhani, B. Deposition Kinetics and Boundary Layer Theory in the Chemical Vapor Deposition of β-SiC on the Surface of C/C Composite. *Mater. Phys. Mech.* **2020**, *44*, 34–47. https://doi.org/10.18720/MPM.4412020_5.

(81) Rolin, C.; Song, B.; Forrest, S. R. Mass Transport through the Carrier Gas Boundary Layer in Organic Vapor Phase Deposition. *Phys. Rev. Appl.* **2014**, *1* (3), 034002. https://doi.org/10.1103/PhysRevApplied.1.034002.

(82) Song, Y.; Zhuang, J.; Song, M.; Yin, S.; Cheng, Y.; Zhang, X.; Wang, M.; Xiang, R.; Xia, Y.; Maruyama, S.; Zhao, P.; Ding, F.; Wang, H. Epitaxial Nucleation of CVD Bilayer Graphene on Copper. *Nanoscale* **2016**, *8* (48), 20001–20007. https://doi.org/10.1039/C6NR04557J.

(83) Mameli, A.; Tapily, K.; Shen, J.; Roozeboom, F.; Lu, M.; O'Meara, D.; Semproni, S. P.; Chen, J.-R.; Clark, R.; Leusink, G.; Clendenning, S. Unfolding an Elusive Area-Selective

Deposition Process: Atomic Layer Deposition of TiO_2 and TiON on SiN vs SiO_2. *ACS Appl. Mater. Interfaces* **2024**, *16* (11), 14288–14295. https://doi.org/10.1021/acsami.3c17917.

(84) Fraser, J. P.; Masaityte, L.; Zhang, J.; Laing, S.; Moreno-López, J. C.; McKenzie, A. F.; McGlynn, J. C.; Panchal, V.; Graham, D.; Kazakova, O.; Pichler, T.; MacLaren, D. A.; Moran, D. A. J.; Ganin, A. Y. Selective Phase Growth and Precise-Layer Control in MoTe2. *Commun. Mater.* **2020**, *1* (1), 48. https://doi.org/10.1038/s43246-020-00048-4.

(85) Lin, L.; Zhang, J.; Su, H.; Li, J.; Sun, L.; Wang, Z.; Xu, F.; Liu, C.; Lopatin, S.; Zhu, Y.; Jia, K.; Chen, S.; Rui, D.; Sun, J.; Xue, R.; Gao, P.; Kang, N.; Han, Y.; Xu, H. Q.; Cao, Y.; Novoselov, K. S.; Tian, Z.; Ren, B.; Peng, H.; Liu, Z. Towards Super-Clean Graphene. *Nat. Commun.* **2019**, *10*, 1912. https://doi.org/10.1038/s41467-019-09565-4.

(86) Amano, H.; Sawaki, N.; Akasaki, I.; Toyoda, Y. Metalorganic Vapor Phase Epitaxial Growth of a High Quality GaN Film Using an AlN Buffer Layer. *Appl. Phys. Lett.* **1986**, *48* (5), 353–355. https://doi.org/10.1063/1.96549.

(87) Isamu Akasaki; Hiroshi Amano; Masahiro Kito; Kazumasa Hiramatsu. Photoluminescence of Mg-Doped p-Type GaN and Electroluminescence of GaN p-n Junction LED. *J. Lumin.* **1991**, *48–49*, 666–670. https://doi.org/10.1016/0022-2313(91)90215-H.

(88) Nakamura, S.; Mukai, T.; Senoh, M. Candela-Class High-Brightness InGaN/AlGaN Double-Heterostructure Blue-Light-Emitting Diodes. *Appl. Phys. Lett.* **1994**, *64* (13), 1687–1689. https://doi.org/10.1063/1.111832.

(89) Tang, L.; Tan, J.; Nong, H.; Liu, B.; Cheng, H.-M. Chemical Vapor Deposition Growth of Two-Dimensional Compound Materials: Controllability, Material Quality, and Growth Mechanism. *Acc. Mater. Res.* **2021**, *2* (1), 36–47. https://doi.org/10.1021/accountsmr.0c00063.

(90) Kessler, D. A.; Levine, H.; Sander, L. M. Molecular-Beam Epitaxial Growth and Surface Diffusion. *Phys. Rev. Lett.* **1992**, *69* (1), 100–103. https://doi.org/10.1103/PhysRevLett.69.100.

(91) Karpov, S. Yu.; Maiorov, M. A. Model of the Adsorption/Desorption Kinetics on a Growing III–V Compound Surface. *Surf. Sci.* **1997**, *393* (1–3), 108–125. https://doi.org/10.1016/S0039-6028(97)00563-3.

(92) Politi, P.; Grenet, G.; Marty, A.; Ponchet, A.; Villain, J. Instabilities in Crystal Growth by Atomic or Molecular Beams. *Phys. Rep.* **2000**, *324* (5–6), 271–404. https://doi.org/10.1016/S0370-1573(99)00046-0.

(93) Schaefer, S.; Febba, D.; Egbo, K.; Teeter, G.; Zakutayev, A.; Tellekamp, B. Rapid Screening of Molecular Beam Epitaxy Conditions for Monoclinic (In x Ga 1−x) 2 O 3 Alloys. *J. Mater. Chem. A* **2024**, *12* (9), 5508–5519. https://doi.org/10.1039/D3TA07220G.

(94) Ploog, K. Molecular Beam Epitaxy of III-V Compounds: Technology and Growth Process. *Annu. Rev. Mater. Sci.* **1981**, *11* (1), 171–210. https://doi.org/10.1146/annurev.ms.11.080181.001131.

(95) Choudhary, R.; Jalan, B. Atomically Precise Synthesis of Oxides with Hybrid Molecular Beam Epitaxy. *Device* **2025**, *3* (3), 100711. https://doi.org/10.1016/j.device.2025.100711.

(96) Sghaier, H. RHEED Digital Image Analysis System for In-Situ Growth Rate and Alloy Composition Measurements of GaAs-Based Nanostructures. *Semicond. Phys. Quantum Electron. Optoelectron.* **2004**, *7* (2), 147–153. https://doi.org/10.15407/spqeo7.02.147.

(97) Kajdos, A. P.; Stemmer, S. Surface Reconstructions in Molecular Beam Epitaxy of $SrTiO_3$. *Appl. Phys. Lett.* **2014**, *105* (19), 191901. https://doi.org/10.1063/1.4901726.

(98) Fazlioglu-Yalcin, B.; Hilse, M.; Engel-Herbert, R. Thermogravimetric Study of Metal–Organic Precursors and Their Suitability for Hybrid Molecular Beam Epitaxy. *J. Mater. Res.* **2024**, *39* (3), 436–448. https://doi.org/10.1557/s43578-023-01237-w.

(99) Nunn, W.; Manjeshwar, A. K.; Yue, J.; Rajapitamahuni, A.; Truttmann, T. K.; Jalan, B. Novel Synthesis Approach for “Stubborn” Metals and Metal Oxides. *Proc. Natl. Acad. Sci. U. S. A.* **2021**, *118* (32), e2105713118. https://doi.org/10.1073/pnas.2105713118.

(100) Choudhary, R.; Jalan, B. Atomically Precise Synthesis of Oxides with Hybrid Molecular Beam Epitaxy. *Device* **2025**, *3* (3), 100711. https://doi.org/10.1016/j.device.2025.100711.

(101) Kim, Y.-S.; Bansal, N.; Oh, S. Crucible Aperture: An Effective Way to Reduce Source Oxidation in Oxide Molecular Beam Epitaxy Process. *J. Vac. Sci. Technol. A* **2010**, *28* (4), 600–602. https://doi.org/10.1116/1.3449051.

(102) Kaganer, V. M.; Jenichen, B.; Shayduk, R.; Braun, W.; Riechert, H. Kinetic Optimum of Volmer-Weber Growth. *Phys. Rev. Lett.* **2009**, *102* (1), 016103. https://doi.org/10.1103/PhysRevLett.102.016103.

(103) Ponchet, A.; Patriarche, G.; Rodriguez, J. B.; Cerutti, L.; Tournié, E. Interface Energy Analysis of III–V Islands on Si (001) in the Volmer-Weber Growth Mode. *Appl. Phys. Lett.* **2018**, *113* (19), 191601. https://doi.org/10.1063/1.5055056.

(104) Kaufmann, Nils. A. K.; Lahourcade, L.; Hourahine, B.; Martin, D.; Grandjean, N. Critical Impact of Ehrlich–Schwöbel Barrier on GaN Surface Morphology during Homoepitaxial Growth. *J. Cryst. Growth* **2016**, *433*, 36–42. https://doi.org/10.1016/j.jcrysgro.2015.06.013.

(105) Schinzer, S.; Köhler, S.; Reents, G. Ehrlich-Schwoebel Barrier Controlled Slope Selection in Epitaxial Growth. *Eur. Phys. J. B* **2000**, *15* (1), 161–168. https://doi.org/10.1007/s100510051111.

(106) Manfra, M. J. Molecular Beam Epitaxy of Ultra-High-Quality AlGaAs/GaAs Heterostructures: Enabling Physics in Low-Dimensional Electronic Systems. *Annu. Rev. Condens. Matter Phys.* **2014**, *5* (1), 347–373. https://doi.org/10.1146/annurev-conmatphys-031113-133905.

(107) Nunn, W.; Truttmann, T. K.; Jalan, B. A Review of Molecular-Beam Epitaxy of Wide Bandgap Complex Oxide Semiconductors. *J. Mater. Res.* **2021**, *36* (23), 4846–4864. https://doi.org/10.1557/s43578-021-00377-1.

(108) Nakayama, Y.; Tsuruta, R.; Koganezawa, T. 'Molecular Beam Epitaxy' on Organic Semiconductor Single Crystals: Characterization of Well-Defined Molecular Interfaces by Synchrotron Radiation X-Ray Diffraction Techniques. *Materials* **2022**, *15* (20), 7119. https://doi.org/10.3390/ma15207119.

(109) Sassella, A.; Campione, M.; Raimondo, L.; Tavazzi, S.; Borghesi, A.; Goletti, C.; Bussetti, G.; Chiaradia, P. Epitaxial Growth of Organic Heterostructures: Morphology,

Structure, and Growth Mode. *Surf. Sci.* **2007**, *601* (13), 2571–2575. https://doi.org/10.1016/j.susc.2006.11.072.

(110) Luo, S.; Wang, Z.; Li, X.; Liu, X.; Wang, H.; Ma, W.; Zhang, L.; Zhu, L.; Zhang, X. Growth of Lithium-Indium Dendrites in All-Solid-State Lithium-Based Batteries with Sulfide Electrolytes. *Nat. Commun.* **2021**, *12* (1), 6968. https://doi.org/10.1038/s41467-021-27311-7.

(111) Wang, J.; Panchal, A. A.; Gautam, G. S.; Canepa, P. The Resistive Nature of Decomposing Interfaces of Solid Electrolytes with Alkali Metal Electrodes. *J. Mater. Chem. A* **2022**, *10* (37), 19732–19742. https://doi.org/10.1039/D2TA02202H.

(112) Byeon, Y.-W.; Kim, H. Review on Interface and Interphase Issues in Sulfide Solid-State Electrolytes for All-Solid-State Li-Metal Batteries. *Electrochem* **2021**, *2* (3), 452–471. https://doi.org/10.3390/electrochem2030030.

(113) Liu, M.; Song, A.; Zhang, X.; Wang, J.; Fan, Y.; Wang, G.; Tian, H.; Ma, Z.; Shao, G. Interfacial Lithium-Ion Transportation in Solid-State Batteries: Challenges and Prospects. *Nano Energy* **2025**, *136*, 110749. https://doi.org/10.1016/j.nanoen.2025.110749.

(114) Kol, S.; Oral, A. Hf-Based High-κ Dielectrics: A Review. *Acta Phys. Pol. A* **2019**, *136* (6), 873–881. https://doi.org/10.12693/APhysPolA.136.873.

(115) Wilk, G. D.; Wallace, R. M.; Anthony, J. M. High-κ Gate Dielectrics: Current Status and Materials Properties Considerations. *J. Appl. Phys.* **2001**, *89* (10), 5243–5275. https://doi.org/10.1063/1.1361065.

(116) Robertson, J. High Dielectric Constant Gate Oxides for Metal Oxide Si Transistors. *Rep. Prog. Phys.* **2006**, *69* (2), 327–396. https://doi.org/10.1088/0034-4885/69/2/R02.

(117) Gougousi, T. Atomic Layer Deposition of High-k Dielectrics on III–V Semiconductor Surfaces. *Prog. Cryst. Growth Charact. Mater.* **2016**, *62* (4), 1–21. https://doi.org/10.1016/j.pcrysgrow.2016.11.001.

(118) Johnson, D. C. Controlled Synthesis of New Compounds Using Modulated Elemental Reactants. *Curr. Opin. Solid State Mater. Sci.* **1998**, *3* (2), 159–167. https://doi.org/10.1016/S1359-0286(98)80082-X.

(119) Lemon, M.; Harvel, F. G.; Gannon, R. N.; Lu, P.; Rudin, S. P.; Johnson, D. C. Targeted Synthesis of Predicted Metastable Compounds Using Modulated Elemental Reactants. *J. Vac. Sci. Technol. A* **2023**, *41* (2), 022203. https://doi.org/10.1116/6.0002260.

(120) Geim, A. K.; Grigorieva, I. V. Van Der Waals Heterostructures. *Nature* **2013**, *499* (7459), 419–425. https://doi.org/10.1038/nature12385.

(121) Beekman, M.; Heideman, C. L.; Johnson, D. C. Ferecrystals: Non-Epitaxial Layered Intergrowths. *Semicond. Sci. Technol.* **2014**, *29* (6), 064012. https://doi.org/10.1088/0268-1242/29/6/064012.

(122) Westover, R.; Atkins, R. A.; Falmbigl, M.; Ditto, J. J.; Johnson, D. C. Self-Assembly of Designed Precursors: A Route to Crystallographically Aligned New Materials with Controlled Nanoarchitecture. *J. Solid State Chem.* **2016**, *236*, 173–185. https://doi.org/10.1016/j.jssc.2015.08.018.

CHAPTER II

(1) Hamann, D. M.; Bardgett, D.; Cordova, D. L. M.; Maynard, L. A.; Hadland, E. C.; Lygo, A. C.; Wood, S. R.; Esters, M.; Johnson, D. C. Sub-Monolayer Accuracy in Determining the Number of Atoms per Unit Area in Ultrathin Films Using X-Ray Fluorescence. *Chem. Mater.* **2018**, *30* (18), 6209–6216. https://doi.org/10.1021/acs.chemmater.8b02591.

(2) Parratt, L. G. Surface Studies of Solids by Total Reflection of X-Rays. *Phys. Rev.* **1954**, *95* (2), 359–369. https://doi.org/10.1103/PhysRev.95.359.

(3) Nellist, P. D.; Pennycook, S. J. The Principles and Interpretation of Annular Dark-Field Z-Contrast Imaging. In *Advances in Imaging and Electron Physics*; Elsevier, 2000; Vol. 113, pp 147–203. https://doi.org/10.1016/S1076-5670(00)80013-0.

(4) Liu, J.; Cowley, J. M. High-Resolution Scanning Transmission Electron Microscopy. *Ultramicroscopy* **1993**, *52* (3), 335–346. https://doi.org/10.1016/0304-3991(93)90044-X.

(5) J, V. D. P. L. A Method of Measuring the Resistivity and Hall Coefficient on Lamellae of Arbitrary Shape. *Philips Tech. Rev.* **1958**, *20*, 220–224.

CHAPTER III

(1) Geim, A. K.; Grigorieva, I. V. Van der Waals heterostructures. *Nature* **2013**, *499* (7459), 419-425. DOI: 10.1038/nature12385.

(2) Haigh, S. J.; Gholinia, A.; Jalil, R.; Romani, S.; Britnell, L.; Elias, D. C.; Novoselov, K. S.; Ponomarenko, L. A.; Geim, A. K.; Gorbachev, R. Cross-sectional imaging of individual layers and buried interfaces of graphene-based heterostructures and superlattices. *Nature Materials* **2012**, *11* (9), 764-767. DOI: 10.1038/nmat3386.

(3) Venkatasubramanian, R.; Siivola, E.; Colpitts, T.; O'Quinn, B. Thin-film thermoelectric devices with high room-temperature figures of merit. *Nature* **2001**, *413* (6856), 597-602. DOI: 10.1038/35098012.

(4) Hamann, D. M.; Hadland, E. C.; Johnson, D. C. Heterostructures containing dichalcogenides-new materials with predictable nanoarchitectures and novel emergent properties. *Semiconductor Science and Technology* **2017**, *32* (9), 093004. DOI: 10.1088/1361-6641/aa7785.

(5) Silin, A. P. Semiconductor superlattices. *Soviet Physics Uspekhi* **1985**, *28* (11), 972. DOI: 10.1070/PU1985v028n11ABEH003967.

(6) Collier, C. P.; Vossmeyer, T.; Heath, J. R. Nanocrystal superlattices. *Annual Review of Physical Chemistry* **1998**, *49* (1), 371-404. DOI: 10.1146/annurev.physchem.49.1.371

(7) Thompson, A. G. MOCVD technology for semiconductors. *Materials Letters* **1997**, *30* (4), 255-263.

(8) Ludowise, M. Metalorganic chemical vapor deposition of III-V semiconductors. *Journal of Applied Physics* **1985**, *58* (8), R31-R55.

(9) Liu, Y.; Weiss, N. O.; Duan, X.; Cheng, H.-C.; Huang, Y.; Duan, X. Van der Waals heterostructures and devices. *Nature Reviews Materials* **2016**, *1* (9), 16042. DOI: 10.1038/natrevmats.2016.42.

(10) Cheng, R.; Wang, F.; Yin, L.; Wang, Z.; Wen, Y.; Shifa, T. A.; He, J. High-performance, multifunctional devices based on asymmetric van der Waals heterostructures. *Nature Electronics* **2018**, *1* (6), 356-361. DOI: 10.1038/s41928-018-0086-0.

(11) Hong, X.; Kim, J.; Shi, S.-F.; Zhang, Y.; Jin, C.; Sun, Y.; Tongay, S.; Wu, J.; Zhang, Y.; Wang, F. Ultrafast charge transfer in atomically thin MoS_2/WS_2 heterostructures. *Nat. Nanotechnol.* **2014**, *9* (9), 682-686. DOI: 10.1038/nnano.2014.167.

(12) Yu, W. J.; Liu, Y.; Zhou, H.; Yin, A.; Li, Z.; Huang, Y.; Duan, X. Highly efficient gate-tunable photocurrent generation in vertical heterostructures of layered materials. *Nat. Nanotechnol.* **2013**, online DOI: 10.1038/NNANO.2013.1219.

(13) Palacios-Berraquero, C.; Barbone, M.; Kara, D. M.; Chen, X.; Goykhman, I.; Yoon, D.; Ott, A. K.; Beitner, J.; Watanabe, K.; Taniguchi, T.; et al. Atomically thin quantum light-emitting diodes. *Nature Communications* **2016**, *7* (1), 12978. DOI: 10.1038/ncomms12978.

(14) Britnell, L.; Gorbachev, R. V.; Jalil, R.; Belle, B. D.; Schedin, F.; Mishchenko, A.; Georgiou, T.; Katsnelson, M. I.; Eaves, L.; Morozov, S. V.; et al. Field-Effect Tunneling Transistor Based on Vertical Graphene Heterostructures. *Science* **2012**, *335* (6071), 947-950. DOI: doi:10.1126/science.1218461.

(15) Liu, Y.; Huang, Y.; Duan, X. Van der Waals integration before and beyond two-dimensional materials. *Nature* **2019**, *567* (7748), 323-333. DOI: 10.1038/s41586-019-1013-x.

(16) Sarkar, D.; Xie, X.; Liu, W.; Cao, W.; Kang, J.; Gong, Y.; Kraemer, S.; Ajayan, P. M.; Banerjee, K. A subthermionic tunnel field-effect transistor with an atomically thin channel. *Nature* **2015**, *526* (7571), 91-95. DOI: 10.1038/nature15387.

(17) Montgomery, H. C. Method for Measuring Electrical Resistivity of Anisotropic Materials. *Journal of Applied Physics* **2003**, *42* (7), 2971-2975. DOI: 10.1063/1.1660656 (acccessed 6/7/2023).

(18) dos Santos, C. A. M.; de Campos, A.; da Luz, M. S.; White, B. D.; Neumeier, J. J.; de Lima, B. S.; Shigue, C. Y. Procedure for measuring electrical resistivity of anisotropic

materials: A revision of the Montgomery method. *Journal of Applied Physics* **2011**, *110* (8). DOI: 10.1063/1.3652905 (acccessed 6/7/2023).

(19) Y ang, B.; Liu, W. L.; Liu, J. L.; Wang, K. L.; Chen, G. Measurements of anisotropic thermoelectric properties in superlattices. *Applied Physics Letters* **2002**, *81* (19), 3588-3590. DOI: 10.1063/1.1515876 (acccessed 2021/05/05).

(20) Chen, J.; Hamann, D. M.; Choi, D. S.; Poudel, N.; Shen, L.; Shi, L.; Johnson, D. C.; Cronin, S. B. Enhanced Cross-plane Thermoelectric Transport of Rotationally-disordered $SnSe_2$ via Se Vapor Annealing. *Nano Lett*. **2018**, *18* (11), 6876-6881.

(21) Kwon, H.; Khan, A. I.; Perez, C.; Asheghi, M.; Pop, E.; Goodson, K. E. Uncovering thermal and electrical properties of Sb2Te3/GeTe superlattice films. *Nano Letters* **2021**, *21* (14), 5984-5990.

(22) Ber, E.; Grady, R. W.; Pop, E.; Yalon, E. Uncovering the Different Components of Contact Resistance to Atomically Thin Semiconductors. *Advanced Electronic Materials* n/a (n/a), 2201342. DOI: https://doi.org/10.1002/aelm.202201342.

(23) Schroder, D. K. Contact Resistance and Schottky Barriers. In Semiconductor Material and Device Characterization, *Wiley*, **2005**; pp 127-184.

(24) Najmaei, S.; Neupane, M. R.; Nichols, B. M.; Burke, R. A.; Mazzoni, A. L.; Chin, M. L.; Rhodes, D. A.; Balicas, L.; Franklin, A. D.; Dubey, M. Cross-Plane Carrier Transport in Van der Waals Layered Materials. *Small* **2018**, *14* (20), 1703808. DOI: 10.1002/smll.201703808.

(25) Murrmann, H.; Widmann, D. Current crowding on metal contacts to planar devices. *IEEE Transactions on Electron Devices* **1969**, *16* (12), 1022-1024.

(26) Schroder, D. K. Semiconductor material and device characterization; John Wiley & Sons, **2015**.

(27) Berger, H. Solid State Electron. Solid-State Electron **1972**, *15* (145).

(28) Wang, L.; Zhang, Z.-H.; Wang, N. Current crowding phenomenon: Theoretical and direct correlation with the efficiency droop of light emitting diodes by a modified ABC model. *IEEE Journal of Quantum Electronics* **2015**, *51* (5), 1-9.

(29) Yongsunthon, R.; Tao, C.; Rous, P.; Williams, E. Surface electromigration and current crowding. *Nanophenomena at Surfaces: Fundamentals of Exotic Condensed Matter Properties* **2011**, 113-143.

(30) Wang, Y.; Hamann, D. M.; Cordova, D. L. M.; Chen, J.; Wang, B.; Shen, L.; Cai, Z.; Shi, H.; Karapetrova, E.; Aravind, I. Enhanced Low-Temperature Thermoelectric Performance in $(PbSe)_{1+\delta}(VSe_2)_1$ Heterostructures due to Highly Correlated Electrons in Charge Density Waves. *Nano Letters* **2020**, *20* (11), 8008-8014.

(31) Hite, O. K.; Falmbigl, M.; Alemayehu, M. B.; Esters, M.; Wood, S. R.; Johnson, D. C. Charge density wave transition in $(PbSe)_{1+\delta}(VSe_2)_n$ compounds with n= 1, 2, and 3. Chemistry of *Materials* **2017**, *29* (13), 5646-5653.

(32) Cordova, D. L. M.; Fender, S. S.; Kam, T. M.; Seyd, J.; Albrecht, M.; Lu, P.; Fischer, R.; Johnson, D. C. Designed synthesis and structure–property relationships of kinetically stable $[(PbSe)_{1+\delta}]_m(VSe_2)_1$ (m= 1, 2, 3, 4) heterostructures. *Chemistry of Materials* **2019**, *31* (20), 8473-8483.

(33) Falmbigl, M.; Putzky, D.; Ditto, J.; Esters, M.; Bauers, S. R.; Ronning, F.; Johnson, D. C. Influence of defects on the charge density wave of $([SnSe]_{1+\delta})_1(VSe_2)_1$ ferecrystals. *ACS Nano* **2015**, *9* (8), 8440-8448.

(34) Berger, H. Contact resistance on diffused resistors. *IEEE International Solid-State Circuits Conference. Digest of Technical Papers* **1969**, *12*, pp 160-161. DOI: 10.1109/ISSCC.1969.1154702.

(35) Hamann, D. M.; Bardgett, D.; Cordova, D. L. M.; Maynard, L. A.; Hadland, E. C.; Lygo, A. C.; Wood, S. R.; Esters, M.; Johnson, D. C. Sub-Monolayer Accuracy in Determining the Number of Atoms per Unit Area in Ultrathin Films Using X-Ray Fluorescence. *Chemistry of Materials* **2018**, *30* (18), 6209–6216. https://doi.org/10.1021/acs.chemmater.8b02591.

(36) Cordova, D. L. M.; Fender, S. S.; Kam, T. M.; Seyd, J.; Albrecht, M.; Lu, P.; Fischer, R.; Johnson, D. C. Designed Synthesis and Structure–Property Relationships of Kinetically Stable $[(PbSe)_{1+\delta}]_m(VSe_2)_1$ (m = 1, 2, 3, 4) Heterostructures. *Chemistry of Materials* **2019**, *31* (20), 8473-8483. DOI: 10.1021/acs.chemmater.9b02826.

(37) Wang, Y.; Hamann, D. M.; Cordova, D. L. M.; Chen, J.; Wang, B.; Shen, L.; Cai, Z.; Shi, H.; Karapetrova, E.; Aravind, I.; et al. Enhanced Low-Temperature Thermoelectric Performance in $(PbSe)_{1+\delta}(VSe_2)_1$ Heterostructures due to Highly Correlated Electrons in Charge Density Waves. *Nano Lett.* **2020**, *20* (11), 8008-8014. DOI: 10.1021/acs.nanolett.0c02882.

(38) Ting, C.-Y.; Chen, C. Y. A study of the contacts of a diffused resistor. *Solid-State Electronics* **1971**, *14* (6), 433-438. DOI: https://doi.org/10.1016/0038-1101(71)90051-7.

(39) Scorzoni, A.; Finetti, M. Metal/semiconductor contact resistivity and its determination from contact resistance measurements. *Materials Science Reports* **1988**, *3* (2), 79-137. DOI: https://doi.org/10.1016/S0920-2307(88)80006-9.

(40) Moon, I.; Choi, M. S.; Lee, S.; Nipane, A.; Hone, J.; Yoo, W. J. Analytical measurements of contact resistivity in two-dimensional WSe2 field-effect transistors. *2D Materials* **2021**, *8* (4), 045019. DOI: 10.1088/2053-1583/ac1adb.

(41) Sambles, J. R.; Elsom, K. C.; Jarvis, D. J. The electrical resistivity of gold films. Philosophical transactions of the Royal Society of London. *Series A, mathematical and physical sciences* **1982**, *304* (1486), 365-396.

(42) De Vries, J. Temperature and thickness dependence of the resistivity of thin polycrystalline aluminium, cobalt, nickel, palladium, silver and gold films. *Thin Solid Films* **1988**, *167* (1-2), 25-32.

(43) Vazirisereshk, M. R.; Sumaiya, S. A.; Martini, A.; Baykara, M. Z. Measurement of electrical contact resistance at nanoscale gold-graphite interfaces. *Applied Physics Letters* **2019**, *115* (9).

(44) Matsubara, K.; Sugihara, K.; Tsuzuku, T. Electrical resistance in the c direction of graphite. *Physical Review B* **1990**, *41* (2), 969-974. DOI: 10.1103/PhysRevB.41.969.

(45) Peng, H.; Xie, C.; Schoen, D. T.; Cui, Y. Large Anisotropy of Electrical Properties in Layer-Structured In_2Se_3 Nanowires. *Nano Lett.* **2008**, *8* (5), 1511-1516. DOI: 10.1021/nl080524d.

(46) Najmaei, S.; Neupane, M. R.; Nichols, B. M.; Burke, R. A.; Mazzoni, A. L.; Chin, M. L.; Rhodes, D. A.; Balicas, L.; Franklin, A. D.; Dubey, M. Cross-Plane Carrier Transport in Van der Waals Layered Materials. *Small* **2018**, *14* (20), 1703808.

(47) Cao, W.; Huang, M.; Yeh, C.-H.; Parto, K.; Banerjee, K. Impact of transport anisotropy on the performance of van der Waals materials-based electron devices. *IEEE Transactions on Electron Devices* **2020**, *67* (3), 1310-1316.

(48) Wiegers, a. G. Misfit layer compounds: Structures and physical properties. *Progress in Solid State Chemistry* **1996**, *24* (1-2), 1-139.

(49) Li, Y.; Gao, C.; Long, R.; Xiong, Y. Photocatalyst design based on two-dimensional materials. *Materials Today Chemistry* **2019**, *11*, 197-216. DOI: https://doi.org/10.1016/j.mtchem.2018.11.002.

(50) Chen, J.; Bailey, C. S.; Hong, Y.; Wang, L.; Cai, Z.; Shen, L.; Hou, B.; Wang, Y.; Shi, H.; Sambur, J.; et al. Plasmon-Resonant Enhancement of Photocatalysis on Monolayer WSe_2. *ACS Photonics* **2019**, *6* (3), 787-792. DOI: 10.1021/acsphotonics.9b00089.

(51) Jun, S. E.; Lee, J. K.; Jang, H. W. Two-dimensional materials for photoelectrochemical water splitting. *Energy Advances* **2023**, *2* (1), 34-53, 10.1039/D2YA00231K. DOI: 10.1039/D2YA00231K.

(52) Chen, J.; Bailey, C. S.; Cui, D.; Wang, Y.; Wang, B.; Shi, H.; Cai, Z.; Pop, E.; Zhou, C.; Cronin, S. B. Stacking Independence and Resonant Interlayer Excitation of Monolayer $WSe_2/MoSe_2$ Heterostructures for Photocatalytic Energy Conversion. *ACS Applied Nano Materials* **2020**, *3* (2), 1175-1181. DOI: 10.1021/acsanm.9b01898.

(53) Lin, Y.-R.; Cheng, W.-H.; Richter, M. H.; DuChene, J. S.; Peterson, E. A.; Went, C. M.; Al Balushi, Z. Y.; Jariwala, D.; Neaton, J. B.; Chen, L.-C.; et al. Band Edge Tailoring in Few-Layer Two-Dimensional Molybdenum Sulfide/Selenide Alloys. *The Journal of Physical Chemistry C* **2020**, *124* (42), 22893-22902. DOI: 10.1021/acs.jpcc.0c04719.

CHAPTER IV

(1) Mueller, P.; Fach, A.; John, J.; Tiwari, A. N.; Zogg, H.; Kostorz, G. Structure of Epitaxial PbSe Grown on Si(111) and Si(100) without a Fluoride Buffer Layer. *J. Appl. Phys.* **1996**, *79* (4), 1911–1916. https://doi.org/10.1063/1.361076.

(2) Zhang, K.; Ramalingom Pillai, A. D.; Nminibapiel, D.; Tangirala, M.; Chakravadhanula, V. S.; Kubel, C.; Baumgart, H.; Kochergin, V. ALD Growth of PbTe and PbSe Superlattices for Thermoelectric Applications. *ECS Trans*. **2013**, *58* (10), 131–139. https://doi.org/10.1149/05810.0131ecst.

(3) Pillai, A. D. R.; Zhang, K.; Bollenbach, K.; Nminibapiel, D.; Cao, W.; Baumgart, H.; Chakravadhanula, V. S. K.; Kubel, C.; Kochergin, V. ALD Growth of PbTe and PbSe Superlattices for Thermoelectric Applications. *ECS Trans.* **2013**, *58* (10, Atomic Layer Deposition Applications 9), 131–139, 10 pp. https://doi.org/10.1149/05810.0131ecst.

(4) Jang, M. H.; Yoo, S. S.; Kramer, M. T.; Dhar, N. K.; Gupta, M. C. Properties of Chemical Bath Deposited and Sensitized PbSe Thin Films for IR Detection. *Semicond. Sci. Technol.* **2019**, *34* (11), 115010. https://doi.org/10.1088/1361-6641/ab4789.

(5) El-Shazly, E. A. A.; Zedan, I. T.; Abd El-Rahman, K. F. Determination and Analysis of Optical Constants for Thermally Evaporated PbSe Thin Films. *Vacuum* **2011**, *86* (3), 318–323. https://doi.org/10.1016/j.vacuum.2011.07.051.

(6) Manga, K. K.; Wang, J.; Lin, M.; Zhang, J.; Nesladek, M.; Nalla, V.; Ji, W.; Loh, K. P. High-Performance Broadband Photodetector Using Solution-Processible PbSe-TiO_2-Graphene Hybrids. *Adv. Mater.* **2012**, *24* (13), 1697–1702. https://doi.org/10.1002/adma.201104399.

(7) Luther, J. M.; Law, M.; Song, Q.; Perkins, C. L.; Beard, M. C.; Nozik, A. J. Structural, Optical, and Electrical Properties of Self-Assembled Films of PbSe Nanocrystals Treated with 1,2-Ethanedithiol. *ACS Nano* **2008**, *2* (2), 271–280.

(8) Kar, A. I. Amorphous Pbse Thin Film Produced by Chemical Bath Deposition at Ph of 5-8. S*urf. Rev. Lett.* **2019**, *27* (4), 1950128. https://doi.org/10.1142/S0218625X19501282.

(9) Androulakis, J.; Todorov, I.; He, J.; Chung, D. Y.; Dravid, V.; Kanatzidis, M. Thermoelectrics from Abundant Chemical Elements: High-Performance Nanostructured PbSe-PbS. *J. Am. Chem. Soc.* **2011**, *133* (28), 10920–10927. https://doi.org/10.1021/ja203022c.

(10) Wang, H.; Pei, Y.; Lalonde, A. D.; Snyder, G. J. Heavily Doped P-Type PbSe with High Thermoelectric Performance: An Alternative for PbTe. *Adv. Mater*. **2011**, *23* (11), 1366–1370. https://doi.org/10.1002/adma.201004200.

(11) Rogacheva, E. I.; Nashchekina, O. N.; Ol'khovskaya, S. I.; Dresselhaus, M. S. Thermoelectric Transport in PbSe Quantum Wells. *AIP Conf. Proc*. **2012**, *1449* (9th European Conference on Thermoelectrics, 2011), 151–154. https://doi.org/10.1063/1.4731519.

(12) Luo, P.; Zhuge, F.; Wang, F.; Lian, L.; Liu, K.; Zhang, J.; Zhai, T. PbSe Quantum Dots Sensitized High-Mobility Bi_2O_2Se Nanosheets for High-Performance and Broadband Photodetection Beyond 2 Mm. *ACS Nano*. **2019**, *13* (8). https://doi.org/10.1021/acsnano.9b03124.

(13) Schaller, R. D.; Klimov, V. I. High Efficiency Carrier Multiplication in PbSe Nanocrystals: Implications for Solar Energy Conversion. *Phys. Rev. Lett.* **2004**, *92* (18). https://doi.org/10.1103/PhysRevLett.92.186601.

(14) Fang, X. M.; Chao, I.-N.; Strecker, B. N.; McCann, P. J.; Yuan, S.; Liu, W. K.; Santos, M. B. Molecular Beam Epitaxial Growth of Bi_2Se_3 and Ti_2Se-Doped PbSe and PbEuSe on CaF_2/Si(111). *J. Vac. Sci. Technol. B Microelectron. Nanom. Struct*. **1998**, *16* (3), 1459–1462. https://doi.org/10.1116/1.589965.

(15) Freik, D. M.; Voitkiv, V. V; Gaiduchok, G. M.; Brodin, I. I. X-Ray Diffraction Studies of Lead Chalcogenide-Based Compositions in Thin Layers. *Izv. Vyss. Uchebnykh Zaved. Fiz.* **1972**, *15* (11), 132–134.

(16) Jensen, J. D.; Schoolar, R. B. Surface Charge Transport in Lead Sulfur Selenide (PbS_xSe_{1-x}) and Lead Tin Selenide ($Pb_{1-y}Sn_ySe$) Epitaxial Films. *J. Vac. Sci. Technol.* **1976**, *13* (4), 920–925. https://doi.org/10.1116/1.569022.

(17) Tedenac, J. C.; Dal Corso, S.; Liautard, B.; Brun, G.; Charar, S.; Ohadi, A.; Fau, C.; El Kholdi, M. Heterostructures of Ternary IV-VI Semiconductors of Lead Selenide Telluride/Barium Difluoride and Lead Tin Selenide/Barium Difluoride. *Proc. Electrochem. Soc.* **1993**, *93* (10), 255–268.

(18) Wu, H. Z.; Fang, X. M.; Salas Jr., R.; McAlister, D.; McCann, P. J. Molecular Beam Epitaxy Growth of PbSe on BaF_2-Coated Si(111) and Observation of the PbSe Growth Interface. *J. Vac. Sci. Technol. B Microelectron. Nanom. Struct.* **1999**, *17* (3), 1263–1266. https://doi.org/10.1116/1.590736.

(19) Hohnke, D. K.; Hurley, M. D. Growth and Electrical Properties of Epitaxial Lead Selenide Telluride ($PbSe_xTe_{1-x}$) Layers. *J. Appl. Phys.* **1976**, *47* (11), 4975–4979. https://doi.org/10.1063/1.322506.

(20) Sachar, H. K.; Chao, I.; McCann, P. J.; Fang, X. M. Growth and Characterization of PbSe and $Pb_{1-x}Sn_xSe$ on Si (100). *J. Appl. Phys.* **1999**, *85* (10), 7398–7403. https://doi.org/10.1063/1.369369.

(21) Pashaev, A. M.; Davarashvili, O. I.; Akhvlediani, Z. G.; Enukashvili, M. I.; Bychkova, L. P.; Dzagania, M. A. Study on the Forbidden Gap Width of Strained Epitaxial Lead Selenide Layers by Optical Transmission. *J. Mater. Sci. Eng. B* **2012**, *2* (2), 142–150.

(22) McLane, G.; Zemel, J. N. Surface Interaction of Atomic Hydrogen and Molecular Oxygen on Thin Lead Selenide Epitaxic Films. *Thin Solid Films* **1971**, *7* (3/4), 229–246. https://doi.org/10.1016/0040-6090(71)90070-8.

(23) A, B. M.; D, I. B.; D, T. G.; A, Y. A.; V, S. R.; U, M. E. Some Studies on Chemically Deposited N-PbSe Thin Films. *Res. J. Chem. Sci.* **2011**, *1* (9), 37–41.

(24) Hone, F. G.; Dejene, F. B. Tuning the Optical Band Gap and Stoichiometric Ratio of Chemically Synthesized Lead Selenide Thin Films by Controlling Film Thickness. *J.*

Mater. Sci. Mater. Electron. **2017**, *28* (8), 5979–5989. https://doi.org/10.1007/s10854-016-6273-8.

(25) Wrasse, E. O.; Schmidt, T. M. Prediction of Two-Dimensional Topological Crystalline Insulator in PbSe Monolayer. *Nano Lett.* **2014**, *14* (10). https://doi.org/10.1021/nl502481f.

(26) Sachar, H. K.; Chao, I.; Fang, X. M.; McCann, P. J. Growth and Characterization of Pbse and $Pb_{1-x}Sn_1$ Se Layers on Si (100). *MRS Proc.* **1997**, *487*. https://doi.org/10.1557/proc-487-651.

(27) Strecker, B. N.; McCann, P. J.; Fang, X. M.; Hauenstein, R. J.; O'Steen, M.; Johnson, M. B. LPE Growth of Crack-Free PbSe Layers on Si(100) Using MBE-Grown PbSe/BaF_2/CaF_2 Buffer Layers. *J. Electron. Mater.* **1997**, *26* (5). https://doi.org/10.1007/s11664-997-0117-5.

(28) Zhao, F.; Ma, J.; Weng, B.; Li, D.; Bi, G.; Chen, A.; Xu, J.; Shi, Z. MBE Growth of PbSe Thin Film with a 9×105 Cm-2 Etch-Pits Density on Patterned (1 1 1)-Oriented Si Substrate. *J. Cryst. Growth* **2010**, *312* (19), 2695–2698. https://doi.org/10.1016/j.jcrysgro.2010.05.041.

(29) Zogg, H.; Maissen, C.; Blunier, S.; Teodoropol, S.; Overney, R. M.; Richmond, T.; Tomm, J. W. Thermal-Mismatch Strain Relaxation Mechanisms in Heteroepitaxial Lead Chalcogenide Layers on Silicon Substrates. *Semicond. Sci. Technol.* **1993**, *8* (1S), S337–S341. https://doi.org/10.1088/0268-1242/8/1S/075.

(30) Xu, T. N.; Wu, H. Z.; Si, J. X.; Cao, C. F. Observation of Triangle Pits in PbSe Grown by Molecular Beam Epitaxy. *Appl. Surf. Sci*. **2007**, *253* (12), 5457–5461. https://doi.org/10.1016/j.apsusc.2006.12.028.

(31) Freik, D. M.; Chobanyuk, V. M.; Sokolov, O. L.; Lopyanko, M. A. Misfit Dislocations and Electronic Processes in the Two-Layer Epitaxial Structures of Lead Chalcogenides. *Fiz. i Khimiya Tverd. Tila* **2009**, *10* (1), 9–18.

(32) Osherov, A.; Shandalov, M.; Ezersky, V.; Golan, Y. EPITAXY and Orientation Control in Chemical Solution Deposited PbS and PbSe Monocrystalline Films. *J. Cryst. Growth* **2007**, *304* (1), 169–178. https://doi.org/10.1016/j.jcrysgro.2007.02.021.

(33) Zogg, H.; Tiwari, A. N.; Blunier, S.; Maissen, C.; Masek, J. Heteroepitaxy of II-VI and IV-VI Semiconductors on Silicon Substrates. Proc. *The Int. Soc. Opt. Eng.* **1991**, *1361* (Phys. Concepts Mater. Novel Optoelectron. Device Appl. 1, Pt. 1), 406–413. https://doi.org/10.1117/12.24409.

(34) Sachar, H. K.; Chao, I.; Fang, X. M.; McCann, P. J. Growth and Characterization of PbSe and $Pb_{1-x}Sn_xSe$ Layers on Si (100). *Mater. Res. Soc. Symp. Proc.* **1998**, *487* (Semiconductors for Room-Temperature Radiation Detector Applications II), 651–656. https://doi.org/10.1557/proc-487-651.

(35) Breton, G.; Maurice, T.; Masri, P.; Charar, S.; Averous, M. Epitaxy Induced Phase Stabilization: A Comparative Experimental and Elasticity-Based Theoretical Study on MBE Grown PbSe/CaF_2/Si Epilayer. *Int. J. Inorg. Mater.* **2001**, *3* (8), 1237–1239. https://doi.org/10.1016/S1466-6049(01)00142-8.

(36) Chen, T.; Fan, C.; Zhou, W.; Zou, X.; Xu, X.; Wang, S.; Wan, Q.; Zhang, Q. Epitaxial Growth of Non-Layered PbSe Nanoplates on MoS_2 Monolayer for Infrared Photoresponse. *Appl. Phys. Express* **2019**, *12* (5). https://doi.org/10.7567/1882-0786/ab10e5.

(37) Smeller, M. M.; Heideman, C. L.; Lin, Q.; Beekman, M.; Anderson, M. D.; Zschack, P.; Anderson, I. M.; Johnson, D. C. Structure of Turbostratically Disordered Misfit Layer Compounds $[(PbSe)_{0.99}]_1[WSe_2]_1$, $[(PbSe)_{1.00}]_1[MoSe_2]_1$, and $[(SnSe)_{1.03}]_1[MoSe_2]_1$. *Zeitschrift fur Anorg. und Allg. Chemie* **2012**, *638* (15). https://doi.org/10.1002/zaac.201200408.

(38) Moore, D. B.; Stolt, M. J.; Atkins, R.; Sitts, L.; Jones, Z.; Disch, S.; Beekman, M.; Johnson, D. C. Structural and Electrical Properties of $(PbSe)_{1.16}TiSe_2$. *Emerg. Mater. Res.* **2012**, *1* (6). https://doi.org/10.1680/emr.12.00024.

(39) B. Moore, D.; Beekman, M.; Disch, S.; Zschack, P.; Häusler, I.; Neumann, W.; C. Johnson, D. Synthesis, Structure, and Properties of Turbostratically Disordered $(PbSe)_{1.18}(TiSe_2)_2$. *Chem. Mater.* **2013**, *25* (12), 2404–2409. https://doi.org/10.1021/cm400090f.

(40) Hite, O. K.; Falmbigl, M.; Alemayehu, M. B.; Esters, M.; Wood, S. R.; Johnson, D. C. Charge Density Wave Transition in $(PbSe)_{1+\delta}(VSe_2)_n$ Compounds with n = 1, 2, and 3. *Chem. Mater.* **2017**. https://doi.org/10.1021/acs.chemmater.7b01383.

(41) Cordova, D. L. M.; Kam, T. M.; Fender, S. S.; Tsai, Y. H.; Johnson, D. C. Strong Non-Epitaxial Interactions: Crystallographically Aligned PbSe on VSe_2. Phys. Status Solid Appl. Mater. Sci. 2019, 216 (15). https://doi.org/10.1002/pssa.201800896.

(42) Grosse, C.; Alemayehu, M. B.; Falmbigl, M.; Mogilatenko, A.; Chiatti, O.; Johnson, D. C.; Fischer, S. F. Superconducting Ferecrystals: Turbostratically Disordered Atomic-Scale Layered $(PbSe)_{1.14}(NbSe_2)_n$ Thin Films. *Sci. Rep*. **2016**, *6*. https://doi.org/10.1038/srep33457.

(43) Bauer, E. Phänomenologische Theorie Der Kristallabscheidung An Oberflächen. I. Zeitschrift fur Krist. - New Cryst. Struct. **1958**, *110* (1–6). https://doi.org/10.1524/zkri.1958.110.1-6.372.

(44) Parratt, L. G. Surface Studies of Solids by Total Reflection of X-Rays. *Phys. Rev.* **1954**, *95* (2). https://doi.org/10.1103/PhysRev.95.359.

(45) Mariano, A. N.; Chopra, K. L. Polymorphism in Some IV-VI Compounds Induced by High Pressure and Thin-Film Epitaxial GROWTH. *Appl. Phys. Lett.* **1967**, *10* (10). https://doi.org/10.1063/1.1754812.

(46) Hohnke, D. K.; Kaiser, S. W. Epitaxial PbSe and $Pb_{1-x}Sn_xSe$: Growth and Electrical Properties. *J. Appl. Phys.* **1974**, *45* (2). https://doi.org/10.1063/1.1663334.

(47) Miller, A. M.; Hamann, D. M.; Hadland, E. C.; Johnson, D. C. Investigating the Formation of $MoSe_2$ and $TiSe_2$ Films from Artificially Layered Precursors. *Inorg. Chem.* **2020**. https://doi.org/10.1021/acs.inorgchem.0c01626.

(48) Bronsema, K. D.; De Boer, J. L.; Jellinek, F. On the Structure of Molybdenum Diselenide and Disulfide. *ZAAC - J. Inorg. Gen. Chem.* **1986**, *540* (9–10). https://doi.org/10.1002/zaac.19865400904.

CHAPTER V

(1) Murarka, S. P. Transition Metal Silicides. *Annu. Rev. Mater. Sci.* **1983**, 13, 117–137. https://doi.org/10.1146/annurev.ms.13.080183.001001.

(2) Walser, R. M.; Bené, R. W. First Phase Nucleation in Silicon-Transition-Metal Planar Interfaces. *Appl. Phys. Lett.* **1976**, 28 (10), 624–625. https://doi.org/10.1063/1.88590.

(3) Hornbostel, M. D.; Sellinschegg, H.; Johnson, D. C. Synthesis of New Thermoelectrics Using Modulated Elemental Reactants. *Mater. Res. Soc. Symp. Proc.* **1997**, 478, 211–216. https://doi.org/10.1557/proc-478-211.

(4) Aykol, M.; Dwaraknath, S. S.; Sun, W.; Persson, K. A. Thermodynamic Limit for Synthesis of Metastable Inorganic Materials. *Sci. Adv.* **2018,** 4 (4), 1–8. https://doi.org/10.1126/sciadv.aaq0148.

(5) Novet, T.; Johnson, D. C. New Synthetic Approach to Extended Solids: Selective Synthesis of Iron Silicides via the Amorphous State. *J. Am. Chem. Soc.* **1991**, 113 (9), 3398–3403.

(6) Jones, H. Splat Cooling and Metastable Phases. *Reports Prog. Phys.* **1973**, 36 (11), 1425–1497. https://doi.org/10.1088/0034-4885/36/11/002.

(7) Kinder, J.; Arzt, E. Microstructure and Phase Composition in High-Strength Aluminium Alloys Produced by a Splat-Cooling Technique. *Int. J. Mater. Res.* **1991**, 82(7) 503–509.

(8) Scott, M. G. The Role of Melt Superheat in Splat-Quenching. *J. Mater. Sci.* **1975**, 10 (2), 269–273. https://doi.org/10.1007/BF00540350.

(9) Sare, I. R.; Honeycombe, R. W. K. Splat Cooling of Iron-Molybdenum-Carbon Alloys. *J. Mater. Sci.* **1978**, 13 (9), 1991–2002. https://doi.org/10.1007/BF00552907.

(10) Vitek, J.; Grant, N. J. Cooling-Rates in Splat-Cooling. *J. Mater. Sci*. **1972**, 7 (11), 1343–1344.

(11) Jones, H. Cooling Rates during Rapid Solidification from a Chill Surface. *Mater. Lett.* **1996**, 26 (3), 133–136. https://doi.org/10.1016/0167-577X(95)00213-8.

(12) Kugler, S.; Shimakawa, K. Preparation Techniques. *Amorph. Semicond.* **2015**, 14–23. https://doi.org/10.1017/cbo9781139094337.003.

(13) Koffel, S.; Claverie, A.; BenAssayag, G.; Scheiblin, P. Amorphization Kinetics of Germanium under Ion Implantation. *Mater. Sci. Semicond. Process*. **2006**, 9 (4-5 SPEC. ISS.), 664–667. https://doi.org/10.1016/j.mssp.2006.08.015.

(14) Impellizzeri, G.; Mirabella, S.; Grimaldi, M. G. Ion Implantation Damage and Crystalline-Amorphous Transition in Ge. *Appl. Phys. A Mater. Sci. Process.* **2011**, 103 (2), 323–328. https://doi.org/10.1007/s00339-010-6123-0.

(15) Van Der Weg, W. F.; Berntsen, A. J. M.; Saris, F. W.; Polman, A. Ion Implantation into Amorphous Solids. *Mater. Chem. Phys.* **1996**, 46 (2–3), 140–146. https://doi.org/10.1016/S0254-0584(97)80007-7.

(16) Laaziri, K.; Kycia, S.; Roorda, S.; Chicoine, M.; Robertson, J. L.; Wang, J.; Moss, S. C. High Resolution Radial Distribution Function of Pure Amorphous Silicon. *Phys. Rev. Lett.* **1999**, 82 (17), 3460–3463. https://doi.org/10.1103/PhysRevLett.82.3460.

(17) Ridgway, M. C.; Azevedo, G. D. M.; Glover, C. J.; Yu, K. M.; Foran, G. J. Common Structure in Amorphised Compound Semiconductors. *Nucl. Instruments Methods Phys. Res. Sect. B Beam Interact. with Mater. Atoms* . **2003**, 199 (1-4), 235–239. https://doi.org/10.1016/S0168-583X(02)01531-8.

(18) Koroni, C.; Olsen, T.; Wharry, J. P.; Xiong, H. Irradiation-Induced Amorphous-to-Crystalline Phase Transformations in Ceramic Materials. *Materials.* **2022**, 15 (17), 5924. https://doi.org/10.3390/ma15175924.

(19) León-Gutierrez, E.; Garcia, G.; Lopeandía, A. F.; Fraxedas, J.; Clavaguera-Mora, M. T.; Rodríguez-Viejo, J. In Situ Nanocalorimetry of Thin Glassy Organic Films. *J. Chem. Phys.* **2008**, 129 (18), 1–5. https://doi.org/10.1063/1.3009766.

(20) Swallen, S. F.; Kearns, K. L.; Mapes, M. K.; Kim, Y. S.; McMahon, R. J.; Ediger, M. D.; Wu, T.; Yu, L.; Satija, S. Organic Glasses with Exceptional Thermodynamic and Kinetic Stability. *Science*. **2007**, 315 (5810), 353–356. https://doi.org/10.1126/science.1135795.

(21) Dawson, K. J.; Kearns, K. L.; Yu, L.; Steffen, W.; Ediger, M. D. Physical Vapor Deposition as a Route to Hidden Amorphous States. *Proc. Natl. Acad. Sci. U. S. A.* **2009**, 106 (36), 15164–15170. https://doi.org/10.1073/pnas.0901469106.

(22) Kearns, K. L.; Swallen, S. F.; Ediger, M. D.; Wu, T.; Sun, Y.; Yu, L. Hiking down the Energy Landscape: Progress toward the Kauzmann Temperature via Vapor Deposition. *J. Phys. Chem. B*. **2008**, 112 (16), 4934–4942. https://doi.org/10.1021/jp7113384.

(23) Ishii, K.; Nakayama, H.; Hirabayashi, S.; Moriyama, R. Anomalously High-Density Glass of Ethylbenzene Prepared by Vapor Deposition at Temperatures Close to the Glass-Transition Temperature. *Chem. Phys. Lett.* **2008**, 459 (1–6), 109–112. https://doi.org/10.1016/j.cplett.2008.05.050.

(24) Kearns, K. L.; Swallen, S. F.; Ediger, M. D.; Wu, T.; Yu, L. Influence of Substrate Temperature on the Stability of Glasses Prepared by Vapor Deposition. *J. Chem. Phys.* **2007**, 127 (15), 154702. https://doi.org/10.1063/1.2789438.

(25) Hornbostel, M. D.; Hyer, E. J.; Thiel, J.; Johnson, D. C. Rational Synthesis of Metastable Skutterudite Compounds Using Multilayer Precursors. *J. Am. Chem. Soc.* **1997**, 119 (11), 2665–2668. https://doi.org/10.1021/ja964084g.

(26) Johnson, D. C. Controlled Synthesis of New Compounds Using Modulated Elemental Reactants. *Curr. Opin. Solid State Mater. Sci.* **1998**, 3 (2), 159–167. https://doi.org/10.1016/S1359-0286(98)80082-X.

(27) Lemon, M.; Harvel, F. G.; Gannon, R. N.; Lu, P.; Rudin, S. P.; Johnson, D. C. Targeted Synthesis of Predicted Metastable Compounds Using Modulated Elemental Reactants. *J. Vac. Sci. Technol. A.* **2023**, 41 (2), 022203. https://doi.org/10.1116/6.0002260.

(28) Martin, J. D.; Sullivan, R. M. Composition Dependence of the Nucleation Energy of Iron Antimonides from Modulated Elemental Reactants. *Chemtracts.* **2002**, 15 (1), 17–25.

(29) Pienack, N.; Bensch, W. In-Situ Monitoring of the Formation of Crystalline Solids. *Angew. Chemie - Int. Ed.* **2011**, 50 (9), 2014–2034. https://doi.org/10.1002/anie.201001180.

(30) Regus, M.; Mankovsky, S.; Polesya, S.; Kuhn, G.; Ditto, J.; Schürmann, U.; Jacquot, A.; Bartholomé, K.; Näther, C.; Winkler, M.; et al. Characterization of Cr-Rich Cr-Sb Multilayer Films: Syntheses of a New Metastable Phase Using Modulated Elemental Reactants. *J. Solid State Chem.* **2015**, 230, 254–265. https://doi.org/10.1016/j.jssc.2015.06.038.

(31) Novet, T.; Mcconnell, J. M.; Johnson, D. C. Low-Temperature Reaction of Buried Metal-Silicon Interfaces: The Evolution of Interfacial Structure. *Chem. Mater.* **1992**, 4, 473–478.

(32) Fister, L.; Johnson, D. C. Controlling Solid-State Reaction. *J. Am. Chem. Soc*. **1992**, 114, 4639–4644.

(33) Fukuto, M.; Hornbostel, M. D.; Johnson, D. C. Use of Superlattice Structure To Control Reaction Mechanism: Kinetics and Energetics of Nb_5Se_4 Formation. *J. Am. Chem. Soc.* **1994**, 116 (20), 9136–9140. https://doi.org/10.1021/ja00099a031.

(34) Bauers, S. R.; Wood, S. R.; Jensen, K. M. Ø.; Blichfeld, A. B.; Iversen, B. B.; Billinge, S. J. L.; Johnson, D. C. Structural Evolution of Iron Antimonides from Amorphous Precursors to Crystalline Products Studied by Total Scattering Techniques. *J. Am. Chem. Soc*. **2015**, 137 (30), 9652–9658. https://doi.org/10.1021/jacs.5b04838.

(35) Cordova, D. L. M.; Fender, S. S.; Hooshmand, M. S.; Buchanan, M. R.; Davis, J.; Kam, T. M.; Gannon, R. N.; Fischer, R.; Lu, P.; Hanken, B. E.; et al. The Instability of Monolayer-Thick PbSe on VSe_2. *Chem. Mater.* **2020**, 32 (18), 7992–8003. https://doi.org/10.1021/acs.chemmater.0c02922.

(36) Hadland, E. C.; Jang, H.; Wolff, N.; Robert, F.; Lygo, A. C.; Mitchson, G.; Li, D.; Lorenz, K.; Cahill, D. G.; Johnson, D. C. Ultralow Thermal Conductivity of Turbostratically Disordered $MoSe_2$ Ultra-Thin Films and Implications for Heterostructures. *Nanotechnology*. **2019**, 30, 285401. https://doi.org/10.1088/1361-6528/aafea2.

(37) Fister, L.; Li, X.-M.; McConnell, J.; Novet, T.; Johnson, D. C. Deposition System for the Synthesis of Modulated, Ultrathin-Film Composites. *J. Vac. Sci. Technol. A.* **1993**, 11 (6), 3014–3019. https://doi.org/10.1116/1.578290.

(38) Hamann, D. M.; Bardgett, D.; Cordova, D. L. M.; Maynard, L. A.; Hadland, E. C.; Lygo, A. C.; Wood, S. R.; Esters, M.; Johnson, D. C. Sub-Monolayer Accuracy in Determining the Number of Atoms per Unit Area in Ultrathin Films Using X-Ray Fluorescence. *Chem. Mater.* **2018**, 30 (18), 6209–6216. https://doi.org/10.1021/acs.chemmater.8b02591.

(39) Schneemeyer, L. F.; Sienko, M. J. Crystal Data for Mixed-Anion Molybdenum Dichalcogenides. *Inorg. Chem.* **1980**, 19 (3), 789–791.

(40) Miller, A. M.; Hamann, D. M.; Hadland, E. C.; Johnson, D. C. Investigating the Formation of $MoSe_2$ and $TiSe_2$ Films from Artificially Layered Precursors. *Inorg. Chem.* **2020**, 59 (17), 12536–12544. https://doi.org/10.1021/acs.inorgchem.0c01626.

(41) Gannon, R. N.; Choffel, M. A.; Blackwood, H. R.; Wolff, N.; Lotnyk, A.; Kienle, L.; Johnson, D. C. Growth of Crystallographically Aligned PbSe Films of Controlled Thickness on Amorphous Substrates. *Zeitschrift fur Anorg. und Allg. Chemie*. **2022**, 648, e202200015.

CHAPTER VI

(1) J. R. Chamorro, T. M. McQueen, *Acc. Chem. Res*. **2018**, *51* (11), 2918–2925

(2) G. V. Kidson, *Journal of Nuclear Materials*. **1961**, *3* (1), 21–29

(3) E. Mura, Y. Ding, Adv. *Colloid Interface Sci.* **2021**, *289*, 102361

(4) J. H. Perepezko, *Prog. Mater. Sci.* **2004**, *49* (3–4), 263–284

(5) A. M. Miller, D. C. Johnson, *J. Mater. Chem. C. Mater*. **2022**, 10, 6546–6562

(6) A. M. Gusak, A. V. Nazarov, *Journal of Physics: Condensed Matter*. **1992**, *4* (20), 4753–4758

(7) K. C. Russell, *Adv. Colloid Interface Sci*. **1980**, *13* (3–4), 205–318

(8) E. B. Watson, J. D. Price, *Geochim. Cosmochim. Acta.* **2002**, *66* (12), 2123–2138

(9) L. Fei, X. Gan, S. M. Ng, H. Wang, M. Xu, W. Lu, Y. Zhou, C. W. Leung, C. L. Mak, Y. Wang, *ACS Nano*. **2019**, *13* (1), 681–688

(10) M. Aykol, J. H. Montoya, J. Hummelshøj, *J. Am. Chem. Soc*. **2021**, *143* (24), 9244–9259

(11) S. Karthika, T. K. Radhakrishnan, P. Kalaichelvi, *Cryst. Growth Des*. **2016**, *16* (11), 6663–6681

(12) J. S. Du, Y. Bae, J. J. De Yoreo, *Nat. Rev. Mater*. **2024**, *9* (4), 229–248

(13) Z. Zhang, Y. Tang, Y. Ying, J. Guo, M. Gan, Y. Jiang, C. Xing, S. Pan, M. Xu, Y. Zhou, H. Zhang, C. W. Leung, H. Huang, C. L. Mak, L. Fei, *Mater. Horiz*. **2022**, *9* (6), 1670–1678

(14) D. Turnbull, J. C. Fisher, *J. Chem. Phys.* **1949**, *17* (1), 71–73

(15) D. Turnbull, B. Vonnegut, *Ind. Eng. Chem.* **1952**, *44* (6), 1292–1298

(16) D. Larouche, *Philosophical Magazine* **2018**, *98* (22), 2035–2060

(17) Y. Peng, F. Wang, Z. Wang, A. M. Alsayed, Z. Zhang, A. G. Yodh, Y. Han, *Nat. Mater.* **2015**, *14* (1), 101–108

(18) F. Podmaniczky, L. Gránásy, *Crystals (Basel)* 2021, *11* (4), 437

(19) D. Erdemir, A. Y. Lee, A. S. Myerson, *Acc. Chem. Res.* **2009**, *42* (5), 621–629

(20) H. Jones, *Reports on Progress in Physics*. **1973**, *36* (11), 1425–1497

(21) N. Chen, L. Martin, D. V. Luzguine-Luzgin, A. Inoue, *Materials*. **2010**, *3* (12), 5320–5339

(22) D. L. M. Cordova, D. C. Johnson, *ChemPhysChem*. **2020**, *21* (13), 1345–1368

(23) J. R. Williams, D. C. Johnson, *Inorg. Chem*. **2002**, *41* (16), 4127–4130

(24) W. Zhang, W. Zhang, J. Tan, Y. Tang, Q. Gao, *Mater. Chem. Front*. **2023**, *7* (22), 5500–5518

(25) D. M. Hamann, S. P. Rudin, T. Asaba, F. Ronning, D. L. M. Cordova, P. Lu, D. C. Johnson, *Chemistry of Materials*. **2021**, *33* (13), 5076–5084

(26) H. R. Blackwood, A. Walker, D. C. Johnson, *Chemistry of Materials*. **2024**, *36* (9), 4766–4774

(27) A. M. Miller, D. M. Hamann, E. C. Hadland, D. C. Johnson, *Inorg. Chem*. **2020**, *59* (17), 12536–12544

(28) A. M. Miller, M. Lemon, M. A. Choffel, S. R. Rich, F. Harvel, D. C. Johnson, *Zeitschrift fur Naturforschung - Section B Journal of Chemical Sciences* **2022**, *77* (4–5), 313–322

(29) N. Wainfan, L. G. Parratt, *J. Appl. Phys.* **1960**, *31* (8), 1331–1337

(30) K. D. Bronsema, J. L. De Boer, F. Jellinek, *ZAAC - Journal of Inorganic and General Chemistry* **1986**, *540* (9–10), 15–17

(31) Y. Wang, Y. Zhao, K. Liu, S. Wang, N. Li, C. Shao, F. Wang, P. Zhang, *Carbon Energy* **2023**, *5* (2)

(32) P. B. James, M. T. Lavik, *Acta. Crystallogr*. **1963**, *16* (11), 1183–1183

(33) B. L. Evans, R. A. Hazelwood, *Physica Status Solidi (a)* **1971**, *4* (1), 181–192

(34) L. H. Brixner, *Journal of Inorganic and Nuclear Chemistry* **1962**, *24* (3), 257–263

(35) E. R. Jette, F. J. Foote, *Chem. Phys*. **1935**, *3* (10), 605–616

(36) A. W. Hull, *Physical Review* **1921**, *17* (5), 571–588

(37) D. C. Johnson, *Curr. Opin. Solid State Mater. Sci*. **1998**, *3* (2), 159–167

(38) L. Fister, X. M. Li, J. McConnell, T. Novet, D. C. Johnson, *Journal of Vacuum Science & Technology A: Vacuum, Surfaces, and Films* **1993**, *11* (6), 3014–3019

(39) D. M. Hamann, D. Bardgett, D. L. M. Cordova, L. A. Maynard, E. C. Hadland, A. C. Lygo, S. R. Wood, M. Esters, D. C. Johnson, *Chemistry of Materials* **2018**, *30* (18), 6209–6216

(40) Johnson, D. C. *Curr Opin Solid State Mater Sci* **1998**, *3* (2), 159–167.

(41) Fister, L.; Li, X.-M.; McConnell, J.; Novet, T.; Johnson, D. C. *Journal of Vacuum Science & Technology A: Vacuum, Surfaces, and Films* **1993**, *11* (6), 3014–3019.

(42) Hamann, D. M.; Bardgett, D.; Cordova, D. L. M.; Maynard, L. A.; Hadland, E. C.; Lygo, A. C.; Wood, S. R.; Esters, M.; Johnson, D. C. *Chemistry of Materials* **2018**, *30* (18), 6209–6216.

(43) Kresse, G.; Furthmüller, J. *Phys. Rev. B* **1996**, *54* (16), 11169–11186.

(44) Kresse, G.; Joubert, D. *Phys. Rev. B* **1999**, *59* (3), 1758–1775.

(45) Blöchl, P. E. *Phys. Rev. B* **1994**, *50* (24), 17953–17979.

(46) Perdew, J. P.; Burke, K.; Ernzerhof, M. *Phys. Rev. Lett.* **1996**, *77* (18), 3865–3868.

(47) Methfessel, M.; Paxton, A. T. *Phys. Rev. B* **1989**, *40* (6), 3616–3621.

(48) Tkatchenko, A.; Scheffler, M. *Phys. Rev. Lett.* **2009**, *102* (7), 073005.

CHAPTER VII

(1) K. S. Novoselov, A. K. Geim, S. V. Morozov, D. Jiang, Y. Zhang, S. V. Dubonos, I. V. G. and A. A. F.; K. S. Novoselov et al. Electric Field Effect in Atomically Thin Carbon Films. **2016**, *306* (5696), 666–669.

(2) Hunt, B.; Sanchez-Yamagishi, J. D.; Young, A. F.; Yankowitz, M.; LeRoy, B. J.; Watanabe, K.; Taniguchi, T.; Moon, P.; Koshino, M.; Jarillo-Herrero, P.; Ashoori, R. C. Massive Dirac Fermions and Hofstadter Butterfly in a van Der Waals Heterostructure. *Science* **2013**, *340* (6139), 1427–1430. https://doi.org/10.1126/science.1237240.

(3) Mak, K. F.; Lee, C.; Hone, J.; Shan, J.; Heinz, T. F. Atomically Thin MoS_2 : A New Direct-Gap Semiconductor. *Phys. Rev. Lett.* **2010**, *105* (13), 136805. https://doi.org/10.1103/PhysRevLett.105.136805.

(4) Splendiani, A.; Sun, L.; Zhang, Y.; Li, T.; Kim, J.; Chim, C.-Y.; Galli, G.; Wang, F. Emerging Photoluminescence in Monolayer MoS_2. *Nano Lett.* **2010**, *10* (4), 1271–1275. https://doi.org/10.1021/nl903868w.

(5) Zhao, W.; Ghorannevis, Z.; Chu, L.; Toh, M.; Kloc, C.; Tan, P.-H.; Eda, G. Evolution of Electronic Structure in Atomically Thin Sheets of WS_2 and WSe_2. *ACS Nano* **2013**, *7* (1), 791–797. https://doi.org/10.1021/nn305275h.

(6) Ramasubramaniam, A. Large Excitonic Effects in Monolayers of Molybdenum and Tungsten Dichalcogenides. *Phys. Rev. B* **2012**, *86* (11), 115409. https://doi.org/10.1103/PhysRevB.86.115409.

(7) Costanzo, D.; Jo, S.; Berger, H.; Morpurgo, A. F. Gate-Induced Superconductivity in Atomically Thin MoS_2 Crystals. *Nat. Nanotechnol.* **2016**, *11* (4), 339–344. https://doi.org/10.1038/nnano.2015.314.

(8) Sajadi, E.; Palomaki, T.; Fei, Z.; Zhao, W.; Bement, P.; Olsen, C.; Luescher, S.; Xu, X.; Folk, J. A.; Cobden, D. H. Gate-Induced Superconductivity in a Monolayer Topological Insulator. *Science* **2018**, *362* (6417), 922–925. https://doi.org/10.1126/science.aar4426.

(9) Zhang, H.; Liu, C.-X.; Qi, X.-L.; Dai, X.; Fang, Z.; Zhang, S.-C. Topological Insulators in Bi_2Se_3, Bi_2Te_3 and Sb_2Te_3 with a Single Dirac Cone on the Surface. *Nat. Phys.* **2009**, *5* (6), 438–442. https://doi.org/10.1038/nphys1270.

(10) Hsieh, D.; Xia, Y.; Qian, D.; Wray, L.; Meier, F.; Dil, J. H.; Osterwalder, J.; Patthey, L.; Fedorov, A. V.; Lin, H.; Bansil, A.; Grauer, D.; Hor, Y. S.; Cava, R. J.; Hasan, M. Z. Observation of Time-Reversal-Protected Single-Dirac-Cone Topological-Insulator States in Bi_2Te_3 and Sb_2Te_3. *Phys. Rev. Lett.* **2009**, *103* (14), 146401. https://doi.org/10.1103/PhysRevLett.103.146401.

(11) Deng, K.; Wan, G.; Deng, P.; Zhang, K.; Ding, S.; Wang, E.; Yan, M.; Huang, H.; Zhang, H.; Xu, Z.; Denlinger, J.; Fedorov, A.; Yang, H.; Duan, W.; Yao, H.; Wu, Y.; Fan, S.; Zhang, H.; Chen, X.; Zhou, S. Experimental Observation of Topological Fermi Arcs in Type-II Weyl Semimetal $MoTe_2$. *Nat. Phys.* **2016**, *12* (12), 1105–1110. https://doi.org/10.1038/nphys3871.

(12) Hadland, E. C.; Jang, H.; Wolff, N.; Fischer, R.; Lygo, A. C.; Mitchson, G.; Li, D.; Kienle, L.; Cahill, D. G.; Johnson, D. C. Ultralow Thermal Conductivity of Turbostratically Disordered $MoSe_2$ Ultra-Thin Films and Implications for Heterostructures. *Nanotechnology* **2019**, *30* (28). https://doi.org/10.1088/1361-6528/aafea2.

(13) Ugeda, M. M.; Bradley, A. J.; Zhang, Y.; Onishi, S.; Chen, Y.; Ruan, W.; Ojeda-Aristizabal, C.; Ryu, H.; Edmonds, M. T.; Tsai, H.-Z.; Riss, A.; Mo, S.-K.; Lee, D.; Zettl, A.; Hussain, Z.; Shen, Z.-X.; Crommie, M. F. Characterization of Collective Ground States in Single-Layer $NbSe_2$. *Nat. Phys.* **2016**, *12* (1), 92–97. https://doi.org/10.1038/nphys3527.

(14) Xi, X.; Zhao, L.; Wang, Z.; Berger, H.; Forró, L.; Shan, J.; Mak, K. F. Strongly Enhanced Charge-Density-Wave Order in Monolayer $NbSe_2$. *Nat. Nanotechnol.* **2015**, *10* (9), 765–769. https://doi.org/10.1038/nnano.2015.143.

(15) Yang, W.; Kim, D.; Kim, H. K.; Kim, T.-H. Thickness Dependent Charge Density Wave Networks on Thin 1T-TaS_2. *J. Korean Phys. Soc.* **2023**, *82* (3), 293–297. https://doi.org/10.1007/s40042-023-00704-1.

(16) Hite, O. K.; Falmbigl, M.; Alemayehu, M. B.; Esters, M.; Wood, S. R.; Johnson, D. C. Charge Density Wave Transition in $(PbSe)_{1+\delta}(VSe_2)_n$ Compounds with n = 1, 2, and 3. *Chem. Mater.* **2017**, *29* (13), 5646–5653. https://doi.org/10.1021/acs.chemmater.7b01383.

(17) Li, X.; Zhu, H. Two-Dimensional MoS_2: Properties, Preparation, and Applications. *J. Materiomics* **2015**, *1* (1), 33–44. https://doi.org/10.1016/j.jmat.2015.03.003.

(18) Akinwande, D.; Brennan, C. J.; Bunch, J. S.; Egberts, P.; Felts, J. R.; Gao, H.; Huang, R.; Kim, J.-S.; Li, T.; Li, Y.; Liechti, K. M.; Lu, N.; Park, H. S.; Reed, E. J.; Wang, P.; Yakobson, B. I.; Zhang, T.; Zhang, Y.-W.; Zhou, Y.; Zhu, Y. A Review on Mechanics and Mechanical Properties of 2D Materials—Graphene and Beyond. *Extreme Mech. Lett.* **2017**, *13*, 42–77. https://doi.org/10.1016/j.eml.2017.01.008.

(19) Andrei, E. Y.; MacDonald, A. H. Graphene Bilayers with a Twist. *Nat. Mater.* **2020**, *19* (12), 1265–1275. https://doi.org/10.1038/s41563-020-00840-0.

(20) Zhou, S. Y.; Gweon, G.-H.; Fedorov, A. V.; First, P. N.; de Heer, W. A.; Lee, D.-H.; Guinea, F.; Castro Neto, A. H.; Lanzara, A. Substrate-Induced Bandgap Opening in Epitaxial Graphene. *Nat. Mater.* **2007**, *6* (10), 770–775. https://doi.org/10.1038/nmat2003.

(21) Geim, A. K.; Grigorieva, I. V. Van Der Waals Heterostructures. *Nature* **2013**, *499* (7459), 419–425. https://doi.org/10.1038/nature12385.

(22) Liu, Y.; Weiss, N. O.; Duan, X.; Cheng, H.-C.; Huang, Y.; Duan, X. Van Der Waals Heterostructures and Devices. *Nat. Rev. Mater.* **2016**, *1* (9), 16042. https://doi.org/10.1038/natrevmats.2016.42.

(23) Ajayan, P.; Kim, P.; Banerjee, K. Two-Dimensional van Der Waals Materials. *Phys. Today* **2016**, *69* (9), 38–44. https://doi.org/10.1063/PT.3.3297.

(24) Rivera, P.; Yu, H.; Seyler, K. L.; Wilson, N. P.; Yao, W.; Xu, X. Interlayer Valley Excitons in Heterobilayers of Transition Metal Dichalcogenides. *Nat. Nanotechnol.* **2018**, *13* (11), 1004–1015. https://doi.org/10.1038/s41565-018-0193-0.

(25) Novoselov, K. S.; Mishchenko, A.; Carvalho, A.; Castro Neto, A. H. 2D Materials and van Der Waals Heterostructures. *Science* **2016**, *353* (6298), aac9439. https://doi.org/10.1126/science.aac9439.

(26) Liu, Y.; Huang, Y.; Duan, X. Van Der Waals Integration before and beyond Two-Dimensional Materials. *Nature* **2019**, *567* (7748), 323–333. https://doi.org/10.1038/s41586-019-1013-x.

(27) Wang, W.; Clark, N.; Hamer, M.; Carl, A.; Tovari, E.; Sullivan-Allsop, S.; Tillotson, E.; Gao, Y.; de Latour, H.; Selles, F.; Howarth, J.; Castanon, E. G.; Zhou, M.; Bai, H.; Li, X.; Weston, A.; Watanabe, K.; Taniguchi, T.; Mattevi, C.; Bointon, T. H.; Wiper, P. V.; Strudwick, A. J.; Ponomarenko, L. A.; Kretinin, A. V.; Haigh, S. J.; Summerfield, A.; Gorbachev, R. Clean Assembly of van Der Waals Heterostructures Using Silicon Nitride Membranes. *Nat. Electron.* **2023**, *6* (12), 981–990. https://doi.org/10.1038/s41928-023-01075-y.

(28) Rivera, P.; Schaibley, J. R.; Jones, A. M.; Ross, J. S.; Wu, S.; Aivazian, G.; Klement, P.; Seyler, K.; Clark, G.; Ghimire, N. J.; Yan, J.; Mandrus, D. G.; Yao, W.; Xu, X. Observation of Long-Lived Interlayer Excitons in Monolayer $MoSe_2$–WSe_2 Heterostructures. *Nat. Commun.* **2015**, *6* (1), 6242. https://doi.org/10.1038/ncomms7242.

(29) Lei, C.; Chen, S.; MacDonald, A. H. Magnetized Topological Insulator Multilayers. *Proc. Natl. Acad. Sci.* **2020**, *117* (44), 27224–27230. https://doi.org/10.1073/pnas.2014004117.

(30) Coelho, P. M.; Nguyen Cong, K.; Bonilla, M.; Kolekar, S.; Phan, M.-H.; Avila, J.; Asensio, M. C.; Oleynik, I. I.; Batzill, M. Charge Density Wave State Suppresses Ferromagnetic Ordering in VSe2 Monolayers. *J. Phys. Chem. C* **2019**, *123* (22), 14089–14096. https://doi.org/10.1021/acs.jpcc.9b04281.

(31) Ma, Y.; Dai, Y.; Guo, M.; Niu, C.; Zhu, Y.; Huang, B. Evidence of the Existence of Magnetism in Pristine VX_2 Monolayers (X = S, Se) and Their Strain-Induced Tunable Magnetic Properties. *ACS Nano* **2012**, *6* (2), 1695–1701. https://doi.org/10.1021/nn204667z.

(32) Esters, M.; Hennig, R. G.; Johnson, D. C. Dynamic Instabilities in Strongly Correlated VSe_2 Monolayers and Bilayers. *Phys. Rev. B* **2017**, *96* (23), 235147. https://doi.org/10.1103/PhysRevB.96.235147.

(33) Pan, H. Electronic and Magnetic Properties of Vanadium Dichalcogenides Monolayers Tuned by Hydrogenation. *J. Phys. Chem. C* **2014**, *118* (24), 13248–13253. https://doi.org/10.1021/jp503030b.

(34) Manchanda, P.; Skomski, R. 2D Transition-Metal Diselenides: Phase Segregation, Electronic Structure, and Magnetism. *J. Phys. Condens. Matter* **2016**, *28* (6), 064002. https://doi.org/10.1088/0953-8984/28/6/064002.

(35) Du, J.; Xia, C.; Xiong, W.; Wang, T.; Jia, Y.; Li, J. Two-Dimensional Transition-Metal Dichalcogenides-Based Ferromagnetic van Der Waals Heterostructures. *Nanoscale* **2017**, *9* (44), 17585–17592. https://doi.org/10.1039/C7NR06473J.

(36) Fuh, H.-R.; Chang, C.-R.; Wang, Y.-K.; Evans, R. F. L.; Chantrell, R. W.; Jeng, H.-T. Newtype Single-Layer Magnetic Semiconductor in Transition-Metal Dichalcogenides VX_2 (X = S, Se and Te). *Sci. Rep.* **2016**, *6* (1), 32625. https://doi.org/10.1038/srep32625.

(37) Bayard, M.; Sienko, M. J. Anomalous Electrical and Magnetic Properties of Vanadium Diselenide. *J. Solid State Chem.* **1976**, *19* (4), 325–329. https://doi.org/10.1016/0022-4596(76)90184-5.

(38) Strocov, V. N.; Shi, M.; Kobayashi, M.; Monney, C.; Wang, X.; Krempasky, J.; Schmitt, T.; Patthey, L.; Berger, H.; Blaha, P. Three-Dimensional Electron Realm in VSe_2 by Soft-X-Ray Photoelectron Spectroscopy: Origin of Charge-Density Waves. *Phys. Rev. Lett.* **2012**, *109* (8), 086401. https://doi.org/10.1103/PhysRevLett.109.086401.

(39) Diego, J.; Subires, D.; Said, A. H.; Chaney, D. A.; Korshunov, A.; Garbarino, G.; Diekmann, F.; Mahatha, S. K.; Pardo, V.; Wilkinson, J. M.; Lord, J. S.; Strempfer, J.; Perez, P. J. B.; Francoual, S.; Popescu, C.; Tallarida, M.; Dai, J.; Bianco, R.; Monacelli, L.; Calandra, M.; Bosak, A.; Mauri, F.; Rossnagel, K.; Fumega, A. O.; Errea, I.; Blanco-Canosa, S. Electronic Structure and Lattice Dynamics of 1T-VSe_2: Origin of the Three-Dimensional Charge Density Wave. *Phys. Rev. B* **2024**, *109* (3), 035133. https://doi.org/10.1103/PhysRevB.109.035133.

(40) Bonilla, M.; Kolekar, S.; Ma, Y.; Diaz, H. C.; Kalappattil, V.; Das, R.; Eggers, T.; Gutierrez, H. R.; Phan, M.-H.; Batzill, M. Strong Room-Temperature Ferromagnetism in VSe_2 Monolayers on van Der Waals Substrates. *Nat. Nanotechnol.* **2018**, *13* (4), 289–293. https://doi.org/10.1038/s41565-018-0063-9.

(41) Feng, J.; Biswas, D.; Rajan, A.; Watson, M. D.; Mazzola, F.; Clark, O. J.; Underwood, K.; Marković, I.; McLaren, M.; Hunter, A.; Burn, D. M.; Duffy, L. B.; Barua, S.; Balakrishnan, G.; Bertran, F.; Le Fèvre, P.; Kim, T. K.; Van Der Laan, G.; Hesjedal, T.; Wahl, P.; King, P. D. C. Electronic Structure and Enhanced Charge-Density Wave Order of Monolayer VSe_2. *Nano Lett.* **2018**, *18* (7), 4493–4499. https://doi.org/10.1021/acs.nanolett.8b01649.

(42) Yin, L.; Berlijn, T.; Juneja, R.; Lindsay, L.; Parker, D. S. Competing Magnetic and Nonmagnetic States in Monolayer VSe_2 with Charge Density Wave. *Phys. Rev. B* **2022**, *106* (8), 085117. https://doi.org/10.1103/PhysRevB.106.085117.

(43) Atkins, R.; Dolgos, M.; Fiedler, A.; Grosse, C.; Fischer, S. F.; Rudin, S. P.; Johnson, D. C. Synthesis and Systematic Trends in Structure and Electrical Properties of $[(SnSe)_{1.15}]_m(VSe_2)_1$, m = 1, 2, 3, and 4. *Chem. Mater.* **2014**, *26* (9), 2862–2872. https://doi.org/10.1021/cm5004774.

(44) Cordova, D. L. M.; Fender, S. S.; Kam, T. M.; Seyd, J.; Albrecht, M.; Lu, P.; Fischer, R.; Johnson, D. C. Designed Synthesis and Structure-Property Relationships of Kinetically Stable $[(PbSe)_{1+\delta}]_m(VSe_2)_1$ (m = 1, 2, 3, 4) Heterostructures. *Chem. Mater.* **2019**, *31* (20), 8473–8483. https://doi.org/10.1021/acs.chemmater.9b02826.

(45) Fister, L.; Li, X.-M.; McConnell, J.; Novet, T.; Johnson, D. C. Deposition System for the Synthesis of Modulated, Ultrathin-Film Composites. *J. Vac. Sci. Technol. Vac. Surf. Films* **1993**, *11* (6), 3014–3019. https://doi.org/10.1116/1.578290.

(46) Johnson, D. C. Controlled Synthesis of New Compounds Using Modulated Elemental Reactants. *Curr. Opin. Solid State Mater. Sci.* **1998**, *3* (2), 159–167. https://doi.org/10.1016/S1359-0286(98)80082-X.

(47) Hamann, D. M.; Bardgett, D.; Cordova, D. L. M.; Maynard, L. A.; Hadland, E. C.; Lygo, A. C.; Wood, S. R.; Esters, M.; Johnson, D. C. Sub-Monolayer Accuracy in Determining the Number of Atoms per Unit Area in Ultrathin Films Using X-Ray Fluorescence. *Chem. Mater.* **2018**, *30* (18), 6209–6216. https://doi.org/10.1021/acs.chemmater.8b02591.

(48) J, V. D. P. L. A Method of Measuring the Resistivity and Hall Coefficient on Lamellae of Arbitrary Shape. *Philips Tech. Rev.* **1958**, *20*, 220–224.

(49) Westover, R.; Atkins, R. A.; Falmbigl, M.; Ditto, J. J.; Johnson, D. C. Self-Assembly of Designed Precursors: A Route to Crystallographically Aligned New Materials with Controlled Nanoarchitecture. *J. Solid State Chem.* **2016**, *236*, 173–185. https://doi.org/10.1016/j.jssc.2015.08.018.

(50) Wainfan, N.; Parratt, L. G. X-Ray Reflection Studies of the Anneal and Oxidation of Some Thin Solid Films. *J. Appl. Phys.* **1960**, *31* (8), 1331–1337. https://doi.org/10.1063/1.1735837.

(51) Rudin, S. P.; Johnson, D. C. Density Functional Theory Calculations of the Turbostratically Disordered Compound $[(SnSe)_{1+y}](VSe_2)_n$. *Phys. Rev. B* **2015**, *91* (14), 144203. https://doi.org/10.1103/PhysRevB.91.144203.

(52) Wang, Y.; Hamann, D. M.; Cordova, D. L. M.; Chen, J.; Wang, B.; Shen, L.; Cai, Z.; Shi, H.; Karapetrova, E.; Aravind, I.; Shi, L.; Johnson, D. C.; Cronin, S. B. Enhanced Low-Temperature Thermoelectric Performance in $(PbSe)_{1+\delta}(VSe_2)_1$ Heterostructures Due to

Highly Correlated Electrons in Charge Density Waves. *Nano Lett.* **2020**, *20* (11), 8008–8014. https://doi.org/10.1021/acs.nanolett.0c02882.

(53) Falmbigl, M.; Fiedler, A.; Atkins, R. E.; Fischer, S. F.; Johnson, D. C. Suppressing a Charge Density Wave by Changing Dimensionality in the Ferecrystalline Compounds $([SnSe]_{1.15})_1(VSe_2)_n$ with n = 1, 2, 3, 4. *Nano Lett.* **2015**, *15* (2), 943–948. https://doi.org/10.1021/nl503708j.

(54) Alemayehu, M. B.; Mitchson, G.; Ditto, J.; Hanken, B. E.; Asta, M.; Johnson, D. C. Charge Transfer between PbSe and $NbSe_2$ in $[(PbSe)_{1.14}]_m(NbSe_2)_1$ Ferecrystalline Compounds. *Chem. Mater.* **2014**, *26* (5), 1859–1866. https://doi.org/10.1021/cm404018a.

(55) B. Alemayehu, M.; Ta, K.; Falmbigl, M.; C. Johnson, D. Charge Transfer vs. Dimensionality: What Affects the Transport Properties of Ferecrystals? **2015**. https://doi.org/10.1039/C4NR07338J.

(56) Falmbigl, M.; Putzky, D.; Ditto, J.; Esters, M.; Bauers, S. R.; Ronning, F.; Johnson, D. C. Influence of Defects on the Charge Density Wave of $([SnSe]_{1+\delta})_1(VSe_2)_1$ Ferecrystals. *ACS Nano* **2015**, *9* (8), 8440–8448. https://doi.org/10.1021/acsnano.5b03361.

(57) Zunger, A.; Freeman, A. J. Electronic Structure of 1T-VSe_2. *Phys. Rev. B - Condens. Matter Mater. Phys.* **1979**, *19* (12), 6001–6009.

(58) Falmbigl, M.; Hay, Z.; Ditto, J.; Mitchson, G.; Johnson, D. C. Modifying a Charge Density Wave Transition by Modulation Doping: Ferecrystalline Compounds $([Sn_{1-x}Bi_xSe]_{1.15})_1(VSe_2)_1$ with $0 \leq x \leq 0.66$. *J. Mater. Chem. C* **2015**, *3* (47), 12308–12315. https://doi.org/10.1039/c5tc03130c.

CHAPTER VIII

(1) K. S. Novoselov, A. K. Geim, S. V. Morozov, D. Jiang, Y. Zhang, S. V. Dubonos, I. V. G. and A. A. F.; K. S. Novoselov et al. Electric Field Effect in Atomically Thin Carbon Films. **2016**, *306* (5696), 666–669.

(2) Fan, F. R.; Wu, W. Emerging Devices Based on Two-Dimensional Monolayer Materials for Energy Harvesting. *Research* **2019**, *2019*, 2019/7367828. https://doi.org/10.34133/2019/7367828.

(3) Gong, C.; Zhang, Y.; Chen, W.; Chu, J.; Lei, T.; Pu, J.; Dai, L.; Wu, C.; Cheng, Y.; Zhai, T.; Li, L.; Xiong, J. Electronic and Optoelectronic Applications Based on 2D Novel Anisotropic Transition Metal Dichalcogenides. *Adv. Sci.* **2017**, *4* (12), 1700231. https://doi.org/10.1002/advs.201700231.

(4) Huang, X.; Liu, C.; Zhou, P. 2D Semiconductors for Specific Electronic Applications: From Device to System. *Npj 2D Mater. Appl.* **2022**, *6* (1), 51. https://doi.org/10.1038/s41699-022-00327-3.

(5) Mueller, T.; Malic, E. Exciton Physics and Device Application of Two-Dimensional Transition Metal Dichalcogenide Semiconductors. *Npj 2D Mater. Appl.* **2018**, *2* (1), 29. https://doi.org/10.1038/s41699-018-0074-2.

(6) Radisavljevic, B.; Radenovic, A.; Brivio, J.; Giacometti, V.; Kis, A. Single-Layer MoS2 Transistors. *Nat. Nanotechnol.* **2011**, *6* (3), 147–150. https://doi.org/10.1038/nnano.2010.279.

(7) Lopez-Sanchez, O.; Lembke, D.; Kayci, M.; Radenovic, A.; Kis, A. Ultrasensitive Photodetectors Based on Monolayer MoS2. *Nat. Nanotechnol.* **2013**, *8* (7), 497–501. https://doi.org/10.1038/nnano.2013.100.

(8) Sangwan, V. K.; Jariwala, D.; Kim, I. S.; Chen, K.-S.; Marks, T. J.; Lauhon, L. J.; Hersam, M. C. Gate-Tunable Memristive Phenomena Mediated by Grain Boundaries in Single-Layer MoS_2. *Nat. Nanotechnol.* **2015**, *10* (5), 403–406. https://doi.org/10.1038/nnano.2015.56.

(9) Mak, K. F.; He, K.; Shan, J.; Heinz, T. F. Control of Valley Polarization in Monolayer MoS_2 by Optical Helicity. *Nat. Nanotechnol.* **2012**, *7* (8), 494–498. https://doi.org/10.1038/nnano.2012.96.

(10) Kazemi, S. A.; Yengejeh, S. I.; Wang, V.; Wen, W.; Wang, Y. Theoretical Understanding of Electronic and Mechanical Properties of 1T′ Transition Metal Dichalcogenide Crystals. *Beilstein J. Nanotechnol.* **2022**, *13* (1), 160–171. https://doi.org/10.3762/bjnano.13.11.

(11) Molina-Sánchez, A.; Hummer, K.; Wirtz, L. Vibrational and Optical Properties of MoS_2: From Monolayer to Bulk. *Surf. Sci. Rep.* **2015**, *70* (4), 554–586. https://doi.org/10.1016/j.surfrep.2015.10.001.

(12) Ermolaev, G. A.; Stebunov, Y. V.; Vyshnevyy, A. A.; Tatarkin, D. E.; Yakubovsky, D. I.; Novikov, S. M.; Baranov, D. G.; Shegai, T.; Nikitin, A. Y.; Arsenin, A. V.; Volkov, V. S. Broadband Optical Properties of Monolayer and Bulk MoS_2. *Npj 2D Mater. Appl.* **2020**, *4* (1), 21. https://doi.org/10.1038/s41699-020-0155-x.

(13) Velický, M.; Toth, P. S. From Two-Dimensional Materials to Their Heterostructures: An Electrochemist's Perspective. *Appl. Mater. Today* **2017**, *8*, 68–103. https://doi.org/10.1016/j.apmt.2017.05.003.

(14) Wang, P.; Jia, C.; Huang, Y.; Duan, X. Van Der Waals Heterostructures by Design: From 1D and 2D to 3D. *Matter* **2021**, *4* (2), 552–581. https://doi.org/10.1016/j.matt.2020.12.015.

(15) Mukhopadhyay, T.; Mahata, A.; Adhikari, S.; Zaeem, M. A. Effective Mechanical Properties of Multilayer Nano-Heterostructures. *Sci. Rep.* **2017**, *7* (1), 15818. https://doi.org/10.1038/s41598-017-15664-3.

(16) Duong, D. L.; Yun, S. J.; Lee, Y. H. Van Der Waals Layered Materials: Opportunities and Challenges. *ACS Nano* **2017**, *11* (12), 11803–11830. https://doi.org/10.1021/acsnano.7b07436.

(17) Zullo, L.; Marini, G.; Cren, T.; Calandra, M. Misfit Layer Compounds as Ultratunable Field Effect Transistors: From Charge Transfer Control to Emergent Superconductivity. *Nano Lett.* **2023**, *23* (14), 6658–6663. https://doi.org/10.1021/acs.nanolett.3c01860.

(18) Ng, N.; McQueen, T. M. Misfit Layered Compounds: Unique, Tunable Heterostructured Materials with Untapped Properties. *APL Mater.* **2022**, *10* (10), 100901. https://doi.org/10.1063/5.0101429.

(19) Lin, Q.; Smeller, M.; Heideman, C. L.; Zschack, P.; Koyano, M.; Anderson, M. D.; Kykyneshi, R.; Keszler, D. A.; Anderson, I. M.; Johnson, D. C. Rational Synthesis and Characterization of a New Family of Low Thermal Conductivity Misfit Layer Compounds [(PbSe)0.99]m(WSe2)n'. *Chem. Mater.* **2010**, *22* (3), 1002–1009. https://doi.org/10.1021/cm901952v.

(20) Leriche, R. T.; Palacio-Morales, A.; Campetella, M.; Tresca, C.; Sasaki, S.; Brun, C.; Debontridder, F.; David, P.; Arfaoui, I.; Šofranko, O.; Samuely, T.; Kremer, G.; Monney, C.; Jaouen, T.; Cario, L.; Calandra, M.; Cren, T. Misfit Layer Compounds: A Platform for Heavily Doped 2D Transition Metal Dichalcogenides. *Adv. Funct. Mater.* **2021**, *31* (6), 2007706. https://doi.org/10.1002/adfm.202007706.

(21) Khadiev, A.; Sreedhara, M. B.; Hettler, S.; Novikov, D.; Arenal, R.; Tenne, R. Misfit Layered Compounds: Insights into Chemical, Kinetic, and Thermodynamic Stability of Nanophases. *Acc. Chem. Res.* **2024**, *57* (22), 3243–3253. https://doi.org/10.1021/acs.accounts.4c00412.

(22) Zullo, L.; Marini, G.; Cren, T.; Calandra, M. Misfit Layer Compounds as Ultratunable Field Effect Transistors: From Charge Transfer Control to Emergent Superconductivity. *Nano Lett.* **2023**, *23* (14), 6658–6663. https://doi.org/10.1021/acs.nanolett.3c01860.

(23) Esters, M.; Hennig, R. G.; Johnson, D. C. Insights into the Charge-Transfer Stabilization of Heterostructure Components with Unstable Bulk Analogs. *Chem. Mater.* **2018**, *30* (14), 4738–4747. https://doi.org/10.1021/acs.chemmater.8b01594.

(24) Choffel, M. A.; Gannon, R. N.; Göhler, F.; Miller, A. M.; Medlin, D. L.; Seyller, T.; Johnson, D. C. Synthesis and Electrical Properties of a New Compound $(BiSe)_{0.97}(Bi_2Se_3)_{1.26}(BiSe)_{0.97}(MoSe_2)$ Containing Metallic 1T-$MoSe_2$. *Chem. Mater.* **2021**, *33* (16), 6403–6411. https://doi.org/10.1021/acs.chemmater.1c01623.

(25) Choffel, M. A.; Kam, T. M.; Johnson, D. C. Substituent Effects in the Synthesis of Heterostructures. *Inorg. Chem.* **2021**, *60* (13), 9598–9606. https://doi.org/10.1021/acs.inorgchem.1c00811.

(26) Zhang, Y.; Chang, T.-R.; Zhou, B.; Cui, Y.-T.; Yan, H.; Liu, Z.; Schmitt, F.; Lee, J.; Moore, R.; Chen, Y.; Lin, H.; Jeng, H.-T.; Mo, S.-K.; Hussain, Z.; Bansil, A.; Shen, Z.-X. Direct Observation of the Transition from Indirect to Direct Bandgap in Atomically Thin Epitaxial $MoSe_2$. *Nat. Nanotechnol.* **2014**, *9* (2), 111–115. https://doi.org/10.1038/nnano.2013.277.

(27) Ugeda, M. M.; Bradley, A. J.; Shi, S.-F.; da Jornada, F. H.; Zhang, Y.; Qiu, D. Y.; Ruan, W.; Mo, S.-K.; Hussain, Z.; Shen, Z.-X.; Wang, F.; Louie, S. G.; Crommie, M. F. Giant Bandgap Renormalization and Excitonic Effects in a Monolayer Transition Metal Dichalcogenide Semiconductor. *Nat. Mater.* **2014**, *13* (12), 1091–1095. https://doi.org/10.1038/nmat4061.

(28) Rivera, P.; Schaibley, J. R.; Jones, A. M.; Ross, J. S.; Wu, S.; Aivazian, G.; Klement, P.; Seyler, K.; Clark, G.; Ghimire, N. J.; Yan, J.; Mandrus, D. G.; Yao, W.; Xu, X. Observation of Long-Lived Interlayer Excitons in Monolayer MoSe2–WSe2 Heterostructures. *Nat. Commun.* **2015**, *6* (1), 6242. https://doi.org/10.1038/ncomms7242.

(29) Creazzo, F. Engineering of MoSe2 and WSe2 Monolayers and Heterostructures by DFT-Molecular Dynamics Simulations. *ACS Appl. Mater. Interfaces* **2025**. https://doi.org/10.1021/acsami.5c07971.

(30) Gupta, P.; Solanki, R. G.; Patel, P.; Sujata, K. M.; Kumar, R.; Pandit, A. Enhanced Antibacterial and Photoluminescence Activities of ZnSe Nanostructures. *ACS Omega* **2023**, *8* (15), 13670–13679. https://doi.org/10.1021/acsomega.2c07654.

(31) Zuala, L.; Agarwal, P. Growth and Characterization of ZnSe Nanocrystals Synthesized Using Solvothermal Process. *J. Mater. Sci. Mater. Electron.* **2020**, *31* (17), 14756–14766. https://doi.org/10.1007/s10854-020-04039-6.

(32) Jørgensen, J. E.; Jensen, T. R.; Hanson, J. C. Hydrothermal Synthesis of Nanocrystalline ZnSe: An in Situ Synchrotron Radiation X-Ray Powder Diffraction Study. *J. Solid State Chem.* **2008**, *181* (8), 1925–1929. https://doi.org/10.1016/j.jssc.2008.04.026.

(33) Yadav, B. K.; Singh, P.; Pandey, D. K. Synthesis and Non-Destructive Characterization of Zinc Selenide Thin Films. *Z. Naturforschung - Sect. J. Phys. Sci.* **2019**, *74* (11), 993–999. https://doi.org/10.1515/zna-2019-0112.

(34) Suryanarayana, C.; Al-Joubori, A. A.; Türker, F.; Seelam, U. R. Synthesis of Nanocrystalline ZnSe by Mechanical Alloying. *J. Mater. Res.* **2023**, *38* (18), 4261–4271. https://doi.org/10.1557/s43578-023-01139-x.

(35) Che, J.; Yao, X.; Wan, X.; Jiang, H. Q.; Wang, M. Q. Synthesis of ZnSe Nanocrystalline Powders by Mechanochemical Reaction. *J. Electroceramics* **2008**, *21* (1-4 SPEC. ISS.), 729–732. https://doi.org/10.1007/s10832-007-9288-y.

(36) Lee, H. K.; Ng, E. K.; Lau, K. Y.; Mohd Yusoff, N.; Mahdi, M. A.; Ng, S. P.; Kamarudin, M. A.; Latif, A. A.; Osman, N. H.; Talib, Z. A.; Liew, J. Y. C. Zinc Selenide Saturable Absorber for Ultrashort Pulse Fiber Laser Generation in C–Band Region. *Opt. Mater.* **2020**, *107* (May), 110100. https://doi.org/10.1016/j.optmat.2020.110100.

(37) Miller, A. M.; Lemon, M.; Choffel, M. A.; Rich, S. R.; Harvel, F.; Johnson, D. C. Extracting Information from X-Ray Diffraction Patterns Containing Laue Oscillations. *Z. Naturforschung - Sect. B J. Chem. Sci.* **2022**, *77* (4–5), 313–322. https://doi.org/10.1515/znb-2022-0020.

(38) Blackwood, H. R.; Walker, A.; Johnson, D. C. Synthesizing Amorphous Precursors through Control of Local Composition. *Chem. Mater.* **2024**, *36* (9), 4766–4774. https://doi.org/10.1021/acs.chemmater.4c00554.

(39) Park, Y. S.; Chan, F. L. Photoconductivity Spectral Response and Lattice Parameters of Hexagonal ZnSe. *J. Appl. Phys.* **1965**, *36* (3), 800–801. https://doi.org/10.1063/1.1714222.

(40) Lin, W.; Tamargo, M. C.; Steiner, J.; Wei, H.-Y.; Sarney, W.; Salamanca-Riba, L.; Fitzpatrick, B. J. Growth and Characterization of Hexagonal (Zn,Mg)(S,Se) Bulk Substrates. *J. Cryst. Growth* **2000**, *212* (1), 83–91. https://doi.org/10.1016/S0022-0248(00)00027-0.

(41) Bieker, S.; Pfeuffer, R.; Kiessling, T.; Tarakina, N.; Schumacher, C.; Ossau, W.; Molenkamp, L. W.; Karczewski, G. Polytypism and Band Alignment in ZnSe Nanowires

Revealed by Photoluminescence Spectroscopy of Embedded (Zn,Cd)Se Quantum Dots. *Phys. Rev. B* **2015**, *91* (12), 125301. https://doi.org/10.1103/PhysRevB.91.125301.

(42) Boutaiba, F.; Belabbes, A.; Ferhat, M.; Bechstedt, F. Polytypism in ZnS, ZnSe, and ZnTe: First-Principles Study. *Phys. Rev. B* **2014**, *89* (24), 245308. https://doi.org/10.1103/PhysRevB.89.245308.

APPENDIX A

(1) Mesoza Cordova, D. L.; Kam, T. M.; Gannon, R. N.; Lu, P.; Johnson, D. C. Controlling the Self-Assembly of New Metastable Tin Vanadium Selenides Using Composition and Nanoarchitecture of Precursors. *J. Am. Chem. Soc.* **2020**, *142* (30), 13145–13154.

(2) Falmbigl, M.; Putzky, D.; Ditto, J.; Esters, M.; Bauers, S. R.; Ronning, F.; Johnson, D. C. Influence of Defects on the Charge Density Wave of ([SnSe]1+δ)1(VSe2)1 Ferecrystals. *ACS Nano* **2015**, *9* (8), 8440–8448.

(3) Cordova, D. L. M.; Fender, S. S.; Kam, T. M.; Seyd, J.; Albrecht, M.; Lu, P.; Fischer, R.; Johnson, D. C. Designed Synthesis and Structure–Property Relationships of Kinetically Stable [(PbSe)1+δ]m(VSe2)1 (m = 1, 2, 3, 4) Heterostructures. *Chem. Mater.* **2019**, *31* (20), 8473–8483.

APPENDIX D

(1) Johnson, D. C. Controlled Synthesis of New Compounds Using Modulated Elemental Reactants. *Curr Opin Solid State Mater Sci* **1998**, *3* (2), 159–167. https://doi.org/10.1016/S1359-0286(98)80082-X.

(2) Fister, L.; Li, X.-M.; McConnell, J.; Novet, T.; Johnson, D. C. Deposition System for the Synthesis of Modulated, Ultrathin-Film Composites. *Journal of Vacuum Science & Technology A: Vacuum, Surfaces, and Films* **1993**, *11* (6), 3014–3019. https://doi.org/10.1116/1.578290.

(3) Hamann, D. M.; Bardgett, D.; Cordova, D. L. M.; Maynard, L. A.; Hadland, E. C.; Lygo, A. C.; Wood, S. R.; Esters, M.; Johnson, D. C. Sub-Monolayer Accuracy in Determining the Number of Atoms per Unit Area in Ultrathin Films Using X-Ray Fluorescence. *Chemistry of Materials* **2018**, *30* (18), 6209–6216. https://doi.org/10.1021/acs.chemmater.8b02591.

(4) Kresse, G.; Furthmüller, J. Efficient Iterative Schemes for *Ab Initio* Total-Energy Calculations Using a Plane-Wave Basis Set. *Phys. Rev. B* **1996**, *54* (16), 11169–11186. https://doi.org/10.1103/PhysRevB.54.11169.

(5) Kresse, G.; Joubert, D. From Ultrasoft Pseudopotentials to the Projector Augmented-Wave Method. *Phys. Rev. B* **1999**, *59* (3), 1758–1775. https://doi.org/10.1103/PhysRevB.59.1758.

(6) Blöchl, P. E. Projector Augmented-Wave Method. *Phys. Rev. B* **1994**, *50* (24), 17953–17979. https://doi.org/10.1103/PhysRevB.50.17953.

(7) Perdew, J. P.; Burke, K.; Ernzerhof, M. Generalized Gradient Approximation Made Simple. *Phys. Rev. Lett.* **1996**, *77* (18), 3865–3868. https://doi.org/10.1103/PhysRevLett.77.3865.

(8) Methfessel, M.; Paxton, A. T. High-Precision Sampling for Brillouin-Zone Integration in Metals. *Phys. Rev. B* **1989**, *40* (6), 3616–3621. https://doi.org/10.1103/PhysRevB.40.3616.

(9) Tkatchenko, A.; Scheffler, M. Accurate Molecular Van Der Waals Interactions from Ground-State Electron Density and Free-Atom Reference Data. *Phys. Rev. Lett.* **2009**, *102* (7), 073005. https://doi.org/10.1103/PhysRevLett.102.073005.